frontiers | Research Topics

Multiphase flow behavior in the deep-stratum and deep-water wellbores

Edited by
Zhiyuan Wang, Weiqi Fu, Huazhou Li and Jianjun Zhu

Published in
Frontiers in Physics

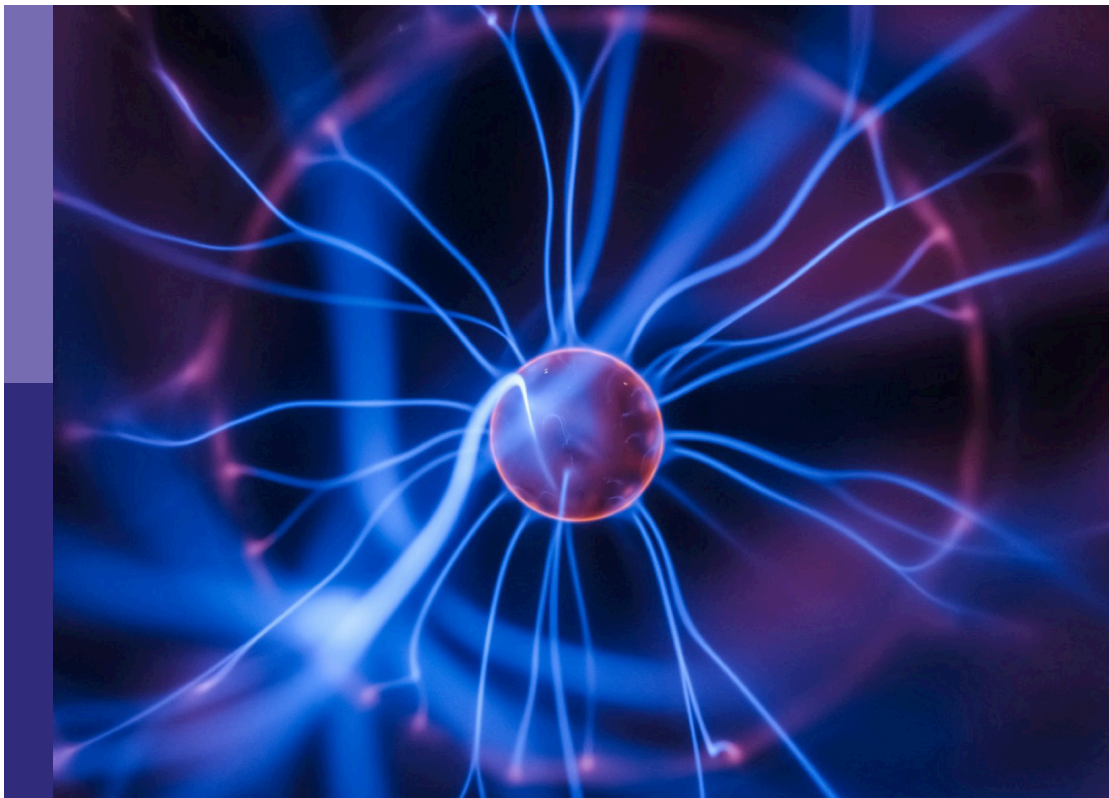

ISSN 1664-8714
ISBN 978-2-83251-686-7
DOI 10.3389/978-2-83251-686-7

About Frontiers

Frontiers is more than just an open access publisher of scholarly articles: it is a pioneering approach to the world of academia, radically improving the way scholarly research is managed. The grand vision of Frontiers is a world where all people have an equal opportunity to seek, share and generate knowledge. Frontiers provides immediate and permanent online open access to all its publications, but this alone is not enough to realize our grand goals.

Frontiers journal series

The Frontiers journal series is a multi-tier and interdisciplinary set of open-access, online journals, promising a paradigm shift from the current review, selection and dissemination processes in academic publishing. All Frontiers journals are driven by researchers for researchers; therefore, they constitute a service to the scholarly community. At the same time, the *Frontiers journal series* operates on a revolutionary invention, the tiered publishing system, initially addressing specific communities of scholars, and gradually climbing up to broader public understanding, thus serving the interests of the lay society, too.

Dedication to quality

Each Frontiers article is a landmark of the highest quality, thanks to genuinely collaborative interactions between authors and review editors, who include some of the world's best academicians. Research must be certified by peers before entering a stream of knowledge that may eventually reach the public - and shape society; therefore, Frontiers only applies the most rigorous and unbiased reviews. Frontiers revolutionizes research publishing by freely delivering the most outstanding research, evaluated with no bias from both the academic and social point of view. By applying the most advanced information technologies, Frontiers is catapulting scholarly publishing into a new generation.

What are Frontiers Research Topics?

Frontiers Research Topics are very popular trademarks of the *Frontiers journals series*: they are collections of at least ten articles, all centered on a particular subject. With their unique mix of varied contributions from Original Research to Review Articles, Frontiers Research Topics unify the most influential researchers, the latest key findings and historical advances in a hot research area.

Find out more on how to host your own Frontiers Research Topic or contribute to one as an author by contacting the Frontiers editorial office: frontiersin.org/about/contact

Multiphase flow behavior in the deep-stratum and deep-water wellbores

Topic editors

Zhiyuan Wang — China University of Petroleum, Huadong, China
Weiqi Fu — China University of Mining and Technology, China
Huazhou Li — University of Alberta, Canada
Jianjun Zhu — China University of Petroleum, Beijing, China

Citation

Wang, Z., Fu, W., Li, H., Zhu, J., eds. (2023). *Multiphase flow behavior in the deep-stratum and deep-water wellbores*. Lausanne: Frontiers Media SA.
doi: 10.3389/978-2-83251-686-7

Table of contents

frontiers | Frontiers in Physics

TYPE Editorial
PUBLISHED 01 February 2023
DOI 10.3389/fphy.2023.1141293

OPEN ACCESS

EDITED AND REVIEWED BY
Alex Hansen,
Norwegian University of Science and Technology, Norway

*CORRESPONDENCE
Weiqi Fu,
weiqi_fu@126.com

SPECIALTY SECTION
This article was submitted to Interdisciplinary Physics, a section of the journal Frontiers in Physics

RECEIVED 10 January 2023
ACCEPTED 24 January 2023
PUBLISHED 01 February 2023

CITATION
Fu W, Zhu J, Li H and Wang Z (2023), Editorial: Multiphase flow behavior in the deep-stratum and deep-water wellbores. *Front. Phys.* 11:1141293.
doi: 10.3389/fphy.2023.1141293

Editorial: Multiphase flow behavior in the deep-stratum and deep-water wellbores

Weiqi Fu[1]*, Jianjun Zhu[2], Huazhou Li[3] and Zhiyuan Wang[4]

[1]State Key Laboratory of Coal Resources and Safe Mining (CUMT), China University of Mining and Technology, Xuzhou, China, [2]School of Mechanical and Transportation Engineering, China University of Petroleum (Beijing), Beijing, China, [3]School of Mining and Petroleum Engineering, University of Alberta, Edmonton, AB, Canada, [4]School of Petroleum Engineering, China University of Petroleum (East China), Qingdao, China

KEYWORDS

hydrodynamic, multiphase flow, flow assurance, drilling and completion, phase transition

Editorial on the Research Topic
Multiphaseflow behavior in the deep-stratum and deep-water wellbores

In recent years, the exploration and development of hydrocarbon energy, such as crude oil, natural gas, and natural gas hydrate, has come to deep-water and deep-stratum regions. The field engineers must face challenges resulting from the multiphase flow of complex fluids under elevated temperature/pressure conditions. These challenges require developing in-depth understanding of multiphase flow in porous media under conditions that typically are not studied in a conventional setting. For example, the temperature and pressure of a 24,000 ft deep wellbore can reach over 200°C and 100 MPa in the Tarim oilfield. In deep-water wells, the wellbore temperature can vary from 4°C to 120°C, while the wellbore pressure can range from 10 to 30 MPa. As the phase state, heat/mass transfer between gas and liquid, and fluid hydrodynamics in the wellbore depend highly on the temperature and pressure conditions, the *Multiphase flow behaviors in deep-stratum and deep-water wellbores* become much more complicated. Different from the conventional oil and gas exploitation, the production of oil and gas from the and deep stratum deep-water regions involves multiple complex physical phenomena, such as phase transition (gas-liquid-solid-supercritical), particle deposition (wax, hydrate, water scale, asphaltene, etc.), changes of heat/mass transfer induced by phase change, and so on. It is, therefore, of high importance to discuss the *Multiphase flow behavior in the deep-stratum and deep-water wellbores*.

This Research Topic aims to explore recent developments in this area and focused on the following two aspects: 1) Numerical simulations of gas-liquid or liquid-solid two-phase flow in porous media, 2) Experiments and simulations of multiphase flow in the pipelines and wellbores. There are a total of 12 articles under this Research Topic.

The following articles report results related to the experiments and simulations of multiphase flow in the pipelines and wellbores. Ge et al. conducted dynamic liquid-carrying experiments and evaluated the performance of some foam discharge agents. The agent ZHY-01 had a better resistance to high temperatures and condensate oils than the agents MA/AA and PESA. Wang et al. creatively developed a multiphase flow model to analyze the gas-liquid two-phase flow behavior in a novel deep-water closed-cycle riserless drilling system. Their study provided a theoretical foundation for the selection of subsea pumping power and optimization of gas injection sites and gas displacement. Zhang et al. developed a theoretical model to calculate the temperature profile of the deep gas well by considering the coupling relationship among the temperature, pressure, and gas properties. Their results help mitigate the trapped

annular pressure (TAP) caused by thermal expansion which is one of the serious challenges for the safe production of a deep gas well. Xu et al. numerically studied the erosion of hydraulic fracturing nozzle in deep wells induced by sand-liquid two phase flow. A three-dimensional model was developed to analyze multiple influencing factors on the nozzle erosion, such as multiphase flow field distribution, flow rate, sand diameter, etc. Their findings help engineers to select proper nozzles in hydraulic jet fracturing applications.

The following articles report results related to the numerical simulations of gas-liquid or liquid-solid two-phase flow in porous media. Gong et al. conducted experiments to study the permeability jail range of tight gas reservoirs through conducting gas-water relative permeability experiments. They showed that the Byrnes model showed a good performance in predicting the permeability jail range of tight gas rocks. Shi et al. developed a numerical two-phase flow model to study water-sediment seepage characteristics in rough rock fractures. Their study revealed the effects of the smooth and rough fracture surfaces on multiple parameters, including sediment volume concentration, sediment particle size and sediment particle mass concentration. Their findings help reveal the disaster-causing mechanism of water-sediment inrush in mining and deep-ground engineering. Zhao et al. conducted a series of foam flooding experiments in core samples to evaluate the impact of foam quality and permeability on foam performance. Considering the effects of foam quality and core permeability, they also developed a mechanistic model to describe the dynamic foam performance. The mechanistic model was applied to match foam flow experimental results in the absence and in the presence of oil. Their model captured the high-quality and low-quality foam regimes observed in previous oil-free foam flow experiments. He et al. developed a comprehensive multiphase flow model to study the flow characteristics of CO_2-containing natural gas streams that are invading a wellbore during the drilling process. Their model considered the effect of gas solubility in water/brine solutions. They found that gas solubility has a significant impact on the monitoring of gas invasion in low permeability reservoirs. Wang et al. proposed an improved multiphase flow model to simulate the complicated gas-liquid-solid multiphase flow that will occur during a deep-water drilling process due to the invasion of formation gas into the wellbore. Their results help detect kicks in deep-water wells and develop effective well-control measures accordingly. Miao et al. proposed a mechanistic model to study the behavior of bubble migration and pressure build-up during a dynamic shut-in procedure in the deep-water drilling process. This study helps quantitatively characterize the hydrate growth behaviors and interphase mass transfer rules of gas bubbles during a dynamic well shut-in procedure. Cao et al. established a model to analyze the changing law of the temperature profile inside a production string. The established model considered the frictional loss caused by a high production rate as well as the variations in gas properties. This model is useful in simulating the temperature profile inside a production string in a high-pressure/high-temperature gas well.

Author contributions

WF was a guest associate editor of the Research Topic and wrote the editorial. JZ, ZW, and HL were guest associate editors of the Research Topic and edited the editorial.

Funding

WF is supported by the National Key Research and Development Program of China (2021YFC2902102), the National Natural Science Foundation of China (NSFC) Youth Fund (52104047), the Natural Science Foundation of Jiangsu Province Youth Fund (BK20210507), CNPC Innovation Found (2021DQ02—1005), and Independent Research Project of State Key Laboratory of Coal Resources and Safe Mining, China University of Mining and Technology (SKLCRSM22X002).

Acknowledgments

We thank the authors of the papers published in this Research Topic for their valuable contributions and the review editors for their rigorous review. We also thank the editorial board of Interdisciplinary Physics in Frontiers in Physics and Economic Geology in Frontiers in Earth Science, especially the Frontiers specialist Fang Chen, for their supports.

Conflict of interest

The authors declare that the research was conducted in the absence of any commercial or financial relationships that could be construed as a potential conflict of interest.

Publisher's note

frontiers | Frontiers in Physics

ORIGINAL RESEARCH
published: 04 May 2022
doi: 10.3389/fphy.2022.887036

Optimization and Performance Evaluation of Foam Discharge Agent for Deep Aquatic Condensate Gas Well

Lei Ge[1], Hailin Cui[2], Yingchao Li[3] and Xiuan Sui[3]*

[1]Sinopec Shengli Petroleum Engineering Company Limited Tarim Branch, Kuerle, China, [2]Drilling Technology Research Institute of Sinopec Shengli Oilfield Service Corporation, Dongying, China, [3]School of Petroleum Engineering, China University of Petroleum, Qingdao, China

The block deep condensate gas reservoir in the basin in the southeast of the South China Sea is a bottom water reservoir and is producing in the late effusion, which faces problems such as scaling, condensate oil–water two-phase flow, and low temperature at the subsea wellhead. The mud line for this kind of gas-well has characteristics including high condensate content in low temperature, high downhole temperature, and injection with a foam discharge agent and scale inhibitor. In this article, the influence of low temperature and scale inhibitor is considered for the first time, and a dynamic liquid-carrying experiment for the optimization and performance evaluation of foam discharge agents was carried out according to these characteristics. The experimental results show that the optimized foam discharge agent, ZHY-01, has good resistance to high temperature and condensate oil, and the optimal concentration of the foam discharge agent is recommended to be 0.25%. Under this concentration, the liquid-carrying capacity of the foam discharge agent decreases slightly by 10.17% at low temperature. The scale inhibitor MA/AA reduced the liquid-carrying capacity by 11.86%, and the scale inhibitor PESA reduced the liquid-carrying capacity by 10.17%. The research results in this article have certain reference significance for the chemical screening and evaluation of the foam drainage gas production process in deep-water condensate gas wells.

Keywords: deepwater condensate gas well, foam drainage gas recovery, high temperature resistant, low temperature resistant, oil resistant, foam discharge agent and scale inhibitor

OPEN ACCESS

Edited by:
Weiqi Fu,
China University of Mining and Technology, China

Reviewed by:
Haiwen Zhu,
University of Tulsa, United States
Yang Zhao,
Missouri University of Science and Technology, United States

****Correspondence:***
Yingchao Li
380013162@qq.com

Specialty section:
This article was submitted to Interdisciplinary Physics, a section of the journal Frontiers in Physics

Received: *01 March 2022*
Accepted: *04 April 2022*
Published: *04 May 2022*

Citation:
Ge L, Cui H, Li Y and Sui X (2022) Optimization and Performance Evaluation of Foam Discharge Agent for Deep Aquatic Condensate Gas Well. Front. Phys. 10:887036. doi: 10.3389/fphy.2022.887036

INTRODUCTION

As an economical and effective means of drainage and production, foam drainage and gas recovery is widely used in major oil and gas fields [1–6]. At present, many scholars at home and abroad focus on the research on the foam discharge agent from the aspects of oil resistance and high temperature resistance for the foam drainage of condensate gas wells [7–9]. The high-content condensate-resistant foam discharge agent PQ-Y developed by Junwen Wu [10] improved the gas field production by 56%. Chaochao Qu [11] developed the oil-resistant foam discharge agent COT, which has been applied in 12 gas wells with good results. Guangfeng Liu [12] selected FDA1, a salt-resistant, oil-resistant, and temperature-resistant foam discharge agent suitable for the S75 well area, with an average daily gas production increase of 35.2%. In addition, the high-efficiency foam discharge agent LH developed by Shiqiang Hu [13], the foam discharge agent FHG-1 developed by

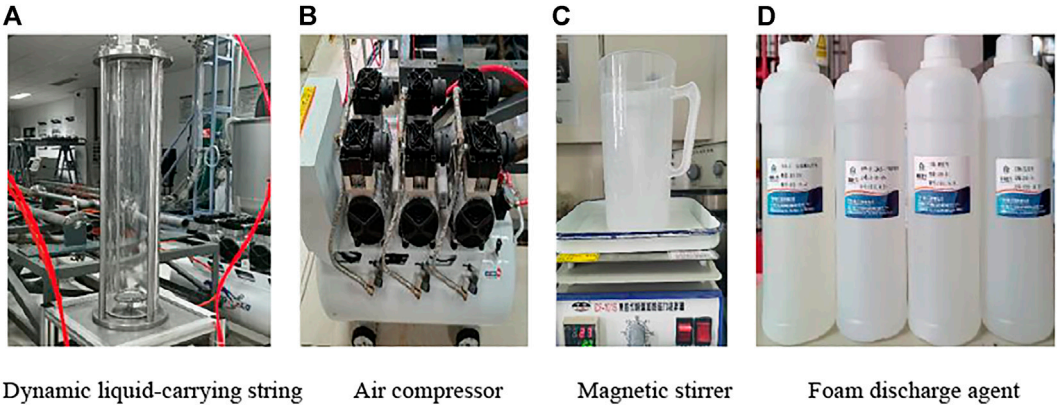

FIGURE 1 | Experimental drugs and related instruments. **(A)** Dynamic liquid-carrying string. **(B)** Air compressor. **(C)** Magnetic stirrer. **(D)** Foam discharge agent.

Qianding Li [14], the foam discharge agent SJF-2 developed by Jifeng Song [15], and the foam discharge agent DC-1 developed by Yang Feng [16] have been proven by experiments to have excellent performance.

The current research status of foam discharge agents shows that many scholars have carried out sufficient experimental research on the foam discharge agent from the aspects of high salinity resistance, high temperature resistance, and oil resistance through the Rosssmile foam instrument, including foaming performance, foam stability, and liquid carrying rate of the foam discharge agent. However, the research on the influencing factors of the liquid carrying rate is not systematic, and the in-depth and optimal evaluation of the currently developed foam discharge agent and the common foam discharge agent on the market does not consider the influence of low temperature under deep-water conditions, and whether its performance is affected when it is co injected with other chemical inhibitors such as scale inhibitors in combination with the actual working conditions of the site.

A deep-water condensate gas reservoir in the Qiongdongnan Basin block in the South China Sea is an edge-bottom water gas reservoir. As the gas field enters the middle and late stages of development, the gas production decreases, and the fluid loading may often occur in the wellbore, affecting normal production. The highest formation temperature of the gas reservoir in this block is 138.7°C, the production wells are subsea wellhead production units [17, 18], the condensate oil content is 10%–50%, and has the characteristics of high temperature and high condensate oil. In addition, the temperature at the mud line of the production well in this block is 4°C. In the production process, due to the risk of scaling in the wellbore, the scale inhibitor is injected through a specific pipeline, and the foam discharge agent needs to be injected through the same pipeline. The low temperature environment at the mud line and the influence of the scale inhibitor on the foam discharge agent need to be fully considered. Therefore, in this study, four kinds of foam discharge agents with certain oil resistance and high temperature resistance were selected. Considering the influence of low temperature and scale inhibitors for the first time, a dynamic liquid-carrying experiment for the optimization and performance evaluation of foam discharge agents was carried out according to these characteristics. The research in this article expands the range of performance evaluation criteria for the foam discharge agents and provides a new perspective for the optimization of foam discharge agents.

MECHANISM OF FOAM DRAINAGE AND GAS RECOVERY

Technical Principle of Foam Drainage Process

Foam drainage gas recovery is a chemical drainage gas recovery method, which manifests as gas–liquid two-phase flow in the production process of gas wells. There are many studies on the gas–liquid two-phase flow [19–21]. The main principle is to inject a certain type of surfactant-based chemical into the bottom of the well that will produce foam when encountering water. When the foam discharge agent encounters water, it generates a large amount of low-density water-containing foam, and under the agitation of natural gas flow, the bottom-hole liquid is converted into a foamy fluid. On the one hand, the formation of foam reduces the density of the flowing medium and reduces the surface tension of water, thereby reducing the required minimum airflow velocity. On the other hand, the relative density of the foam mixed fluid decreases, the friction loss and gravity gradient in the wellbore are reduced, the pressure of the liquid column formed by the accumulated liquid is dispersed, the bottom-hole back pressure is reduced, the production pressure difference of the gas well increases, and the natural gas flow rate in the wellbore increases to achieve the purpose of drainage and gas extraction [22–24]. The performance of the foam drainage agent and quality of the foam directly determine the success of the entire foam drainage construction [25–27].

The Principle of Foam Discharge Agents

Foam discharge agents are mainly surfactants with special molecular structures, and their molecules contain hydrophilic and lipophilic groups, which are amphiphilic. Its drainage function is mainly achieved through the following effects [28].

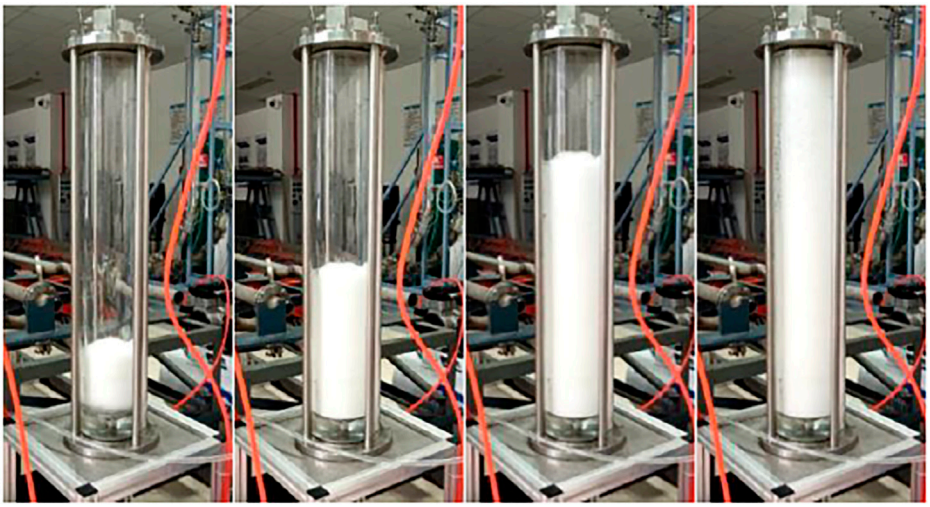

FIGURE 2 | Dynamic process of drainage and gas recovery.

TABLE 1 | Liquid-carrying capacity of different foaming agents at 0.25% concentration.

Type	Concentration/%	Liquid-carrying capacity/ml	Liquid-carrying rate/%	Liquid-carrying capacity/ml	Liquid-carrying rate/%	Standard condition carrying liquid-gas to liquid ratio
		15 min	15 min	1 h	1 h	5 min
AES	0.25	670	67	940	94	537.3
BS12	0.25	540	54	900	90	666.7
ZHY-01	0.25	590	59	920	92	610.2
ZHY-06	0.25	500	50	890	89	720.0

TABLE 2 | Liquid-carrying capacity of different foaming agents at 0.5% concentration.

Type	Concentration/%	Liquid-carrying capacity/ml	Liquid-carrying rate/%	Liquid-carrying capacity/ml	Liquid-carrying rate/%	Standard condition carrying liquid gas to liquid ratio
		15 min	15 min	1 h	1 h	5 min
AES	0.5	710	71	960	96	507.0
BS12	0.5	550	55	915	91.5	654.5
ZHY-01	0.5	600	60	960	96	600.0
ZHY-06	0.5	500	50	930	93	720.0

1) Foaming effect: The foam discharge agent is a kind of surfactant, and only a small amount can make the vertical flow state of gas–water two-phase in oil pipe change evidently. The gas–water two-phase medium is highly foamed during the flow, and the density drops almost 10 times. If the gas-lift formation water previously required at least 5 m/s gas flow velocity, then only 0.5 m/s gas flow velocity is required to take the bottom-hole fluid out of the wellhead in the form of foam.
2) Dispersion effect: In the water-producing gas wells, large and small droplets are dispersed in the airflow, and the degree of agitation and impact of the airflow on the liquid phase determines the dispersing ability. The higher the degree of agitation, the smaller the droplets, and the easier it is to be carried to the wellhead by the airflow. According to the definition of surface tension, when the temperature, pressure, and composition are constant, if the surface area of the system is to increase, work must be carried out on the system; however, the dispersion effect of the airflow on the liquid phase is a process of overcoming surface tension to carry out work. The smaller the dispersion, the larger the specific surface, and the more work carried out. The foam discharge

TABLE 3 | Comparison of liquid-carrying capacity of ZHY-01 aged at room temperature and high temperature at 0.5% concentration.

Concentration/%	Liquid-carrying capacity/ml	Liquid-carrying rate/%	Liquid-carrying capacity/ml	Liquid-carrying rate/%	Standard condition carrying liquid–gas to liquid ratio
	15 min	15 min	1 h	1 h	15 min
0.5	600	60	960	96	600.0
0.5(Ageing)	610	61	950	95	590.2

TABLE 4 | Comparison of liquid-carrying capacity of AES at room temperature and high temperature at 0.5% concentration.

Concentration/%	Liquid-carrying capacity/ml	Liquid-carrying rate/%	Liquid-carrying capacity/ml	Liquid-carrying rate/%	Standard condition carrying liquid–gas to liquid ratio
	15 min	15 min	1 h	1 h	15 min
0.5	710	71	960	96	507.0
0.5 (aging)	620	62	955	95	580.6

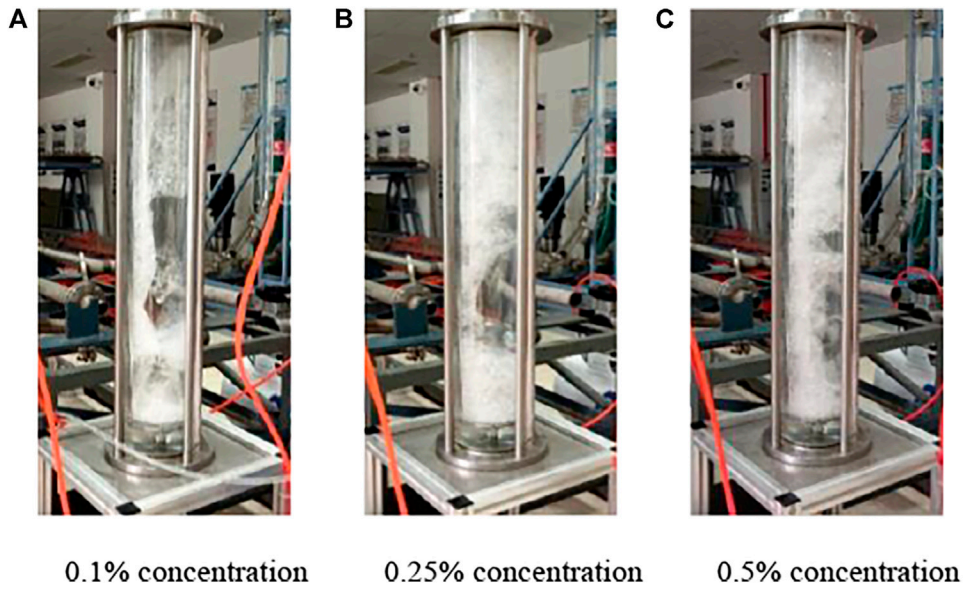

FIGURE 3 | Schematic diagram of the AES liquid carrying process at **(A)** 0.1% concentration. **(B)** 0.25% concentration. **(C)** 0.5% concentration.

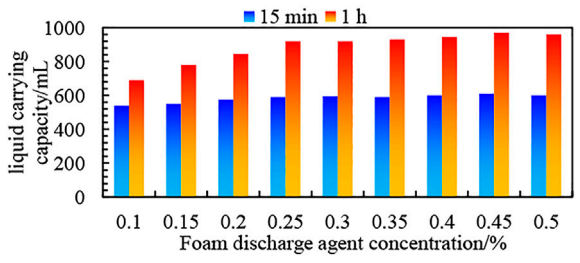

FIGURE 4 | Liquid-carrying capacity of ZHY-01 at different concentrations.

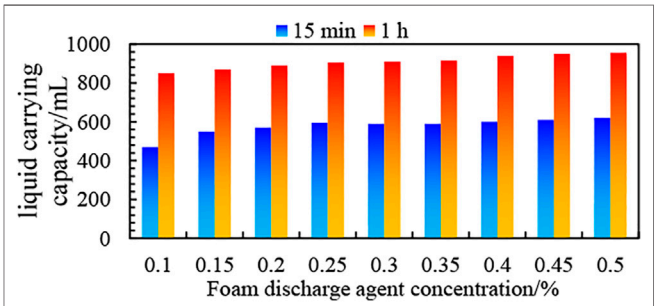

FIGURE 5 | Liquid-carrying energy of AES at different concentrations.

TABLE 5 | Liquid-carrying capacity of ZHY-01 at different concentrations.

Concentration/%	Liquid-carrying capacity/ml	Liquid-carrying rate/%	Liquid-carrying capacity/ml	Liquid-carrying rate/%	Standard condition carrying liquid–gas to liquid ratio
	15 min	15 min	1 h	1 h	15 min
0.1	540	54	690	69	666.7
0.15	550	55	780	78	654.5
0.2	575	57.5	845	84.5	626.1
0.25	590	59	920	92	610.2
0.3	595	59.5	920	92	605.0
0.35	590	59	930	93	610.2
0.4	600	60	945	94.5	600.0
0.45	610	61	970	97	590.2
0.5	600	60	960	96	600.0

TABLE 6 | Liquid-carrying capacity of AES at different concentrations.

Concentration/%	Liquid-carrying capacity/ml	Liquid-carrying rate/%	Liquid-carrying capacity/ml	Liquid-carrying rate/%	Standard condition carrying liquid–gas to liquid ratio
	15 min	15 min	1 h	1 h	15 min
0.1 (aging)	470	47	850	85	766.0
0.15 (aging)	550	55	870	87	654.5
0.2 (aging)	570	57	890	89	631.6
0.25 (aging)	595	59.5	905	90.5	605.0
0.3 (aging)	590	59	910	91	610.2
0.35 (aging)	590	59	915	91.5	610.2
0.4 (aging)	600	60	940	94	600.0
0.45 (aging)	610	61	950	95	590.2
0.5 (aging)	620	62	955	95	580.6

agent is an active agent that can greatly reduce the surface tension of formation water. After the formation water is added with the foam discharge agent and because the surface tension of the liquid phase (formation water) is greatly reduced, if the same dispersion degree is to be achieved, the work carried out will be greatly reduced when the surface tension is greatly reduced.

OPTIMIZATION EXPERIMENT OF FOAM DISCHARGE AGENTS

Experimental Instruments and Procedures

1) Laboratory reagents

Formation water sample, petroleum ether (instead of condensate), and foam discharge agents AES, BS12, ZHY-01, and ZHY-06.

2) Experimental instruments

Dynamic liquid carrying tester (self-made in the laboratory), constant temperature treatment box, air compressor, float flowmeter, magnetic stirrer, electronic balance, stopwatch, measuring cylinder, and conventional glass instruments. A part of the experimental equipment diagram is shown in **Figure 1**.

3) Experimental method

Based on the industry standards "SY/T6465-2000 Evaluation Method of Foaming Agent for Drainage and Gas Extraction" [29] and "SY/T5761-1995 Foaming Agent for Drainage and Gas Recovery CT5-2" [30], a self-made wellbore dynamic liquid carrying measurement device is used.

Combined with the production plan of the target block and formation water data, a formation water solution with a certain degree of salinity is prepared, taking into account the influence of condensate oil (adding petroleum ether) and formation high temperature (transferring the foam discharge agent into a constant temperature box for high-temperature treatment) and the low temperature at the mud line influence (adding the foam discharge agent into the refrigerator for low-temperature treatment). Liquid samples of different concentrations are prepared, and the foam dynamic liquid carrying measurement method is used to calculate the liquid-carrying gas–liquid ratio and liquid-carrying rate. The specific steps are as follows:

a. 1,000 ml of distilled water is measured with a measuring cylinder, transferred into the batching bucket, calibrated the volume scale of 1,000 ml, and then added the solute 27.8 g NaCl in turn while stirring. A certain mass of foaming agent is weighed and added, and a magnetic stirrer is used to make it fully mixed. A glass rod is used

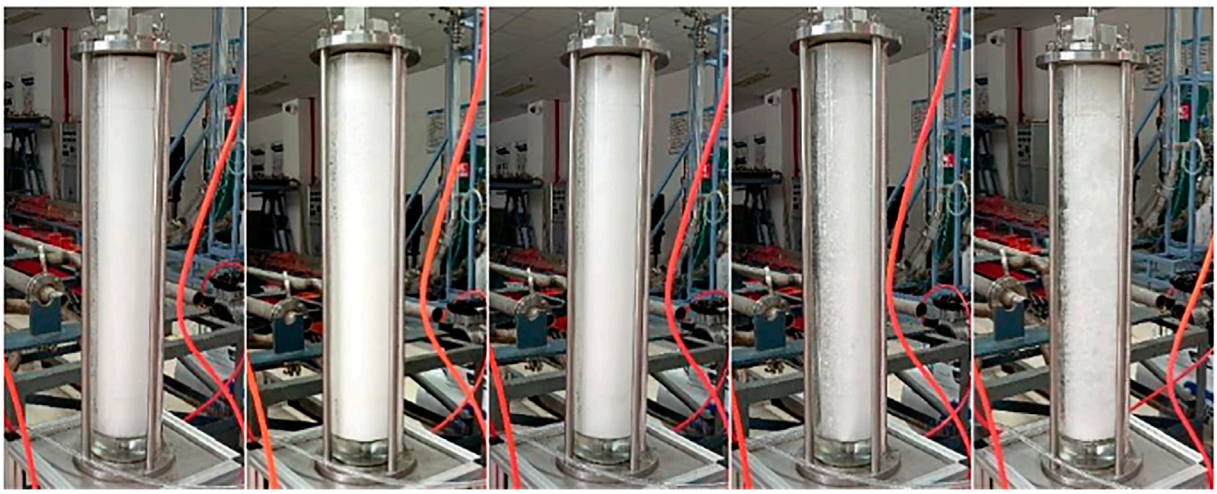

FIGURE 6 | Dynamic bubble drainage and liquid-carrying process under the condensate content of 10%, 20%, 30%, 40%, and 50%.

TABLE 7 | Condensate content of 10%, 20%, 30%, 40%, and 50% foam and liquid-carrying capacity.

Condensate content/%	Liquid-carrying capacity/ml	Liquid-carrying rate/%	Liquid-carrying capacity/ml	Liquid-carrying rate/%	Standard condition carrying liquid–gas to liquid ratio
	15 min	15 min	1 h	1 h	15 min
10	590	59	920	92	610.2
20	590	59	860	86	610.2
30	570	57	830	83	631.6
40	490	48.5	795	79.5	734.7
50	450	45	720	72	800.0

to lead it into the liquid-carrying column, and a certain amount of petroleum ether is added when considering the influence of the condensate oil.

b. Using an air compressor, the reading of the gas flowmeter is adjusted so that the flowmeter value is constant at 4 L/min, and the time is adjusted with a stopwatch.
c. The time period when the foam collection device begins to generate foam is 15 min. After 15 min, the collected foam and liquid are defoamed and the volume is read. Ventilation is continuously provided, and the air compressor is turned off at 1 h. The final collected foam and the liquid volume after the liquid is defoamed are read.
d. The abovementioned steps are repeated two–four times to calculate the average value of the three experimental data, and this average value is the final result.
e. All the instruments are turned off, the experiment is ended, and the instruments are cleaned. The liquid-carrying rate (liquid-carrying rate = liquid carried out/total volume of sample liquid × 100%) is calculated, which is the liquid-carrying capacity of the experimental sample.

Preferred Type of Foam Discharge Agent

According to the results of previous studies on foam discharge agents, the concentration range of the foam discharge agents is generally selected between 0.1–1% [31, 32]. In this article, under the conditions of 0.25 and 0.5% of foam discharge agent concentration, four kinds of foam discharge agents, AES, BS12, ZHY-01, and ZHY-06, were used to evaluate the liquid-carrying performance. The dynamic process of foam drainage and gas production is shown in **Figure 2**, and the experimental results are shown in **Table 1** and **Table 2**.

The experimental results show that the liquid-carrying capacity of the four foam-discharging agents in 15 min is 710, 550, 600, and 500 ml, respectively. Under this condition, the liquid-carrying performance is the worst, and AES and ZHY-01 are initially recommended as the target block.

Evaluation of High Temperature Performance of Foam Discharge Agents

Because the formation temperature of the production well in the target block is as high as 138.7°C, the foam discharge agent is in a high-temperature condition when it is injected into the bottom of the well, and the high temperature may affect the liquid-carrying performance of the foam discharge agent to a certain extent. AES and ZHY-01, which have better performance, were subjected to comparative experiments after high-temperature aging. After the

TABLE 8 | Performance evaluation of ZHY-01 at low temperature.

Type	Concentration/%	Liquid-carrying capacity/ml		Liquid-carrying rate/%		Liquid-carrying capacity/ml		Liquid-carrying rate/%		Standard condition carrying liquid–gas to liquid ratio	
		15 min		15 min		1 h		1 h		15 min	
ZHY-01	0.25	590		59		920		92		610.2	
ZHY-01 (Low temperature)	0.25	530		53		930		93		679.2	

aging treatment (138.7°C) for 24 h of the two kinds of foam discharge agents in a constant temperature box, a dynamic liquid-carrying experiment was carried out. The experimental results are shown in **Tables 3**, **4**.

The experimental results show that at 0.5% concentration, the liquid-carrying capacity of AES decreases after aging, and the liquid-carrying gas–liquid ratio decreases by 12.68% at 15 min. It can be seen that AES is greatly affected by high temperature, but it still has better performance after aging. The liquid-carrying ability of the foam discharge agent ZHY-01 changed little after aging, indicating that the foam discharge agent ZHY-01 was less affected by temperature and was more resistant to high temperature than the foam discharge agent AES.

Determination of Optimal Concentration of Foam Discharge Agents

The injection concentration of the foam discharge agent is an important parameter in the foam discharge process. When the concentration is too low, the amount of foam is insufficient and the drainage effect is poor. When the injection concentration is too high, it is not conducive to reduce the economic cost of foam discharge, and it is not easy to defoam, so the injection concentration of the foam discharge agent should be kept appropriate. For the two selected foam unloading agents ZHY-01 and AES, the dynamic liquid-carrying experiments were carried out under the conditions of 0.1%, 0.15%, 0.2%, 0.25%, 0.3%, 0.35%, 0.4%, 0.45%, and 0.5% of the foam discharge agent. It should be noted that because the foam discharge agent AES is greatly affected by high temperature and mainly plays a role in mixing with the fluid at the bottom of the well, in order to better fit the actual production, the foam discharge agent AES after high-temperature aging is used for different concentrations. However, ZHY-01 was little affected by high temperature, so the experiment was carried out at room temperature.

Through the experiments, it was found that when the concentration of the foam discharge agent was as low as 0.1% and 0.15%, the foaming ability in the later period of liquid-carrying became weak, the amount of foam produced was reduced, and the liquid in the wellbore could not be completely removed, indicating that the liquid-carrying ability in the later period of liquid-carrying was insufficient. When the concentration of the foam discharge agent reaches 0.25% or more, it can be found that the liquid-carrying capacity is still sufficient in the later stage of liquid-carrying, and the liquid in the wellbore is basically carried up. The final liquid-carrying process is shown in **Figure 3**, and the results of the liquid-carrying experiments of the foam discharge agent ZHY-01 and AES under different concentrations are shown in **Figure 4**, **Figure 5**, **Table 5** and **Table 6**.

It can be inferred from the liquid-carrying results of the two foam discharge agents at different concentrations that when the concentration of the foam discharge agent is 0.25%, the liquid-carrying rate does not increase significantly. Considering that the foam discharge agent AES is a light yellow paste, the viscosity is much higher than that of the foam discharge agent ZHY-01, and the dilution process and injection process are limited. Therefore, considering the overall consideration, it is recommended to use the foam discharge agent ZHY-01 as the target block foam discharge agent, with a concentration of 0.25%.

FIGURE 7 | Compatibility test of the foaming agent and scale inhibitor.

Evaluation of Anti-Condensate Performance of Foam Discharge Agents

Considering the coproduction of production well water and condensate oil in the target block, condensate oil, as a natural defoamer, has a weakening effect on the liquid-carrying ability of the foam discharge agent. The condensate content of the production wells in the target block is between 10% and 50%. Therefore, the volume proportion of the condensate is selected as 10%, 20%, 30%, 40%, and 50%. When the optimal concentration of the foam discharge agent was 0.25%, the oil resistance and liquid-carrying evaluation experiment of the selected foam discharge agent ZHY-01 was carried out. **Figure 6** shows the dynamic bubble discharge and liquid-carrying process at the condensate content of 10%, 20%, 30%, 40%, and 50%, and the experimental results are shown in **Table 7**.

The results of the liquid-carrying evaluation experiment show that ZHY-01 has good oil resistance and sufficient liquid-carrying capacity under the condition of 50% oil content. As shown in **Figure 6**, from left to right, the condensate content increases. When the condensate content is 10%, 20%, and 30%, it can be seen that the generated foam is uniform and fine, and the foaming ability is relatively good. When the oil separation content is 40% and 50%, it can be seen that the foam becomes larger and sparser with the naked eye, and the foaming ability decreases.

Evaluation of Anti–Low-Temperature Performance of Foam Discharge Agents

The development well in the target block is a production operation in a deep-water environment, and the ambient temperature at the mud line is relatively low. Considering that high temperature will affect the relevant properties of some foam discharge agents, the foam discharge agent may also be affected by the low ambient temperature during the injection or flowback process. Therefore, in addition to the conventional performance evaluation experiments of the foam discharge agent at high temperature, it is still necessary to analyze the performance of the foam discharge agent at low temperature. After placing the foam discharge agent ZHY-01 in a refrigerator (0°C) for 24 h, at its optimal concentration of 0.25%, the liquid-carrying experiment was carried out to evaluate the low-temperature performance of the foam discharge agent. The experimental results are shown in **Table 8**. The experimental results show that low temperature slightly reduces the liquid-carrying capacity of the foam discharge agent, and the liquid-carrying rate decreases by 10.17%, but the liquid-carrying capacity meets the demand.

Evaluation of the Compound Properties of Foam Discharge Agents and Scale Inhibitors

Considering that there is a certain scaling risk in the production wells in the study block in the middle and later stages of production, the physical antiscaling method is limited by the structure of the wellbore and the difficulty in the operation of the technological antiscaling method, combined with the developmental characteristics of deep-water gas wells; it is recommended to adopt the chemical antiscaling method with low cost, good effect, and wide application range to prevent and control wellbore fouling and flow obstacles, guaranteeing the normal production of deep-water gas wells. The predicted scaling risk in the study block is recommended to use antiscalants to inject the pipeline for chemical scale prevention, and the risk of liquid loading in the case well is formulated. In the case of long-term foam drainage and gas production plan, the foam drainage agent can be injected into the bottom hole through the scale inhibitor pipeline. When the scale inhibitor and the foam discharge agent are mixed and injected, it is necessary to fully consider whether the scale inhibitor has an influence on the performance of the foam discharge agent. Therefore, it is necessary to carry out the compound experiment of scale inhibitors and foam discharge agents. For the concentration of the 0.25% foam discharge agent ZHY-01, the compatibility test was carried out with two excellent scale inhibitors, MA/AA and PESA (60 mg/L), selected from the research block. The results are shown in **Figure 7**. The compatibility test results show that ZHY-01 has good compatibility with the scale inhibitor PESA and scale inhibitor MA/AA. After compounding with PESA, the solution becomes colorless and transparent. After compounding with MA/AA, the solution becomes colorless and transparent. The solution turned slightly white, and the whole solution was transparent, and no obvious precipitate was formed. On this basis, the liquid-carrying

TABLE 9 | Evaluation results of the liquid-carrying performance of ZHY-01 combined with the scale inhibitors MA/AA and PESA.

Type	Concentration/%	Liquid-carrying capacity/ml	Liquid-carrying rate/%	Liquid-carrying capacity/ml	Liquid-carrying rate/%	Standard condition carrying liquid–gas to liquid ratio
		15 min	15 min	1 h	1 h	15 min
ZHY-01(Before compounding)	0.25	590	59	920	92	610.2
ZHY-01 + MA/AA	0.25	520	53	900	90	692.3
ZHY-01 + PESA	0.25	530	53	910	91	679.2

experiment, after compounding, was carried out, and the experimental results are shown in **Table 9**.

The test results show that both the antiscalants reduce the liquid-carrying performance of the foam discharge agent. The addition of the scale inhibitor MA/AA reduces the liquid-carrying rate by 11.86%, and the scale inhibitor PESA reduces the liquid-carrying rate by 10.17%. In comparison, the scale inhibitor MA/AA has a great influence on the liquid-carrying performance of the foam discharge agent ZHY-01.

CONCLUSION AND OUTLOOK

1) Considering the characteristics of high formation temperature and high yield of the condensate oil in the study block, the high-temperature performance evaluation, optimal concentration screening, and anti-condensate oil performance comparison of the four existing foam discharge agents with good performance were carried out. In the end, ZHY-01 was selected as the foam discharge agent for the gas well at a risk of liquid loading in this block, and the optimal concentration was 0.25%.
2) In addition to the conventional performance evaluation of the foam discharge agent, such as high temperature resistance and anticondensation oil, this study takes into account the low production temperature of the subsea wellhead of the production well; considering the low production temperature of the subsea wellhead of the production well, a comparative experiment was carried out for the first time on the performance evaluation of the anti-low temperature of the foam discharge agent. The experimental results show that low temperature makes the liquid-carrying ability of the foam discharge agent ZHY-01 decrease slightly, and the decrease rate is 10.17%.
3) Considering the characteristics of coinjection of the foam discharge agent and scale inhibitor in the later stage of production, the actual comparative experiment of the dynamic liquid-carrying evaluation after the combination of the foam discharge agent with the scale inhibitor MA/AA and scale inhibitor PESA was carried out for the first time. The experimental results show that both the antiscalants reduce the liquid-carrying performance of the foam discharge agent. The addition of the scale inhibitor MA/AA reduces the liquid-carrying capacity by 11.86%, and the scale inhibitor PESA reduces the liquid-carrying capacity by 10.17%.
4) The research in this article expands the range of performance evaluation criteria of the foam discharge agents, provides a new viewpoint for the optimal study of the foam discharge agents, and provides effective theoretical support for the foam-draining liquid–gas recovery process of production wells in the deep-water condensate gas reservoirs.

DATA AVAILABILITY STATEMENT

The original contributions presented in the study are included in the article/Supplementary Material, further inquiries can be directed to the corresponding author.

AUTHOR CONTRIBUTIONS

LG: conceptualization, methodology, supervision, writing-original draft, and writing—review and editing. HC: data curation, resources, investigation, experimental data analysis, and writing—review and editing. YL: investigation, methodology, experimental operation, experimental data sorting, and writing—review and editing. XS: investigation, methodology, experimental operation, and writing—review and editing.

REFERENCES

1. Jia H, Zhu J, Cao G, Lu Y, Lu B, Zhu H. *A Model Ranking Approach for Liquid Loading Onset predictions[C]* (2021). SPE209578.
2. Jelinek W, Schramm LL. *Improved Production from Mature Gas wells by Introducing Surfactants intowells[J]*. Doha: International Petroleum Technology conference (2005).
3. Price BP, Gothard B. *Foam Assisted Lift-Importance of Selection and application[C]* (2007). SPE106465.
4. Campbell S, Ramachandran S, Bartrip K. *Corrosion Inhibition/foamer Combination Treatment to Enhance Gas production[C]* (2001). SPE67325.
5. Liu Q, Jiang J, Shi Q, Feng M Analysis of the Application Effect of Liquid Drainage and Gas Recovery Methods at home and Abroad[J]. *Nat Gas Exploration Develop* (2006) 2006(03):51-4–65+73.
6. Yu Y. *Research on Gas Recovery Technology of Gas Well Drainage in Offshore Oil and Gas fields[D]*. Daqing, China: Daqing Petroleum Institute (2009).
7. Uddin MFM, Tayyab I, Koondhar NH, Ahmed QI, Soomro AA. *Production Optimization of Foam Assisted Lift (FAL) wells and Evaluation of Good and Bad Practices to Ensure Maximum production[C]* (2015). SPE181121.
8. Nimwegen DV, Portela LM, Henkes RAWM. *The Effect of Surfactants on Vertical Air/water Flow for Prevention of Liquid Loading[C]* (2015). SPE164095.
9. Solesa M, Sevic S. Production Optimization Challenges of Gas wells with Liquid Loading Problem Using Foam Discharge Agents (Russian)[J]. *Der Anaesthesist* (2006) 52(6):516–21.
10. Wu J, Zhang R, Wang H, Cen X, Jia W, Xiao Z, et al. Development and Field Application of High-Content Condensate-Resistant Foam-Removing Agent [J]. *Oilfield Chem* (2019) 36(03):508–12+534.
11. Qu C, Liu Z, Yin H, Lu G, Li Z, Feng Y, et al. A New Type of Anti-condensation Oil Bubble Discharge Agent for Drainage and Gas Production[J]. *Chin J Pet* (2020) 41(07):865–74.
12. Liu G, Gao Y, Zhang J, Chen S, Li X, et al. Development of Salt-Resistant, Oil-Resistant and Temperature-Resistant Foam-Removing Agent in S75 Well Area of Sulige Gas Field[J]. *Spec oil gas reservoirs* (2015) 22(02):133-6–157-8.
13. Hu S, Liu J, Li Y, Ye C, Du X, et al. Study on the Foam Performance of a New Type of High-Efficiency Foaming Agent LH[J]. *Nat Gas Industry* (2007) 2007(01):102–4+159.
14. Li Q, Song J, Xue D, Li H, et al. Research on an Oil-Resistant and Methanol-Resistant Gas Well Foam Removal Agent [J]. *Oilfield Chem* (2013) 30(01): 29–32.
15. Song J. *Research on the Selection of Foaming Agents and Optimization of Filling System in Block Su 20 of Sulige Gas Field [D]*. Xi'an, China: Xi'an Petroleum University (2013).
16. Feng Y, Li Q, Guan C, Dong J, Guo L, et al. Performance Evaluation of Amine Oxide Type Foaming Agent for Gas wells in Northern Shaanxi [J]. *Chem Technol Develop* (2020) 49(10):12–4.
17. Wang Z, Zhang J, Meng W, Sun B, Sun J, Wang J, et al. Formation, Deposition Characteristics and Control Methods of Gas Hydrate in Deep Water Gas Wells [J]. *Chin J Pet* (2021) 42(06):776–90.
18. Fu W, Wang Z, Chen L, Sun B. Experimental Investigation of Methane Hydrate Formation in the Carboxmethylcellulose (CMC) Aqueous Solution. *SPE J* (2020) 25:1042–56. doi:10.2118/199367-pa
19. Fu W, Yu J, Xiao Y, Wang C, Huang B, Sun B. A Pressure Drop Prediction Model for Hydrate Slurry Based on Energy Dissipation under Turbulent Flow Condition. *Fuel* (2022) 311:122188. doi:10.1016/j.fuel.2021.122188
20. Fu W, Yu J, Xu Y, Wang C, Huang B, Sun B. *A Pressure Drop Prediction Model for Hydrate Slurry Based on Energy Dissipation under Laminar Flow condition [C]* (2022). SPE209586.
21. Fu W, Wang Z, Zhang J, Cao Y, Sun B. Investigation of Rheological Properties of Methane Hydrate Slurry with Carboxmethylcellulose. *J Pet Sci Eng* (2020) 184:106504. doi:10.1016/j.petrol.2019.106504
22. Zhu J, Zhu H, Wang Z, Zhang J, Cuamatzi-Melendez R, Farfan JAM, et al. Surfactant Effect on Air/water Flow in a Multistage Electrical Submersible Pump (ESP). *Exp Therm Fluid Sci* (2018) 98:95–111. doi:10.1016/j.expthermflusci.2018.05.013
23. Zhao Q, Zhu J, Cao G, Zhu H, Zhang H-Q. Transient Modeling of Plunger Lift for Gas Well Deliquification. *SPE J* (2021) 26(05):2928–47. doi:10.2118/205386-pa
24. Wang X. *Optimization of Foam Drainage Technology for Low-Pressure Gas wells in Daniudi Gas field[D]*. Xi'an, China: Xi'an Shiyou University (2014).
25. Kanda M, Schechter RS. Mechanism of Foam Formation in Porous Media[J]. *AmericanInst Mining Metallurgical Pet Eng Dallas* (1976).
26. Sun W, Littleton HE, Bates CE. Formation Mechanism of Gas Cavity Defects in Lost Foam Iron Castings. *Int J Cast Met Res* (2003) 16(6):549–53. doi:10.1080/13640461.2003.11819634
27. Xiao C. Evaluation of Foam Discharge Agent for Foam Complex Flooding[J]. *Adv Fine Petrochemicals* (2008).
28. Qin M. *Research and Application of Foam Drainage Gas Recovery technology [D]*. Daqing, China: Northeast Petroleum University (2011).
29. SY/T 6645-2000. *Foam Discharge Agent Evaluation Method for Foam Drainage Gas recovery[S]* (2000).
30. SY/T 5761-1995. *Foam Discharge Agent CT5-2 for Drainage Gas recovery[S]* (1995).
31. Zhang S. *Performance Evaluation Method of Foaming Agent and its Application in Sulige Gas field[D]*. Xi'an, China: Xi'an Petroleum University (2018).
32. Li A. *Research on the Selection of Foam and Discharge Agent and Optimization of Filling System in Su 20 block[D]*. Xi'an, China: Xi'an Petroleum University (2014).

Conflict of Interest: Author LG was employed by Sinopec Shengli Petroleum Engineering Company Limited Tarim branch. Author HC was employed by Drilling Technology Research Institute of Sinopec Shengli Oilfield Service Corporation.

The remaining authors declare that the research was conducted in the absence of any commercial or financial relationships that could be construed as a potential conflict of interest.

frontiers | Frontiers in Physics

ORIGINAL RESEARCH
published: 10 May 2022
doi: 10.3389/fphy.2022.889359

Numerical Simulation of Water-Sediment Two-Phase Seepage Characteristics and Inrush Mechanism in Rough Rock Fractures

*Xuyang Shi[1], Ming Li[2], Yu Han[2], Qingxiang Cai[1], Zhanqing Chen[2], Yanlong Chen[2] and Dan Ma[1]**

[1]School of Mines, China University of Mining and Technology, Xuzhou, China, [2]State Key Laboratory for Geomechanics and Deep Underground Engineering, China University of Mining and Technology, Xuzhou, China

The water-sediment two-phase flow in the rough fracture is one of the main causes of water-sediment inrush. In this study, numerical simulation models of the water-sediment two-phase flow in the smooth and rough fractures were established by ANSYS Fluent software based on the seepage theory; the mechanical properties of the water-sediment two-phase flow under different conditions were systematically investigated, and the influence laws of the surface morphology of the fracture on sediment volume concentration, sediment particle size, and sediment particle mass density were analyzed. In addition, the influence laws of the sediment volume concentration, sediment particle size, and sediment particle mass density on the absolute value of the pressure gradient, mean velocity of the fluid, and fluid turbulent kinetic energy were also illustrated from the perspective of sediment particle distribution. Research shows that during the water-sediment flow in the smooth fracture, the absolute value of pressure gradient Gp, the sediment volume concentration Φ, the sediment particle size D_p, and the sediment mass density ρ_p are approximately linear, and the linearity of G_p and D_p is the lowest; during the water-sediment flow in the smooth fracture, the mean velocity v of the continuous-phase fluid rarely changes with Φ, D_p, and ρ_p. However, during the water-sediment flow in the rough fracture, v is greatly affected by Φ, D_p, and ρ_p. During the water-sediment flow in the smooth fracture, the fluid turbulent kinetic energy kt decreases with the increase of ρ_p and Φ and decreases with the decrease of ρ_p. During the water-sediment flow in the rough fracture, k_t is significantly affected by Φ, Dp, and ρ_p, which was manifested in the changes of curve shapes and deviation of the extreme points.

Keywords: water-sediment, two-phase flow, fracture characteristics, seepage characteristics, fluid turbulent kinetic energy

OPEN ACCESS

Edited by:
Zhiyuan Wang,
China University of Petroleum, China

Reviewed by:
Guangyao Si,
University of New South Wales, Australia
Yan Peng,
China University of Petroleum, China

****Correspondence:***
Dan Ma
dan.ma@cumt.edu.cn

Specialty section:
This article was submitted to Interdisciplinary Physics, a section of the journal Frontiers in Physics

Received: *04 March 2022*
Accepted: *05 April 2022*
Published: *10 May 2022*

Citation:
Shi X, Li M, Han Y, Cai Q, Chen Z, Chen Y and Ma D (2022) Numerical Simulation of Water-Sediment Two-Phase Seepage Characteristics and Inrush Mechanism in Rough Rock Fractures. Front. Phys. 10:889359. doi: 10.3389/fphy.2022.889359

1 INTRODUCTION

Although coal resources are abundant in Northwest China, coal mining in this area is relatively difficult because of the fragile ecological environment and the thick sediment layer on the coal seam [1–4]. During the exploitation process of shallow coal seams, most faults are directly connected with overburden aquifers; in some extreme cases, subsidence areas may be directly connected with aquifers. At this point, the surface sediment layers and aquifers will be mixed;

when the mixture flows underground, water-sediment inrush accidents will be induced [5–9]. Therefore, water-sediment flow characteristics in fractures should be comprehensively investigated so as to understand the disaster-causing mechanism of water-sediment inrush accidents and prevent the occurrence of water-sediment inrush accidents.

The physical and mechanical characteristics of the water-sediment mixture and the fracture surface characteristics are two key factors affecting the water-sediment two-phase flow [10, 12]. The characteristics of the water-sediment mixture, such as sediment volume concentration, sediment particle size, and sediment particle density, have been studied through laboratory experiments and theoretical analysis [13–17]. Jiang et al. investigated the flowing properties of crushed red sandstone with different particle sizes. It was concluded that the broken rocks with finer particles were likely to become unstable [13]. Through a self-developed seepage test system, Zhang et al. conducted the indoor tests and determined the optimal sand-filtration rate [18]. Pu et al. analyzed the influence of particle size grading on water-sediment seepage and found that the flow and height of the water-sediment mixture can be effectively reduced by decreasing the height of the aquifer by drilling [19].

The water-sediment mixtures show significant differences in fractures with different surface characteristics. In the initial stage of the research, parallel smooth fractures were prefabricated in these experiments. With the gradual progress of technology, the water-sediment two-phase flow in rough fractures has been studied, and some results have been achieved [20–24]. Researchers also have studied the influence of fracture aperture, directions, and amounts of fractures on the water-sediment two-phase flow [25–28]. In real working conditions, the factors affecting the water-sediment two-phase seepage are much more complex than those in the indoor seepage tests. For example, vortexes around the concave fracture surface greatly affect the pressure, sediment concentration distribution, and energy consumption during the water-sediment flow in fractures [29–36]. Although pressure gradient and flow rate can be used to analyze and invert the whole flow process in the laboratory tests, the evolution of water-sediment two-phase seepage in fractures cannot be illustrated. Therefore, it is necessary to adopt the numerical simulation method to study the water-sediment two-phase seepage in fractured rock masses.

In this study, considering the principle of water-sediment two-phase seepage, the mechanical models of water-sediment two-phase flow in smooth and rough fractures were established, and the numerical simulation experiment was performed by ANSYS Fluent. In addition, the influence of sediment volume concentration, sediment particle size, sediment mass density on pressure gradient, mean velocity distribution, and turbulent kinetic energy distribution was analyzed comprehensively. This study aims to reveal the disaster-causing mechanism of the water-sediment inrush and provide a reference for the precursor research of water-sediment inrush.

2 EXPERIMENTAL PRINCIPLE AND MODEL OVERVIEW

2.1 Principles of Water-Sediment Two-Phase Flow

2.1.1 Euler–Lagrange Method

The material description (or Lagrangian description) and spatial description method (or Eulerian description) are the main methods describing the motion of a continuous medium. In this study, the volume fraction of the sediment phase was less than 10%; thus, water was treated as the continuous phase and sediment particles were treated as the discrete phase. Specifically, the water phase was described by the conservation equation and transport equation of the turbulence in the Euler coordinate system, and the sediment movement was simulated by the discrete phase model (DPM) in the Lagrange coordinate system [37, 38]. It should be noted that the temperature change of the flow field [38] was ignored and water was treated as an incompressible fluid in this study.

2.1.2 Continuous Phase Governing Equations

As mentioned previously, water is treated as the continuous phase, and its flow is governed by the law of conservation. The governing equations included the mass conservation equation and momentum conservation equation. The former can be expressed by **Eq. 1**.

$$\frac{\partial \rho}{\partial t} + \frac{\partial}{\partial \vec{X}}\left(\rho \vec{v}\right) = S_m. \tag{1}$$

The latter can be expressed by **Eq. 2**.

$$\frac{\partial\left(\rho \vec{v}\right)}{\partial t} + \vec{\nabla}\cdot\left(\rho \vec{v}\vec{v}\right) = \vec{\nabla}\cdot\overleftrightarrow{\Sigma} + \rho\vec{\mathrm{g}} + \vec{S}_{DPM}, \tag{2}$$

where $\overleftrightarrow{\Sigma}$ is the stress tensor, $\overleftrightarrow{\Sigma} = \sigma_{ij}\vec{e}_i\vec{e}_j$; $\vec{g}$ is the acceleration of gravity; and $\vec{S}_{DPM}$ is the momentum source term reflecting the interaction between the sediment particle and water.

2.1.3 Discrete Phase Governing Equations

Both the rotation and moving of sediment particles should be considered to study the water-sediment flow in fractures. Based on the momentum theorem and the moment of momentum theorem, the governing equations of the discrete phase particles can be expressed by **Eqs 3–5** in the Lagrange coordinate system:

$$\frac{dX_{pi}}{dt} = v_{pi}, \tag{3}$$

$$m_p\frac{dv_{p_i}}{dt} = F_{Di} + m_p\frac{g_i\left(\rho_p - \rho\right)}{\rho_p} + \widehat{F}_{\mathrm{i}}, \tag{4}$$

$$I_{ij}\frac{d\omega_{pj}}{dt} + \varepsilon_{ijk}I_{kl}\omega_j\omega_l = M_i, \tag{5}$$

where Ω_i is the angular velocity component of the water relative to the particle; F_{Di} is the drag force component; Re_p is the Reynolds number of the particle; C_D is the

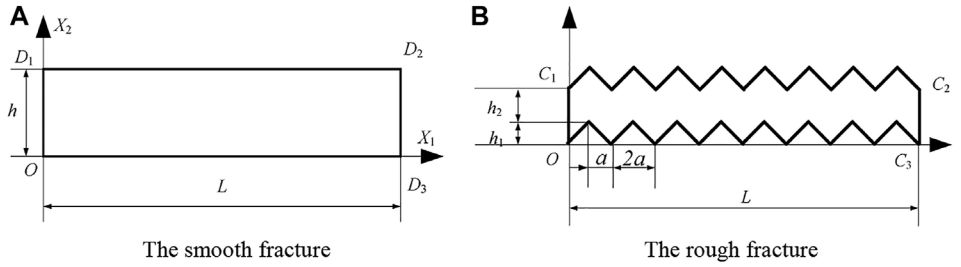

FIGURE 1 | Flow domains of fractures. **(A)** Smooth fracture; **(B)** rough fracture.

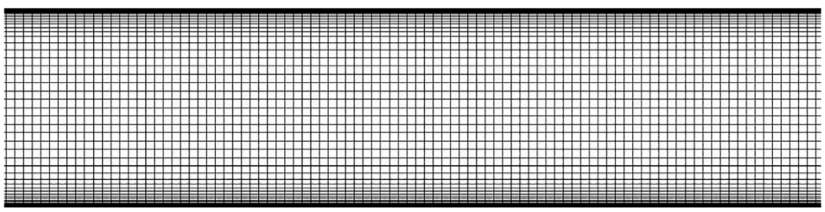

FIGURE 2 | Grids of the smooth fracture.

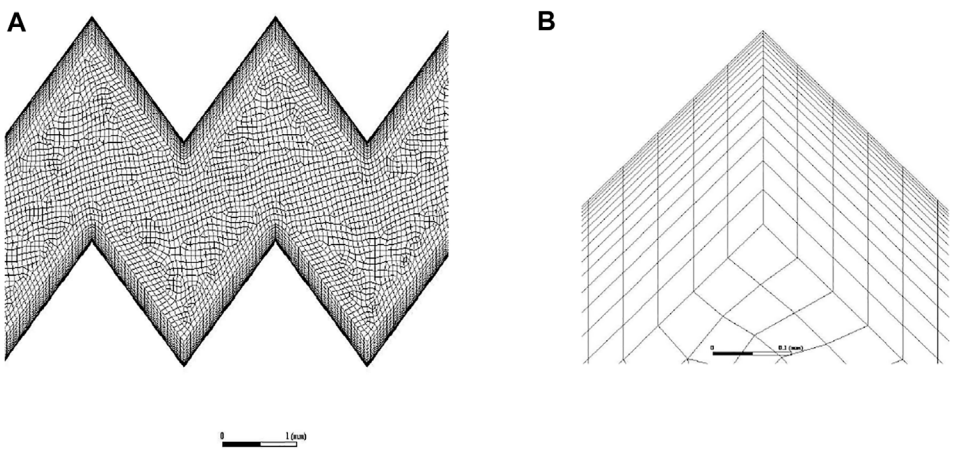

FIGURE 3 | Grids of the rough fracture. **(A)** Grids of the rough fracture; **(B)** boundary grids of the rough fracture.

dragging force coefficient; and M_i is the torque applied to the particle and is proportional to the angular velocity of the particle.

2.2 Models of the Water-Sediment Two-Phase Flow in Fractures

In the numerical simulation of water-sediment flow in fractures, three basic assumptions are proposed as follows: (1) water is incompressible, and its density is a constant; (2) the sediment particle is assumed to be a rigid sphere of fixed radius, without obvious damage; and (3) the flow rate is uniformly distributed around the cross section of the fracture inlet, and the fluid velocity of the discrete phase sediment particle is the same as that of the continuous phase particle.

Figure 1 shows the computational domains of the smooth and rough fractures. In **Figure 1A**, the water-sediment flow in the area is defined by two parallel smooth fracture surfaces. The distance between the two surfaces is h, and the length of the fracture is L. The projection of the upper and lower surfaces on the OX_1X_2 section is a straight line. The boundary of the flow domain Ω comprises the inlet section $\overline{OD_1}$, the upper surface $\overline{D_1D_2}$, the outlet surface $\overline{D_2D_3}$, and the lower surface $\overline{D_3O}$. In **Figure 1B**, the water-sediment flow in the area is defined by two coincident

TABLE 1 | Material properties.

	Water	Sediment particles
Density/kg·m^{-3}	998.2	2650
Dynamic viscosity/kg·m^{-1}·s^{-1}	1.003 × 10^{-3}	—
Elastic modulus/GPa	—	55.9
Poisson's ratio	—	0.13
Particle size/mm	—	0.04

surfaces. The projections of the upper and lower surfaces on the OX_1X section are broken lines, dividing the fracture surface into 50 equal broken line segments FL_i^u and FL_i^d, where $i = 1, ...50$. The boundary of the flow domain Ω consists of the inlet section $\overline{OC_1}$, upper surface $\cup \sum_{i=1}^{50} FL_i^u$, outlet section $\overline{C_2C_3}$, and lower surface $\cup \sum_{i=1}^{50} FL_i^d$.

ANSYS Fluent 17.0 numerical simulation software was used to establish models of the water-sediment two-phase flow in smooth and rough fractures. Since the boundary of the smooth fracture model was relatively regular, structured grids were used for division in the ANSYS ICEM CFD. The evenly distributed grid nodes were arranged at the inlet to make the sediment particles uniformly distributed along the X_2 direction. In addition, the Stress-Omega RSM turbulence model was used in this study. It was required that y^+ (the dimensionless distance to the wall) at the first layer of grid nodes near the wall was approximately 1; thus, fine grids were arranged. After calculation, y^+ was checked. To ensure the accuracy and efficiency of the calculation results, after the grid independence test, the boundary layer grid size was set as 0.005 mm, and the global grid size was 0.08 mm. **Figure 2** shows the final division result.

Considering the severe bending of the wall boundary of the rough fracture model, hybrid grids were chosen for division in the meshing module on ANSYS Workbench, as shown in **Figure 3**. Multilayer structured grids were arranged in the boundary layer, and unstructured quadrilateral-dominant grids were used in other domains. After the division, y^+ was checked and a grid-independent test was conducted. The total number of the grids was 145,000, as shown in **Figure 3A**. **Figure 3B** shows the grids in the boundary layer.

The parameters were adjusted according to the results of the laboratory test, and the material properties were determined, as shown in **Table 1**. Similarly, the interaction parameters between the sediment particle and the wall were determined. The friction coefficient, normal restitution coefficient, and tangential restitution coefficient were 0.45, 0.2, and 0.9, respectively. The interaction parameters among sediment particles were fixed. The static friction coefficient, sliding friction coefficient, and restitution coefficient were 0.3, 0.2, and 0.05, respectively.

2.3 Numerical Simulation Schemes and Methods

In this study, the sediment volume concentration, sediment particle size, and sediment mass density were taken as variables to investigate the evolution characteristics of the pressure gradient, mean velocity distribution, and turbulent kinetic energy distribution of the water-sediment two-phase flow under two fracture surface conditions. When a variable was used, the other two variables were fixed. **Table 2** shows the specific values.

In particular, the inlet segment (X_1 = 5 mm), the middle segment (X_1 = 50 mm) of the smooth fracture surface, the bending segment (X_1 = 5 mm), and the parallel segment (X_1 = 50.5 mm) of the rough fracture surface were selected as the typical segments to comprehensively study the change laws of mean velocity distributions. Similarly, the inlet velocity was fixed as 0.869 m/s, the observation time node t was 0.3 s, and the number of variables was reduced.

3 ANALYSIS OF THE NUMERICAL SIMULATION RESULTS

3.1 Change Law of the Absolute Value of the Pressure Gradient

Pressure gradient is one of the main parameters describing the seepage, which can reflect the pressure change along the flow direction. **Figure 4** shows the absolute value of pressure gradient–sediment volume concentration (G_p–Φ) curves. In **Figure 4A**, when the water-sediment flowed in the smooth fracture, with a gradual increase of Φ, G_p decreased linearly from 6.51 kPa m^{-1} to 6.39 kPa m^{-1}, decreasing by 1.72%. In **Figure 4B**, during the flow of water-sediment in the rough fracture, with a gradual increase of Φ, G_p first increased and then decreased. When Φ increased from 0 to 1.02%, G_p sharply decreased from 191.68 kPa m^{-1} to 181.57 kPa m^{-1}, decreasing by 5.27%. When Φ increased from 1.02 to 4.06%, G_p gradually increased from 181.57 kPa m^{-1} to 185.08 kPa m^{-1}, increasing by 1.93%. Through comparisons, it can be found that under the same conditions, the absolute value of the pressure gradient of the water-sediment flow in the rough fracture was about 40 times that in the smooth fracture. In addition, the change characteristics of the absolute value of the pressure gradient with the volume

TABLE 2 | Parameters in the numerical simulation.

No	Variables		
	Sediment volume concentration (Φ)	Sediment particle size (ρ_p)	Sediment mass density (D_p)
I	1.02%, 2.07%, 3.04%, 4.06%	2650 kg/m^3	2650 kg/m^3
II	2,650 kg/m^3	0.01 mm, 0.02 mm, 0.08 mm, 0.12 mmm	2650 kg/m^3
III	2,650 kg/m^3	2,650 kg/m^3	1,500 kg/m^3, 2,650 kg/m^3, 3,500 kg/m^3, 4,500 kg/m^3

Note: The italic values are the variables.

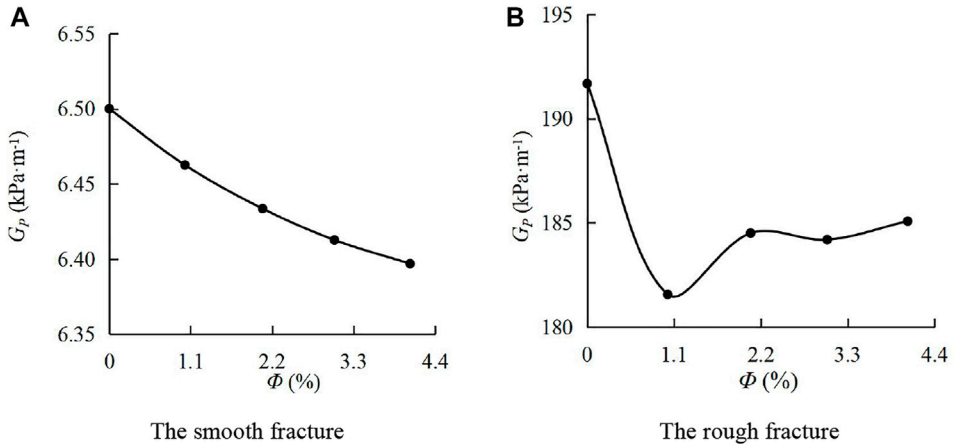

FIGURE 4 | Absolute value of the pressure gradient–volume concentration of sediment particle curves. **(A)** Smooth fracture; **(B)** rough fracture.

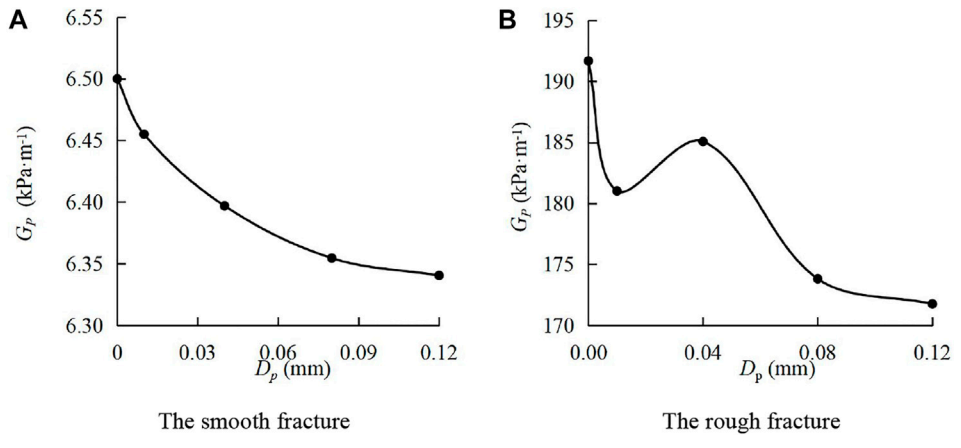

FIGURE 5 | Absolute value of the pressure gradient–sediment particle size curves. **(A)** Smooth fracture; **(B)** rough fracture.

concentration of sediment particles were different under different fracture conditions. It indicates that the fracture surface morphology affects the influence of the volume concentration of sediment particles on the pressure gradient.

Figure 5 shows the absolute value of the pressure gradient–sediment particle size (G_p-D_p) curves. In **Figure 5A**, during the water-sediment flow in the smooth fracture, G_p gradually decreased in a nonlinear form with the increase of D_p. As D_p increased from 0 to 0.12 mm, G_p quickly decreased from 6.51kPa m^{-1} to 6.34 kPa m^{-1}, decreasing by 2.61%. In **Figure 5B**, during the water-sediment flow in the rough fracture, G_p first decreased, then increased, and decreased again. As D_p increased from 0 to 0.12 mm, G_p rapidly decreased from 191.68 kPa m^{-1} to 171.76 kPa m^{-1}, decreasing by 10.39%. It can be found that during the water-sediment flow in the rough fracture, when the sediment particle size is small, the pressure loss increases with the increase of the particle size; when the sediment particle size is relatively large, the pressure loss decreases with the increase of the particle size. Through the comparisons, it can be found that the absolute value of the pressure gradient varies with the change of the sediment volume concentration under two types of fractures. It proves that the surface morphology of fractures affects the influence of sediment particle size on the pressure gradient.

Figure 6 shows the absolute value of the pressure gradient–sediment particle mass density (G_P-ρ_p) curves. In **Figure 6A**, when the water sediment flowed in the smooth fracture, with the increase of ρ_p, G_P decreased in an approximately linear form. As ρ_p increased from 0 kg/m^3 to 4,500 kg/m^3, G_P rapidly decreased from 6.51kPa m^{-1} to 6.33 kPa m^{-1}, decreasing by 2.84%. In **Figure 6B**, during the water-sediment flow in the rough fracture, G_P was smaller than that in the single-phase flow, and it first increased and then decreased with the increase of ρ_p. When ρ_p was 4,500 kg/m^3, the minimum G_P was obtained. Through the comparison, it is found that the absolute value of the pressure gradient during the water-

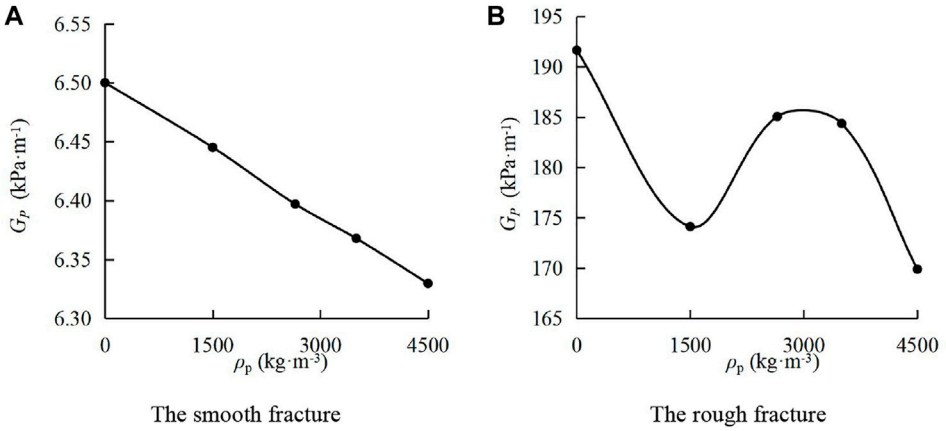

FIGURE 6 | Absolute value of the pressure gradient–sediment particle mass density curves. **(A)** Smooth fracture; **(B)** rough fracture.

sediment flow in the rough fracture is about 30 times that in the smooth fracture under the same conditions. In addition, the absolute value of the pressure gradient varies with the sediment particle mass density. It indicates that the surface morphology of the fracture affects the impact of sediment particle mass density on the pressure gradient.

In summary, under the conditions of two types of surface fractures, the absolute value of the pressure gradient with different sediment particle volume concentrations, sediment particle sizes, and sediment particle mass density in the two-phase flow was smaller than that in the single-phase flow. Under the smooth fracture surface, the absolute value of the pressure gradient changed linearly with the change of sediment particle volume concentrations, sediment particle sizes, and sediment particle mass density, while this value has different changing trends under the rough fracture.

3.2 Variation Law of the Mean Fluid Velocity Distribution

The mean velocity distribution is one of the important technical indicators for the study of seepage problems. **Figure 7** and **Figure 8** show the mean velocity distributions of the continuous-phase fluid on typical cross sections of smooth and rough fractures under various sediment volume concentrations. In **Figure 7A**, at a cross section of $X_1 = 5$ mm, the water-sediment fluid was not fully developed on the smooth fracture surface. In **Figure 7B**, the flow became fully developed. Through the comparison, it can be found that the mean velocity distributions on the two sections rarely change with the sediment volume concentration Φ, and they were symmetrically distributed along the center line of $X_2 = 0.9$ mm.

In **Figure 8**, when the water sediment flowed in the rough fractures, the mean velocity distributions of the continuous-phase fluid presented remarkable differences. In **Figure 8A**, v showed the asymmetric M-shaped distribution at the cross-section of $X_1 = 50$ mm, with two extreme points, and the peak values were within 1.2 mm $\leq X_2 \leq$ 1.5 mm. In **Figure 8B**, there were multiple extreme points at the cross section of $X_1 = 50.5$ mm, and the peak values were near the center line $X_2 = 1.4$ mm. Compared with other positions, v has the greatest change with Φ near the wall.

As shown in **Figure 7** and **Figure 8**, v of the continuous-phase fluid was dramatically different under two types of fracture conditions. The maximum v in the rough fracture was about three times that in the smooth fracture. In addition, the distribution curves are different. During the continuous-phase fluid flow in the smooth fracture, v-X_2 curves are rectangular or semi-sine shaped, while they are M-shaped during the continuous-phase fluid flow in the rough fracture.

Figure 9 and **Figure 10** show the mean velocity distribution of the continuous-phase fluid on the typical cross sections of the smooth and rough fractures under different sediment particle sizes. In **Figure 9A**, when the water sediment flowed in the smooth fracture, the fluid was not fully developed at the cross section of $X_1 = 5$ mm. In **Figure 9B**, the fluid became fully developed at the cross section of $X_1 = 50$ mm. It can be observed that v rarely changed with D_p under two types of cross sections and the distribution of v was symmetrical along the center line of $X_2 = 0.9$ mm.

Figure 10 shows that when the water sediment flowed in the rough fracture, v of the continuous-phase fluid was greatly influenced by D_p. Different v-X_2 curves varied significantly. In **Figure 10A**, on the cross section of $X_1 = 50$ mm, v first increased and then decreased with the increase of X_2, and the maximum value was between 1.2 and 1.5 mm. In **Figure 10B**, at the cross section of X_1=50.5mm, v also first increased and then decreased with the increase of X_2. In addition, there was an upward fluctuation at $X_2 = 2.1$ mm, and the peak value was within 1.2 mm $\leq X_2 \leq$ 1.5 mm.

Figure 11 and **Figure 12** show the mean velocity distribution of the continuous-phase fluid on the typical cross sections of the smooth and rough fractures under different sediment particle mass densities, respectively. In **Figure 11**, at the cross sections of $X_1 = 5$ mm and $X_1 = 50$ mm, v rarely changed with the sediment particle size, and v was symmetrically distributed along the center line of $X_2 = 0.9$ mm.

In **Figure 12**, v was greatly affected by the sediment particle size during the flow in the rough fracture, and multiple extreme points can be observed. On the section of $X_2 = 50$ mm, v of the

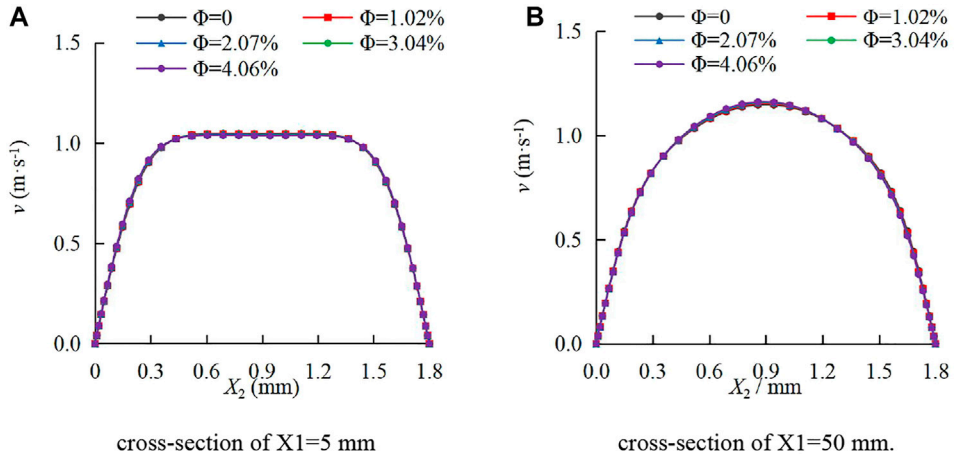

FIGURE 7 | Mean velocity distributions of the continuous-phase fluid on smooth fracture sections under different sediment volume concentrations. **(A)** Cross section of X1=5 mm; **(B)** cross section of X1=50 mm.

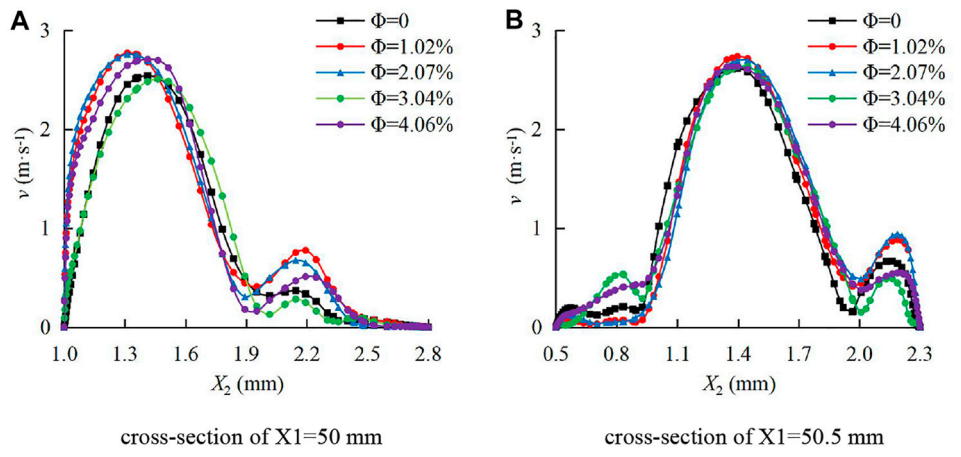

FIGURE 8 | Mean velocity distribution of the continuous-phase fluid on cross sections of the rough fracture with different sediment volume concentrations. **(A)** Cross section of X1=50 mm; **(B)** cross section of X1=50.5 mm.

fluid particle at each position was significantly affected by the sediment volume concentration, and the maximum v was in the range of 1.2 mm ≤ X_2 ≤ 1.5 mm. On the section of X_2 = 50.5 mm, the peak value was near the center line of X_2 = 1.4 mm.

In summary, in the smooth fracture, the changes of the sediment particle volume concentration, sediment particle mass density, and sediment particle size rarely affect the mean velocity distribution of the continuous-phase fluid, while these influencing factors significantly affect the mean velocity distribution of the continuous-phase fluid in the rough fracture.

3.3 Variation Law of the Turbulent Kinetic Energy

The turbulent kinetic energy is an indicator to measure the development and decline of turbulence. **Figure 13** and **Figure 14** show the distribution of turbulent kinetic energy of the continuous-phase fluid on typical cross sections of smooth and rough fractures at various sediment particle volume concentrations. As shown in **Figure 13A**, on the section of X_1 = 5 mm in the smooth fracture, k_t first increased and then decreased with X_2, and k_t reached the maximum at X_2 = 0.9 mm. The distribution curves of k_t are symmetrical along with X_2 = 0.9 mm under various Φ. In particular, within X_2 = 0.15–0.45 mm and X_2 = 1.35–1.65 mm, there was a significant negative correlation between Φ and k_t. It indicates that the movement of sediment particles can inhibit the turbulent kinetic energy of the continuous-phase fluid. However, on the section of X_1 = 50 mm, the k_t–X_2 curves are M-shaped, as shown in **Figure 13B**. Differing from the situation on the section of X_1 = 5 mm, k_t reached a minimum value at X_2 = 0.9 mm. At this point, Φ affected k_t in the entire X_2 interval, namely, the greater the Φ,

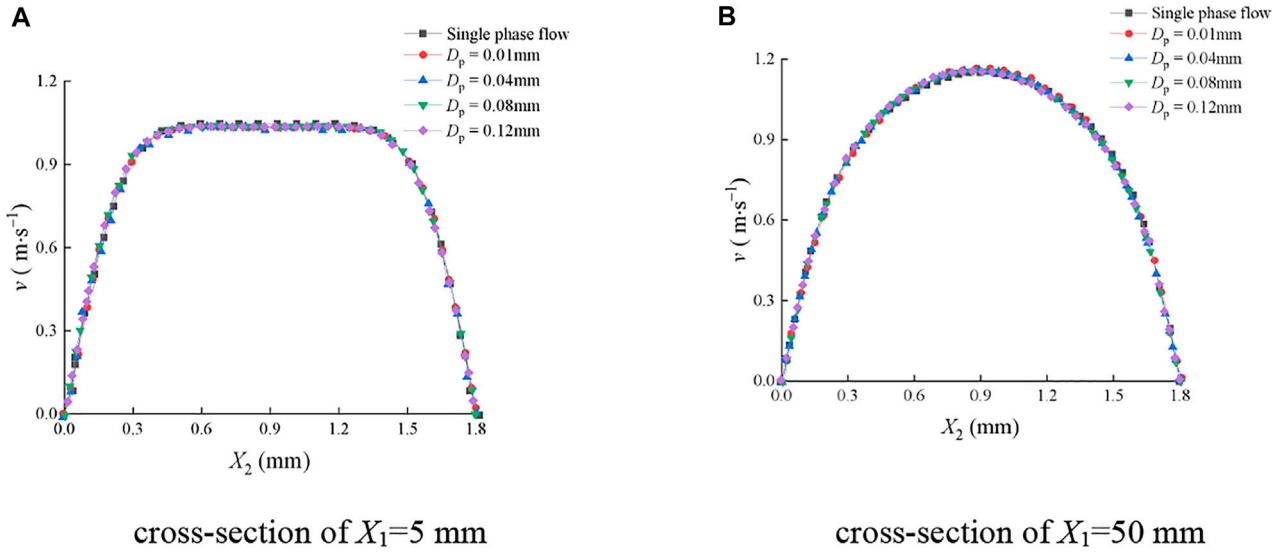

FIGURE 9 | Mean velocity distribution of the continuous-phase fluid on cross sections of the smooth fracture with different sediment particle sizes. **(A)** Cross section of X1=5 mm; **(B)** cross section of X1=50 mm.

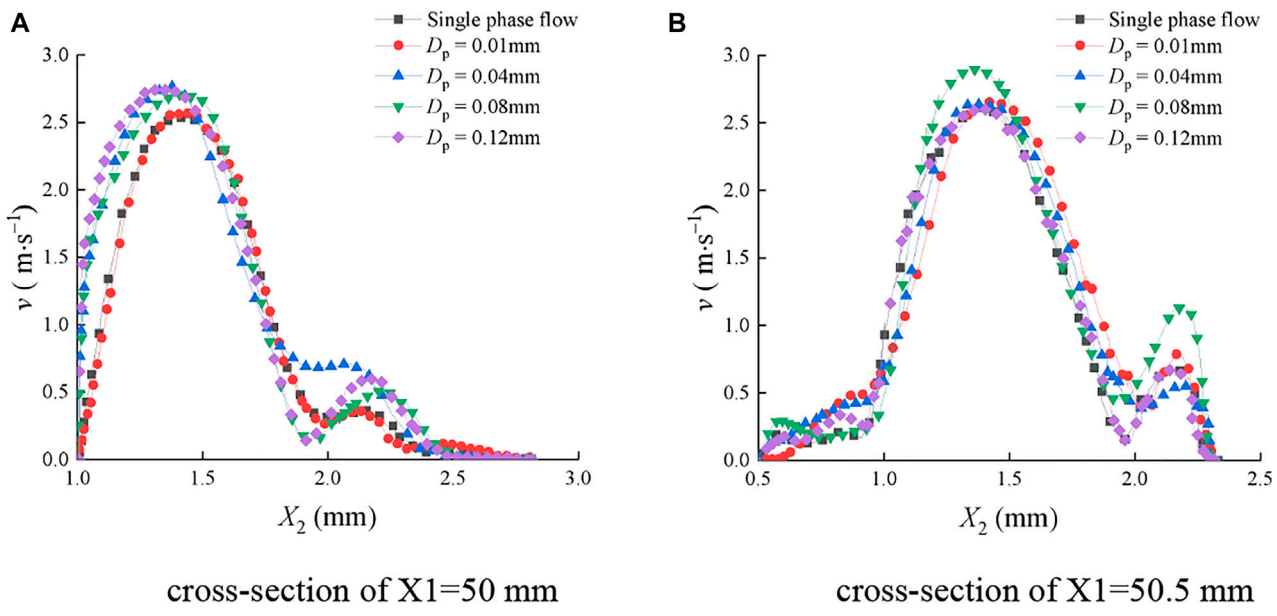

FIGURE 10 | Mean velocity distribution of the continuous-phase fluid on cross sections of the rough fracture with different sediment particle sizes. **(A)** Cross section of X1=50 mm; **(B)** cross section of X1=50.5 mm.

the smaller the k_t. It can be observed that the distribution of k_t–X_2 curves was approximately symmetrical along X_2 = 0.9 mm.

As presented in **Figure 14**, the distribution of k_t on the cross section of the rough fracture can be greatly affected by the sediment particle volume concentration Φ, which was manifested as the deviation of the extreme point position. In **Figure 14A**, on the section of X_1 = 50 mm, k_t fluctuated in the interval of 0 mm ≤ X_2 ≤ 2 mm and gradually decreased within 2 mm ≤ X_2 ≤ 2.8 mm. In **Figure 14B**, on the section of X_1 = 50.5 mm, k_t gradually increased in the interval of 0.5 mm ≤ X_2 ≤ 0.8 mm and fluctuated in the interval of 0.8 mm ≤ X_2 ≤ 2.3 mm. It can be observed that the maximum k_t was in the interval of 1.0 mm ≤ X_2 ≤ 1.3 m on both sections. In addition, the fluctuations of k_t can be found on both sections, indicating that the turbulence intensity was higher in the rough fracture.

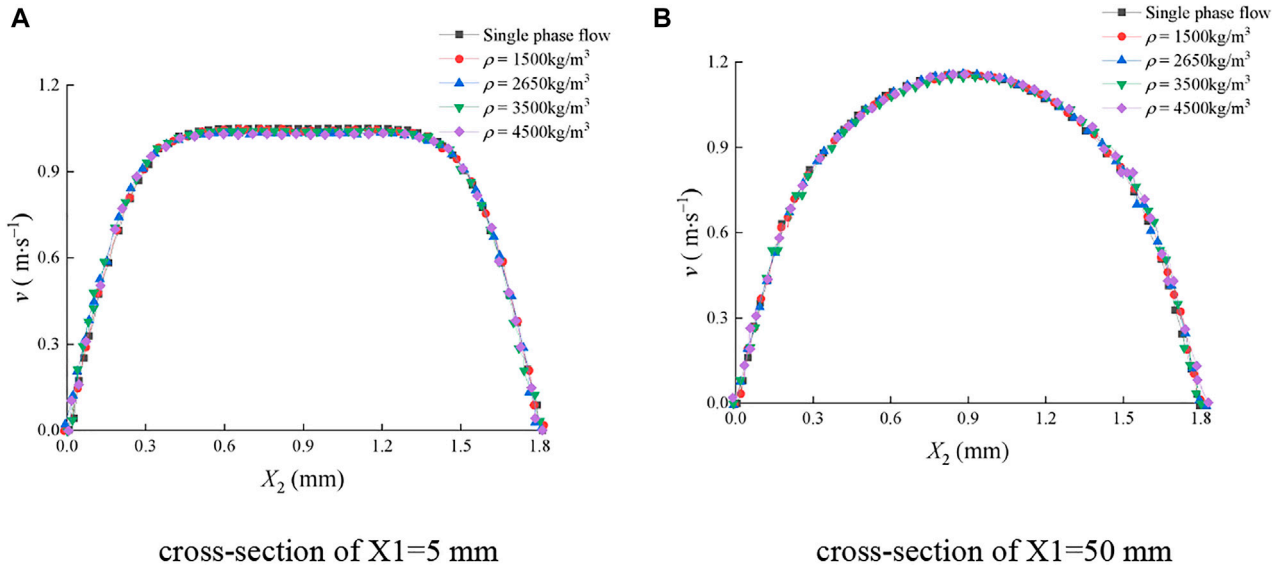

FIGURE 11 | Mean velocity distribution of the continuous-phase fluid on the cross sections of the smooth fracture under different sediment particle mass densities. **(A)** Cross section of X1=5 mm; **(B)** cross section of X1=50 mm.

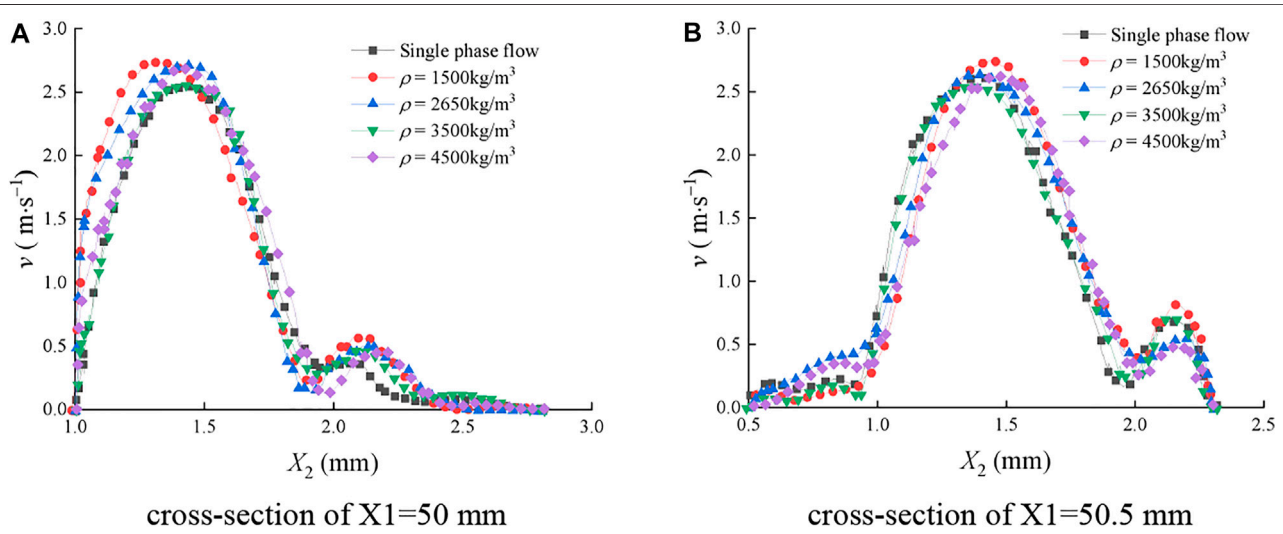

FIGURE 12 | Mean velocity distribution of the continuous-phase fluid on cross sections of the rough fracture under different sediment particle mass density. **(A)** Cross section of X1=50 mm; **(B)** cross section of X1=50.5 mm.

As shown in **Figure 13** and **Figure 14**, the turbulent kinetic energy of the fluid in the rough fracture was an order of magnitude higher than that in the smooth fracture under the same conditions. The distribution of fluid turbulent kinetic energy in the X_1 direction was numerically different, and the distribution curves were completely different during the water-sediment flow in the smooth and rough fractures. The impacts of the sediment volume concentration in the smooth fracture on the continuous-phase fluid turbulent kinetic energy had significant laws, while no obvious laws were observed in the rough fracture.

Figure 15 and **Figure 17** show the distribution of turbulent kinetic energy of the continuous-phase fluid on typical cross sections of smooth and rough fractures under various sediment particle sizes. In **Figure 15A**, on the section of X_1 = 5 mm of the smooth fracture, k_t first increased and then decreased with X_2, and the maximum k_t was obtained at X_2 = 0.9 mm. The sediment particles significantly reduced k_t in the intervals of 0.15 mm ≤ X_2 ≤ 0.45 and 1.35 mm ≤ X_2 ≤ 1.65 mm, but the influence laws were different. In the interval of 0.15 mm ≤ X_2 ≤ 0.45, the distribution curves of k_t were basically consistent, and D_p had no obvious influence on k_t, while in the interval of 1.35 mm ≤ X_2 ≤ 1.65 mm,

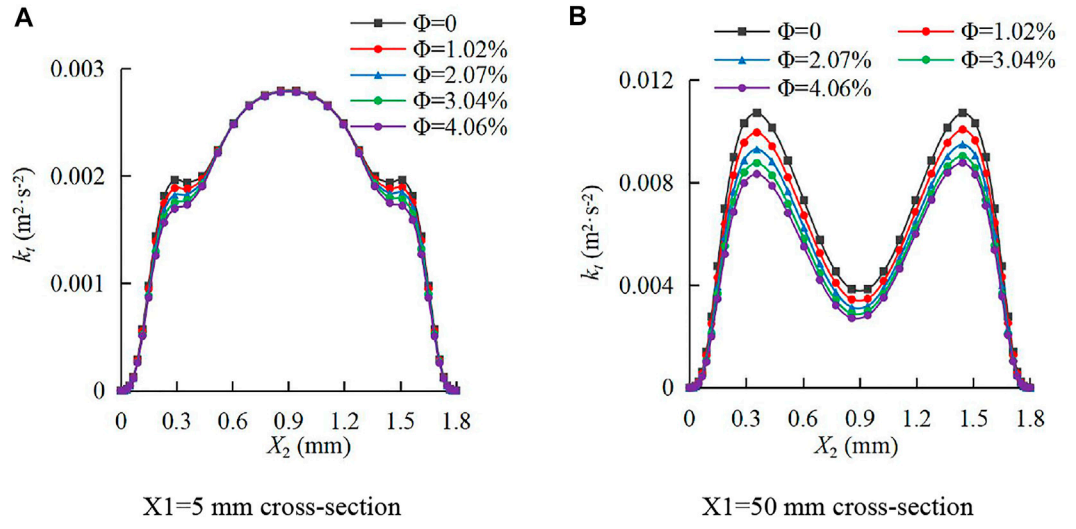

FIGURE 13 | Distribution of turbulent kinetic energy of the continuous-phase fluid on cross sections of the smooth fracture. **(A)** X1=5 mm cross section; **(B)** X1=50 mm cross section.

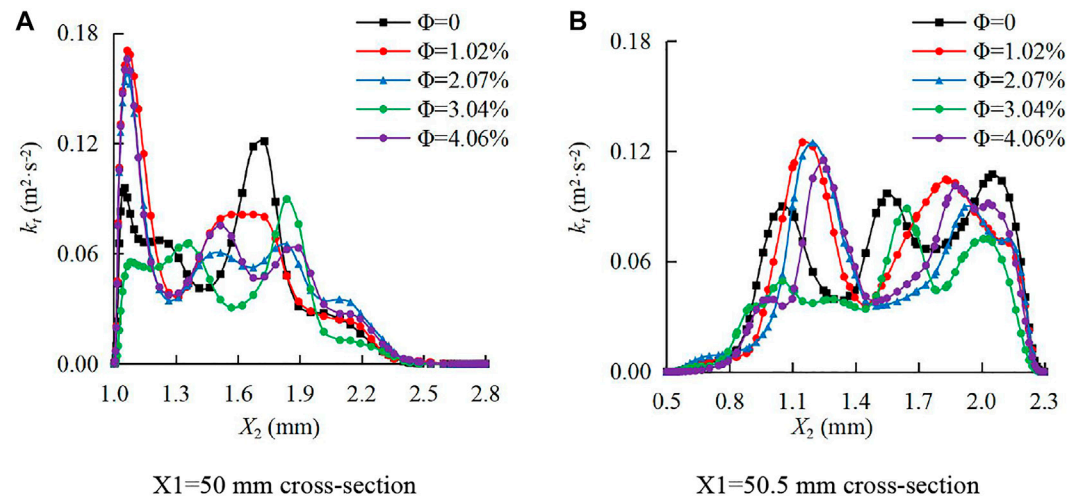

FIGURE 14 | Distribution of turbulent kinetic energy of the continuous-phase fluid on cross sections of the rough fracture. **(A)** X1=50 mm cross section; **(B)** X1=50.5 mm cross section.

k_t gradually decreased with the decrease of D_p. When D_p was 0.01 mm, the distribution curve of k_t was symmetrically distributed along X_2 = 0.9 mm. When the values of D_p were 0.04, 0.08, and 0.12 mm, the distribution curves of k_t were asymmetrical along X_2 = 0.9 mm. On the section of X_1 = 5 mm, k_t was slightly affected by D_p in intervals other than X_2 = 0.15–0.45 mm and X_2 = 1.35–1.65 mm, and the curves were relatively consistent.

In **Figure 15B**, on the section of X_1 = 50 mm, k_t changed with X_2 in an M shape and reached the minimum at X_2 = 0.9 mm. At this point, D_p had effects on k_t in the entire X_2 interval, and k_t gradually decreased with the decrease of D_p. The influence laws of D_p on k_t were different in the intervals of $X_2 \leq 0.9$ mm and $X_2 \geq 0.9$ mm. In the interval of $X_2 \leq 0.9$ mm, the distribution curves of k_t were nearly consistent with various D_p, indicating that D_p had no obvious effect on k_t. However, in the interval of $X_2 \geq 0.9$ mm, k_t gradually reduced with the decrease of D_p. When D_p was 0.01 mm, the distribution curve of k_t was symmetrical along with X_2 = 0.9 mm, and the curves are asymmetrical with a D_p of 0.04, 0.08, and 0.12 mm.

To illustrate the cause of the asymmetry in **Figure 15**, the distributions of sediment particles in fractures were given, as shown in **Figure 16**. The size of the sediment particle was doubled, and the concentration was diluted by one-tenth in order to clearly show the distribution of particles in the fracture. It can be observed that the sediment particles of

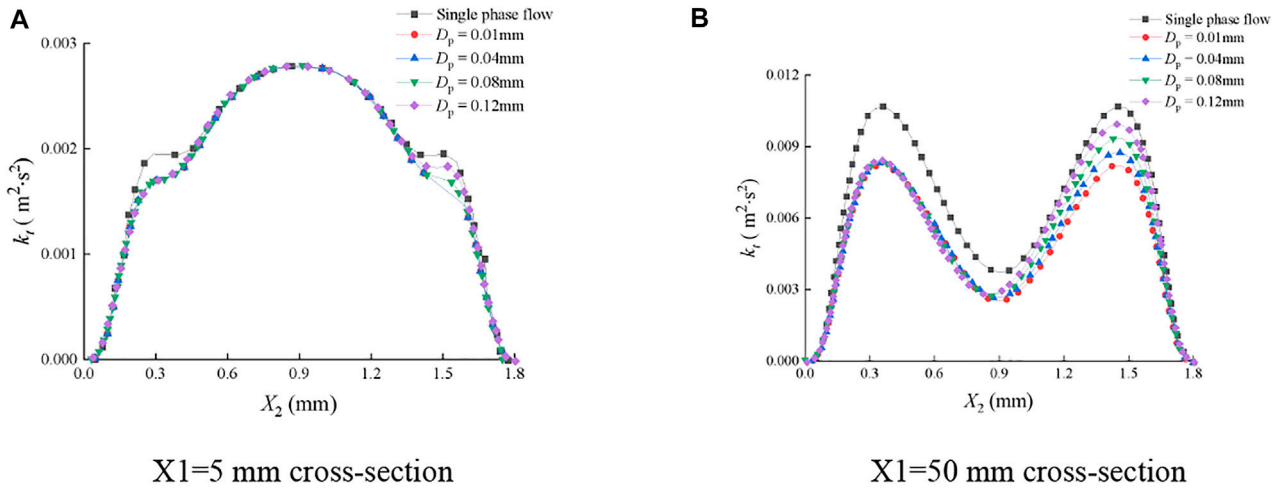

FIGURE 15 | Distribution of turbulent kinetic energy of the continuous-phase fluid on cross sections of the smooth fracture. **(A)** X1=5 mm cross section; **(B)** X1=50 mm cross section.

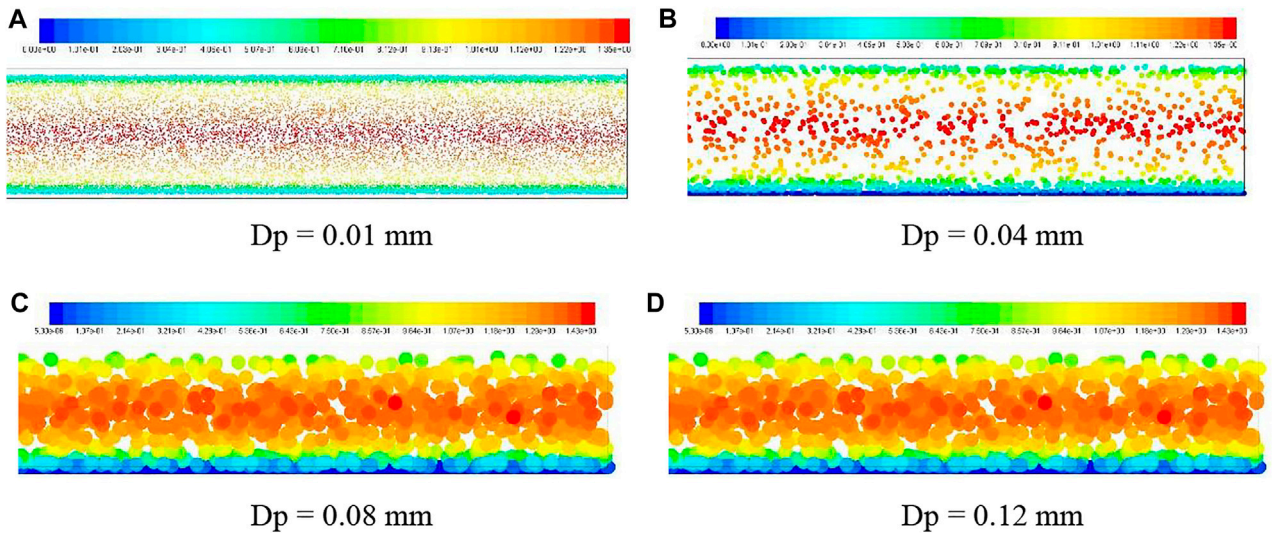

FIGURE 16 | Distributions of sediment particles at the outlet of the fracture. **(A)** Dp = 0.01 mm, **(B)** Dp = 0.04 mm, **(C)** Dp = 0.08 mm, **(D)** Dp = 0.12 mm.

0.01 mm had no contact with the upper and lower walls of the fracture and were distributed symmetrically along X_2 = 0.9 mm. The sediment particles of 0.04, 0.08, and 0.12 mm were gradually shifted downward under the action of gravity, and some of them settled on the bottom wall. This is because the sediment particles with smaller sizes have better flowability and are not easy to settle under the action of gravity, while the sediment particles with larger sizes have larger Stokes numbers and are easily affected by gravity. According to the aforementioned analysis, the sediment particles of 0.01 mm were symmetrically distributed along with X_2 = 0.9 mm, and the turbulent kinetic energy of the fluid subjected to them was also symmetrically distributed along X_2 = 0.9 mm. The sediment particles of 0.04, 0.08, and 0.12 mm were asymmetrical along with X_2 = 0.9 mm and so was the turbulent kinetic energy.

In **Figure 17**, the turbulent kinetic energy distribution of the continuous-phase fluid on the cross section of the fracture was greatly affected by sediment particle size, which was manifested as the deviation of the extreme points. On the section of X_1 = 50 mm, k_t was relatively large in the interval of $X_2 \leq 2$ mm, while it was smaller in the interval of $X_2 \geq 2$ mm. On the section of X_1 = 50.5 mm, k_t was relatively small when $X_2 \leq 0.8$ mm, and it was larger when $X_2 \geq 0.8$. The distribution of the fluid turbulent kinetic energy was disordered on the aforementioned two cross sections, indicating that the fluid pulsation was severe in the rough fracture and the turbulence intensity was high. Through

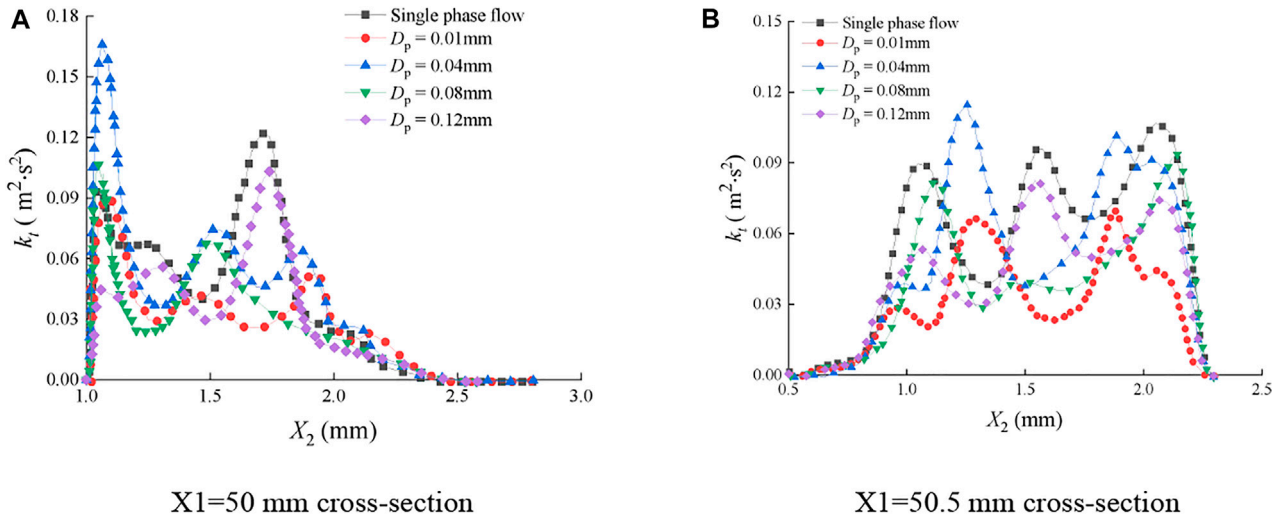

FIGURE 17 | Distribution of turbulent kinetic energy of the continuous-phase fluid on cross sections of the rough fracture. **(A)** X1=50 mm cross section; **(B)** X1=50.5 mm cross section.

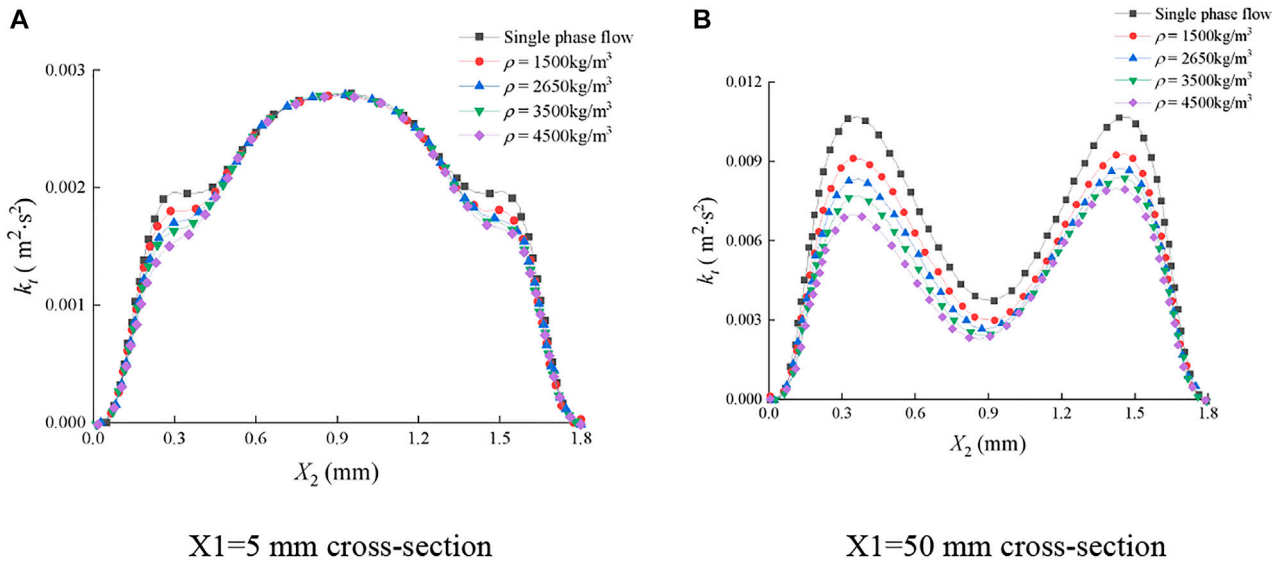

FIGURE 18 | Distribution of turbulent kinetic energy of the continuous-phase fluid on cross sections of the smooth fracture. **(A)** X1=5 mm cross section, **(B)** X1=50 mm cross section.

the comparison of **Figure 15** and **Figure 17**, it is found that the impacts of the sediment particle size on the fluid turbulent kinetic energy are completely different in smooth and rough fractures, and the difference is nearly an order of magnitude.

Figure 18 and **Figure 19** show the distribution of turbulent kinetic energy of the continuous-phase fluid on typical cross sections of the smooth fracture and rough fracture under various sediment mass densities.

In **Figure 18A**, on the section of X_1 = 5 mm of the smooth fracture, k_t first increased and then decreased and reached the maximum when X_2 = 0.9 mm. Obviously, the effects of the sediment volume concentration on k_t were very significant in the intervals of 0.15 mm ≤ X_2 ≤ 0.45 and 1.35 mm ≤ X_2 ≤ 1.65 mm, where k_t decreased with the increase of ρ_p. It was indicated that the movement of sediment particles can inhibit the turbulent kinetic energy with the increase of ρ_p. During the single-phase flow, when ρ_p was 1,500 kg/m^3, k_t was distributed symmetrically along X_2 = 0.9 mm. When the values of ρ_p were 2650 kg/m^3, 3500 kg/m^3, and 4,500 kg/m^3, k_t in the interval of 0.15 mm ≤ X_2 ≤ 0.45 mm was smaller than that in the interval of

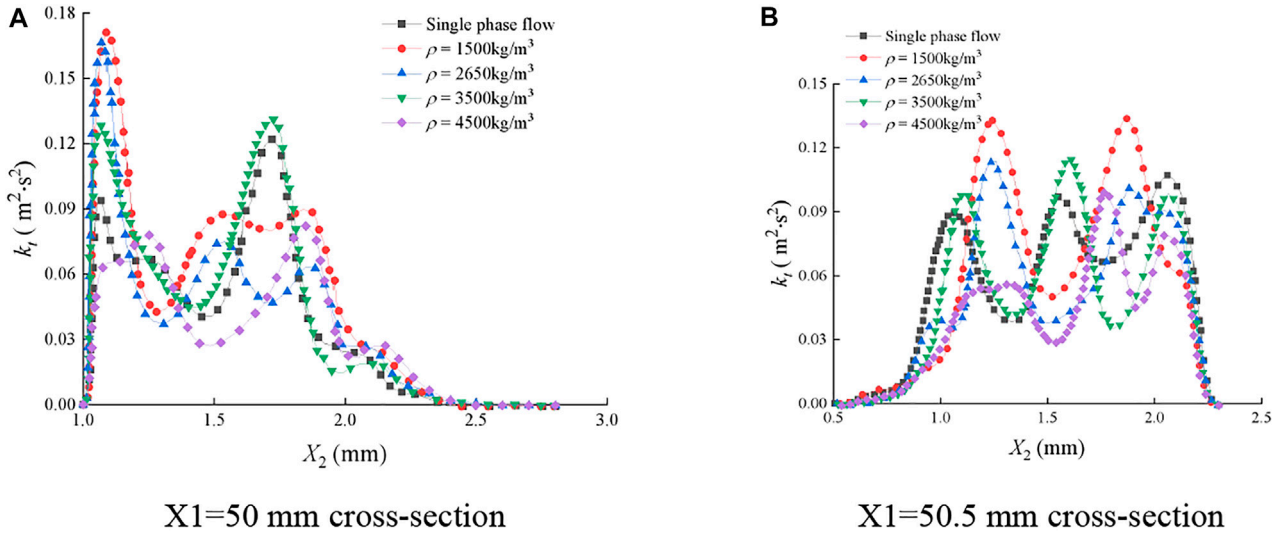

FIGURE 19 | Distribution of turbulent kinetic energy of the continuous-phase fluid on cross sections of the rough fracture. **(A)** X1=50 mm cross section; **(B)** X1=50.5 mm cross section.

1.35 mm ≤ X_2 ≤ 1.65 mm, indicating that the sediment particle in the interval of 0.15 mm ≤ X_2 ≤ 0.45 mm had a greater impact on the turbulent kinetic energy. This is because the sediment particles are more affected by gravity as the mass density increases, and they are easily deposited on the lower wall. In the intervals except for 0.15 mm ≤ X_2 ≤ 0.45 and 1.35 mm ≤ X_2 ≤ 1.65 mm, the distribution curves of k_t were basically consistent and were symmetrical along X_2 = 0.9 mm. It indicated that k_t was slightly affected by the sediment particle mass density in these intervals. In **Figure 18B**, on the section of X_1 = 50 mm, k_t- X_2 curves were M-shaped, and ρ_p affected k_t in the whole X_2 interval. The larger the ρ_p, the smaller the k_t. In the single-phase flow, when ρ_p was 1,500 kg/m^3, k_t was symmetrically distributed along X_2 = 0.9 mm. When the values of ρ_p were 2650 kg/m^3, 3500 kg/m^3, and 4,500 kg/m^3, k_t under X_2 ≤ 0.9 mm was smaller than that under X_2 ≥ 0.9 mm. It indicates that the sediment particles with the aforementioned mass densities have a greater influence on the turbulent kinetic energy in the interval of X_2 ≤ 0.9 mm. This is because the sediment particles are more affected by gravity and easily deposited on the lower wall, as the mass density of sediment particles increases.

In **Figure 19**, the distribution of k_t was greatly affected by ρ_p during the water-sediment flow in the rough fracture. The extreme points were shifted. On the section of X_1 = 50 mm, k_t was larger in the interval of X_2 ≤ 2 mm than that in the interval of X_2 ≥ 2 mm. On the section of X_1 = 50.5 mm, k_t was smaller when X_2 ≤ 0.8 mm. It can be observed that the distribution of k_t was disordered on both the cross sections, suggesting that the fluid pulsation was violent in the rough fracture and the turbulence intensity was high.

In summary, under the conditions of the same sediment mass density, same sediment size, same sediment volume concentration, and same inlet velocity, the influence of sediment mass density on fluid turbulent kinetic energy exhibits completely different laws in smooth and rough fractures, with the difference of nearly an order of magnitude.

4 CONCLUSION

In this study, ANSYS Fluent software was used to perform numerical simulations on the water-sediment two-phase flow in smooth and rough fractures. Then, the influences of the sediment volume concentration, sediment particle size, and sediment mass density on pressure gradient, mean velocity distribution, and turbulent kinetic energy distribution were analyzed. The following conclusions were obtained:

(1) During the water-sediment flow in the smooth fracture, the absolute values of pressure gradient G_p, the sediment volume concentration Φ, the sediment particle size D_p, and the sediment mass density ρ_p are approximately linear, and the linearity of G_p and D_p is the lowest. In other words, G_p decreases with the increase of Φ, D_p, and ρ_p. During the water-sediment flow in the rough fracture, the pressure loss of sediment particles is reduced. When Φ is 1.02%, G_p is the smallest. When Φ ≥ 2.07%, G_p changes slightly. When D_p is small, the pressure loss increases with the increase of D_p. When D_p is relatively large, the pressure loss decreases with the increase of D_p, and G_p first increased and then decreased with the increase of ρ_p.

(2) During the water-sediment flow in the smooth fracture, the mean velocity v of the continuous-phase fluid rarely changes with Φ, D_p, and ρ_p. However, during the water-sediment flow in the rough fracture, v is greatly affected by Φ, D_p, and ρ_p, which can be observed through the changes of curve shapes and deviations of extreme points.

(3) During the water-sediment flow in the smooth fracture, the fluid turbulent kinetic energy k_t decreases with the increase of ρ_p and Φ and decreases with the decrease of ρ_p. During the water-sediment flow in the rough fracture, k_t is significantly affected by Φ, D_p, and ρ_p, which was manifested in the changes of curve shapes and the deviation of the extreme points. This is obtained based on the distribution of sediment particle sizes and Stokes number.

DATA AVAILABILITY STATEMENT

The original contributions presented in the study are included in the article/Supplementary Materials, further inquiries can be directed to the corresponding author.

AUTHOR CONTRIBUTIONS

XS: conceptualization, methodology, funding acquisition, writing—original draft, and writing—review and editing; ML: methodology; YH: writing—original draft, and writing–review and editing; QC: writing—review and editing; ZC: writing—original draft and writing—review and editing; YC: writing—original draft and writing—review and editing; DM: conceptualization, supervision, funding acquisition, writing—original draft, and review and editing.

FUNDING

This research was funded by the National Natural Science Foundation of China for Young (52104153), the National Natural Science Foundation of China (41977238), and the National Science Fund for Excellent Young Scholars of China (52122404).

ACKNOWLEDGMENTS

The authors would like to acknowledge the editor and reviewers for their valuable comments for the improvement of this article.

REFERENCES

1. Zhang D, Fan G, Wang X. Characteristics and Stability of Slope Movement Response to Underground Mining of Shallow Coal Seams Away from Gullies. *Int J Mining Sci Technol* (2012) 22:47–50. doi:10.1016/j.ijmst.2011.06.005
2. Fan G, Zhang D, Zhang S, Zhang C. Assessment and Prevention of Water and Sand Inrush Associated with Coal Mining under a Water-Filled Buried Gully: A Case Study. *Mine Water Environ* (2018) 37:565–76. doi:10.1007/s10230-017-0487-8
3. Ma D, Zhang J, Duan H, Huang Y, Li M, Sun Q, et al. Reutilization of Gangue Wastes in Underground Backfilling Mining: Overburden Aquifer protection. *Chemosphere* (2021) 264:128400. doi:10.1016/j.chemosphere.2020.128400
4. Xue Y, Liu J, Liang X, Wang S, Ma Z. Ecological Risk Assessment of Soil and Water Loss by thermal Enhanced Methane Recovery: Numerical Study Using Two-phase Flow Simulation. *J Clean Prod* (2022) 334:130183. doi:10.1016/j.jclepro.2021.130183
5. Wu Q, Zhou W. Prediction of Groundwater Inrush into Coal Mines from Aquifers Underlying the Coal Seams in China: Vulnerability index Method and its Construction. *Environ Geol* (2008) 56:245–54. doi:10.1007/s00254-007-1160-5
6. Elbaz K, Shen JS, Arulrajah A, Horpibulsuk S. Geohazards Induced by Anthropic Activities of Geoconstruction: a Review of Recent Failure Cases. *Arab J Geosci* (2016) 9:708. doi:10.1007/s12517-016-2740-z
7. Peng K, Zhou J, Zou Q, Zhang J, Wu F. Effects of Stress Lower Limit during Cyclic Loading and Unloading on Deformation Characteristics of Sandstones. *Construction Building Mater* (2019) 217:202–15. doi:10.1016/j.conbuildmat.2019.04.183
8. Wang XF, Zhang DS, Zhang CG, Fan GW. Mechanism of Mining-Induced Slope Movement for Gullies Overlaying Shallow Coal Seams. *J Mt Sci* (2013) 10:388–97. doi:10.1007/s11629-013-2455-5
9. Ma D, Duan H, Zhang J, Liu X, Li Z. Numerical Simulation of Water-Silt Inrush Hazard of Fault Rock: A Three-Phase Flow Model. *Rock Mech Rock Eng* (2022), in press.
10. Qiao S, Zhong W, Wang S, Sun L, Tan S. Numerical Simulation of Single and Two-phase Flow across 90° Vertical Elbows. *Chem Eng Sci* (2021) 230:116185. doi:10.1016/j.ces.2020.116185
11. Han L, Wang Y, Liu K, Ban Z, Liu H. Theoretical Modeling for Leakage Characteristics of Two-phase Flow in the Cryogenic Labyrinth Seal. *Int J Heat Mass Transfer* (2020) 159:120151. doi:10.1016/j.ijheatmasstransfer.2020.120151
12. Ma D, Duan H, Zhang J. Solid Grain Migration on Hydraulic Properties of Fault Rocks in Underground Mining Tunnel: Radial Seepage Experiments and Verification of Permeability Prediction. *Tunn Undergr Sp Tech* (2022), in press.
13. Liu Y, Li S. Influence of Particle Size on Non-darcy Seepage of Water and Sediment in Fractured Rock. *Springerplus* (2016) 5:2099. doi:10.1186/s40064-016-3778-9
14. Ma D, Wang J, Cai X, Ma X, Zhang J, Zhou Z, et al. Effects of Height/diameter Ratio on Failure and Damage Properties of Granite under Coupled Bending and Splitting Deformation. *Eng Fracture Mech* (2019) 220:106640. doi:10.1016/j.engfracmech.2019.106640
15. Xiao T, Huang M, Gao M. Triaxial Permeability Experimental Study on Deformation and Failure Processes of Single-Fractured Rock Specimens. *Shock and Vibration* (2020) 2020:1–12. doi:10.1155/2020/7329825
16. Ye F, Duan JC, Fu WX, Yuan XY. Permeability Properties of Jointed Rock with Periodic Partially Filled Fractures. *Geofluids* (2019) 2019:1–14. doi:10.1155/2019/4039024
17. Guo B, Wang C, Wang L, Chen Y, Cheng T. A Modified Cubic Law for Rough-Walled Marble Fracture by Embedding Peak Density. *Adv Civil Eng* (2020) 2020:1–10. doi:10.1155/2020/9198356
18. Zhang B, He Q, Lin Z, Li Z. Experimental Study on the Flow Behaviour of Water-Sand Mixtures in Fractured Rock Specimens. *Int J Mining Sci Technol* (2021) 31:377–85. doi:10.1016/j.ijmst.2020.09.001
19. Xu J, Pu H, Chen J, Sha Z. Experimental Study on Sand Inrush Hazard of Water-Sand Two-phase Flow in Broken Rock Mass. *Geofluids* (2021) 2021:1–9. doi:10.1155/2021/5542440
20. Zhou Z, Zhang J, Cai X, Wang S, Du X, Zang H. Permeability Experiment of Fractured Rock with Rough Surfaces under Different Stress Conditions. *Geofluids* (2020) 2020:1–15. doi:10.1155/2020/9030484
21. Liu Q, Liu B. Experiment Study of the Failure Mechanism and Evolution Characteristics of Water-Sand Inrush Geo-Hazards. *Appl Sci* (2020) 10:3374. doi:10.3390/app10103374
22. Yin Q, Ma G, Jing H, Wang H, Su H, Wang Y, et al. Hydraulic Properties of 3D Rough-Walled Fractures during Shearing: An Experimental Study. *J Hydrol* (2017) 555:169–84. doi:10.1016/j.jhydrol.2017.10.019
23. Wang J, Ma D, Li Z, Huang Y, Du F. Experimental Investigation of Damage Evolution and Failure Criterion on Hollow Cylindrical Rock Samples with Different Bore Diameters. *Eng Fracture Mech* (2022) 260:108182. doi:10.1016/j.engfracmech.2021.108182
24. Zhong Z, Wang L, Song L, Gao C, Hu Y, Gao H, et al. Size Effect on the Hydraulic Behavior of Fluid Flow through a Single Rough-Walled Fracture.

Soil Dyn Earthquake Eng (2021) 143:106615. doi:10.1016/j.soildyn.2021.106615

25. Ma D, Duan H, Li X, Li Z, Zhou Z, Li T. Effects of Seepage-Induced Erosion on Nonlinear Hydraulic Properties of Broken Red Sandstones. *Tunnelling Underground Space Technol* (2019) 91:102993. doi:10.1016/j.tust.2019.102993
26. Ma D, Duan H, Liu W, Ma X, Tao M. Water-Sediment Two-phase Flow Inrush Hazard in Rock Fractures of Overburden Strata during Coal Mining. *Mine Water Environ* (2020) 39:308–19. doi:10.1007/s10230-020-00687-6
27. Liu J, Xue Y, Zhang Q, Wang H, Wang S. Coupled Thermo-Hydro-Mechanical Modelling for Geothermal Doublet System with 3D Fractal Fracture. *Appl Therm Eng* (2022) 200:117716. doi:10.1016/j.applthermaleng.2021.117716
28. Yang Z, Li D, Xue S, Hu R, Chen Y-F. Effect of Aperture Field Anisotropy on Two-phase Flow in Rough Fractures. *Adv Water Resour* (2019) 132:103390. doi:10.1016/j.advwatres.2019.103390
29. Yang X, Liu YJ, Xue M, Yang TH, Yang B. Experimental Investigation of Water-Sand Mixed Fluid Initiation and Migration in Porous Skeleton during Water and Sand Inrush. *Geofluids* (2020) 2020:1–18. doi:10.1155/2020/8679861
30. Yang W, Jin L, Zhang X. Simulation Test on Mixed Water and Sand Inrush Disaster Induced by Mining under the Thin Bedrock. *J Loss Prev Process Industries* (2019) 57:1–6. doi:10.1016/j.jlp.2018.11.007
31. Yu Y, Xin Q, Cheng W, Rui J, Zhang X. Numerical Simulation Study on the Seepage Characteristics of Coal Seam Infusion Effected by Mining-Induced Stress. *Bull Eng Geol Environ* (2021) 80:9015–28. doi:10.1007/s10064-021-02483-0
32. Ma D, Kong S, Li Z, Zhang Q, Wang Z, Zhou Z. Effect of Wetting-Drying Cycle on Hydraulic and Mechanical Properties of Cemented Paste Backfill of the Recycled Solid Wastes. *Chemosphere* (2021) 282:131163. doi:10.1016/j.chemosphere.2021.131163
33. Khan MIH, Wellard RM, Nagy SA, Joardder MUH, Karim MA. Experimental Investigation of Bound and Free Water Transport Process during Drying of Hygroscopic Food Material. *Int J Therm Sci* (2017) 117:266–73. doi:10.1016/j.ijthermalsci.2017.04.006
34. Si G, Belle B. Performance Analysis of Vertical Goaf Gas Drainage Holes Using Gas Indicators in Australian Coal Mines. *Int J Coal Geology* (2019) 216:103301. doi:10.1016/j.coal.2019.103301
35. Chen J, Zhu C, Du J, Pu Y, Pan P, Bai J, et al. A Quantitative Pre-warning for Coal Burst hazard in a Deep Coal Mine Based on the Spatio-Temporal Forecast of Microseismic Events. *Process Saf Environ Prot* (2022) 159:1105. doi:10.1016/j.psep.2022.01.082
36. Si G, Cai W, Wang S, Li X. Prediction of Relatively High-Energy Seismic Events Using Spatial-Temporal Parametrisation of Mining-Induced Seismicity. *Rock Mech Rock Eng* (2020) 53:5111–32. doi:10.1007/s00603-020-02210-3
37. Cao W, Shi J-Q, Durucan S, Si G, Korre A. Gas-driven Rapid Fracture Propagation under Unloading Conditions in Coal and Gas Outbursts. *Int J Rock Mech Mining Sci* (2020) 130:104325. doi:10.1016/j.ijrmms.2020.104325
38. Si G, Durucan S, Shi JQ, Korre A, Cao W. Parametric Analysis of Slotting Operation Induced Failure Zones to Stimulate Low Permeability Coal Seams. *Rock Mech Rock Eng* (2019) 52(1):163–82. doi:10.1007/s00603-018-1579-x
39. Li Q, Ma D, Zhang Y, Liu Y, Ma Y. Insights into Controlling Factors of Pore Structure and Hydraulic Properties of Broken Rock Mass in a Geothermal Reservoir. *Lithosphere* (2022) 2021(5):3887832. doi:10.2113/2022/3887832

Conflict of Interest: The authors declare that the research was conducted in the absence of any commercial or financial relationships that could be construed as a potential conflict of interest.

Publisher's Note: All claims expressed in this article are solely those of the authors and do not necessarily represent those of their affiliated organizations, or those of the publisher, the editors, and the reviewers. Any product that may be evaluated in this article, or claim that may be made by its manufacturer, is not guaranteed or endorsed by the publisher.

frontiers | Frontiers in Physics

ORIGINAL RESEARCH
published: 28 June 2022
doi: 10.3389/fphy.2022.946516

Simulation and Analysis of Multiphase Flow in a Novel Deepwater Closed-Cycle Riserless Drilling Method With a Subsea pump+gas Combined Lift

Jintang Wang[1,2]*, *Jinsheng Sun*[1,3], *Wenwei Xie*[1,4], *Haowen Chen*[1,4], *Cai Wang*[1,3], *Yanjiang Yu*[1,3] and *Rulei Qin*[1,4]

[1]Southern Marine Science and Engineering Guangdong Laboratory (Guangzhou), Guangzhou, China, [2]School of Petroleum Engineering, China University of Petroleum (East China), Qingdao, China, [3]Guangzhou Marine Geological Survey, China Geological Survey, Guangzhou, China, [4]Institute of Exploration Techniques, China Academy of Geological Sciences, Langfang, China

OPEN ACCESS

Edited by:
Weiqi Fu,
China University of Mining and Technology, China

Reviewed by:
Yiqun Zhang,
China University of Petroleum, Beijing, China
Jiaxin Sun,
China University of Geosciences Wuhan, China
Haiwen Zhu,
University of Tulsa, United States

***Correspondence:**
Jintang Wang
wangjintang@upc.edu.cn

Specialty section:
This article was submitted to Interdisciplinary Physics, a section of the journal Frontiers in Physics

Received: 17 May 2022
Accepted: 30 May 2022
Published: 28 June 2022

Citation:
Wang J, Sun J, Xie W, Chen H, Wang C, Yu Y and Qin R (2022) Simulation and Analysis of Multiphase Flow in a Novel Deepwater Closed-Cycle Riserless Drilling Method With a Subsea pump+gas Combined Lift. Front. Phys. 10:946516. doi: 10.3389/fphy.2022.946516

Recently, deepwater resource exploration has grown rapidly. Because the conditions of marine environment and seabed geology are more complex, deepwater drilling needs to numerous confront challenges, such as more complicated wellbore situations, low drilling efficiency, and high cost. Advanced novel drilling methods serve as significant impetus to facilitate the rapid advancement in deepwater oil-and-gas exploration and development. However, adopting riserless drilling methods may pollute marine environment and yield poor wall protective effects, while drilling methods with risers may suffer from relatively high cost and risk. Based on these dilemmas, in this study, a novel deepwater closed-cycle riserless drilling method with a subsea pump + gas combined lift is proposed. The proposed novel closed-cycle method has also established a multiphase flow drilling model and analyzed the effects of drilling fluid displacement, gas injection displacement, gas injection site and seawater depth on the multiphase flow in the wellbore. The simulation results revealed the following: As the gas migrates upward along the pipeline, its flow velocity first increases slowly and then rapidly owing to the volume expansion of gas. Larger displacement of drilling fluid demands greater working power of the subsea lifting pump, which is characterized by a nonlinear relationship. The gas injection displacement can effectively mitigate the load-bearing capacity of the pump, and increasing gas injection displacement leads to a decreased subsea lifting pump working power requirement; the decreasing effect on pump power load is more significant in the case of low gas injection displacement. Increasing the depth of gas injection sites reduces the subsea pump working with a decreasing slope with respect to the power descent. Finally, the subsea pump lifting power demand increases approximately linearly with an increasing seawater depth. Subsequently, an optimization method of hydraulic parameters for deepwater closed-cycle riserless drilling was proposed, which provides a theoretical foundation for the selection of subsea pumping power as well as the optimization of gas injection sites and displacement.

Keywords: novel riserless drilling, gas+pump combined lift, multiphase flow, displacement, pumping power

1 INTRODUCTION

70% of the earth is covered by sea. In the future, 40% of global gas-and-oil reserves are projected to come from deepwater; moreover, the foreseeable alternative energy "natural gas hydrate" mainly originates from deepwater as well. Consequently, deepwater study has become a Frontier field to explore essential scientific problems such as the origins of multicellular life, evolution of the earth, and climate change. Offshore drilling is the most intuitive approach to acquiring subsea stratigraphic information, which is also a leading method of marine resource exploration.

In Offshore drilling, the drilling equipment must meet high safety and reliability because it can withstand the effects of wind, wave and current, gas hydrate, strong tropical storm and the corrosion damage of marine environment to the equipment. At present, two mature deepwater drilling units have been developed: deepwater drilling ship and deepwater semi submersible drilling platform [1, 2]. Drilling ship is one of the most mobile drilling units. It has the advantages of flexible movement, simple berthing and wide range of water depth, and is especially suitable for drilling in deep water or deeper water. Drilling ships are mainly active in the waters of Brazil, the Gulf of Mexico and West Africa. Since the emergence of semi submersible drilling platform in the 1960s, it has experienced six generations of development. The sixth generation semi submersible drilling platform appeared at the beginning of the 21st century. With dynamic positioning, the hull structure is more optimized and the quality is reduced. It is equipped with automatic control system, with larger variable load, operating water depth of more than 3,000 m, maximum drilling depth of 12,000 m, strong derrick bearing capacity and high power of drilling winch.

With advancements in offshore oil drilling, deepwater drilling technology has been developing consistently, which has promoted the development of conductor jetting, dynamic killing, well logging while-drilling and pressure while-drilling techniques [1]. However, the exploration and development of deepwater resources still suffer from many challenges, which mainly span following three aspects [3–8]. First, if a riser is adopted during operation, riser length must grow with increasing water depth, yielding a heavy and cumbersome structure, especially for the upper riser, which must bear a larger tension. Second, difficulties arise during advancing in the horizontal section; when drilling in the horizontal section, it is difficult for the drilling fluid to carry the rocks. Moreover, the borehole friction increases rapidly, resulting in extra weight constraints. Third, owing to the narrow pore-fraction pressure window, a precise control of wellbore pressure is required for formations with severe leakage, reservoir pressure failure, and high sulfur content. Therefore, focusing on a series of challenges in deepwater drilling, a subsea closed-cycle riserless drilling method with pump + gas combined lift is proposed in this study, providing the theoretical foundation and design basis for efficient, economical, and safe subsea drilling applications.

In this work, the advantages of closed-cycle riserless drilling method using a pump + gas combined lift are analyzed and its multiphase flow drilling model is proposed. By solving the model, the influence of drilling fluid displacement, gas injection displacement, gas injection site and seawater depth on drilling hydraulic parameters can be obtained. The optimization hydraulic parameters design method of closed-cycle riserless drilling method with a subsea pump + gas combined lift is proposed.

2 ADVANTAGES OF THE NOVEL SUBSEA CLOSED-CYCLE RISERLESS DRILLING METHOD USING A PUMP + GAS COMBINED LIFT IN DEEPWATER DRILLING

In 2001, a Norwegian company called AGR developed a riserless mud recovery (RMR) drilling technology based on its cutting transportation system (CTS). The principle of this technology is to pump mud subsea to the drilling platform by leveraging the mud suction module at the wellhead, subsea mud lifting pump, as well as mud return pipeline, thereby forming a closed-cycle of drilling fluid. The practice costs and risks are significantly lower than that of methods using risers [9]. First, RMR was merely adopted for shoal-water oil-and-gas exploitation, which is mainly targeted to solve the drilling challenges concerning complex subsea conditions and shallow risks and ensures a smooth borehole drilling operation on the surface layer. In 2003, the first commercial RMR application was performed in the Caspian Sea. As the technology developed, the closed-cycle riserless drilling system has been advancing from shallow sea to deep sea applications. The issues restricting the application of deepwater closed-cycle drilling methods with risers mainly stem from the lifting capacity of mud lifting pump and strength of mud return pipeline. Therefore, AGR, together with Shell, BP America, and DEMO2000, formed an industrial project team to develop the so-called deepwater RMR system, and successfully conducted a field test in the South China Sea (Malaysia) at a depth of 1,419 m in September 2008. The test has proved the feasibility of this technology in deepwater drilling applications and its advantages for drilling in the South China Sea, such as safe drilling in strata with shallow risk, overcoming the mud logging restrictions, extending the setting depth of surface casing, etc. In 2008, the RMR drilling system has been adopted for a drilling operation with self-elevating platform for the first time, which achieved favorable results. The deepwater RMR system is illustrated in **Figure 1**.

Compared with the conventional riserless mud lifting systems, this system has introduced an innovative gas lifting process by adopting a gas + pump combined lifting scheme. This design can effectively decrease the subsea pump working power, enhance the lifting head, reduce the cost and difficulty of construction, improve the reliability of lifting systems, and enable the application of closed-cycle riserless drilling in offshore applications with higher depth. The gas + pump combined lifting system is illustrated in **Figure 2**.

Major advantages of this novel subsea closed-cycle riserless drilling method with a subsea pump + gas combined lift in deepwater drilling are as follows:

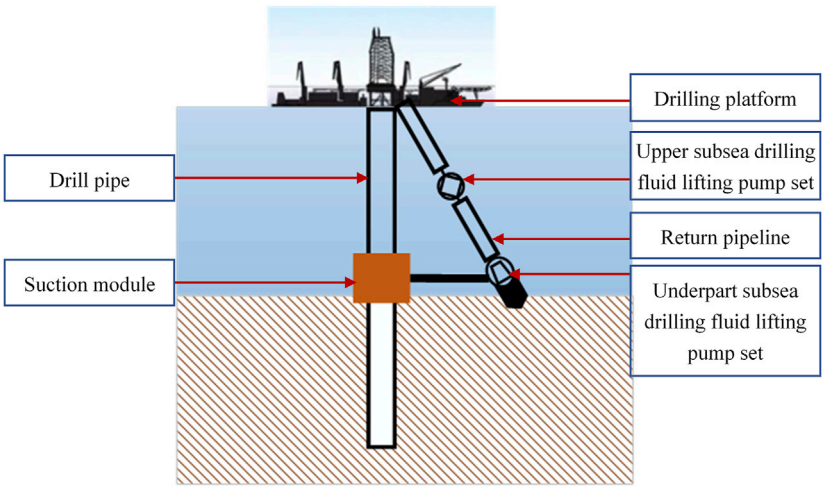

FIGURE 1 | Deepwater RMR system.

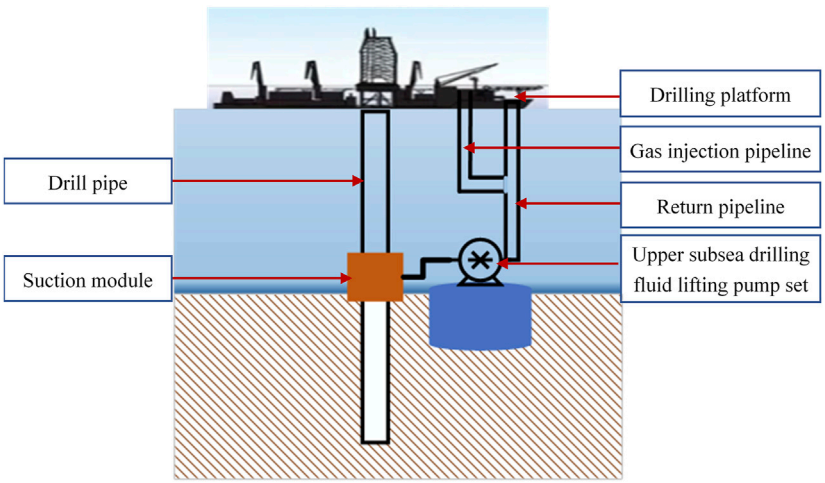

FIGURE 2 | Schematic of the gas + pump combined lifting system.

(1) Riserless drilling: Conventional offshore drilling adopts risers to isolate seawater inside the drilling fluid system. The dual-channel drill pipeline exposed to seawater replaces the cumbersome riser system and its components, thereby reducing the amount of drilling fluid and number of drilling pumps required, as well as the bearing capacity and space requirements for drilling rig deck. Moreover, it can reduce the quantity of casing, optimize the structure along well depth, and obtain a wellbore with a single diameter.

(2) Closed-cycle system: When a subsea pump + gas combined lift is used, drilling fluid is pumped to the well bottom through the inner pipe of the drilling pipeline; then, it impacts the rock stratum via jet from the drill bit. The fluid, carrying rock debris cut by the drilling bit, is then lifted to the subsea mud pipeline along the annular channel formed between the wellbore and drilling pipe. Exploiting the drilling fluid return pipeline, rock debris are carried to the drilling platform via the subsea pump + gas combined lift. Closed-cycle serves as the basis for the implementation of deepwater drilling technology with pressure control. Via precise control of bottom hole pressure and drilling fluid flow, this technique can address the narrow safety density window issue in deepwater drilling, while reducing down-time and well control risks.

(3) High cutting carrying efficiency: In conventional offshore drilling applications, the drilling fluid is pumped in via drill pipe and returned through the borehole annulus and riser annulus after carrying the cuttings. By leveraging the subsea pump + gas combined lift, carried drilling fluid cuttings return to the wellhead via the drilling fluid return pipeline. The drilling fluid is not required to be

transported at high velocities for carrying cuttings to the wellhead, which reduces the scouring of the borehole wall, which is greatly applicable to wells with large displacement and horizontal wells.

(4) Enlarging the working water depth of third- and fourth-generation drilling rigs: deepwater and ultra-deepwater operations mandate significant load-bearing requirements on drilling rigs and deck space. Hence, for conventional offshore drilling, fifth-, sixth- or seventh-generation drilling rigs are required. The novel closed-cycle riserless drilling method using a subsea pump + gas lift alleviates the load-bearing capacity and space requirements on the drilling rig deck. Consequently, third- and fourth-generation drilling rigs can be adopted for such drilling operations, which reduces the daily running costs of drilling rigs and increases their working water depth.

3 MULTIPHASE FLOW PATTERNS IN THE PROPOSED NOVEL CLOSED-CYCLE RISERLESS DRILLING METHOD WITH A SUBSEA PUMP + GAS COMBINED LIFT

This technology aims to optimize the hydraulic parameters in deepwater drilling. The hydraulic parameter accuracy directly affects the safety and efficiency of drilling. Significant discrepancies exist between the novel closed-cycle riserless drilling with a subsea pump + gas combined lift and conventional deepwater drilling applications, which are mainly observed in the calculation of gas-liquid-solid three-phase flow in the upper return pipeline, wellbore pressure, and cutting carrying efficiency when subsea pump is online. The wellbore multiphase flow model states the fundamental theory for calculating the hydraulic parameters of the novel closed-cycle riserless drilling with a subsea pump + gas combined lift.

The foremost multiphase flow simulation of the well kick adopts homogeneous flow models. Leblanc and Leuis (1968) established the first multiphase flow model of a well kick suitable for gas overflow [10]. This model assumes that the overflowing gas exists as a continuous column inside the wellbore; then, performs simple calculations regarding the pressure change in the annulus during overflow without considering the mutual slippage between gas and liquid phases. Similarly, based on the concept of homogeneous flow, Horberock and Stanbery (1981) calculated the average value of gas-liquid characteristic parameters [11]; then, they established the continuity and momentum conservation equations of the homogeneous fluid in vertical pipeline. Subsequently, they simulated the pressure change in the wellbore. Santos (1982) established a relatively comprehensive multiphase flow model of deepwater kick by assuming a bubbly status in the wellbore during overflow [12]. In their model, they introduced the void fraction concept, as well as the effects of gas-liquid slippage and friction pressure losses in two-phase flows. Nickens (1987) considered the velocity slippage between different phases as well as the friction pressure loss of single and multiple flows. By numerically solving the dynamic equations of mass conservation for gas and liquid phases simultaneously, a comprehensive multiphase flow model in the wellbore has been established [13]. However, many factors, such as temperature variation, gas dissolution, etc., were not considered in this model. Adopting the established model, the effects of wellbore shape and hydraulic parameters of drilling assembly on the borehole pressure distribution were investigated. Moreover, many scholars, such as White and Walton (1990), Van Slyke and Huang (1990), Szczepanski et al. (1998), Nunes et al. (2002), and Velmurugan et al. (2016), applied the classic model of gas-liquid two-phase flow during well kick to analyze the multiphase flow pattern in the wellbore under different working conditions, namely, varying mud types [14, 15], overflowing gas composition, and deepwater drilling [16–18]. Sun et al. (2017, 2022) integrated the hydrate phase balance equilibrium and phase transition rate models with the multiphase flow model of deepwater well kick [19, 20]. Based on their analysis, they discovered that during well kick, the phase transition of hydrate would lead to concealment in the early stage and burstiness in the later stage. Fu et al. (2020, 2022) revealed that the hydrate formation makes drilling fluid exhibit the shear-thinning at low shear rate condition and the shear-thickening at high shear rate condition. The corresponding rheological model of drilling fluid is developed incorporating hydrate concentration, shear rate and additive concentration, which has an important contribution to improvement of the multiphase flow [21–23].

Because the novel closed-cycle riserless drilling method with a subsea pump + gas combined lift is still in its initial stage globally, current research on the multiphase flow pattern in wellbore is mainly based on the working conditions of deepwater drilling applications with risers. The multiphase flow patterns in wellbore that are affected by multiple factors, such as subsea pump and gas injection, are rarely reported. Hence, the existing theoretical model is difficult to apply in most cases.

3.1 Multiphase Flow Model of the Novel Deepwater Closed-Cycle Riserless Drilling Method With a Subsea pump + gas Combined Lift

When using the novel deepwater closed-cycle riserless drilling with a subsea pump + gas combined lift, gas lifting module enters wellbore through the mud return pipeline and changes the flow patterns of drilling fluid from liquid-solid two-phase flow to complex three-phase flow comprising gas, liquid, and solid. The selection process of pump + gas combined lifting parameters is constrained by various restrictions, such as borehole cleanliness, mud pump capacity, formation stability, rated power of lifting pump, etc. The following requirements should be fulfilled:

(1) The cutting carrying capacity of the wellbore must be ≥ 50%.
(2) The cutting bed height in inclined and horizontal sections must be smaller than 10% of the pipe size.
(3) The cutting concentration in the pipeline must be < 9%.

(4) The bottom hole pressure must be maintained between the fracture pressure and pore pressure of weak formation.
(5) The power of mud pump and subsea lifting pump must be within the rated power requirements.

3.1.1 Multiphase Flow Model of Closed-Cycle Riserless Drilling

The drilling fluid return pipeline is divided into two sections, namely, sections a and b. Along the drilling fluid return pipeline, the section from the subsea lifting pump to the intersection of gas injection pipeline and drilling fluid return pipeline is named section a of the return pipeline (as shown in **Figure 2**). Accordingly, the section from subsea lifting pump to the intersection of the gas injection pipeline and drilling fluid return pipeline to the drilling ship is named section b of return pipeline. The multiphase flow equations of sections a and b are established. No gas phase exists in section a of drilling fluid return pipeline. By considering only the liquid and cutting phases, the multiphase flow equations in section a of drilling fluid return pipeline are stated as follows:

① Continuity equations: **Eq. 1**

Liquid phase:

$$\frac{\partial}{\partial t}\left(A\rho_l E_l\right)+\frac{\partial}{\partial s}\left(A\rho_l v_l E_l\right)=0 \tag{1}$$

Cutting phase: **Eq. 2**

$$\frac{\partial}{\partial t}\left(A\rho_c E_c\right)+\frac{\partial}{\partial s}\left(A\rho_c v_c E_c\right)=0 \tag{2}$$

②Momentum equation: **Eq. 3**

$$\begin{aligned}&\frac{\partial}{\partial t}\left(AE_l\rho_l v_l+AE_c\rho_c v_c\right)+\frac{\partial}{\partial s}\left(AE_l\rho_l v_l^2+AE_c\rho_c v_c^2\right)\\&+Ag\cos\alpha\left(E_l\rho_l+E_c\rho_c\right)+\frac{d(Ap)}{ds}+\frac{d(Af_r)}{ds}=0\end{aligned} \tag{3}$$

③Energy equation: **Eq. 4**

$$\begin{aligned}&\frac{\partial}{\partial t}\rho_l E_l\left(h+\frac{1}{2}v^2-g\cdot s\cdot\cos\alpha\right)-\frac{\partial\left(w_l\left(h+\frac{1}{2}v^2-g\cdot s\cdot\cos\alpha\right)\right)}{\partial s}\\&=2\left[\frac{1}{A'}\left(T_{ei}-T_t\right)\right]\end{aligned} \tag{4}$$

Of which, **Eq. 5**

$$A'=\frac{1}{2\pi}\left[\frac{k_e+r_{co}U_aT_D}{r_{co}U_ak_e}\right] \tag{5}$$

where A denotes the sectional area of annulus (m^2);E_l and E_c denote the volume fraction of drilling fluid and cutting phases, respectively (dimensionless); v_c and v_l denote the velocity of cutting and drilling fluid phases (m/s); ρ_c and ρ_l denote the density of cutting and drilling fluid phases, respectively, (kg/m^3); q_c denotes the generation rate of cuttings (kg/s); f_r denotes the on-way friction pressure drop (Pa); s is the coordinate along the flow direction (m); α is the deviation angle of the well (°); p denotes the pressure (Pa); T_a is fluid temperature in the drilling fluid return pipeline (°C); k_e is the thermal conductivity of seawater (W/(m°C)); r_{co} is the outer diameter of drilling fluid return pipeline (m); w_c is the mass flow rate of cuttings (kg/s); w_l is the mass flow of drilling fluid (kg/s); C_{pg} is the specific heat of gas phase (J/kg°C); T_{ei} and T_t denote the temperatures of seawater and drilling fluid, respectively, in return pipeline (°C); U_a is the total heat transfer coefficient between fluid in drilling fluid return pipeline and seawater (W/(m^2·°C)); T_D is the transient heat transfer coefficient; g is the gravitational acceleration (m/s^2); h is the well depth at a certain point (m); A' is an intermediate parameter.

The gas lifting system injects gas into the drilling fluid return pipeline, which alters the flow characteristics of drilling fluid from the original liquid-solid two-phase flow to the more complex gas-liquid-solid three-phase flow. Consequently, the multiphase flow equations in section b of drilling fluid return pipeline are stated as follows:

① Continuity equations:

Gas phase: **Eq. 6**

$$\frac{\partial}{\partial t}\left(A\rho_g E_g\right)+\frac{\partial}{\partial s}\left(A\rho_g v_g E_g\right)=0 \tag{6}$$

Liquid phase: **Eq. 7**

$$\frac{\partial}{\partial t}\left(A\rho_l E_l\right)+\frac{\partial}{\partial s}\left(A\rho_l v_l E_l\right)=0 \tag{7}$$

Cutting phase: **Eq. 8**

$$\frac{\partial}{\partial t}\left(A\rho_c E_c\right)+\frac{\partial}{\partial s}\left(A\rho_c v_c E_c\right)=0 \tag{8}$$

②Momentum equation: **Eq. 9**

$$\begin{aligned}&\frac{\partial}{\partial t}\left(AE_g\rho_g v_g+AE_l\rho_l v_l+AE_c\rho_c v_c\right)+\frac{\partial}{\partial s}\left(AE_g\rho_g v_g^2+AE_l\rho_l v_l^2+AE_c\rho_c v_c^2\right)\\&+Ag\cos\alpha\left(E_g\rho_g+E_l\rho_l+E_c\rho_c\right)+\frac{d(Ap)}{ds}+\frac{d(Af_r)}{ds}=0\end{aligned} \tag{9}$$

③Energy equation: **Eq. 10**

$$\begin{aligned}&\frac{\partial}{\partial t}\left[\left(\rho_l E_l\left(h+\frac{1}{2}v^2-g\cdot s\cdot\cos\alpha\right)\right)+\left(\rho_g E_g\left(h+\frac{1}{2}v^2-g\cdot s\cdot\cos\alpha\right)\right)\right]\\&-\left[\frac{\partial\left(w_l\left(h+\frac{1}{2}v^2-g\cdot s\cdot\cos\alpha\right)\right)}{\partial s}+\frac{\partial\left(w_g\left(h+\frac{1}{2}v^2-g\cdot s\cdot\cos\alpha\right)\right)}{\partial s}\right]\\&=2\left[\frac{1}{A'}(T_{ei}-T)_t\right]\end{aligned} \tag{10}$$

where E_g is the volume fraction of gas (dimensionless); v_g denotes the gas velocity (m/s); ρ_g denotes the gas density (g/m^3); q_g is the gas injection rate (kg/s); w_g is the mass flow of gas (kg/s).

3.1.2 Auxiliary Equations and Boundary Conditions

(1) Auxiliary equations

To solve control equations of multiphase flow, it is necessary to combine the calculation equations of gas phase volume

fraction, drilling fluid rheology, distribution coefficient, and drift velocity[19].

The gas phase volume fraction, E_g, is calculated using **Eq. 11**; gas distribution coefficient, C_0, is calculated using **Eq. 12**; drift velocity, V_{gr}, is calculated using **Eq. 13**; rheological properties of drilling fluid in the pipeline are calculated using **Eq. 13**, including the apparent viscosity, plastic viscosity, and dynamic shear force of the drilling fluid: **Eq. 14**

$$E_g = \frac{V_{sg}}{C_0 V_m + V_{gr}} \tag{11}$$

$$C_0 = \frac{2}{1+\left(\frac{\mathrm{Re}_{tp}}{1000}\right)^2} + \frac{1.2-0.2\theta^4}{1+1+\left(\frac{1000}{\mathrm{Re}_{tp}}\right)^2} \tag{12}$$

$$V_{gr} = 1.53\left(\frac{g\sigma\left(\rho_l-\rho_g\right)}{\rho_l^2}\right)^{0.25} + 0.35\sqrt{\frac{gD_0\left(\rho_l-\rho_g\right)}{\rho_l}}\theta(1-\theta)^{0.25} \tag{13}$$

$$f(p,T) = f(p_0,T_0)e^{\left[A(T-T_0)+B\left(p-p_0\right)+C(T-T_0)\left(p-p_0\right)+D(T-T_0)^2\right]} \tag{14}$$

where V_{sg} denotes the apparent flow velocity of gas (m/s); V_m denotes the mixing flow velocity of drilling fluid and cuttings (m/s); σ is the surface tension (Pa); C_0 is the distribution coefficient (dimensionless); D_0 is the pipe diameter (m); Re_{tp} is the two-phase Reynolds number (dimensionless); θ is the average sectional void fraction (dimensionless); f (p,T) represents μ_a (p,T), μ_p (p,T), and τ_a (p,T), respectively, namely, apparent viscosity, plastic viscosity, and dynamic shear force under pressure p and temperature T; p_0 is the atmospheric pressure (MPa); T_0 is the ambient temperature (°C); A, B, C, and D denote the characteristic constants of drilling fluid, whose values are related to the composition of drilling fluid.

The equation to calculate the sinking velocity of cuttings in the pipe is as follows: **Eq. 15**

$$\begin{aligned} v_s &= \frac{k_1 d_p^2\left(\rho_s-\rho_f\right)}{\mu_e} \quad N_R \le 10 \\ v_s &= \frac{k_2 d_p^2\left(\rho_s-\rho_f\right)^{0.6667}}{\left(\rho_f\mu_e\right)^{0.3333}} \quad 10 < N_R \le 100 \\ v_s &= \frac{k_3\left[d_p\left(\rho_s-\rho_f\right)\right]^{0.5}}{\left(\rho_f\right)^{0.5}} \quad N_R > 100 \end{aligned} \tag{15}$$

where k_1, k_2, and k_3 are experimental coefficients, whose values are 0.3268, 0.07068, and 0.0813, respectively; N_R is the sinking Reynolds number of particles; μ_e is the plastic viscosity of drilling fluid (mPa·s); ρ_f and ρ_s are the density of drilling fluid and cuttings, respectively (g/cm^3).

The power outputs for mud and subsea lifting pumps are calculated using **Eqs 16**, **17**, respectively:

$$P_s = p_s Q \tag{16}$$

$$P_o = p_o Q \tag{17}$$

where, P_s is the power output of the mud pump (W); P_o is the power output of the subsea lifting pump (W); Q is displacement of drilling fluid (m^3/s).

Because PR equation has high accuracy in estimating liquid density and describing the phase behavior of high-pressure system, and is widely used in practical engineering, the state of gas in this paper is mainly calculated by PR equation (24).

Equation 18–23

$$p = \frac{RT}{V-b} - \frac{a}{V(V+b)+b(V-b)} \tag{18}$$

$$a = a_c \cdot \alpha(T_r) \tag{19}$$

$$b = \frac{0.07780RT_c}{p_c} \tag{20}$$

$$a_c = \frac{0.45724R^2T_c^2}{p_c} \tag{21}$$

$$\alpha(T_r) = \left[1+m\left(1-T_r^{0.5}\right)\right]^2 \tag{22}$$

$$m = 0.37464 + 1.5226w - 0.26992w^2 \tag{23}$$

Where, p is the environmental pressure (Pa); T is the environmental temperature (°C); p_c is the critical pressure of gas (Pa); T_c is the critical temperature of gas (°C); w is the eccentricity factor of gas, dimensionless; V is molar volume (m^3/kmol); Z is the compression factor, dimensionless.

(2) Boundary conditions

The temperature and pressure of drilling fluid inside the return pipeline on sea surface are measured using thermometer and pressure gauges at the wellhead. The displacement of drilling fluid is calculated based on the mud pump readings. The air injection displacement is measured according to the gas flowmeter, and the cutting displacement is calculated based on the mechanical drilling speed.

The boundary conditions of well section b are as follows: **Eq. 24**

$$\begin{cases} P(0,t) = P_0 \\ T(0,t) = T_0 \\ q_g(h_1,t) = q_0 \\ q_c(0,t) = q_c \\ q_l(0,t) = q_l \end{cases} \tag{24}$$

Well section a adapts to well section b, when only the liquid-solid two phases are considered. The initial conditions are **Eqs 25–27**

$$E_g(h_1,0) = 0 \tag{25}$$

$$E_c(h_1,0) = \frac{V_{sc}(h_1,0)}{C_c V_{sl}(h_1,0) + V_{cr}(h_1,0)} \tag{26}$$

$$E_m = 1 - E_c \tag{27}$$

where V_{sc}, V_{sl}, and V_{cr} are the drift velocity of cuttings, liquid phase, and cutting settlement, respectively (kg/m^3), and h_1 is the insertion depth of gas injection pipeline (m).

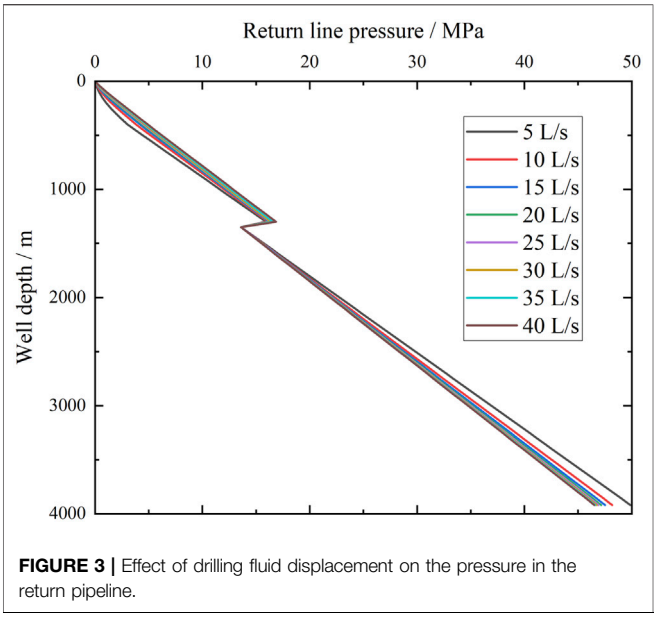

FIGURE 3 | Effect of drilling fluid displacement on the pressure in the return pipeline.

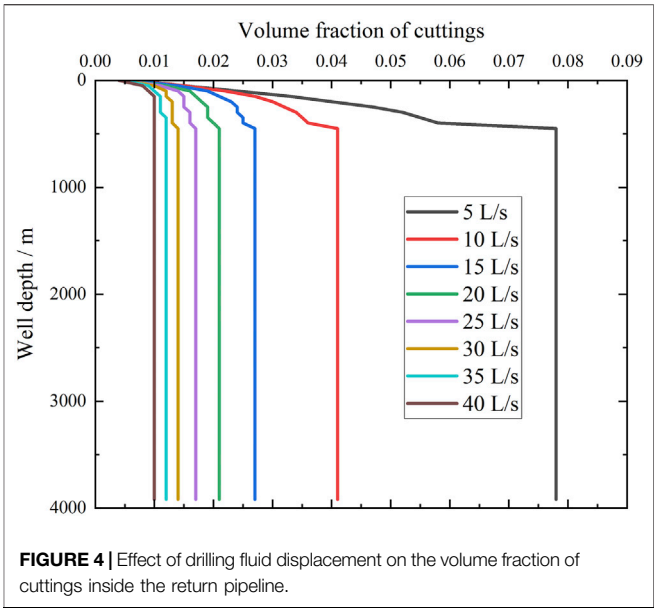

FIGURE 4 | Effect of drilling fluid displacement on the volume fraction of cuttings inside the return pipeline.

A method similar to the so-called SIMPLE method is adopted to solve the multiphase flow equations. When solving the equations, the first-order backward difference is used for the time partial derivation. Taking the mass conservation equation of gas phase as an example, the difference scheme of its time partial derivative is described as follows: **Eq. 28**

$$\frac{\left(E_g\rho_g\right)^j-\left(E_g\rho_g\right)^{j-1}}{\Delta t}+\frac{\partial\left(E_g\rho_g v_g\right)^j}{\partial s}=0 \tag{28}$$

For the spatial partial derivative, the finite volume method of a staggered grid is used for calculating the difference. The scalar variables (pressure, void fraction, liquid holdup, liquid density, and gas density) are located in the center of the control unit, while the vector variables (liquid velocity and gas velocity) are located at the boundaries.

The first-order upwind differential scheme is adopted for the mass and momentum conservation equations. Taking the mass conservation equation as an example, the differential scheme of its convection term is described as follows: **Eq. 29**

$$\left.\frac{\partial\left(E_g\rho_g v_g\right)}{\partial s}\right|_i=\frac{1}{\Delta s}\left[\left(E_g\rho_g v_g\right)_{\frac{i+1}{2}}-\left(E_g\rho_g v_g\right)_{\frac{i-1}{2}}\right] \tag{29}$$

where I and j are the time and space nodes, respectively, and Δs and Δt are the space and time steps, respectively. Basic parameters obtained in step 1 are substituted into the discrete formula to calculate the gas injection displacement of current step, q_g, as well as the pressure, gas velocity, drilling fluid return velocity, cutting return velocity, and cutting concentration distribution along the drilling fluid return pipeline at a depth of h_1 for the gas injection pipeline.

3.2Analysis of Simulation Results

The basic simulation parameters are the actual parameters of a wellbore in the South China Sea, which include a well depth of 3,918 m, water depth of 1,340 m, drilling fluid density of 1,200 kg/m^3, mechanical rate of penetration of 40 m/h, injection pipe depth of 400 m, diameter of 50 mm, injection gas flow of 120 m^3/h, and inner diameter of drilling fluid return pipeline of 80 mm.

3.2.1 Effect of Drilling Fluid Displacement on the Multiphase Flow Inside the Wellbore

With the same pumping parameters, the drilling fluid displacement varies from 5 L/s to 40 L/s with 5 L/s increments. The multiphase flow model for the closed-cycle riserless drilling is used during the analysis, and the influence of subsea pump displacement on the multiphase flow in the return pipeline is examined, as demonstrated in **Figure 3**. The simulation results indicate that in the section mudline, the pressure along depth inside the return pipeline increases with increasing drilling fluid displacement values; moreover, in the section below mudline, the pressure along depth inside the return pipeline decreases with increasing drilling fluid displacement. This is because the subsea pump is located at the mudline level. In the section above the mudline, increasing the liquid phase displacement will result in higher subsea pump discharge pressure and larger fluid kinetic energy in the pipeline. Hence, the pressure inside the pipe increases. In the section below mudline, as the fluid in the pipeline is not affected by the subsea pump, the well bottom pressure decreases with an increasing drilling fluid displacement, decreasing the pressure inside the pipeline.

As illustrated in **Figure 4**, the variation in drilling fluid displacement affects the cutting distribution inside the return pipeline. Higher displacement yields smaller volume fraction of cuttings in the pipeline. Affected by the gas injection in the pipeline at 400 m, the volume fraction of cuttings gradually decreases along the return pipeline and eventually becomes consistent. Gas injection will enhance the turbulence intensity of the fluid in the pipeline, which increases the fluid flow velocity

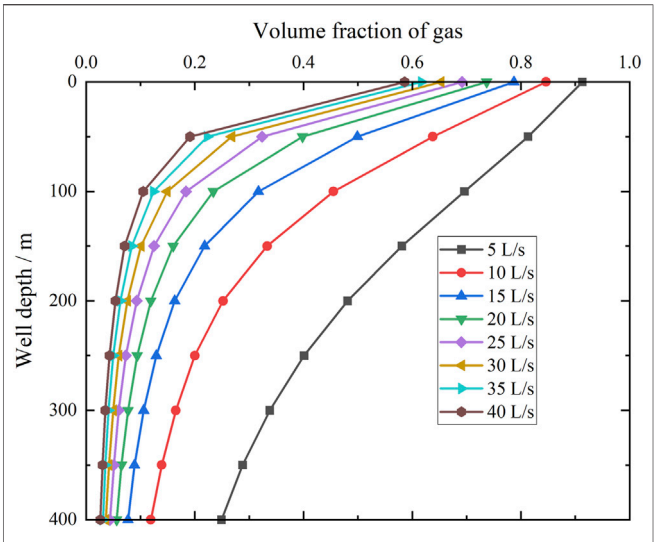

FIGURE 5 | Effect of drilling fluid displacement on the gas volume fraction inside the return pipeline.

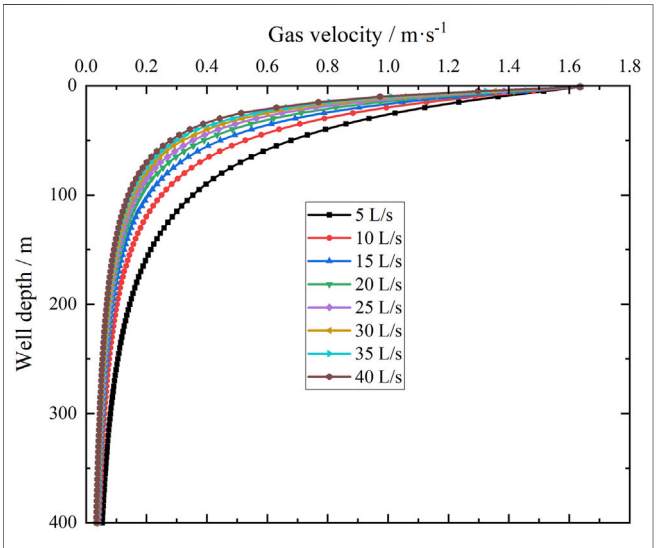

FIGURE 6 | Gas velocity distribution in the wellbore with respect to different drilling fluid displacements.

and decreases the sectional volume fraction of cuttings. Therefore, migrating cuttings to the wellhead becomes easier.

Effect of drilling fluid displacement on gas volume fraction inside the return pipeline is calculated and demonstrated in **Figure 5**. As the gas migrates from the gas injection point at a depth of 400 m, the gas volume fraction decreases with increasing drilling fluid displacement. When the drilling fluid displacement is 5 L/s, 10 L/s, 15 L/s, 20 L/s, 25 L/s, 30 L/s, 35 L/s, and 40 L/s, the gas volume fraction returning to the wellhead is 0.913, 0.846, 0.787, 0.737, 0.692, 0.653, 0.617, and 0.586, respectively. Lowering the subsea pump displacement will result in a larger sectional gas volume fraction in the pipeline, which significantly increases effects of gas injection on cutting migration. As shown in

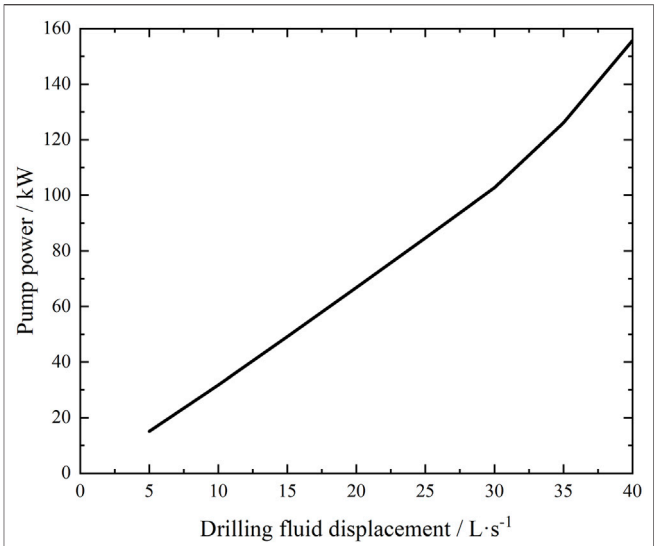

FIGURE 7 | Effect of drilling fluid displacement on pump lifting power.

Figure 6, during the upward migration of gas along the pipeline, the flow velocity first increases slowly and then rapidly owing to the gas volume expansion. The gas velocity in gas injection section increases gradually with an increasing drilling fluid displacement. The effects of a fluid displacement lower than 15 L/s are more significant compared with those of other setpoints.

The drilling fluid displacement is closely associated with pump lifting power. As illustrated in **Figure 7**, the results of calculating the drilling fluid displacement effect on pump lifting power indicate that a higher drilling fluid displacement results in a higher subsea pump working power, which exhibits a nonlinear relationship. During the actual riserless drilling process, considering the power configuration of drilling platform or drilling ship, the subsea pumps should be selected to combine the effects of sites and amount of gas injection. Moreover, to optimize cutting carrying efficiency, a minimum drilling fluid displacement is obtained for selecting the corresponding pump power, which serves as a theoretical basis for selecting the proper subsea pumps.

3.2.2 Effect of Gas Injection Displacement on the Multiphase Flow Inside the Wellbore

The most prominent characteristic of novel riserless drilling is the combination of gas injection and subsea pump lift processes. The variations in the gas injection displacement has great impact on the pressure and volume fraction in the pipeline as well as the subsea pump power. By setting the gas injection displacement to 60 m^3/h, 80 m^3/h, 100 m^3/h, 120 m^3/h, 140 m^3/h, 160 m^3/h, 180 m^3/h, and 240 m^3/h, the effect of gas injection displacement on the multiphase flow in wellbore can be calculated.

As shown in **Figure 8**, the pressure along depth inside the return pipeline decreases with increasing gas injection displacement values above the mudline level. In the section

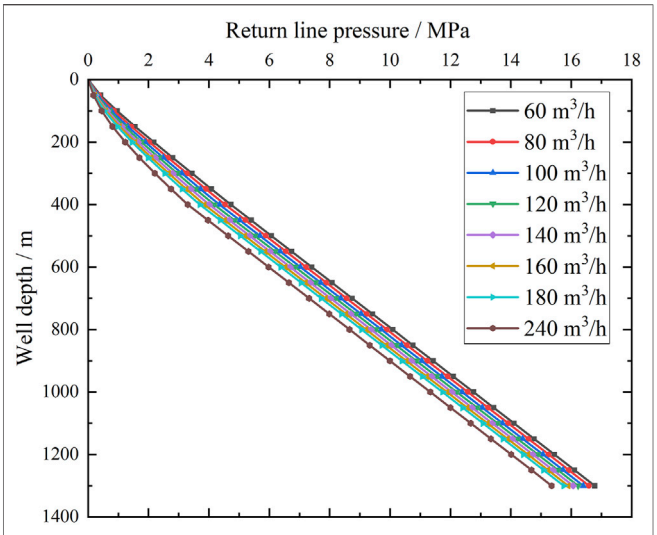

FIGURE 8 | Effect of gas injection displacement on pressure in return pipeline.

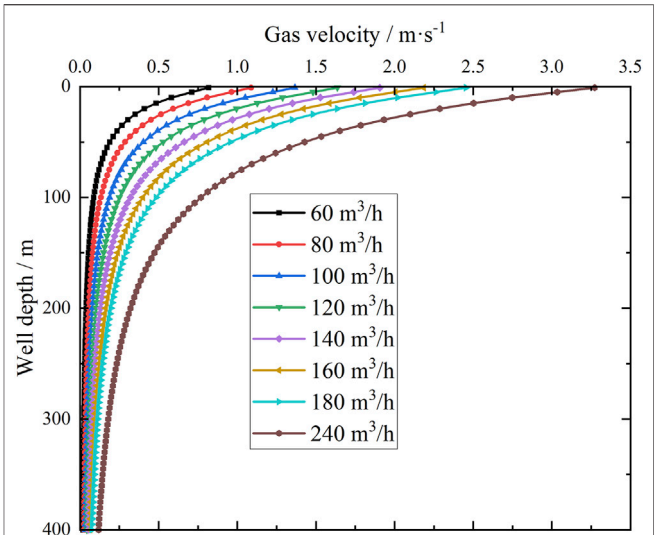

FIGURE 10 | Gas velocity distribution in the wellbore with different gas injection displacement values.

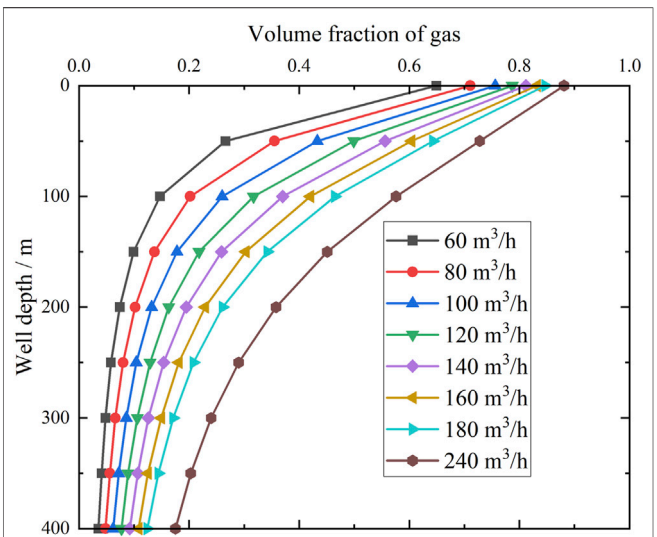

FIGURE 9 | Effect of gas injection displacement on gas volume fraction in the return pipeline.

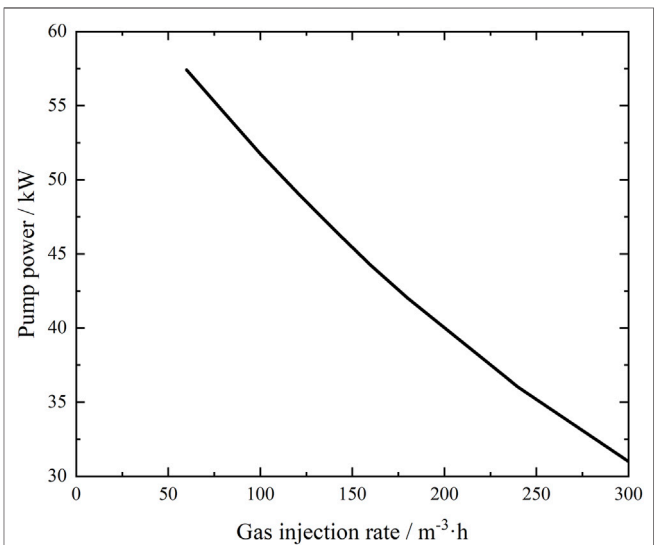

FIGURE 11 | Effect of gas injection displacement on pump lifting power.

below the mudline, the gas injection displacement has no effect on pressure in the pipeline is shown. Therefore, in this study, only pressure simulation results in the section above mudline are considered. Affected by gas injection displacement, the discharge pressure of the subsea pump fluctuates greatly. When the gas injection displacement changes from 60 m^3/h to 240 m^3/h, the pump discharge pressure decreases from 17.288 to 5.527 MPa. A higher gas injection displacement results in smaller pressure losses in the return pipeline and a higher pressure in the pipeline with the same depth.

Gas injection displacement is crucial for ensuring the efficient migration of cuttings and enhance the pumping capacity. **Figure 9** demonstrates the effect of varying gas injection displacement using an injection site at 400 m on the gas volume fraction in the return pipeline. A larger gas injection displacement results in a higher gas proportion and fluid kinetic energy throughout the section inside the pipeline; therefore, cuttings can be carried to the wellhead more easily. From the calculation procedure depicted in **Figure 10**, the gas flow velocity increases with increasing gas injection displacement; its cutting carrying capacity is enhanced significantly as well. When the gas injection displacement elevates from 60 m^3/h to 240 m^3/h, the gas flow velocity at the wellhead increases from 0.8182 m/s to 3.273 m/s.

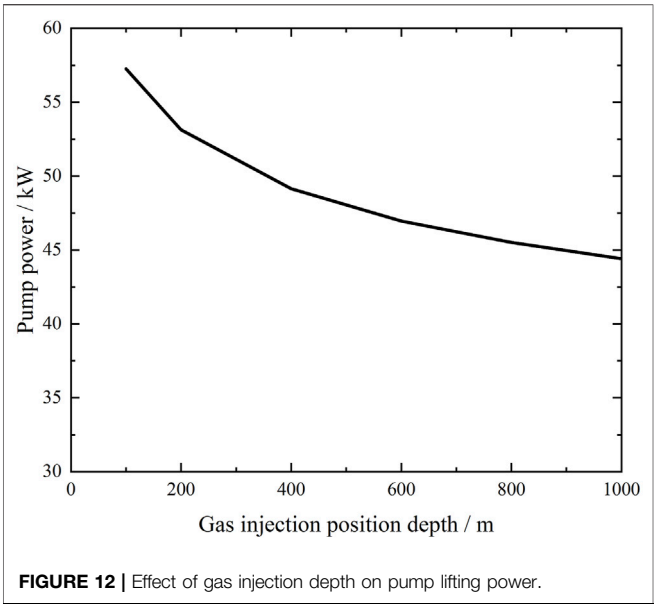

FIGURE 12 | Effect of gas injection depth on pump lifting power.

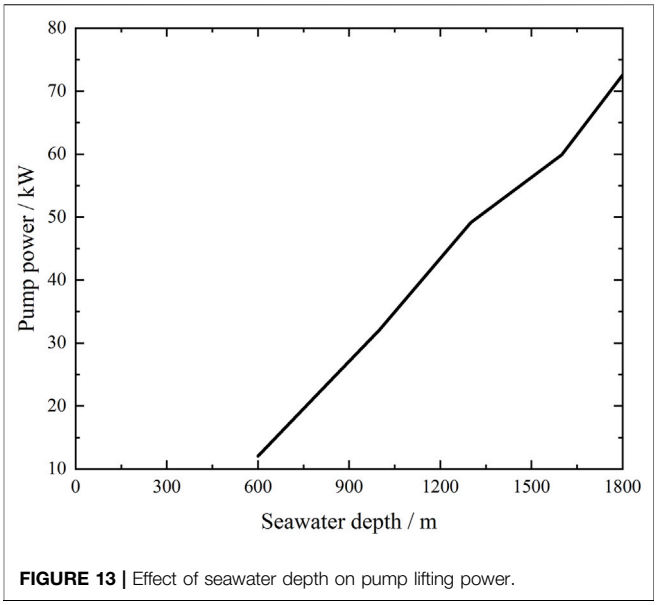

FIGURE 13 | Effect of seawater depth on pump lifting power.

The effect of gas injection displacement on pump power is analyzed, which can greatly decrease the load-bearing capacity of pump. By increasing gas injection displacement, the subsea lifting pump power decreases (see **Figure 11**). Especially in the case of low gas injection displacement, its effect on pump power is more significant. As gas injection displacement elevates from 60 m^3/h to 120 m^3/h, the pump power decreases by 8.28 kW. In the case of high gas injection displacement, as gas injection displacement increases from 180 m^3/h to 240 m^3/h, the pump power decreases by 6.01 kW. Therefore, the subsea pump and gas lifting equipment cannot be operated at a high operation efficiency simply by constantly increasing the gas injection displacement. Consequently, in the design stage, the lifting capacity of subsea pump and optimal gas injection displacement should be thoroughly considered.

3.2.3 Effect of Gas Injection Site on the Subsea Pump Lifting Power

Gas injection displacement and sites are the key parameters of gas lifting. Properly selecting the gas injection sites significantly affects the subsea pump power requirements. The interaction between the depth of gas injection sites and pump lifting power is calculated as shown in **Figure 12**. Keeping the gas injection displacement constant, as the depth of gas injection sites increases, the subsea pump power requirement is reduced with a decreasing slope. As the gas injection site depth changes from 100 to 400 m, the pump power decreases from 57.255 to 49.14 kW, an 8.115 kW reduction. As the gas injection site depth changes from 400 to 700 m, the pump power is reduced by 2.903 kW. A deeper gas injection site results in higher requirements for the air compressor on the platform. Based on the conditions of this example, the recommended depth of gas injection site is 400 m.

3.2.4 Effect of Seawater Depth on the Subsea Pump Lifting Power

During deepwater drilling, as seawater depth increases, the requirements regarding drilling equipment and engineering risks will increase as well. The subsea pumping power variations with respect to different seawater depths are calculated as illustrated in **Figure 13**. The calculation results exhibit that as seawater depth increases, the subsea pump lifting power increases almost linearly. The subsea pump power requirements increase with an increasing depth, during which the effect of gas lifting increases as well. Based on the conditions of this example, subsea pump power increases by 4.97 kW for every additional 100 m in seawater depth.

4 OPTIMIZATION OF HYDRAULIC PARAMETERS IN THE NOVEL DEEPWATER CLOSED-CYCLE RISERLESS DRILLING METHOD WITH A SUBSEA PUMP + GAS COMBINED LIFT

The novel deepwater closed-cycle riserless drilling method with a subsea pump + gas combined lift aims to address the marine environment pollution and poor wall protection issues caused by open-cycle drilling operation, while avoiding the high costs and risks associated with drilling operations that use risers. In a conventional closed-cycle riserless drilling system, the return of mud is only powered by the subsea lifting pump. Therefore, the flow rate and cutting carrying effect of mud return can be solely controlled by adjusting the lifting pump. For the novel deepwater closed-cycle riserless drilling method with a subsea pump + gas combined lift, the interaction between process parameters of gas lift and flow pattern of mud return, as well as the coupling between each process parameter during pump +

gas combined lifting, should be considered to achieve efficient cutting carrying.

In a fixed deepwater drilling block, given the drilling depth, seawater depth, and other drilling parameters, the minimum return velocity of cutting carrying and its corresponding subsea pump rated power with gas lifting can be calculated. By designing orthogonal experiments, the subsea pump power can be simulated and calculated, which can fulfill the cutting carrying requirements with respect to different gas injection depths of gas injection pipeline, gas injection displacements, and drilling fluid displacements. The minimum subsea pump power is selected to optimize and maximize the cutting carrying efficiency by gas injection. In the block with large seawater depth, it might be preferred to first increase gas injection displacement and then increase the depth of gas injection sites. Consequently, the subsea pump load can be decreased as much as possible; in other words, a high-efficiency deepwater drilling process with a low-power subsea pump can be achieved.

5 CONCLUSION

The multiphase flow model of the deepwater closed-cycle riserless drilling with a subsea pump + gas combined lift has been proposed to analyze the effects of drilling fluid displacement, gas injection displacement, gas injection site, and seawater depth on the multiphase flow in the novel closed-cycle riserless drilling wellbore. Subsequently, the following conclusions are obtained:

(1) With increasing drilling fluid displacement, the volume fraction of cuttings in the pipeline decreases; whereas, the gas velocity in gas injection pipeline increases gradually. When the drilling fluid displacement is lower than 15 L/s, the effects are more prominent.
(2) With increasing gas injection displacement, it is easier to carry the cuttings and return them to the wellhead, which reduces the subsea lifting pump power requirement.
(3) With an increasing depth of gas injection sites, the subsea pump power requirement is reduced with a decreasing slope.
(4) Greater seawater depths result in higher power requirements for the subsea pump; accordingly, the lifting power increases almost linearly.

DATA AVAILABILITY STATEMENT

The raw data supporting the conclusions of this article will be made available by the authors, without undue reservation.

AUTHOR CONTRIBUTIONS

JW Overall structure design and numerical simulation. JS: Multiphase flow model of closed-cycle riserless drilling biulding. WX: Advantages of the novel subsea closed-cycle riserless drilling method using a pump + gas combined lift in deep-sea drilling analysis. HC: Mesh generation and solution of multiphase flow model. CW: Effect of gas injection site on the subsea pump lifting power analysis and language check. YY: Effect of seawater depth on the subsea pump lifting power analysis. RQ: Optimization of hydraulic parameters analysis.

FUNDING

This work was supported by the Key Special Project for Introduced Talents Team of Southern Marine Science and Engineering Guangdong Laboratory (Guangzhou) (GML2019ZD0501), the National Key Research and Development Program of China (2021YFC2800803).

REFERENCES

1. Peter A. *Deepwater Drilling: Well Planning, Design, Engineering, Operations, and Technology Application*. Houston, Texas: Gulf Professional Publishing (2019).
2. Yang X, Sun J, Zhang Z, Xu L, Wang C, Liu Z, et al. Design and Application of Drilling System Digital Prototype for deepwater Drilling Platform. *IOP Conf Ser Mater Sci Eng* (2020) 964:012027. doi:10.1088/1757-899x/964/1/012027
3. Meng X, Zhu J, Chen G, Shi J, Li T, Song G. Dynamic and Quantitative Risk Assessment under Uncertainty during deepwater Managed Pressure Drilling. *J Clean Prod* (2022) 334:130249. doi:10.1016/j.jclepro.2021.130249
4. Li H, Zhang M, Lau HC, Fu S. China's deepwater Development: Subsurface Challenges and Opportunities. *J Pet Sci Eng* (2020) 195:107761. doi:10.1016/j.petrol.2020.107761
5. Huang Y, Lan H, Hong Y-Y, Wen S, Yin H. Optimal Generation Scheduling for a Deep-Water Semi-submersible Drilling Platform with Uncertain Renewable Power Generation and Loads. *Energy* (2019) 181:897–907. doi:10.1016/j.energy.2019.05.157
6. Tian D, Fan H, Leira BJ, Sævik S. Study on the Static Behavior of Installing a Deep-Water Drilling Riser on a Production Platform. *J Pet Sci Eng* (2020) 185:106652. doi:10.1016/j.petrol.2019.106652
7. Gao Y, Chen Y, Zhao X, Wang Z, Li H, Sun B. Risk Analysis on the Blowout in deepwater Drilling when Encountering Hydrate-Bearing Reservoir. *Ocean Eng* (2018) 170:1–5. doi:10.1016/j.oceaneng.2018.08.056
8. Xu Y, Jin Y, Guan Z, Liu Y, Wang X, Zhang B, et al. Evolution of Gas Kick and Overflow in Wellbore during deepwater Drilling and Advantage Analysis of Early Gas Kick Detection in Riser. *J China Univ Pet (Edition Nat Science)* (2019) 43(1):60–7.
9. Li X, Zhang J, Tang X, Mao G, Wang P. Study on Wellbore Temperature of Riserless Mud Recovery System by CFD Approach and Numerical Calculation. *Petroleum* (2020) 6(2):163–9. doi:10.1016/j.petlm.2019.06.006
10. Leblanc JL, Leuis RL. A Mathematical Model of a Gas Kick. *J Pet Tech* (1968) 20(4):888–98. doi:10.2118/1860-pa
11. Hoberock LL, Stanbery SR. Pressure Dynamics in wells during Gas Kick: Part 1-fluid Lines Dynamics. *J Pet Tech* (1981) 33(6):1357–66. doi:10.2118/9256-pa
12. Santos OLA. *A Mathematical Model of a Gas Kick when Drilling in Deep Waters*. Golden: Colorado School of Mines (1982).
13. Nickens HV. A Dynamic Computer Model of a Kicking Well. *SPE Drilling Eng* (1987) 2(02):159–73. doi:10.2118/14183-pa
14. White DB, Walton IC. A Computer Model for Kicks in Water- and Oil-Based Muds. In: IADC/SPE Drilling Conference; February 1990; Houston, Texas (1990). SPE-19975.

15. Van Slyke DC, Huang ETS. Predicting Gas Kick Behavior in Oil-Based Drilling Fluids Using a Pc-Based Dynamic Wellbore Model. In: IADC/SPE Drilling Conference; February 1990; Houston, Texas (1990). SPE 19972.
16. Szczepanski R. Differences between Methane and Condensate Kicks-A Simulation Study. *SPE drilling & completion* (1998) 13(1):36–41. doi:10.2118/37366-pa
17. Nunes JOL, Bannwart AC, Ribeiro PR. Mathematical Modeling of Gas Kicks in Deep Water Scenario. In: IADC/SPE Asia Pacific Drilling Technology; September 2002; Jakarta, Indonesia (2002). SPE 77253.
18. Velmurugan N, Godhavn JM, Hauge E. Dynamic Simulation of Gas Migration in marine Risers. In: SPE Bergen One Day Seminar; April 20, 2016; Bergen, Norway (2016). SPE 180022. doi:10.2118/180022-ms
19. Sun B, Sun X, Wang Z, Chen Y. Effects of Phase Transition on Gas Kick Migration in deepwater Horizontal Drilling. *J Nat Gas Sci Eng* (2017) 46: 710–29. doi:10.1016/j.jngse.2017.09.001
20. Zhang Z, Sun B, Wang Z, Pan S, Lou W, Sun D. Intelligent Well Killing Control Method Driven by Coupling Multiphase Flow Simulation and Real-Time Data. *J Pet Sci Eng* (2022) 213:110337. doi:10.1016/j.petrol.2022.110337
21. Fu W, Chen B, Zhang K, Liu J, Sun X, Huang B, et al. Rheological Behavior of Hydrate Slurry with Xanthan Gum and Carboxmethylcellulose under High Shear Rate Conditions. *Energy Fuels* (2022) 36(6):3169–83. doi:10.1021/acs.energyfuels.1c04359
22. Fu W, Wang Z, Chen L, Sun B. Experimental Investigation of Methane Hydrate Formation in the Carboxmethylcellulose (CMC) Aqueous Solution. *SPE J* (2020) 25(3):1042–56. doi:10.2118/199367-pa
23. Fu W, Wang Z, Sun B, Xu J, Chen L, Wang X. Rheological Properties of Methane Hydrate Slurry in the Presence of Xanthan Gum. *SPE J* (2020) 25(5): 2341–52. doi:10.2118/199903-pa
24. Peng D-Y, Robinson DB. A New Two-Constant Equation of State. *Ind Eng Chem Fund* (1976) 15(1):59–64. doi:10.1021/i160057a011

Conflict of Interest: The authors declare that the research was conducted in the absence of any commercial or financial relationships that could be construed as a potential conflict of interest.

frontiers | Frontiers in Physics

ORIGINAL RESEARCH
published: 14 July 2022
doi: 10.3389/fphy.2022.947094

Numerical Simulation Study of Hydraulic Fracturing Nozzle Erosion in Deep Well

Yuqiang Xu[1,2]*, *Qiandeng Li*[1], *Bingshuo Li*[1,2] and *Zhichuan Guan*[1,2]

[1]School of Petroleum Engineering, China University of Petroleum (East China), Qingdao, China, [2]Shandong Ultra-deep Drilling Process Control Tech RD Center, Qingdao, China

Hydraulic jet fracturing technology is one of the main means to develop low permeability and deep reservoirs. However, due to the large displacement and high sand ratio in the construction process, the erosion wear of high-speed sand particles on the hydraulic jet fracturing nozzle is more serious, which reduces the erosion cutting ability of the nozzle. Therefore, based on Finnie principle, a three-dimensional model of nozzle is established to analyze the influence of internal multiphase flow field distribution, flow rate, sand diameter and etc. on nozzle erosion. The results show that the erosion velocity increases nonlinearly with the increase of inlet pressure. With the increase of erosion time, the erosion rate gradually tends to be stable; with the increase of fluid viscosity, the erosion rate decreases; with the increase of the diameter and mass flow rate of the erosion particles, the erosion speed also increases, indicating that the size and mass flow rate of the erosion particles are the main factors affecting the erosion effect of the nozzle. The research results have important guiding significance for the rational use of the tool and the extension of the service life of the tool.

Keywords: hydraulic fracturing, nozzle, erosion rate, numerical simulation, finnie principle

OPEN ACCESS

Edited by:
Weiqi Fu,
China University of Mining and Technology, China

Reviewed by:
Meng Li,
Chongqing University of Science and Technology, China
Weiqiang Song,
Shandong University of Science and Technology, China

***Correspondence:**
Yuqiang Xu
xuyuqiang@upc.edu.cn

Specialty section:
This article was submitted to Interdisciplinary Physics, a section of the journal Frontiers in Physics

Received: *18 May 2022*
Accepted: *20 June 2022*
Published: *14 July 2022*

Citation:
Xu Y, Li Q, Li B and Guan Z (2022) Numerical Simulation Study of Hydraulic Fracturing Nozzle Erosion in Deep Well. Front. Phys. 10:947094. doi: 10.3389/fphy.2022.947094

INTRODUCTION

Hydraulic jet fracturing converts high-pressure energy carried by abrasive jets into high-speed jets, which impact and cut casing walls and rocks to form perforation holes. During this process, the quartz sand, fracturing fluid and proppant used in sandblasting and perforating all need to pass through the nozzle to reach the formation. Under high pressure and high displacement conditions, due to the small size of the nozzle, when the quartz sand passes through the nozzle, it will erode the nozzle and severely deform the internal flow channel, which will greatly reduce the erosion cutting ability of the nozzle [1–5]. Therefore, studying the erosion law of hydraulic fracturing nozzles under high pressure and high displacement has important guiding significance for tool design and prolonging tool life [6].

In the process of hydraulic fracturing, the quartz sand carried by the nozzle under high pressure and high displacement has a complex erosion process on the nozzle. The main erosion forms are divided into cutting, micro-deformation, fatigue and diffusion [7]. Huang Zhongwei [8] et al. studied the influence of nozzle installation position, nozzle material, jet parameters and nozzle structure on the erosion degree. Li Zhi [9] et al. studied the effect of particle size, hardness and shape on the erosion behavior according to the properties of the abrasive itself, and found that the large-sized abrasive with high hardness under high jet pressure severely

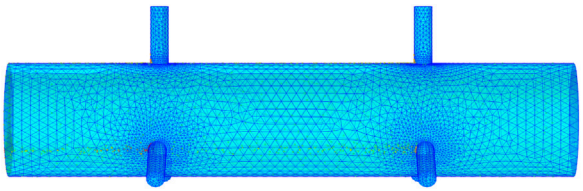

FIGURE 1 | Three dimensional simplified physical model.

eroded the nozzle, and established a corresponding model. However, the established model has not been experimentally verified, so it is difficult to guide the design and application of the nozzle.

For nozzle erosion simulation research generally only the nozzle internal structure, nozzle installation location and internal flow field research, such as Wang Zhiguo [10]; the erosion behavior of nozzle in the process of hydraulic fracturing was not simulated and analyzed by changing the parameters of solid particle size, erosion angle and shape. Therefore, based on the Finne [11, 12] principle, this paper first establishes a three-dimensional model of the nozzle, analyzes the influence of the flow field distribution, flow rate, sand particle diameter and etc. on the nozzle erosion in the hydraulic jet fracturing tool, verifies the established model, and clarifies the erosion mechanism of the nozzle under the conditions of high pressure and high displacement, which provides guidance for the design and application of the nozzle.

EROSION MECHANISM

Erosion is a wear phenomenon caused by the impact of multiphase flow medium on the material surface. According to the different flow media, erosion can be divided into sandblasting erosion and slurry erosion. Sandblasting erosion is the erosion of material by high-speed airflow carrying solid particles, while slurry erosion is the erosion of material by high-speed flow carrying solid particles [6, 13]. Thus, the erosion in the process of hydro-jet fracturing belongs to mud erosion. For hydraulic jet fracturing tools, the body material is No. 45 steel, which is plastic material, so it is mainly affected by cutting erosion. The nozzle material is cemented carbide, brittle material, mainly affected by impact fatigue erosion [14].

Finnie first proposed the plastic material erosion theory in 1958 [12]. He believes that the particles cut through the surface of the material continuously under low angle impact, resulting in pits that cause erosion loss of material quality. In this theory, the erosion volume of the material is

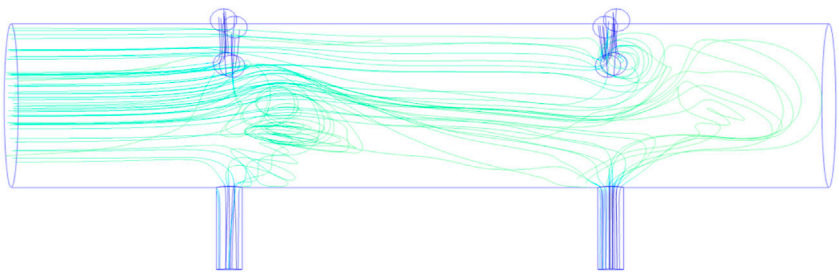

FIGURE 2 | The schematic of streamline of fluid flow.

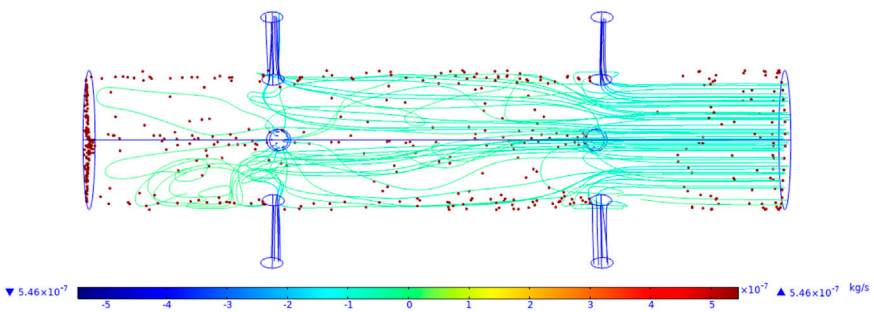

FIGURE 3 | The distribution of the erosion particles in the nozzle.

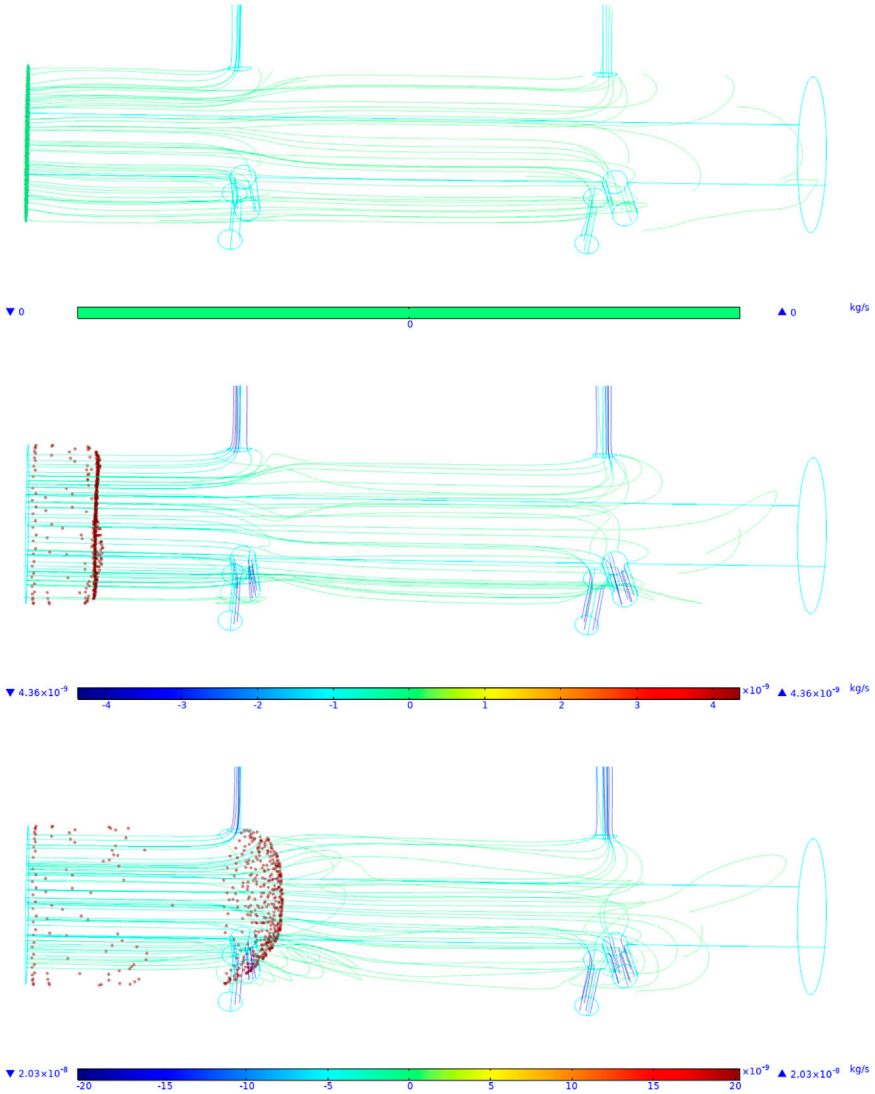

FIGURE 4 | The distribution of the erosion particles at different time.

proportional to the kinetic energy of the particle, which satisfies the functional relationship with the impact angle of the particle, and is inversely proportional to the flow stress of the material itself, which is expressed by **Eq. 1**. Since the erosion wear results caused by particles under large impact angles predicted by the model were smaller than the experimental values, Finnie revised the model in 1960 [11].

$$V = K\frac{mv^2}{p} f(\alpha)$$

$$f(\alpha) = \begin{cases} \sin 2\alpha - \sin^2 \alpha & (\alpha \le 18.5^\circ) \\ \dfrac{\cos^2 \alpha}{3} & (\alpha > = 18.5^\circ) \end{cases}$$

In 1963, Bitter [15] proposed the erosion deformation theory, which is mainly based on the energy balance in the erosion process. Bitter divided the erosion wear into deformation wear and cutting wear.

The erosion amount caused by deformation is:

$$W_D = M\left(v \sin a - K^2\right)/2\varepsilon$$

The erosion caused by cutting is:

$$W_c = \begin{cases} W_{C1} = \dfrac{2MC\left(v \sin a - K^2\right)}{(v \sin \alpha)^{1/2}} \times \left[V \sin \alpha - \dfrac{C(v \sin \alpha - K)^2}{(v \sin a)^{1/2}} Q\right] & (\alpha < \alpha_0) \\ W_{C2} = \dfrac{M}{2Q}\left[v^2 \cos^2 \alpha - K_1 (v \sin \alpha - K)^{3/2}\right] & (\alpha > \alpha_0) \end{cases}$$

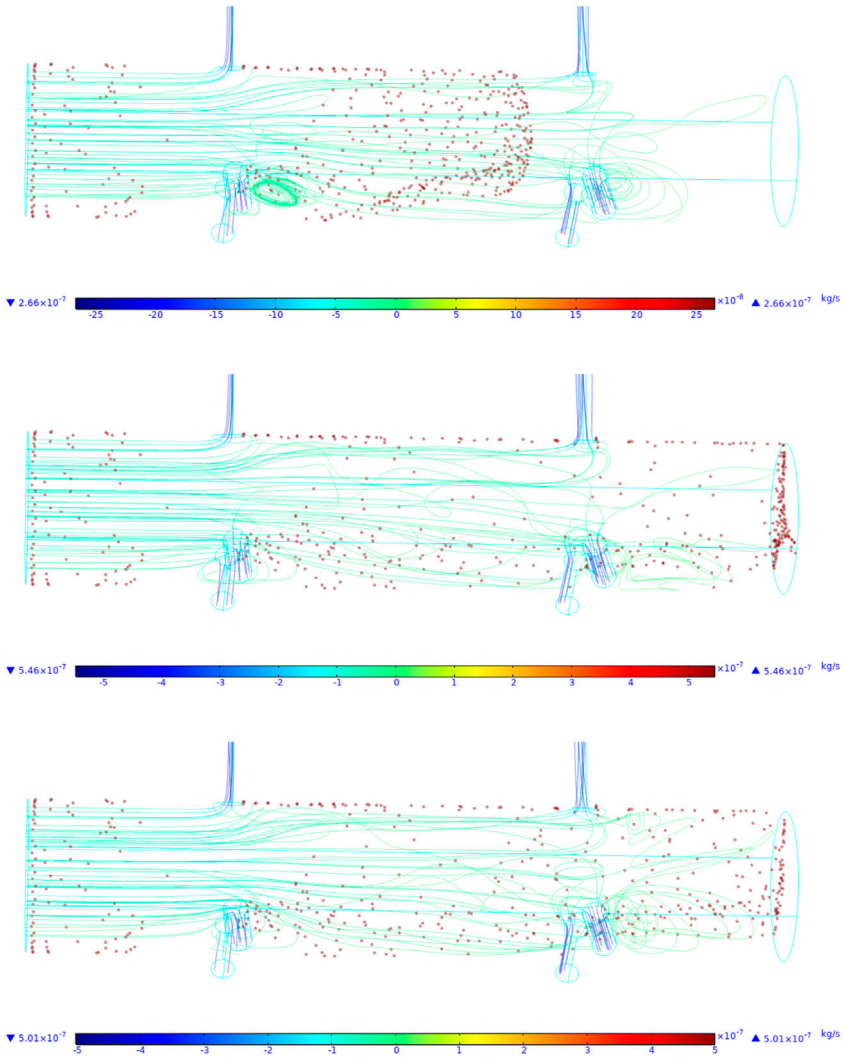

FIGURE 4 | The distribution of the erosion particles at different time.

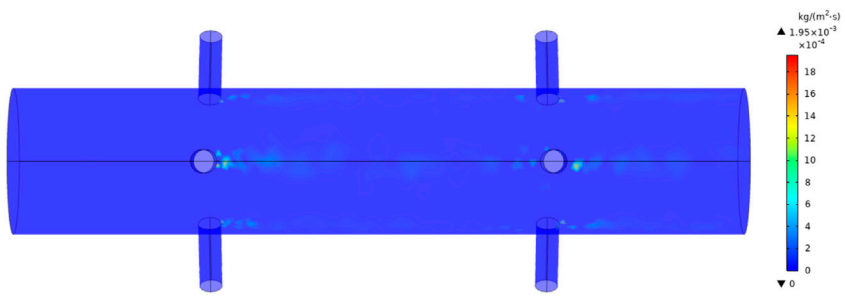

FIGURE 5 | The erosion velocity of the nozzle.

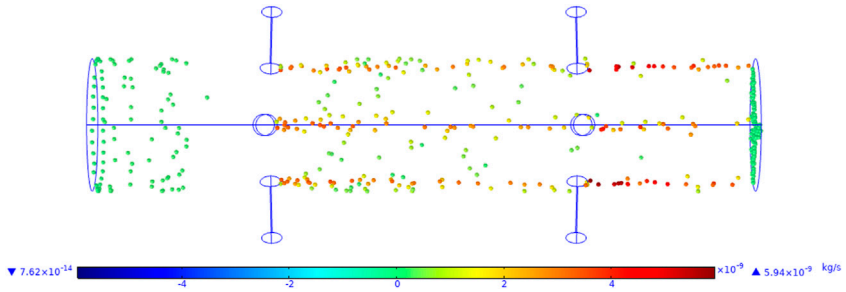

FIGURE 6 | The schematic of erosion velocity of the nozzle.

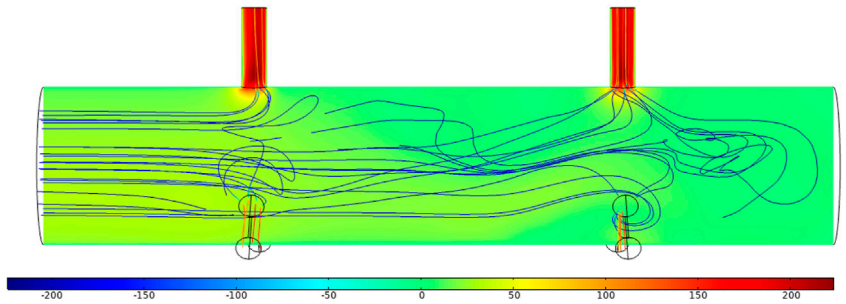

FIGURE 7 | The flow velocity distribution of the tool.

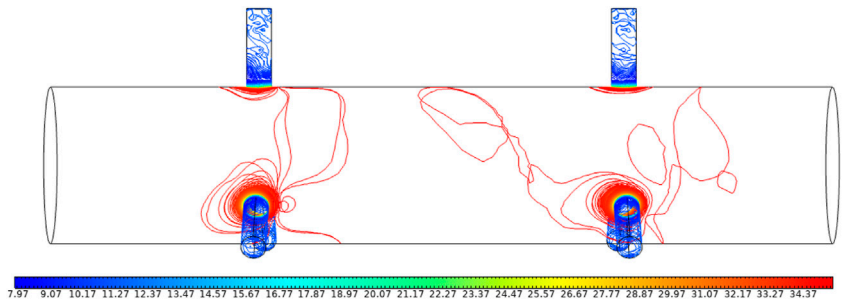

FIGURE 8 | The flow pressure distribution of the tool.

The theory is very consistent with the experimental data of brittle materials under different impact angles, and the erosion wear of plastic materials can also be reasonably explained, but it lacks the support of physical models.

E/CRC model [16–24], after particles impact on the wall, the failure on the wall is related to wall material, particle characteristics, impact angle and other factors. Compared with other models, the E/CRC model takes into account the particle hardness and shape factors, and the numerical results are closer to the experimental results. The wear rate calculation equation in the E/CRC model is:

$$E_M = \sum_i E_{M,i}$$

$$E_{M,j} = C f_{\text{rel}} F_s (\text{BH})^{-0.59\left(\frac{v}{v_{ref}}\right)} F(\alpha_i)$$

$$F(\alpha_i) = \sum_{k=1}^{5} A_k \alpha_i^k$$

TABLE 1 | The erosion velocity with different inlet pressure.

Inlet pressure (MPa)	35	40	45	50
Erosion rate (10-7 kg/s)	5.46	6.11	6.55	6.73
Export speed (m/s)	200	245	250	285

where, ER is the wear rate (mass loss per unit area), kg/m^2; C and n are 2.17×10^{-7} and 2.41, respectively; BH is Brinell Hardness; F_S is the particle shape coefficient, which is 0.2 for spherical particles; Vp is particle velocity, m/s; β is particle impact angle, rad.

Compared with other models, Finnie model considers energy balance in the erosion process, and impact angle; furthermore, in the revised model, the particle shape was taken in to consideration as well, therefore, in this paper, Finnie model is used to explore the hydraulic fracturing nozzle erosion.

PHYSICAL MODEL

Simplification and Definition of Physical Model

According to the nozzle structure for hydraulic fracturing, a three-dimensional physical model is established after simplification, as shown in **Figure 1**. It is mainly composed of nozzle, inlet and outlet. The inlet diameter of fluid channel is 60 mm, the cavity height is 300 mm, the outlet diameter is 9.5 mm, and the number of outlets is 6.

The pressure change at the inlet of the fluid channel is set at 30–50 MPa according to the research needs, with a step size of 5 MPa. The outlet pressure is 10 Pa, the fluid partial density is 1 g/cm^3, the dynamic viscosity is 1 mPa s, and it is incompressible. The fluid partial control equation is:

$$\rho \frac{\partial u_{fluid}}{\partial t} + \rho\left(u_{fluid}\nabla\right)u_{fluid} = \nabla\left\{-\rho I + \mu\left[\nabla u_{fluid} + \left(\nabla u_{fluid}\right)^T\right]\right\} + P \tag{1}$$

Among them, u_{fluid}-fluid velocity, m/s; I—diagonal matrix; P—volume force, N; ρ—Fluid density, kg/m3; μ- Dynamic viscosity coefficient, Pas.

The erosion particle diameter is 0.6 mm, the density is 2.65 g/cm3, and the mass flow rate is 1 kg/s. The control equation is:

$$\frac{d(mp_v)}{dt} = F_t \tag{2}$$

Finnie model is selected for the erosion model, which mainly affects the erosion wear of metal surface from the flow velocity and impact angle of solid particles, and the expression is shown in **Eq. 3**. Since the relative Reynolds number of particles is far less than 1, the fluid drag is Stokes equation.

$$\Delta m = \begin{cases} \dfrac{C_i \rho m_p v_i^2}{4H_V\left(1 + \dfrac{m_p r_p^2}{l_p}\right)}\cos^2(\alpha_i), & \tan(\alpha_i) \geq \dfrac{p}{2} \\ \dfrac{C_i \rho m_p v_i^2}{4H_V\left(1 + m_p r_p^2 / l_p\right)}\dfrac{2}{p}\left[\sin(2\alpha_i) - \dfrac{2}{p}\sin^2(\alpha_i)\right], & \tan(\alpha_i) \leq \dfrac{p}{2} \end{cases} \tag{3}$$

In the formula, m is erosion wear rate, kg/m2; cj cut particle fraction for idealization; HV is particle surface hardness, Pa; α is erosion angle, degree; ρ is particle density, kg/m^3; FD is the drag force, N; K is the normal and tangential force ratio; C_D is drag coefficient, m_p is particle mass, kg; r_p is the particle radius, mm; d_p is particle diameter, mm; u is fluid velocity, m/s; v Particle velocity, m/s; τ_p for particle relaxation time, s; u is fluid viscosity, Pas; P is the yield stress of the eroded material, MPa; l is solid particle erosion depth, mm.

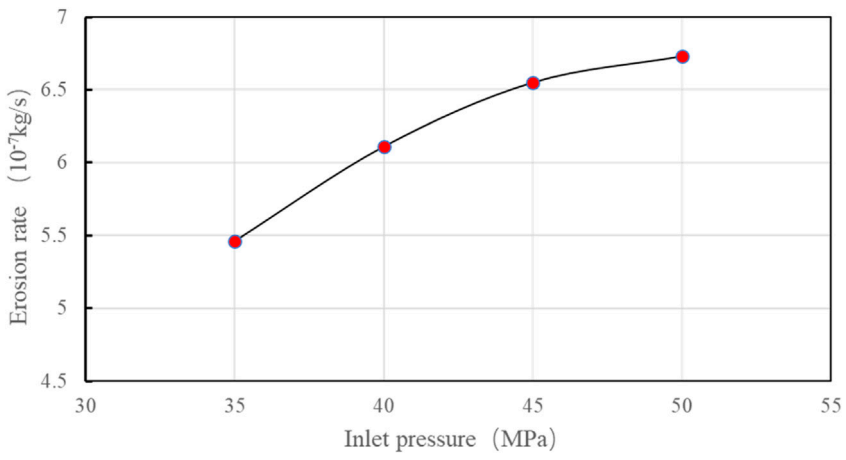

FIGURE 9 | The relation between erosion velocity and inlet pressure.

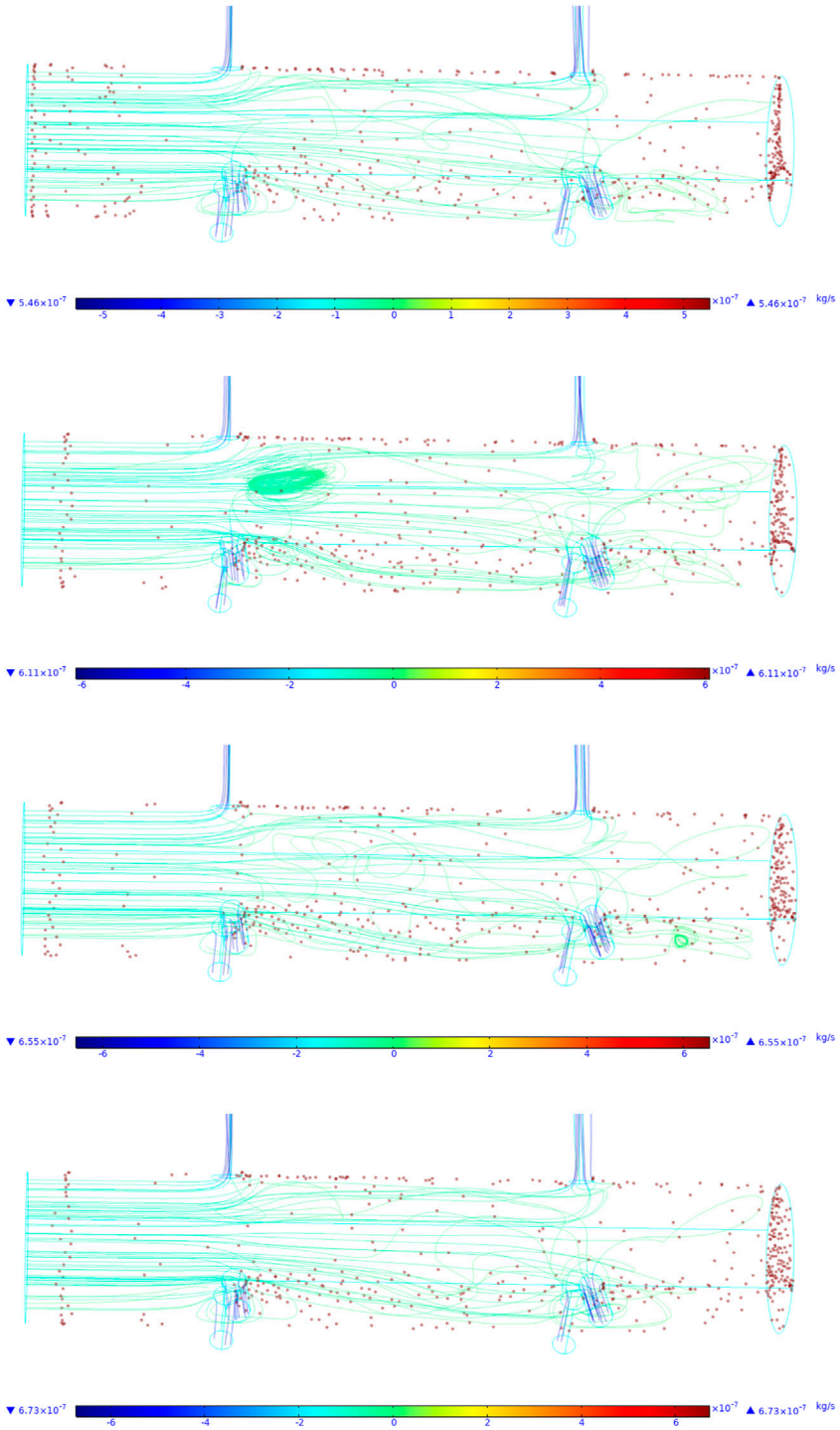

FIGURE 10 | The distribution of the particles under different inlet pressure. Influence of erosion time.

Model Test Verification

In order to verify the validity of the established physical model, the experimental results of Shi et al [25]. were used for verification. In the erosion test, the test scheme is: displacement 3 m^3/min, sand ratio 10%, cumulative injection time from 30 to 175 min, erosion time 30 min, after erosion found that nozzle diameter increased from 9.5 to 10.6 mm, nozzle mass decreased from 95 to 94, reduced by 1 g; the erosion wear of the test was 5.5 × 10^{-7} kg/s. **Figures 2**, **3** show the streamline diagram of the

TABLE 2 | The influence of erosion duration on the nozzle erosion.

Erosion time (s)	0.05	0.06	0.07	0.08
Erosion rate (10^{-7} kg/s)	5.46	6.12	6.24	6.25
Outlet velocity (m/s)	200	245	250	285

nozzle and the distribution of erosion particles when the simulated parameters are consistent with the experimental parameters. It can be seen from the figures that the erosion velocity is the largest at the nozzle.

ANALYSIS AND DISCUSSION ON EROSION RESULTS

The initial values of liquid phase and particle phase were set as follows: the density of fracturing fluid was 1050 kg/m3, the viscosity was 150 mPa s, the sand density was 2650 kg/m3, and the average particle size was 0.6 mm. The inlet velocity is 10 m/s, and the sand mass rate is 1 kg/s. The pressure distribution, velocity distribution, streamline distribution and particle trajectory in the tool are obtained by numerical simulation, as shown in **Figures 4**, **5**.

Figure 5 shows the erosion rate distribution of solid particles in the fluid on the inner surface of the nozzle. It can be seen from the figure that at the root of the nozzle, the erosion rate is the highest, reaching 1.95 × 10–3 kg/(m2 s); it is obvious from the diagram that the main erosion position is around the six nozzles, indicating that the erosion of solid particles on the nozzle is mainly concentrated here; it can be seen from the figure that the erosion performance of the nozzle near the inlet is higher than that of the nozzle far away, indicating that the installation position of the nozzle also affects the erosion performance of the nozzle. **Figure 6** is the distribution of erosion fluid particles. It can be seen from the figure that the solid particles are more concentrated at the bottom, resulting in the accumulation of solid erosion particles at the bottom. However, it can be seen from the figure that this has little effect on the wall erosion. This is because when the high-pressure fluid enters the tool body, the flow rate is high, so that the solid erosion particles carried by the high-pressure fluid are rapidly accumulated at the bottom. With the increase of erosion time, the more erosion particles are accumulated, so that the bottom of the tool is covered, and the erosion effect of the bottom is not obvious. From the overall point of view, the solid particles at the nozzle on the tool are more than the bottom, and the degree of wear on the wall is higher.

Figure 7 shows the distribution of the fluid velocity of the nozzle under the erosion condition. It can be seen from the figure that the fluid velocity inside the whole tool shows that the flow velocity at the nozzle is much higher than that at other parts of the tool. It can be seen from the figure that the flow velocity at the nozzle is about 200 m/s. In terms of the whole tool, the flow velocity at the upper part of the tool is higher than that at the lower part, and the vortex is obviously generated at the lower nozzle position.

Influence of Inlet Pressure

Figure 8 shows the pressure distribution of the tool body and the nozzle. It can be clearly seen from the figure that an annular pressure band is formed at the root of the nozzle, which is about 35 MPa. The pressure difference is formed at the root of the nozzle and the outlet of the nozzle, and the pressure at the outlet of the nozzle is about 7 MPa, which makes the pressure difference at the root of the nozzle and the outlet of the nozzle about 25 MPa, leading to the excessive velocity of the fluid here, which is also the reason for the large erosion rate here. Therefore, in the influence of the inlet pressure on the erosion rate, the inlet pressure is set to change from 35 to 50, and other working parameters are set as follows: the outlet pressure is

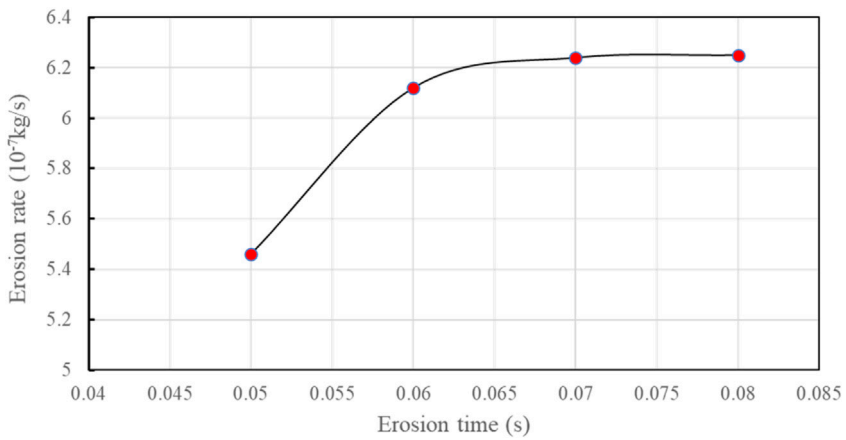

FIGURE 11 | The relation between duration and erosion velocity.

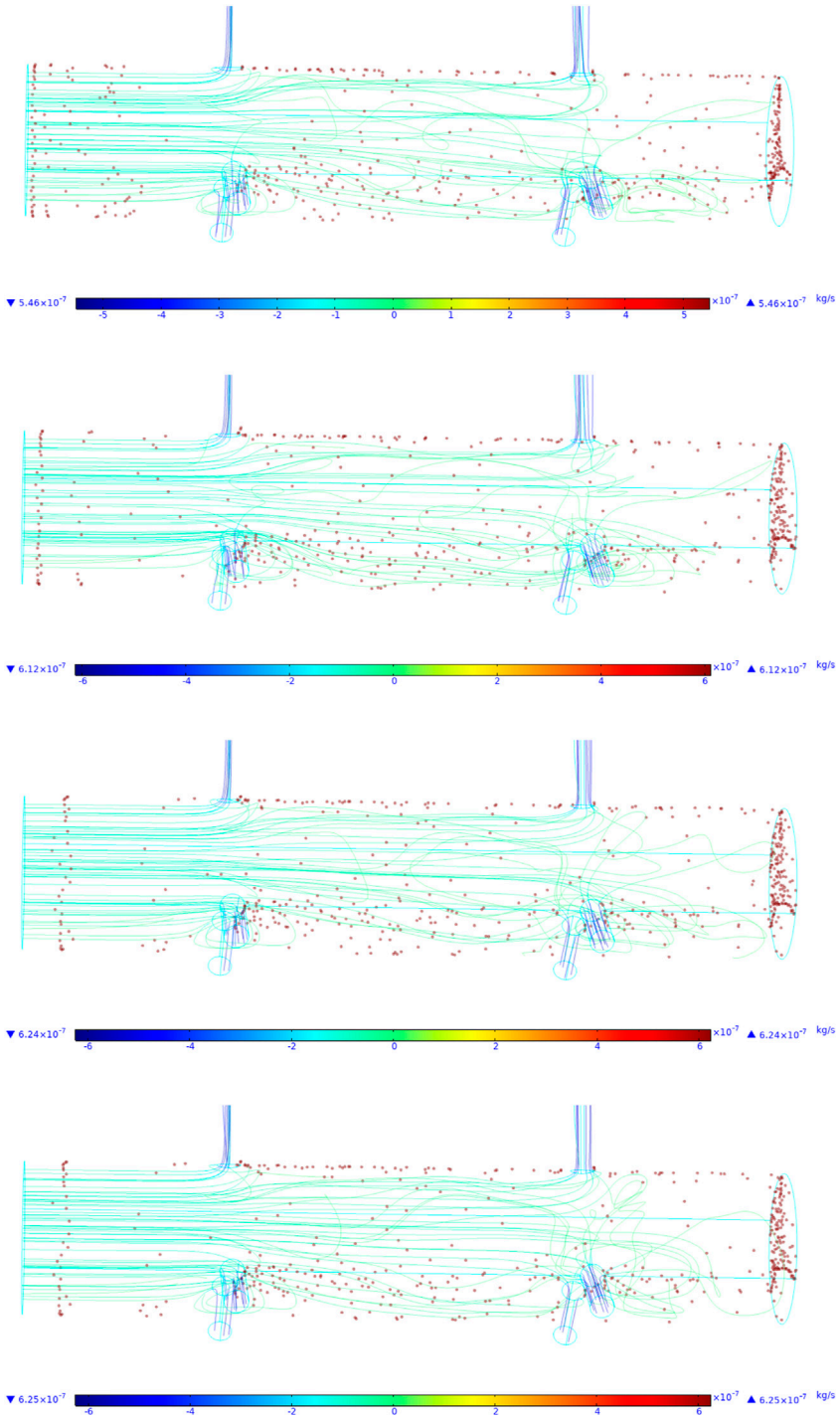

FIGURE 12 | The influence of erosion duration on the nozzle erosion.

10 MPa; the inlet diameter is 60 mm; the outlet diameter is 9.5 mm.

Table 1 shows the impact of erosion rate under different inlet pressures. It can be seen from the table that with the increase of inlet pressure, the erosion rate also increases, and the outlet velocity also increases, indicating that the greater the inlet pressure is, the greater the fluid flow rate is, and the velocity of solid particles carried in the fluid is also increased, resulting in an increase in the erosion of the nozzle. It can also be seen from **Figure 9** that with the increase of inlet pressure, the erosion rate also increases nonlinearly.

TABLE 3 | The influence of viscosity on erosion velocity.

Viscosity (mPa·s)	1	6	7	8
Erosion rate (10^{-7} kg/s)	5.46	5.4	5.32	6.49
Outlet velocity (m/s)	200	245	250	285

Figure 10 shows the erosion of particles on the nozzle under the condition of inlet pressure changing from 40 to 50 MPa. It can be obviously seen from the figure that with the increase of inlet pressure, the erosion particles deposited at the bottom of the tool are significantly reduced. This is because with the increase of inlet pressure, the flow velocity inside the tool increases, so that the erosion particles deposited at the bottom of the tool are blown up, resulting in the decrease of solid particles deposited at the bottom. Under the condition of constant volume content of erosion particles, the erosion particles in the flow state increase, resulting in the increase of erosion velocity of the nozzle.

In the analysis of the impact of erosion time on erosion rate, the inlet pressure was set to 40 MPa, and the erosion time varied from 0.05 to 0.08 s. Other working parameters were as follows: the outlet pressure was 10 MPa; the inlet diameter is 60 mm; the outlet diameter is 9.5 mm.

Table 2 shows the impact of erosion rate under different erosion time conditions. It can be seen from the table that with the increase of erosion time, the erosion rate also increases, and the export velocity remains unchanged. When the erosion time increases from 0.05 to 0.08 s, the erosion rate increases from 5.46 × 10–7 to 6.25 × 10–7 kg/s. At the same time, it can also be seen from **Figure 11** that when the erosion time increases, the erosion rate gradually increases, and with the increase of erosion time, the erosion rate gradually no longer changes.

Figure 12 shows the erosion effect of nozzle under different erosion time conditions. It can be clearly seen from the figure that with the increase of erosion time, the distribution of erosion particles in the tool is more uniform, and the deposition of erosion particles at the bottom of the tool tends to be stable. The accumulation of solid particles blown by high-speed fluid and erosion particles carried by fluid is in a dynamic equilibrium state, indicating that the increase of erosion time does not increase the erosion rate, but makes the erosion rate tend to a stable value. It can be seen from the figure that at the root of the nozzle, it is the main accumulation position of erosion particles.

Influence of Fluid Viscosity

In the analysis of the influence of fluid viscosity on the erosion rate, the inlet pressure was set to 40 MPa, and the dynamic viscosity varied from 1 mPa s to 6 mPa s to 8 mPa s. Other working parameters were as follows: the outlet pressure was 10 MPa; the inlet diameter is 60 mm; the outlet diameter is 9.5 mm.

Table 3 is the impact of erosion rate under different dynamic viscosity conditions. It can be seen from the table that the erosion rate decreases with the increase of fluid viscosity, indicating that the fluid viscosity increases. Under the condition of constant inlet pressure, the fluid velocity decreases, resulting in the decrease of the velocity of the fluid carrying the erosion particles, resulting in the decrease of the erosion velocity and the decrease of the outlet velocity. It shows that under the condition of constant inlet pressure, the greater the fluid viscosity, resulting in the decrease of the flow velocity. It can also be seen from **Figure 13** that under the condition of constant inlet pressure, the erosion rate decreases with the increase of fluid viscosity.

Figure 14 is the distribution of erosion particles under different viscosity conditions. It is obvious from the figure that when the fluid is clear water, the erosion particles accumulate more seriously at the bottom of the tool, but when the viscosity is 7 mPa s, the erosion particles are evenly distributed at the bottom of the tool, and the distribution is also more uniform at the tool body and the nozzle.

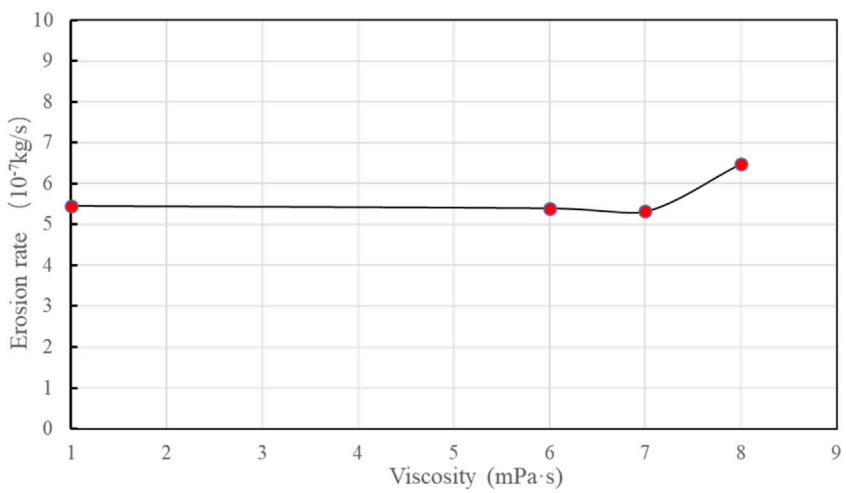

FIGURE 13 | The influence of viscosity on erosion velocity.

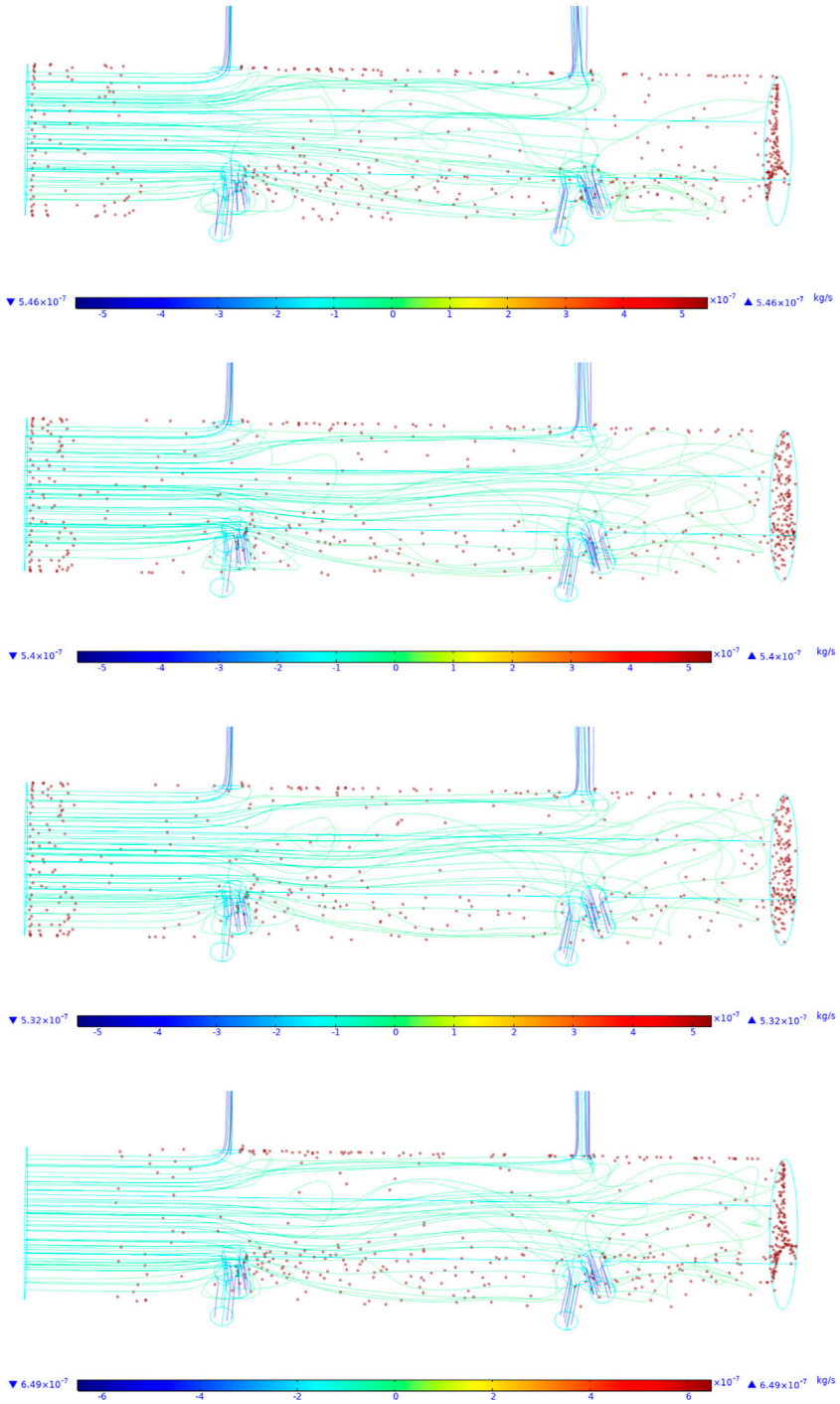

FIGURE 14 | The influence curve of different viscosities on the erosion effect.

TABLE 4 | The influence of diameter on erosion velocity.

Diameter (mm)	0.6	0.8	1.0	1.2
Erosion rate (10−7 kg/s)	5.46	3.11	1.11	0.6
Outlet velocity (m/s)	200	245	250	285

Effect of Erosion Particle Diameter

In the analysis of the impact of erosion particle diameter on erosion rate, the inlet pressure was set to 40 MPa, and the dynamic viscosity varied from 0.6 to 1.2 mm. Other working parameters were as follows: the outlet pressure was 10 MPa; the inlet diameter is 60 mm; the outlet diameter is 9.5 mm.

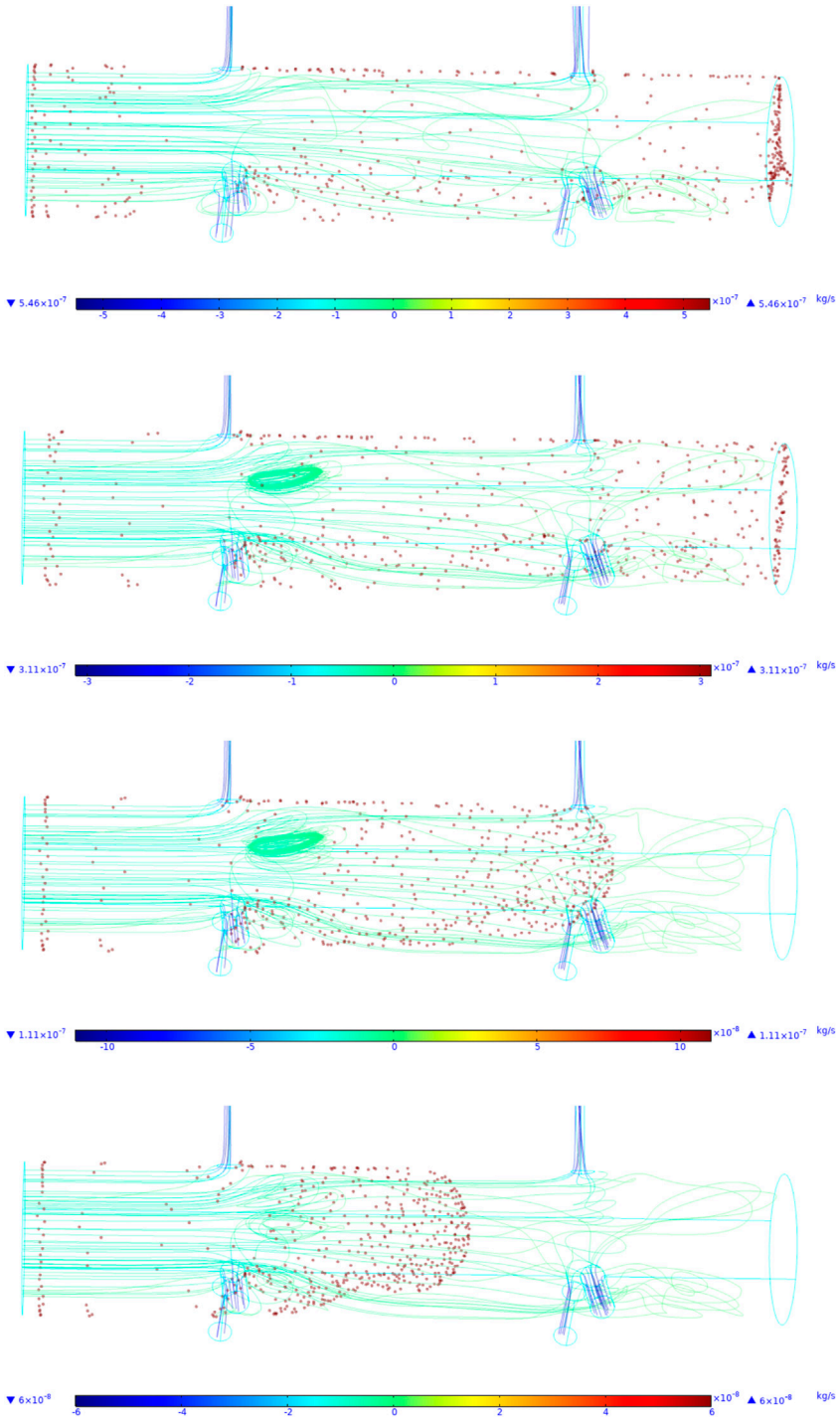

FIGURE 15 | The distribution of different diameters particles.

Table 4 shows the impact of erosion rate of erosion particles under different diameters. It can be seen from the table that with the increase of erosion particle diameter, the erosion rate also increases, and the outlet velocity remains unchanged, indicating that the size of erosion particles is also the main factor affecting the nozzle erosion effect.

Figure 15 erosion of erosion particles on the inner wall of the tool under the condition of different particle sizes. It can be

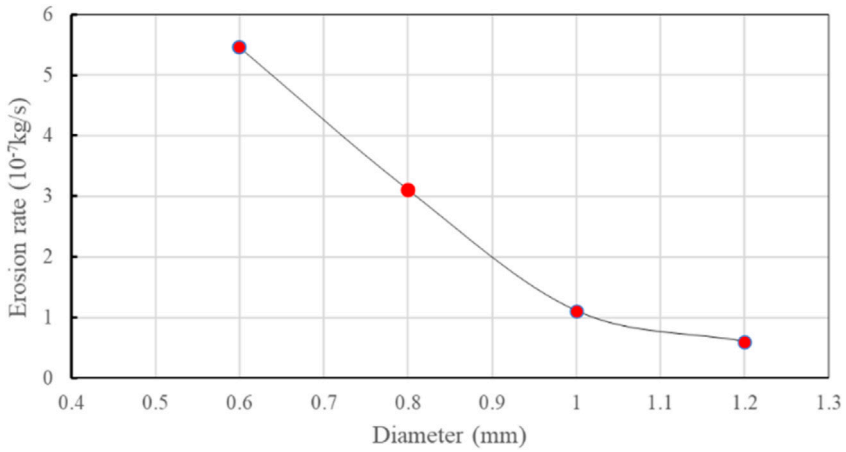

FIGURE 16 | The relation of particles diameter on erosion velocity.

TABLE 5 | The erosion velocity under different mass flow.

Mass flow rate (mm)	1	1.2	1.4	1.6
Erosion rate (10^{-7} kg/s)	5.46	7.37	8.6	9.8
Outlet velocity (m/s)	200	245	250	285

seen from the figure that with the increase of erosion particles, the erosion effect of erosion particles on the tool decreases, which is due to the change of particle mass when the particle size of erosion particles increases. Under the condition of constant inlet velocity, the driving effect of liquid flow on erosion particles becomes worse, resulting in the decrease of particle velocity and the weakening of erosion on the inner wall of the tool. This shows that increasing the diameter of particles will greatly reduce the erosion of fracturing nozzles and effectively prolong the life of the tool. It can also be seen from **Figure 16** that the relationship between erosion particle diameter and erosion velocity decreases with the increase of particle diameter.

Effect of Erosion Particle Mass Flow Rate

In the analysis of the impact of erosion particle diameter on erosion rate, the inlet pressure was set to 40 MPa, and the mass flow rate varied from 1 kg/s to 1.6 kg/s. Other working parameters were as follows: the outlet pressure was 10 MPa; the inlet diameter is 60 mm; the outlet diameter is 9.5 mm.

Table 5 shows the influence of erosion rate of erosion particles under different inlet mass flow rates. It can be seen from the table that with the increase of mass flow rate, the erosion rate also increases, and the outlet velocity remains unchanged, indicating that the mass flow rate of erosion particles is also the main factor affecting the nozzle erosion effect.

It can also be seen from **Figure 17** that the erosion rate increases linearly with the increase of erosion particle mass

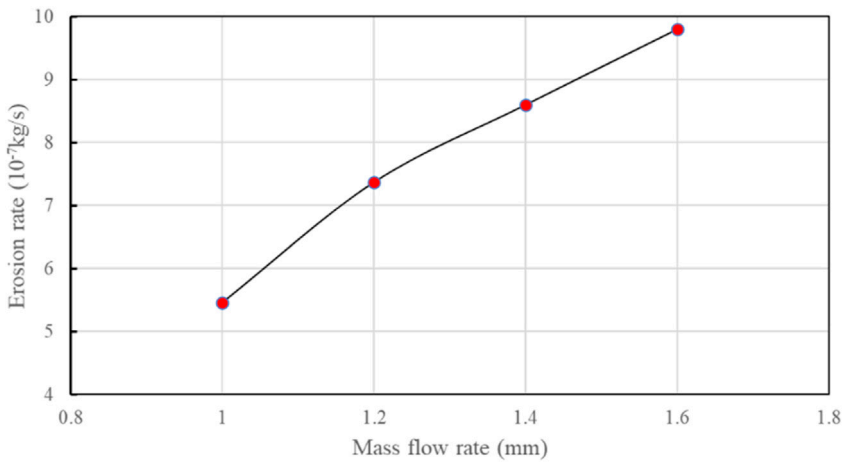

FIGURE 17 | The erosion velocity under different mass flow.

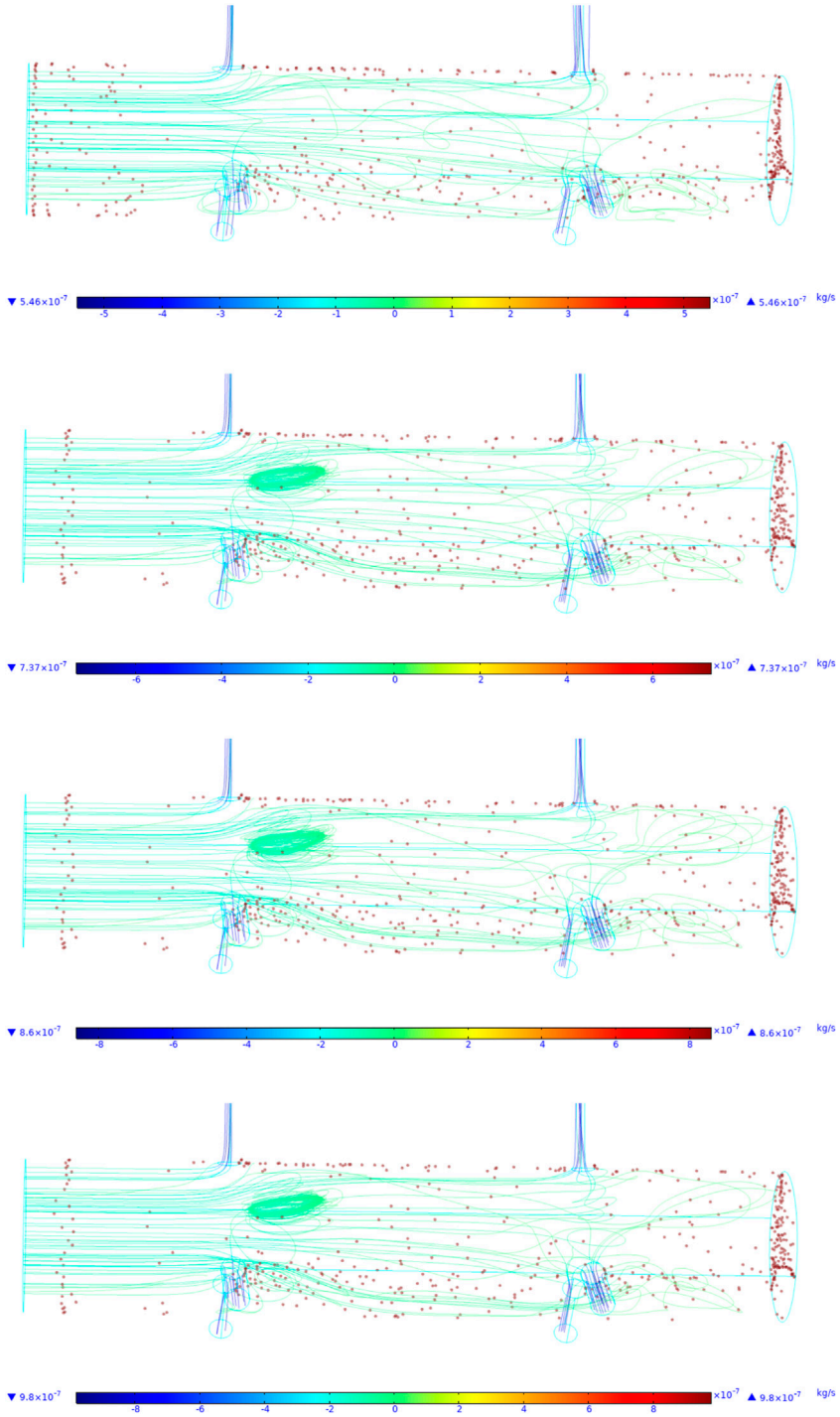

FIGURE 18 | Erosion rate curves under different mass flow rate conditions.

flow rate. At the same time, it can be seen from **Figure 18** that when the mass flow rate is greater than 1 kg/s, there is a vortex at the upper nozzle, and it can be clearly seen from the figure that the distribution of erosion particles is more uniform and the bibliography of particles increases significantly. This is because when the mass flow rate increases, the erosion particles carried by the fluid increase, which also leads to the increase of erosion rate.

In summary, the erosion rate of the device is analyzed from the corresponding working parameters. The results show that the erosion rate increases nonlinearly with the increase of inlet pressure. When

the erosion time increases, the erosion rate increases gradually, with the increase of erosion time, the erosion rate gradually no longer changes; under the condition of constant inlet pressure, the erosion rate decreases with the increase of fluid viscosity. With the increase in the diameter of erosion particles, the erosion velocity increases, and the export velocity remains unchanged, indicating the size of erosion particles.

CONCLUSION

1) By establishing the three-dimensional model of the nozzle and verifying the established model, the error rate between the simulation results and the experimental results is 0.7% under the condition of the same parameters as the test, which indicates that the established physical model is effective and can further carry out the influence of other working parameters on the erosion rate of the nozzle.
2) The analysis of the erosion rate of the device from the aspect of working parameters shows that the erosion rate increases nonlinearly with the increase of inlet pressure; with the increase of erosion time, the erosion rate gradually tends to be stable; with the increase of fluid viscosity, the erosion rate decreases; with the increase of particle diameter and mass flow rate, the erosion velocity increases, which indicates that the particle size and mass flow rate are the main factors affecting the nozzle erosion effect.
3) The results show that the erosion rates of the upper and lower nozzles of the tool are different, and the distribution of sand particles at different positions in the tool is also significantly different. The main erosion position of sand particles on the tool wall is at the root of six nozzles, which is the main accumulation position of erosion particles. The erosion performance of the nozzle near the inlet is higher than that of the nozzle far away, indicating that the installation position of the nozzle also affects the erosion performance of the nozzle, therefore, it is highly suggested that nozzle distribution of the hydraulic fracturing tool need to be installed in upper location of that as much as possible.

DATA AVAILABILITY STATEMENT

The raw data supporting the conclusion of this article will be made available by the authors, without undue reservation.

AUTHOR CONTRIBUTIONS

YX is the main contributor of the paper, providing the overall ideas, methods and financial support of the paper. QL mainly completed the construction of numerical simulation model and the analysis of experimental data, and made great contributions to the writing of the paper. BL mainly completed the collation and analysis of data and the proofreading of papers. ZG completed the review of the overall idea and scheme of the paper, and analyzed some data.

FUNDING

The authors would like to acknowledge the academic and technical supports of China University of Petroleum (East China). This paper is supported by the National Natural Science Foundation of China (No. 52074326).

REFERENCES

1. Changgui J, Kuiwei L, Minhui L. Hydraulic Jet Fracturing Technology [J]. *Oil-Gasfield Surf Eng* (2011) 30(1):89. doi:10.3969/j.issn.1006-6896.2011.1.043
2. Tengfei W, Yun X, Jianfang J, Zhuhong T, Yunhong D. Coiled Tubing Hydraulic Jet Annular Fracturing Technology [J]. *Nat Gas Industry* (2010) 30(1):65–7. doi:10.3787/j.issn.1000-0976.2010.01.018
3. Mcdaniel BW, Surjaatmadja JB, East LE. Hydrajet (Abrasive) Perforating Can Improve Success of Fracturing Stimulations. In: proceedings of the International Petroleum Technology Conference; December 3–5, 2008. Kuala Lumpur, Malaysia: IPTC-12043-MS.(2008).
4. Tang J, Lu Y, Ouyang M, Zhang W, Zhang X. Optimal Design and Performance Evaluation of a New Hydrajet-Fracturing Nozzle [J]. *J China Univ Pet Edition Natrual Sci* (2015) 39(1):72–8. doi:10.3969/j.issn.1673-5005.2015.01.010
5. Fan X, Li G, Huang Z, Niu J, Song X, Sheng M, et al. Field-scale Testing of Hydraulic Isolation in Wellbore during Hydra-Jet Fracturing [J]. *J China Univ Pet Edition Natrual Sci* (2015) 39(2):69–74. doi:10.3969/j.issn.1673-5005.2015.02.011
6. Surjaatmadja JB, Bezanson J, Lindsay SD, Ventosilla P, Rispler K. New Hydra-Jet Tool Demonstrates Improved Life for Perforating and Fracturing Applications. In: proceedings of the SPE/ICoTA Coiled Tubing and Well Intervention Conference and Exhibition; April 1–2, 2008. The Woodlands, Texas, USA: SPE-113722-MS.(2008). doi:10.2118/113722-ms
7. Ma Y, Ren J, Li Y, Chen T, Li B. Development of Research on Erosion of Materials [J]. *J Lanzhou Univ Tech* (2005) 31(1):21–5. doi:10.3969/j.issn.1673-5196.2005.01.006
8. Zhongwei H, Gensheng L, Shouqi T, Prophet S, Mao S, Chunfang W. Wear Investigation of Downhole Tools Applied to Hydra-Jet Multistage F Racturing [J]. *J Chongqing Univ* (2014)(5) 77–82. doi:10.11835/j.issn.1000-582X.2014.05.011
9. Zhi L, Yun X, Zhenduo W, Zuo C, Guangwei Z. Analysis on Nozzle Wear of Hydraulic Sandblast Fracturing Tools [J]. *Oil Field Equipment* (2010) 39(11):25–8. doi:10.3969/j.issn.1001-3482.2010.11.007
10. Zhiguo W, Xiangtong Y, Yihua D, Shengjun L. Erosion Prediction Model for Super 13Cr Tubing during Large-Scale Hydraulic Fracturing [J]. *Oil Drilling Prod Tech* (2016) 38(4):473–8. doi:10.13639/j.odpt.2016.04.013
11. Finnie I. Some Observations on the Erosion of Ductile Metals. *Wear* (1972) 19(1):81–90. doi:10.1016/0043-1648(72)90444-9
12. Finnie I, Stevick GR, Ridgely JR. The Influence of Impingement Angle on the Erosion of Ductile Metals by Angular Abrasive Particles. *Wear* (1992) 152(1):91–8. doi:10.1016/0043-1648(92)90206-n
13. Surjaatmadja JB, Grundmann SR, Mcdaniel B, Deeg WHJ, Brumley JL, Swor LC, et al. Hydrajet Fracturing: An Effective Method for Placing Many Fractures in Openhole Horizontal Wells. In: proceedings of the SPE International Oil and Gas Conference and Exhibition in China; November 2–6, 1998. Beijing, China: SPE-48856-MS.(2008). doi:10.2118/48856-ms
14. Jixin Z, Jianchun F, Xianjue Z, Yongjin X, Hanchuan W. Research on the Erosion Wear Characteristics of 42CrMo Steel in Hydraulic Fracture

Conditions [J]. *China Pet Machinery* (2012) 40(4):100–3. doi:10.16082/j.cnki.issn.1001-4578.2012.04.006
15. Bitter JGA. A Study of Erosion Phenomena Part I. *Wear* (1963) 6(1):5–21. doi:10.1016/0043-1648(63)90003-6
16. Zhang Y, Reuterfors EP, Mclaury BS, Rybicki EF. Comparison of Computed and Measured Particle Velocities and Erosion in Water and Air Flows [J]. *Wear* (2007) 263(1):330–8. doi:10.1016/j.wear.2006.12.048
17. Zhang J, Mclaury BS, Shirazi SA. CFD Simulation and 2-D Modeling of Solid Particle Erosion in Annular Flow. In: proceedings of the 10th North American Conference on Multiphase Technology; June 8–10, 2016. Banff, Canada: BHR-2016-433.(2016).
18. Hutchings IM, Winter RE. Particle Erosion of Ductile Metals: A Mechanism of Material Removal. *Wear* (1974) 27(1):121–8. doi:10.1016/0043-1648(74)90091-x
19. Papini M, Dhar S. Experimental Verification of a Model of Erosion Due to the Impact of Rigid Single Angular Particles on Fully Plastic Targets. *Int J Mech Sci* (2006) 48(5):469–82. doi:10.1016/j.ijmecsci.2005.12.010
20. Takaffoli M, Papini M. Material Deformation and Removal Due to Single Particle Impacts on Ductile Materials Using Smoothed Particle Hydrodynamics. *Wear* (2012) 274-275:50–9. doi:10.1016/j.wear.2011.08.012
21. Azimian M, Schmitt P, Bart HJ. Numerical Investigation of Single and Multi Impacts of Angular Particles on Ductile Surfaces. *Wear* (2015) 342-343:252–61. doi:10.1016/j.wear.2015.08.022
22. Liu M, Wang J, Yan Y, Xie W, Yang X, Yan X, et al. Numerical Simulation on the State of Fluids along the String of Gas Storage Well[J]. *Oil Drilling Prod Tech* (2017) 39(04):449–54. doi:10.13639/j.odpt.2017.04.010
23. Li R, Yamaguchi A, Ninokata H. Computational Fluid Dynamics Study of Liquid Droplet Impingement Erosion in the Inner Wall of a Bent Pipe. *Jpes* (2010) 4:327–36. doi:10.1299/jpes.4.327
24. Suzuki M, Inaba K, Yamamoto M. Numerical Simulation of Sand Erosion in a Square-Section 90-Degree Bend. *Jfst* (2008) 3:868–80. doi:10.1299/jfst.3.868
25. Huaizhong S, Gensheng L, Zhongwei H, Xiaoguang W, Xurong G. Study on Erosion Resistance Experimental Method for Hydra-Jet Fracturing Nozzle [J]. *China Pet Machinery* (2016) 44(12):83–6. doi:10.16082/j.cnki.issn.1001-4578.2016.12.018

Conflict of Interest: The authors declare that the research was conducted in the absence of any commercial or financial relationships that could be construed as a potential conflict of interest.

frontiers | Frontiers in Physics

TYPE Original Research
PUBLISHED 10 August 2022
DOI 10.3389/fphy.2022.923762

OPEN ACCESS

EDITED BY
Huazhou Li,
University of Alberta, Canada

REVIEWED BY
Cuiying Jian,
York University, Canada
Xin Chen,
University of Alberta, Canada
Wenzheng Yue,
China University of Petroleum, China

*CORRESPONDENCE
Wei Gong,
gw0905@126.com

SPECIALTY SECTION
This article was submitted to Interdisciplinary Physics, a section of the journal Frontiers in Physics

RECEIVED 19 April 2022
ACCEPTED 04 July 2022
PUBLISHED 10 August 2022

CITATION
Gong W, You L, Xu J, Kang Y and Zhou Y (2022), Experimental study on the permeability jail range of tight gas reservoirs through the gas–water relative permeability curve. *Front. Phys.* 10:923762. doi: 10.3389/fphy.2022.923762

Experimental study on the permeability jail range of tight gas reservoirs through the gas–water relative permeability curve

Wei Gong[1]*, Lijun You[1], Jieming Xu[2], Yili Kang[1] and Yang Zhou[1]

[1]State Key Laboratory of Oil and Gas Reservoir Geology and Exploitation, Southwest Petroleum University, Chengdu, China, [2]Sinopec Chongqing Shale Gas Co., Ltd., Chongqing, China

The permeability jail refers to a specific water saturation range in a tight gas reservoir, where almost no gas or water phase can flow effectively. In the process of drilling and fracturing, water saturation rises and falls into the permeability jail. To reduce or avoid falling into the permeability jail in the recovery process, a method for measuring gas–water relative permeability of tight sandstone is established here that considers salt sensitivity, gas slippage effect, stress sensitivity, and high bound water saturation. Then, the permeability jail range was determined to provide guidance and suggestions for field application. Considering a typical tight sandstone as an example, the proposed method was used to expand the measurement range of gas–water relative permeability and observe the permeability jail range, laying an experimental foundation for accurately determining the permeability jail range in a given formation. The Byrnes model can preliminarily predict the permeability jail range with accurate bound water saturation and residual gas saturation. When the permeability jail phenomenon occurs in the core, the larger the permeability is, the smaller the permeability jail range will be; and the larger the porosity is, the smaller the permeability jail range will be. When the permeability jail phenomenon occurs in the tight sandstone reservoir, the damage to the reservoir due to external fluid and solid phased particles should be strictly controlled. The damage is stronger, the permeability and porosity decline, and the permeability jail range is wider. Other gases or solvents can be used as fracturing fluids to minimize formation damage.

KEYWORDS

boundary, two-phase flow, spontaneous imbibition, water saturation, Byrnes model

1 Introduction

The permeability jail refers to the condition when gas and water phases almost cannot flow in some water saturation region, and the region is named as the permeability jail range [1, 2]. Tight gas reservoirs are characterized by low permeability and ultra-low water saturation [3]. During drilling and fracturing, water-based fluids enter the reservoir, resulting in a rise in water saturation into the permeability jail due to high water injection and low flow back rate near the wellbore [2, 4, 5]. To reduce or avoid encountering the permeability jail during development, it is necessary to accurately locate the permeability jail range in the gas–water relative permeability.

In 1992, the permeability jail was first described in the Mesaverde tight sandstone of the Eastern Green River Basin, United States [2, 6]. Cluff and Byrnes summarized the characteristics of phase permeability curves of 43 tight cores and suggested that when the permeability is below 0.05 mD, a permeability jail exists in tight cores [2]. Aguilera et al. reported that the gas and water relative permeability in the permeability jail range was less than 0.02 [2, 6, 7]. Fu et al., Silin et al., and Jeannin et al. also observed the permeability jail in the phase permeability experiments of tight sandstone gas reservoirs [8–10]. If fluids are trapped in a permeability jail, it reduces the fracturing effectiveness and production capacity [1]. Thus, the basic and essential aspects indicate that gas well production should be investigated, considering the permeability jail characteristics to reduce economic losses. However, fundamental investigation of the determination of the range of permeability jail involves the relative permeability measurement.

However, numerous influencing factors in relative permeability measurement, such as stress sensitivity, salt sensitivity, gas slippage effect, and low water saturation, are involved in the experiment [1, 11, 12]. High stress reduces the gas–water flow channels (Figure 1A). Measurements of relative permeability are usually made at lower confining pressures. Due to stress sensitivity, the relative permeability at constant confining pressure may differ from that at native stress [13–15]. Li reported that as the effective stress increased, the relative permeability of the gas decreased significantly. When the confining pressure was increased to 34 MPa (5, 511 psi), the porosity of the tight sandstone formation decreased by 5%, resulting in a decrease in permeability [11]. Hao Zhang found that core permeability decreased with increased confining pressure until the critical pressure was reached. Beyond the critical pressure, the core permeability changed only slightly with the increase in confining pressure. In order to attain almost similar formation pressure conditions, it is necessary to conduct gas–water relative permeability experiments under the *in situ* stress conditions [8, 11].

Salt minerals dissolve and migrate, and as a result, salt crystals clog the pores (Figure 1B). The permeability of tight sandstone is affected by the salinity of liquid in the pores [12]. As the burial depth of tight sandstone increases, the salinity of formation water increases; moreover, the salt sensitivity of tight sandstone also increases [8]. When a low-salinity fluid enters the reservoir, it leads to hydration, expansion, dispersion, and migration of clay minerals, thus blocking the pores and throats [3, 12]. The high-salinity fluid that enters the reservoir also reduces the formation permeability because of the crystallization of the salinity fluid in the pore throats [16, 17]. Irrespective of the fluid salinity (high-salinity

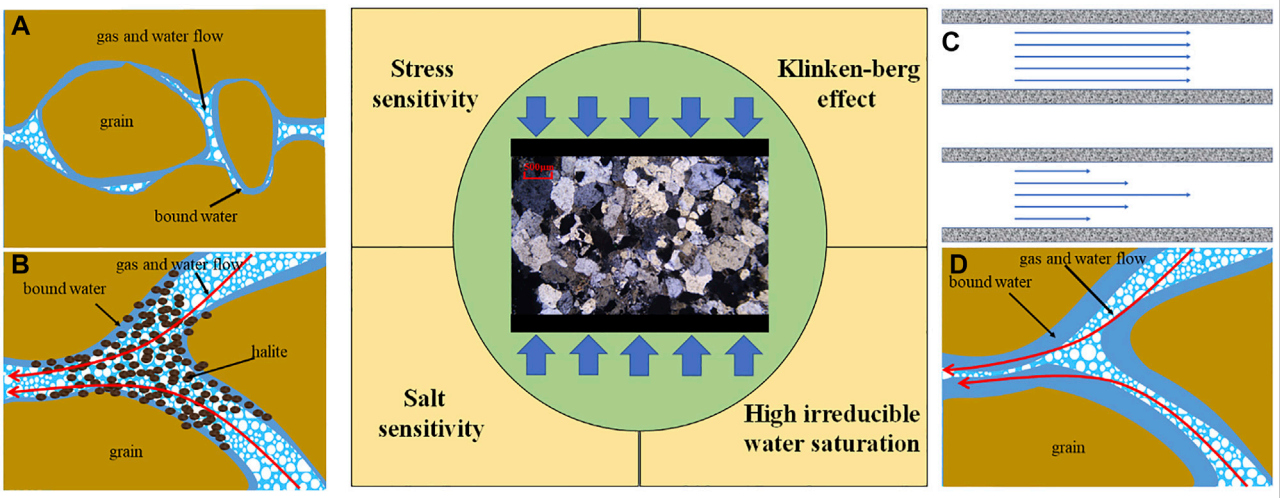

FIGURE 1
Four factors affecting the gas–water relative permeability. **(A)** High stress reduces the gas-water flow channels. **(B)** Salt minerals dissolve and migrate so that salt crystals clog the pores. **(C)** Gas slippage effect results in poor accuracy of the gas relative permeability. **(D)** Difficulty in establishing low bound water saturation.

or low-salinity) that enters the sandstone, permeability decreases, and the influence of the salt content of the displacement fluid on the permeability becomes obvious [16, 18]. During the process of gas–water relative permeability experiments, if the formation water or any fluid other than the simulated formation water is used in the experiments, the gas–water relative permeability gets affected by salt sensitivity, resulting in deviations from the actual gas–water relative permeability [17]. Therefore, residual salt in dry rock samples must be removed in advance to prevent it from dissolving during the experiments, which leads to an increase in the salinity of the displacement fluid, thus leading to a reduction in the reliability of the relative permeability data. The method described in the Chinese Petroleum Industry Standard (SY/T 5336-2006, Practices for core analysis) [19] is suitable for a conventional core to wash off the salt. However, tight sandstone has narrow pores and high capillary pressure, making it difficult for fluid to enter the pore throats of a tight sandstone. Therefore, residual salts need to be washed away without damaging the internal structure of the core, and formation water is used in subsequent experiments to establish water saturation. Notably, only when the simulated formation water displaces the core, its properties do not undergo any change.

The gas slippage effect results in poor accuracy of gas relative permeability (Figure 1C). Water saturation affects the gas slippage, which in turn affects the relative permeability of gas [11, 20]. The conventional measurement methods for gas–water relative permeability do not consider the gas slippage effect; therefore, the reliability of the relative permeability measurement method decreases [2, 6]. Klinkenberg discovered that the effect of gas flow occurred through capillary channels. To avoid the gas slippage effect, gas permeability is usually measured at different flooding pressures to obtain Klinkenberg permeability [21]. However, using this method for different water saturation conditions is time-consuming. During the gas drive experiment for a prolonged time, water evaporation leads to a change in the salinity of pore water, which further affects the measurement of permeability. Undeniably, more systematic explorations are required to eliminate the gas slippage effect without affecting the experiments and speed up the experimental process.

Difficulty is encountered in establishing the low bound water saturation, as presented in Figure 1D. Most of the gas reservoirs in western Canada and the United States have a low initial water saturation, high irreducible water saturation, and low permeability [20]. It is difficult to reduce the water saturation in the gas drive experiments for a tight core saturated with water. Moreover, relative permeability measurement is not ideal [15]. With the increase in displacement pressure and time, the gas drive process fails to keep the water saturation lower than the bound water saturation, and therefore, it becomes difficult to measure the relative permeability of the gas phase at the stage of low water saturation [21]. Prediction of water saturation through centrifugation or drying destroys the pore structure of sandstone and affects the accuracy of the measurement of gas–water relative permeability [1, 3]. Traditional gas drive experiments cannot reduce the water saturation of tight cores below the bound water saturation [3]. Therefore, under the condition of low water saturation, it is essential to select an appropriate method to measure the relative permeability of gas.

According to previous research findings noted earlier, it is difficult for researchers to measure the gas–water relative permeability when the water saturation is lower than the bound water saturation [15]. The effects of various factors such as salt sensitivity [12, 16], stress sensitivity [13, 15], and gas slippage effect were ignored [11, 20, 21]. Based on this, a gas–water phase seepage model was established to calculate the theoretical range of the permeability jail, which aided in the determination of the prediction range of the permeability jail. However, experimental methods to determine the range of gas–water phase permeability are still lacking. Progress in the measurement range of gas–water phase permeability and more accurate experimental data has been significantly impeded.

Therefore, in this study, the influence of stress sensitivity (Figure 1A) and salt sensitivity (Figure 1B) on the permeability of rock samples, gas slippage effect in the process of measuring gas-phase relative permeability (Figure 1C), and the narrow measurement range of gas-water relative permeability (Figure 1D) was considered to establish a complete set of methods for determining the permeability jail range. A measurement method for gas-water relative permeability of tight gas reservoirs is established. First, the residual salt in the core was washed away using saturated ethanol. Simulating spontaneous imbibition of formation water was used to gradually improve the water saturation of a tight sandstone core. Appropriate confining pressure was selected, and applying back pressure weakened the influence of gas slippage on permeability. This study compared the measurement range of gas–water relative permeability corresponding to different water saturation establishment methods, the difference in gas-phase relative permeability under different back pressures, and the range of gas–water relative permeability under different back pressures. The study provides an experimental basis for determining the permeability jail range and has important guiding significance for the rational and practical development of tight sandstone gas reservoirs.

2 Methods and materials

2.1 Samples

The experimental samples were selected from the Permian He 8 section and Shan 1 section tight sandstone gas reservoir from the Ordos Basin, China. The gas reservoir lithology is mainly coarse quartz sandstone, lithic quartz sandstone, and lithic sandstone. The average porosity and permeability of the samples were 7.81% and 0.37 mD, respectively. Ultra-low water saturation existed, with some reservoirs having initial water saturation below 20% (Figure 2). Moreover, the bound water saturation was within the range of

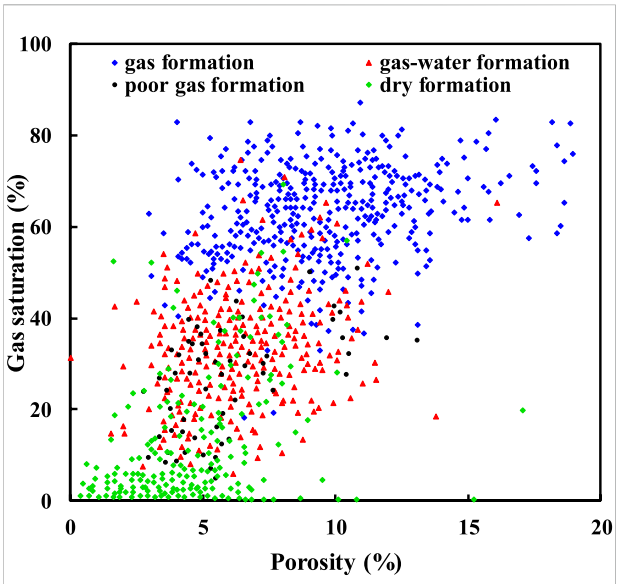

FIGURE 2
Relationship between the gas saturation and porosity in the study area. Initial gas saturation of gas formation ranges from 15% to 85%. Initial gas saturation of gas–water formation ranges from 28% to 45%. Initial gas saturation of poor formation ranges from 7% to 75%. Initial gas saturation of dry formation ranges from 0% to 70%.

32.6–66.98%. The native stress was 25 MPa. The quartz content was generally 60–90%, whereas the feldspar content was very little. The content of cuttings was mainly within the range of 10–40% and consisted mainly of quartz cuttings. The main diagenetic minerals were quartz and clay minerals, including needle-like filamentous illite, chlorite, and interbedded minerals. Furthermore, a part of the reservoir contained Shumen kaolinite.

This tight sandstone from the Ordos Basin in central and western China was selected for the following reasons: (1) it is characterized by deep burial, low permeability, and low porosity; (2) it has a large initial water saturation span, whereas the bound water saturation is larger than the initial water saturation; and (3) the measurement of gas–water relative permeability is difficult for the tight sandstone.

The composition of the formation water in the study area has a total salinity of 66,166.01 mg L^{-1} (as shown in Table 1). Table 2 presents the rock properties (length, diameter, initial permeability, and porosity) of the tight sandstone cores from the Ordos Basin.

2.2 Experimental methods

Before the test for relative permeability measurements, initial water saturation was set up by the spontaneous imbibition method. After every relative permeability measurement, the water saturation by the spontaneous imbibition method was improved, and the next relative permeability was measured.

2.2.1 Salt removal and establishing water saturation

At the beginning of the experiments, it was required to clean the fresh samples to reduce the sensitivity toward salinity. A common method for cleaning fresh samples is the Soxhlet extraction method [19]. However, cleaning tight samples using continuous immersion Soxhlets (Soxhlet extraction) is not feasible because the fluid cannot enter the pores. In this study, the salt and oil in the core were washed away entirely by conducting repeated pressurization to 25 MPa (pore pressure) with methyl alcohol and decompression to thoroughly wash off the salt and oil in the cores. This process was carried out to reduce the influence of residual salts on the experimental evaluation.

The water saturation of the tight sandstone reservoir was established by the spontaneous imbibition method. The method can set the water saturation at a specific value to realize the measurement of gas-water relative permeability. The experimental procedure is as follows.

(1) First, pre-treated cores were dried at 60°C for 2–4 h. Then, the core was taken out and cooled down to room temperature. An accurate measurement of rock pore volume was conducted. Porosity φ and dry weight M_o of the sample were then determined.
(2) Initial water saturation of core S_w was determined according to reservoir data.
(3) The fiber or paper towel was soaked with simulated formation water in advance. The experimental core was rolled back and forth on the fiber or paper towel to ensure that the end face of the core was not soaked. The simulated formation water was allowed to self-imbibe in the core under the capillary force of the experimental core itself (the simulated formation water was configured to stand for 24 h before filtration).
(4) The core weight M_o' was monitored. Step 3 was repeated until the difference between the two weighing times met the conditions given by Eq. 1 as follows:

$$\Delta M = M_o^{'} - M_o = \rho_w S_w \phi V_c, \quad (1)$$

where M_o and M_o' are the weight of dry and saturated rock samples (g), respectively, ρ_w is the formation water density (g cm^{-3}), S_w is the corresponding water saturation (%), and φ denotes the porosity of the core (%).

(5) The core with the initial water saturation was sealed and stored in a cool place for 24 h, for the uniform distribution of the established water saturation under the action of capillary force.
(6) If it was required to improve water saturation, steps (2–5) were repeated.

TABLE 1 Composition of the formation water.

Inorganic salt	NaCl	KCl	$CaCl_2$	Na_2SO_4	$NaHCO_3$	$MgCl_2$	Salinity
Content (mg/L)	18673.2	409.75	33066.9	9046.82	399.84	4569.5	66166.01

TABLE 2 Core basic parameters.

Sample	Length (mm)	Diameter (mm)	Porosity (%)	Permeability (mD)
SS-1	57.30	25.10	15.13	0.0500
SS-2	77.66	25.02	6.69	0.0740
SS-3	59.71	24.74	5.90	0.1500
SS-4	63.95	24.73	1.11	0.2260
SS-5	59.05	24.76	5.65	0.5070
SS-6	62.85	24.73	10.10	1.0900
SS-7	59.17	24.59	12.46	1.3200
S-1	49.38	24.55	4.83	0.2580
S-2	46.14	24.48	7.17	0.3674
S-3	48.42	24.50	11.31	0.9358
S-4	47.10	24.50	6.59	0.4038
S-5	47.72	24.54	4.13	0.2001
S-6	43.94	24.54	8.19	0.0540
S-7	43.60	24.72	6.64	0.0484
S-8	56.30	25.10	7.19	0.0775
S-9	55.70	25.00	10.88	0.1800

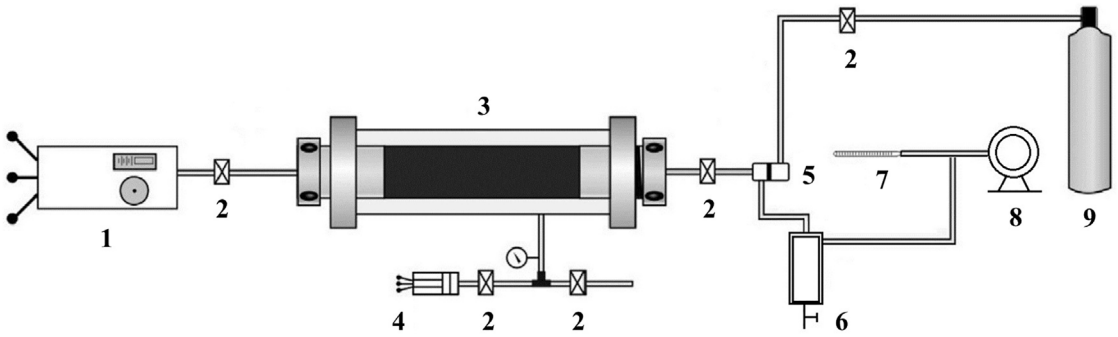

FIGURE 3
Schematic representation of the experimental apparatus. 1-pump, 2-valve, 3-core holder, 4-confining pressure system, 5-back pressure valve, 6-glass gas-water separator, 7-glass tube flow meter,8- wet gas flow meter, and 9-gas cylinder.

2.2.2 Gas–water relative permeability test

The outlet pressure was set at a fixed back pressure up to the limit pressure to eliminate the effect of gas slippage. The limit pressure test was carried out on the sample to obtain its value [22]. The equipment to measure liquid flow rate was designed and assembled (Figure 3). Gas–water relative permeability measurement steps are as follows.

(1) Initial water saturation was established by the spontaneous imbibition method according to porosity.
(2) The sample was installed in the core support. The confining pressure was the formation pressure P_f. The back pressure was the limit pressure P_l, whereas the gas flow rate Q_g and liquid flow rate Q_w were measured after the flow stabilized. According to Eqs.2–5, the effective permeability of the gas

phase K_g and liquid phase K_w and relative permeability were calculated.

(3) The next level of water saturation S_{wi} of the test sample was established by the spontaneous imbibition method.

(4) Steps (2–3) were repeated until the water saturation (core wet weight) could not be increased any further.

The effective permeability of water is given by Eq. 2.

$$K_w = \frac{Q_w \mu_w L}{A\Delta P} \times 10^{-1}. \quad (2)$$

The effective permeability of the gas is given by Eq. 3.

$$K_g = \frac{2Q_g P_o \mu_g L}{A\left(P_1^2 - P_2^2\right)} \times 10^{-1}. \quad (3)$$

The relative permeabilities of gas and water phases are given by Eqs 4 and 5, respectively.

$$K_{rw} = \frac{K_w}{K}, \quad (4)$$

$$K_{rg} = \frac{K_g}{K}, \quad (5)$$

where P_o is the atmospheric pressure (0.1 MPa), μ_w and μ_g are the viscosities of the formation water and nitrogen (mPa·s), respectively, ρ is the formation water density (g cm^{-3}), L is the core length (cm), A is the cross-sectional area of the core (cm^2), Q_g and Q_w denote the volumetric flow rates of gas and water (cm^3 s^{-1}), respectively, and P_1 and P_2 are the upstream and downstream pressures of core (MPa), respectively. In contrast, the displacement pressure difference is given by $\Delta P = P_1 - P_2$. Moreover, K_g and K_w are the effective permeabilities of gas and formation water (mD), respectively, K is the absolute permeability of rock sample (mD), and K_{rg} and K_{rw} are the gas phase and water phase relative permeabilities, respectively.

3 Results and discussion

3.1 Expansion of the measurement range of gas–water phase permeability

There are two types of methods to establish water saturation. One is to displace the wetting phase with the non-wetting phase, which generates a conventional/drainage relative permeability curve, such as the drying method [1] (reduce water saturation by drying at 60°C in an oven) and centrifugation method [3] (reduce water saturation by centrifuging at different rotation speeds in a centrifugal machine). Another is to displace the non-wetting with the wetting phase, such as the gas drive method [3] (establish water saturation by replacing core water with gas) and the spontaneous imbibition method, which generates an imbibition relative permeability curve.

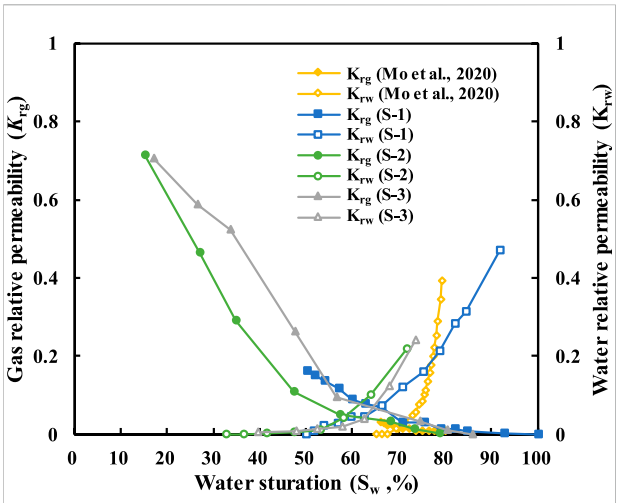

FIGURE 4
Four sets of relative permeability curves (the gas–water relative permeability curve range of S-1 sample and that provided by Mo et al. were lower than the gas–water relative permeability curve range of S-2 and S-3).

In order to prove the uniqueness and novelty of the proposed method in this study, three groups of experiments were carried out to evaluate water saturation. These tests include the relative permeability test (S-1) for the continuous decrease in initial water saturation determined by the gas drive method, the relative permeability test (S-2) for the continuous increase in water saturation measured by the spontaneous imbibition method, and the relative permeability test (S-3) for the continuous decrease in water saturation determined by the centrifugation method.

Figure 4 shows that the gas–water relative permeability curve range given by Mo et al. was small (65% < S_w (water saturation) < 80%) [1], whereas the gas–water relative permeability curve range corresponding to the gas drive method was medium (49% < S_w < 90%). Furthermore, the gas–water relative permeability curve range corresponding to the spontaneous imbibition method was large (15.26% < S_w < 79%) and that corresponding to the centrifugation method also exhibited a large range (17.17% < S_w < 85%).

The gas–water relative permeability curves of water saturation established by different methods are compared. The shape of the gas–water relative permeability curve established by the spontaneous imbibition method was similar to that of the traditional gas–water relative permeability curve; however, the relationship between the gas–phase relative permeability curve and the water saturation in the measurement process of the centrifugation method was closer to a linear relationship (Figure 4). Only the gas–water relative permeability above the bound water saturation could be measured in the gas drive experiment. The spontaneous imbibition method used in this study showed a wide measurement range; therefore, a relatively complete gas–water phase permeability curve was obtained (Figure 4).

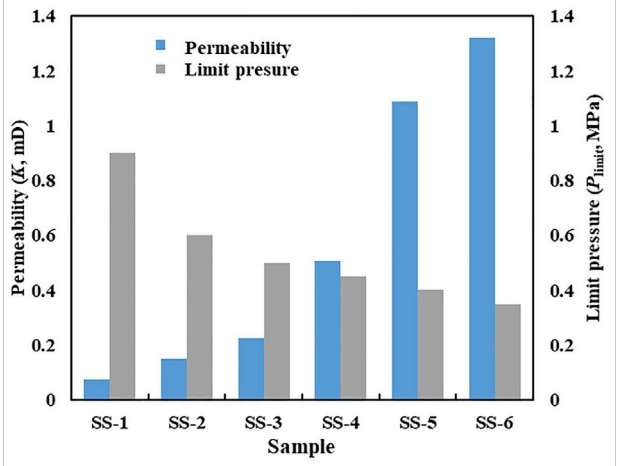

FIGURE 5
Relationship between the permeability and the limit pressure.

In order to measure the relative permeability of the gas phase in the actual production process, it is necessary to measure the relative permeability of the gas phase in the case of a continuous increase in water saturation. At the same time, the drying and centrifugation methods are used to measure the relative permeability of the gas phase in the continuous decrease of water saturation. Moreover, the establishment of initial water saturation by the drying method results in some residual salt in the pore throat, thus reducing the flow pore volume. The establishment of initial water saturation by the centrifugation method damages the integrity of rock samples. In this study, it was proposed to wash the residual salt in the rock sample with saturated ethanol under high pressure. Moreover, the simulated formation water was evenly distributed in the core through strong spontaneous imbibition and hydrophilic characteristics of tight sandstone. The measurement range of water saturation was up to 67.83% by the spontaneous imbibition method, which provides the basis for determining the permeability jail range, and therefore, subsequent measurements are based on using the spontaneous imbibition method to establish water saturation.

3.2 Determination of the range of the permeability jail

Figure 5 shows the relationship between the permeability and the limit pressure of the sample. The gas slippage effect increased with the decrease in the impact force of gas molecules in the rock pores on the unit tube wall area. This is because the gas slippage effect becomes more severe with lower permeability, and a higher upper limit pressure is required. Previous studies indicate that the limit pressure in this study area should be greater than 0.9 MPa [24]. In order to investigate the influence of slippage on gas-phase relative

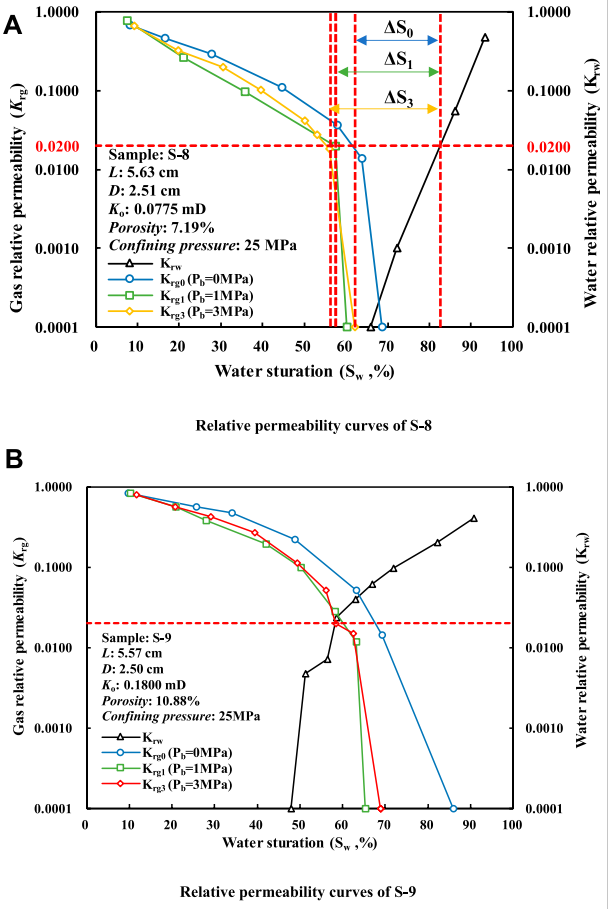

FIGURE 6
Relative permeability curves of S-8 and S-9 at different back pressures (ΔS_0: range of the permeability jail when the back pressure is 0 MPa; ΔS_1: range of the permeability jail when the back pressure is 1 MPa; and ΔS_3: range of the permeability jail when the back pressure is 3 MPa). **(A)** Relative permeability curves of S-8 and **(B)** relative permeability curves of S-9.

permeability at different back pressures, experiments were carried out to measure the gas-phase permeability at 0, 1, and 3 MPa, respectively.

Figure 6 illustrates that the residual gas saturation of S-8 and S-9 in compact samples was about 32.88 and 52.9%, respectively. The relative permeability of water increased with the increase of water saturation and reached the maximum when the water saturation was about 90%. Figure 6A exhibits that ΔS_0 was 21.56% for the back pressure of 0 MPa, while ΔS_1 and ΔS_2 were 25.18 and 27.20% for the back pressures of 1 and 3 MPa, respectively. The core sample with the permeability jail showed a smaller range without the back pressure. The gas slippage effect reduced the permeability jail range. However, when the back pressure was greater than the limit pressure (0.9 MPa), the difference between the two was only 2.02%, whereas the relative permeability of the gas phase showed no noticeable change. Therefore, it can be inferred that the gas slippage effect was weakened.

Figure 6B demonstrates that the measured relative gas permeability of the core sample without permeability jail was relatively large without any increase in the back pressure, and the isotonic point moved to the right. When the back pressure was greater than the limit pressure of 0.9 MPa, the relative permeability of the gas phase did not significantly change. Therefore, it can be inferred that the gas slippage effect was weakened.

3.3 Model validation

In order to predict the gas relative permeability in tight gas sandstones, Bynres (1979) modified Corey's relative permeability model (1954) [13]. In this study, the theoretical relative gas permeability models of S-8 and S-9 are calculated using Eq. 6.

$$K_{\mathrm{rg}} = \left(1 - \frac{S_{\mathrm{w}} - S_{\mathrm{wc,g}}}{1 - S_{\mathrm{gc}} - S_{\mathrm{wc,g}}}\right)^{p}\left[1 - \left(\frac{S_{\mathrm{w}} - S_{\mathrm{wc,g}}}{1 - S_{\mathrm{wc,g}}}\right)^{q}\right], \quad (6)$$

where K_{rg} is the gas relative permeability, S_w is the water saturation, $S_{wc,g}$ is the water saturation when $K_{\mathrm{rg}} = 1$, S_{gc} is residual gas saturation, and p and q are the exponents.

For tight sandstone, where water permeability is less than the Klinkenberg permeability, Eq. 7 is used to estimate the water permeability (K_w) from Klinkenberg permeability (K_l < 1 mD) [23].

$$K_{\mathrm{w}} = K_{\mathrm{l}}^{1.32}, \quad (7)$$

where K_l is the Klinkenberg permeability of the sample, and K_w is the water permeability of the sample.

Based on the estimation of K_w of water relative permeability, the wetting phase correlation can be used to calculate the relative permeability of liquid [24]. In this study, the theoretical relative liquid permeability of S-8 and S-9 is calculated using Eq. 8.

$$K_{\mathrm{rw}} = \left(\frac{S_{\mathrm{w}} - S_{\mathrm{wc}}}{1 - S_{\mathrm{wc}}}\right)^{4}\frac{K_{\mathrm{w}}}{K_{\mathrm{l}}}, \quad (8)$$

where K_{rw} is the relative water permeability, and S_{wc} is the water saturation when $K_{rw} = 0$.

The permeability of S8 was 0.0775 mD, less than 0.1 mD. Moreover, the bound water saturation was 65%, greater than the initial water saturation. When the water saturation was about 60%, the gas–water two-phase permeability was less than 0.02, and there was a permeability jail. The liquid phase permeability gradually increased when the water saturation was close to 70%. The permeability of S-9 was 0.1800 mD, which was greater than 0.1 mD, whereas the bound water saturation was 28%, less than the initial water saturation. The water saturation at the isotonic point was 58.38%, while the relative permeability of gas–liquid phase was greater than 0.02, indicating no permeability jail.

The predicted and experimental results are shown in Figure 7. Among them, the relative permeability curves of two different permeability grades at different back pressures were drawn, including those calculated using the Byrnes model. With an accurate bound water saturation and residual gas saturation, the curves of low permeability and high permeability cores were in good agreement with the relative permeability calculated by using the Byrnes model; if not, the Byrnes model could not predict the relative permeability curve. In fact, it is hard to accurately obtain bound water saturation and residual gas saturation.

Mo et al. considered the gas–water flow resistance characteristics and created a permeability jail model, which could satisfactorily predict the permeability jail range [15].

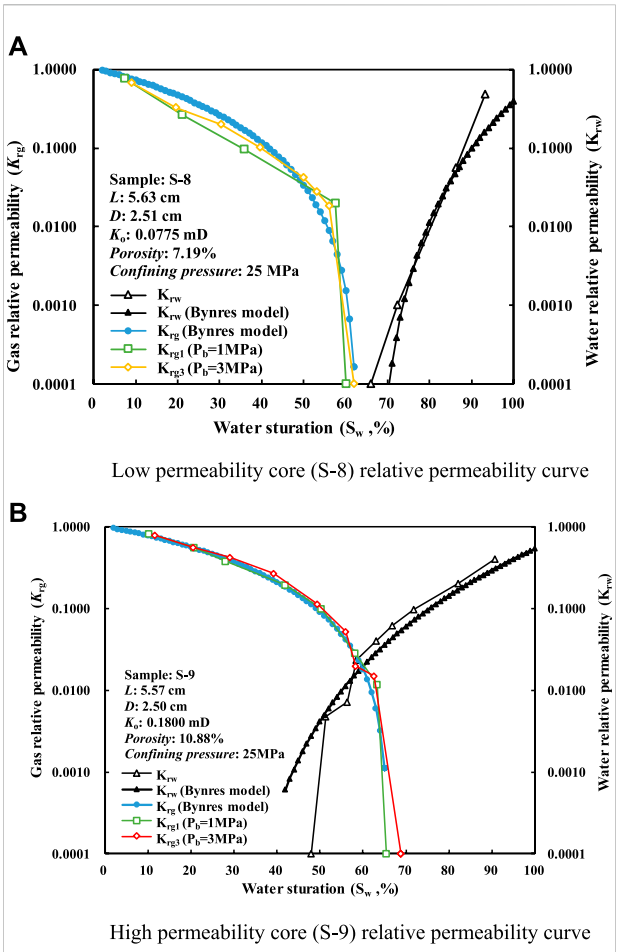

FIGURE 7
Gas–water relative permeability characteristics and model comparison of two sandstone samples. The modified Corey's model [10], represented by Eqs. 6–8, is used to generate the relative permeability curves for low- and high-permeability sandstones with the permeability of K_l = 0.0775 mD and K_l = 0.1800 mD, respectively. For K_l = 0.0775 mD sandstone, the following parametric values are used: $S_{wc,g}$ = 0, S_{gc} =38%, S_{wc} = 65%, p = 2, and q = 2, while for K_l = 0.1800 mD sandstone, the following parametric values are used: $S_{wc,g}$ = 0, S_{gc} = 35%, S_{wc} = 28%, p = 1.5, and q = 2. **(A)** Low permeability core(S-8) relative permeability curve and **(B)** high permeability core(S-9) relative permeability curve.

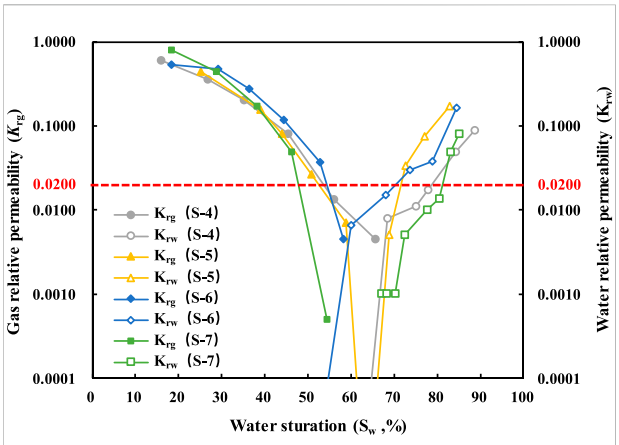

FIGURE 8
Four sets of relative permeability curves (all the four samples showed had a certain range of permeability jail).

However, the experimental data range was narrow, and the model could not measure the gas–water relative permeability below the irreducible water saturation in the experimental process (Figure 8, S-5 gas–water phase permeability curve). If the method proposed herein can be used to obtain a broader gas–water phase permeability curve, it can be more conducive to establishing a permeability jail model.

3.4 Influencing factors of the permeability jail range

The permeability jail refers to the situation when water saturation is within a range, and the relative permeability of the gas and liquid is below 0.02. Moreover, the fluid flow through the core is small. Therefore, it can be considered that the fluid under this flow pressure cannot flow in the rock. Low permeability reservoirs are commonly characterized by high capillary pressure, resulting in the immobility of both the water and gas phases [12, 25]. In tight gas reservoirs, it is common to have a water saturation range where water and gas cannot flow. The proposed method can thus prove the existence of a permeability jail (Figure 8).

In the four experimental groups mentioned earlier, different core samples showed different permeability jail ranges; however, the gas–water relative permeability curves exhibited similar variation trends. With the increase in water saturation, the gas-phase permeability decreased, while the liquid-phase permeability kept increasing. When the water saturation was in the permeability jail range, the gas–water relative permeability in the core was below 0.02 [11–13], which could be regarded as the gas–water two-phase system that could not flow. This indicates that when a reservoir falls into the permeability jail, it produces neither water nor gas.

This study found four groups of low permeability cores to have the permeability jail phenomenon. The results show the permeability confinement range of each sample. The maximum could reach 47.9–81.2% (Figure 8; Table 3, S-7), whereas the minimum could reach 54.2–70.3% (Figure 8; Table 3, S-6). The porosity difference between S-4 and S-7 was small. However, the permeability difference was as high as one order of magnitude, indicating that the smaller the throat radius of S-7, the greater was the Jamin effect. Therefore, the smaller the permeability, the more extensive will be the permeability jail range. The permeability difference between S-6 and S-7 was small. However, the porosity of S-6 was large, indicating that when the permeability difference was small, the larger the porosity, the smaller is the permeability jail range. Moreover, porosity, permeability, and permeability jail range of S-4 were larger than those of S-5, indicating that the larger the permeability, the smaller is the permeability jail range, and the larger the porosity, the smaller is the permeability jail range. The main influencing factors of permeability jail range are permeability and porosity.

3.3 Prospect of field application

Some gas–water formations are possibly defined as dry formations; for example, the core from the dry formation is proven to have a high gas saturation by core analysis. The result of good logs should consider how to avoid defining the gas-water formation as a dry formation.

During the processes of drilling, completion, and exploitation, external fluids should have a good formation protection ability because the main influencing factors are permeability and porosity [26, 27]. External fluids possibly cause the blocking of the fluid channels, which enlarges the permeability jail range, such as velocity sensitivity, water sensitivity, salt sensitivity, acid sensitivity, alkali sensitivity, and water phase trapping [28]. Before drilling, completion, and exploitation, the formation protection ability of the working fluids should be evaluated to reduce the damage to the formation [29].

During drilling, completion, and exploitation, the initial water saturation of the reservoir is usually outside the left boundary of the permeability jail. However, in the early stage of production, various reservoir modification measures, such as hydraulic fracturing, are often used [9]. Nevertheless, the intrusion of working fluid in the reservoir leads to increased water saturation near the borehole, and it is likely to be trapped in the permeability jail [2, 30]. Second, water causes the clay to expand and migrate, resulting in water phase trapping. Due to the effects of fracturing fluid residue and other factors, the water saturation near the good zone increases to the permeability jail, and the gas well production is affected by the permeability jail [25]. Therefore, experiments must be used to determine the range of permeability jail. If the water saturation can be safely developed outside the permeability jail range or reduced to the left boundary of the permeability jail, the

TABLE 3 Four sets of the permeability jail range.

Sample	L (mm)	D (mm)	Φ (%)	K_a (mD)	Permeability jail range
S-4	47.10	24.50	6.59	0.4038	54.3%~79.1% (24.85%)
S-5	47.72	24.54	4.13	0.2001	52.7%~71.8% (19.09%)
S-6	43.94	24.54	8.19	0.0540	54.2%~70.3% (16.06%)
S-7	43.60	24.72	6.64	0.0484	47.9%~81.2% (33.33%)

influence of the permeability jail can be effectively avoided. Currently, other gases or solvents such as CO_2, N_2, C_3H_8, and liquefied natural gas can be used as fracturing fluids to avoid formation damage. However, fracturing fluids with less formation damage (such as LNG) still need to be studied [31].

The result of the gas–water relative permeability experiment shows that the water saturation influences the gas-phase permeability, which is the critical parameter of gas-phase permeability. The water saturation and the thickness of the water film decrease (equivalent to increasing the effective pore radius) by decreasing the abandonment pressure, increasing the formation pressure, heating and evaporation, and changing the rock wettability, which helps recover the gas permeability.

4 Conclusion

In this study, four aspects, namely, pressure, salt content, gas slippage effect, and determination of initial water saturation, were considered to establish the gas–water phase permeability measurement process. Considering a typical tight sandstone as an example, the proposed method was used to expand the measurement range of gas–water relative permeability and observe the permeability jail range, laying an experimental foundation for accurately determining the permeability jail range. Moreover, this method is highly consistent with the gas–water relative permeability curve calculated using the Byrnes model.

(1) Simulating formation pressure conditions and the gradual increase of water saturation is a more accurate and reliable method to obtain the range of the permeability jail.
(2) Under the condition of native stress, the gas–water relative permeability of a tight core was measured with the limit pressure, and the actual waste pressure as the back pressure. The experimental result proves that the gas slip effect can be effectively reduced when the pressure is higher than the limit pressure.
(3) The measurement process established in this study agrees with the calculated results of the Byrnes model and the general law of the gas–water relative permeability curve. The Byrnes model can be used when accurate irreducible water saturation and residual gas saturation can be obtained, and the method used herein can be considered to obtain broader data when establishing the model.
(4) The permeability jail phenomenon is found in the tight sandstone of Ordos Basin by the proposed method, indicating that the larger the permeability, the smaller the permeability area, whereas the larger the porosity, the smaller is the permeability area.
(5) During drilling, completion, and exploitation, the focus should be on the formation protection ability of the working fluids. When the formation falls into permeability jail, the water saturation and the thickness of the water film can be decreased to recover the gas's relative permeability.

Data availability statement

The original contributions presented in the study are included in the article/supplementary materials; further inquiries can be directed to the corresponding author.

Author contributions

WG, LY, and YK contributed to the conception and design of the study. JX contributed to the analysis and/or interpretation of data. YZ contributed to the drafting of the manuscript.

Funding

The authors greatly acknowledge the financial support from the Natural Science Foundation of China (Grant No. 51674209) and the Sichuan Province Youth Science and technology innovation team project (Grant No. 2021JDTD0017).

Acknowledgments

We would like to thank MogoEdit (https://www.mogoedit.com) for its English editing during the preparation of this manuscript.

Conflict of interest

Author JX was employed by Sinopec Chongqing Shale Gas Co., Ltd.

The remaining authors declare that the research was conducted in the absence of any commercial or financial relationships that could be construed as a potential conflict of interest.

Publisher's note

References

1. Mo F, Peng X, Devegowda D, Du Z, Qi Z, Tang Y, et al. Permeability jail for two-phase flow in tight sandstones: Formulation, application and sensitivity studies. *J Pet Sci Eng* (2020) 184:106583. doi:10.1016/j.petrol.2019.106583

2. Cluff RM, Byrnes AP. Relative permeability in tight gas sandstone reservoirs-the permeability jail model. In: *Paper presented at the SPWLA 51st annual logging symposium*. Perth, Australia (2010). SPWLA-2010-58470.

3. Yin X, Shu J, Li YL, Gao W, Ma L, Peng W, et al. Impact of pore structure and clay content on the water-gas relative permeability curve within tight sandstones: A case study from the LS block, eastern Ordos Basin, China. *J Nat Gas Sci Eng* (2020) 81:103418. doi:10.1016/j.jngse.2020.103418

4. Tian J, Kang YL, You LJ, Jia N, Xi Z, Luo P, et al. Investigation on water phase trapping mechanisms in tight gas reservoirs: Pore-scale visualization observation and core-scale flooding analysis. *J Pet Sci Eng* (2021) 198:108185. doi:10.1016/j.petrol.2020.108185

5. Zhang D, Kang Y, Selvadurai APS, You L, Tian J. The role of phase trapping on permeability reduction in an ultra-deep tight sandstone gas reservoirs. *J Pet Sci Eng* (2019) 178:311–23. doi:10.1016/j.petrol.2019.03.045

6. Bahrami N, Dousi N, Lashari A. Evaluation of damage mechanisms in tight gas reservoirs: Integration of laboratory experiments and field data with numerical simulation. In: *Paper presented at the SPE offshore europe conference and exhibition*. Scotland, UK: Aberdeen (2015). SPE-175433-MS. doi:10.2118/175433-MS

7. Shaoul J, van Zelm L, De Pater CJ. Damage mechanisms in unconventional-gas-well stimulation—a new look at an old problem. *SPE Prod Oper* (2011) 26(4):388–400. doi:10.2118/142479-PA

8. Li Z, Zuo J, Shi Y, Xu F, Yu M, Mi C, et al. An experimental study on the slippage effects of sandstone under confining pressure and low pore pressure conditions. *Geofluids* (2020) 1–17. doi:10.1155/2020/9296243

9. Shanley KW, Cluff RM, Robinson JW. Factors controlling prolific gas production from low-permeability sandstone reservoirs: Implications for resource assessment, prospect development, and risk analysis. *Am Assoc Pet Geol Bull* (2004) 88(8):1083–121. doi:10.1306/03250403051

10. Fu X, Agostini F, Skoczylas F, Jeannin L. Experimental study of the stress dependence of the absolute and relative permeabilities of some tight gas sandstones. *Int J Rock Mech Min Sci (1997)* (2015) 77:36–43. doi:10.1016/j.ijrmms.2015.03.005

11. Farahani M, Aghaei H, Asadolahpour SR. Sensitivity of unsteady-state gas-water relative permeability to experimental artefacts and interpretation techniques; case study from a gas reservoir in south Iran. *J Nat Gas Sci Eng* (2019) 71:102998. doi:10.1016/j.jngse.2019.102998

12. Khlaifat A, Qutob H. Formation damage in tight gas reservoirs - prevention, control and remediation. *Nurs Inq* (2011) 21(1):30–8. doi:10.1111/nin.12015

13. Buchsteiner H, Warpinski NR, Economides MJ. Stress-induced permeability reduction in fissured reservoirs. In: *Paper presented at the SPE annual technical conference and exhibition*. Houston, Texas (1993). SPE-26513-MS. doi:10.2118/26513-MS

14. Li Z, Zuo J, Shi Y, Xu F, Yu M, Mi C. An experimental study on the slippage effects of sandstone under confining pressure and low pore pressure conditions. *Geofluids* (2020) 1–17. doi:10.1155/2020/9296243

15. Davies JP, Davies DK. Stress-dependent permeability: Characterization and modeling. *SPE J* (2001) 6(02):224–35. doi:10.2118/71750-PA

16. Putnis CV, Ruiz-Agudo E. Nanoparticles formed during mineral-fluid interactions. *Chem Geol* (2021) 586:120614. doi:10.1016/j.chemgeo.2021.120614

17. Da Silva DC, da Hora LF, de Araujo JDC, Arruda GM, da Costa FMF, Rodrigues MAF, et al. Evaluation of nonylphenol surfactant in enhanced oil recovery by SAG and WAG method. *Fuel* (2022) 314:122717. doi:10.1016/j.fuel.2021.122717

18. Yuan B, Moghanloo RG. Nanofluid pre-treatment, an effective strategy to improve the performance of low-salinity waterflooding. *J Pet Sci Eng* (2018) 165:978–91. doi:10.1016/j.petrol.2017.11.032

19. General Administration of Quality Supervision. *Inspection and quarantine of the people's Republic of China, standardization administration of the people's Republic of China*. Beijing, China: Standards Press of ChinaPetroleum Industry Press (2012). p. 31–5. SY/T 29172-2012.

20. Li J, Chen Z, Wu K, Li R, Xu J, Liu Q, et al. Effect of water saturation on gas slippage in tight rocks. *Fuel* (2018) 225:519–32. doi:10.1016/j.fuel.2018.03.186

21. Da Silva DC, da Hora LF, de Araujo JDC, Arruda GM, da Costa FMF, Rodrigues MAF, et al. Evaluation of nonylphenol surfactant in enhanced oil recovery by SAG and WAG method. *Fuel* (2022) 314:122717. doi:10.1016/j.fuel.2021.122717

22. Jeannin L, Davy CA, Skoczylas F, Portier E, Fu X, Agostini F. Hydraulic cut-off and gas recovery potential of sandstones from tight gas reservoirs: A laboratory investigation. In: *Paper presented at the 45th U.S. Rock mechanics/geomechanics symposium*. San Francisco, California (2011). ARMA-11-348.

23. Silin D, Kneafsey TJ, Ajo-Franklin JB, Nico P. *Pore-scale mechanisms of gas flow in tight sand reservoirs*. San Fransokyo: Lawrence Berkeley National Laboratory (2010).

24. Wu XH, Pu H, Zhu K, Lu S. Formation damage mechanisms and protection technology for Nanpu nearshore tight gas reservoir. *J Pet Sci Eng* (2017) 158:509–15. doi:10.1016/j.petrol.2017.07.033

25. Jones FO, Owens WW. A laboratory study of low-permeability gas sands. *J Petrol Tech* (1980) 32(9):1631–40. doi:10.2118/7551-PA

26. Ward JS, Morrow NR. Capillary pressures and gas relative permeabilities of low-permeability sandstone. *SPE Formation Eval* (1987) 2(3):345–56. doi:10.2118/13882-PA

27. Jing G, Chen Z, Hu X, Hui G. Influence of different shut-in periods after fracturing on productivity of MFHW in Duvernay shale gas formation with high montmorillonite content. *Fuel* (2022) 314:122719. doi:10.1016/j.fuel.2021.122719

28. Cheng B, Li J, Li J, Su H, Tang L, Yu F, et al. Pore-scale formation damage caused by fracturing fluids in low-permeability sandy conglomerate reservoirs. *J Pet Sci Eng* (2022) 208:109301. doi:10.1016/j.petrol.2021.109301

29. Mehdizad A, Pourafshary P, Sedaee B. Visual investigation of simultaneous clay swelling and migration mechanisms and formation damage consequences using micromodels. *J Petrol Sci Eng.J Petrol Sci Eng* (20222017) 158:110561509–15.

30. Jeannin L, Davy CA, Skoczylas F, Portier E, Fu X, Agostini F. Hydraulic cut-off and gas recovery potential of sandstones from tight gas reservoirs: A laboratory investigation. In: *Paper presented at the 45th U.S. Rock mechanics/geomechanics symposium*. San Francisco, California (2011). ARMA-11-348.

31. Gao H, Li HA. Pore structure characterization, permeability evaluation and enhanced gas recovery techniques of tight gas sandstones. *J Nat Gas Sci Eng* (2016) 28:536–47. doi:10.1016/j.jngse.2015.12.018

frontiers | Frontiers in Physics

TYPE Original Research
PUBLISHED 19 August 2022
DOI 10.3389/fphy.2022.976379

OPEN ACCESS

EDITED BY
Weiqi Fu,
China University of Mining and Technology, China

REVIEWED BY
Die Hu,
University of Calgary, Canada
Nu Lu,
Research Institute of Petroleum Exploration and Development (RIPED), China
Jiahui Chen,
University of Alberta, Canada

*CORRESPONDENCE
Chao Han,
hansuper713@hotmail.com

SPECIALTY SECTION
This article was submitted to Interdisciplinary Physics, a section of the journal Frontiers in Physics

RECEIVED 23 June 2022
ACCEPTED 18 July 2022
PUBLISHED 19 August 2022

CITATION
Xu Y, Han C, Sun J, He B, Guan Z and Zhao Y (2022), Formation interval determination method of MPD based on risk aversion and casing level optimization.
Front. Phys. 10:976379.
doi: 10.3389/fphy.2022.976379

Formation interval determination method of MPD based on risk aversion and casing level optimization

Yuqiang Xu[1,2], Chao Han[1,2]*, Jiarui Sun[1], Baolun He[1,2], Zhichuan Guan[1,2] and Yishu Zhao[3]

[1]School of Petroleum Engineering, China University of Petroleum (East China), Qingdao, China, [2]Shandong Ultra-deep Drilling Process Control Tech R&D Center, Qingdao, China, [3]Xibu Drilling Company Drilling Research Institute, Urumqi, China

MPD is one of the effective means to solve the drilling problems in deep-water and deep-stratum complex formations such as narrow pressure window. To reduce the cost, it is mostly implemented only in complex and narrow pressure window strata. However, at present, there is no scientific method to determine the MPD matching stratum interval under the "conventional + MPD" composite drilling mode. Aiming at this problem, by introducing the methods of risk quantitative evaluation and taking the principle of "avoiding risk and reducing MPD cost", combined with the accurate ECD calculation method considering multiphase flow, this paper puts forward the accurate determination method of matching the stratum interval of MPD, which can reduce the section of MPD construction as much as possible and optimize the casing level on the premise of ensuring safety. Based on the artificial bee colony algorithm, the intelligent determination method of casing level and setting depth under the condition of pressure control is established, which can quickly and accurately obtain the maximum casing setting depth and its corresponding optimal pressure control parameters in the open-hole section. The case analysis shows that, compared with the conventional drilling mode, the "upper conventional + lower MPD" drilling method can save one layer of casing while ensuring safety. The proposed method can provide theoretical and scientific basis for the accurate calculation of MPD matching stratum interval under the "conventional + MPD" compound drilling mode and the scientific and efficient design of casing levels and setting depth under the condition of pressure control.

KEYWORDS

managed pressure drilling, risk aversion, formation matching interval, artificial bee colony algorithm, optimization of pressure control parameters

Introduction

Managed pressure drilling (MPD) is one of the powerful methods to improve the safety and efficiency of drilling in deep water and deep strata with narrow safe density window [1, 2]. With the deepening of oil and gas exploration and development into deep water and complex strata, the number of applications of the MPD technique in the world

is increasing year by year [3–5]. The feasibility and applicability of the MPD technique in deep water gas fields in the south China sea are also being studied [6, 7]. In recent years, the research on MPD technique mainly focuses on key equipment and pressure control technology, and gradually forms a variety of MPD techniques with different pressure control principles, such as double gradient and wellhead back pressure. The field practice has also changed from the objective restriction of "feasible or not" to the subjective choice of "use or not" [8–9]. Preliminary research and practice show [1014] that by virtue of its advantages of accurately regulating wellbore ECD under different drilling conditions, the MPD technique can broaden the safe density window, reduce complex downhole risks, and have the certain potential of optimizing well structure. On the other hand, due to the high cost of the MPD technique, to save cost, in the operation of the same well, the MPD technique is only applied in part of the well section. For other uncomplicated strata, the conventional drilling method is still adopted. However, the coordination mechanism between cost investment and risk avoidance of the MPD technique is not clear at present. In the field implementation process, only the stratum interval of MPD can be qualitatively evaluated based on the characteristics of the formation pressure profile and the experience of engineers and technicians. It is difficult to comprehensively consider many factors such as "cost-saving (reducing unnecessary pressure control formation interval)", "reducing complex risks" and "optimizing well structure", and to quantitatively determine the reasonable construction interval of MPD. At the same time, the trial calculation method is still used for casing layer and setting depth design under pressure control, and the efficiency and accuracy need to be further improved.

Given the above problems, quantitative risk evaluation methods are introduced in this paper. Under the principle of "avoiding risks and reducing pressure control costs", a method for determining the matching strata interval of controlled pressure drilling under the "conventional + MPD" compound drilling mode is proposed, as well as an intelligent method for determining casing level and setting depth under controlled pressure conditions. It provides the scientific basis and technical support for the optimal design and safe and efficient implementation of the MPD technique in deep water and complex formations.

Determination method of matching formation interval for MPD

For a well, the upper strata tend to have a normal pressure trend and a wide safe density window that allows the conventional drilling method to be adopted. While the complex and narrow density windows are usually in the deeper strata. Therefore, to save pressure control costs, it is necessary to reduce the pressure control section as much as possible on the premise of ensuring the safety of drilling in the whole well section. So, when determining the pressure-controlled matching formation interval, is the conventional drilling method limited to the normal pressure formation. Are there some wellbore sections suitable for conventional drilling in deep complex/narrow density window formations? Do all narrow density window formations require the MPD technique? The essence of many problems is the formation adaptability of the MPD technique and its risk avoidance. It is necessary to introduce quantitative risk assessment methods to compare and analyze the potential engineering risks of conventional drilling and managed pressure drilling in different wellbore sections. In terms of "saving cost", "reducing complex risks", and "optimizing well structure", MPD is preferred to match the formation interval.

Pre-drilling quantitative evaluation method of downhole engineering risk

Because of the strong uncertainty of deep well complex formation information and the limitations and incompleteness of the existing seismic and logging interpretation model, the author team proposed a quantitative description method of drilling geomechanical parameters under the condition of uncertain information [15–18]. According to the constraint conditions of pressure balance in the open-hole section, a safe drilling fluid density window with credibility is constructed. Combined with the well structure and construction scheme, the underground risk intensity profiles are calculated (as shown in Figure 1), which realizes the quantitative assessment of downhole engineering risk before drilling. The basic principle of this method is shown in Figure 2, the probability distribution of geological characteristic parameters is obtained through probability statistics and Monte Carlo simulation methods, and then combined with the drilling construction methods, based on the stress-strength interference theory, the quantitative risk assessment of the whole well section is realized. The specific method is in literature [15–18], which will not be described here. Since the quantitative risk assessment method is based on the formation pressure profile with credibility, well structure, and construction (drilling fluid density/ECD) scheme, it can satisfy the needs of this paper to compare and analyze the potential engineering risks of conventional drilling and MPD in different wellbore sections.

This method can select two technical routes: Horizontal stratification statistics of regional wells (HSSRW) and vertical rolling statistics of single well (VRSSW) according to the abundance of regional drilled data. Among them, HSSRW refers to the statistical analysis of rock mechanics parameters and tectonic stress coefficient distribution in the region by using the well logging data given the abundant drilling data in the region. In combination with the Monte Carlo simulation method, four pressure profiles with credibility are established. VRSSW refers to the preliminary exploration blocks with few wells or only seismic data in the region, using the normal diffusion estimation method to fully excavate the seismic data

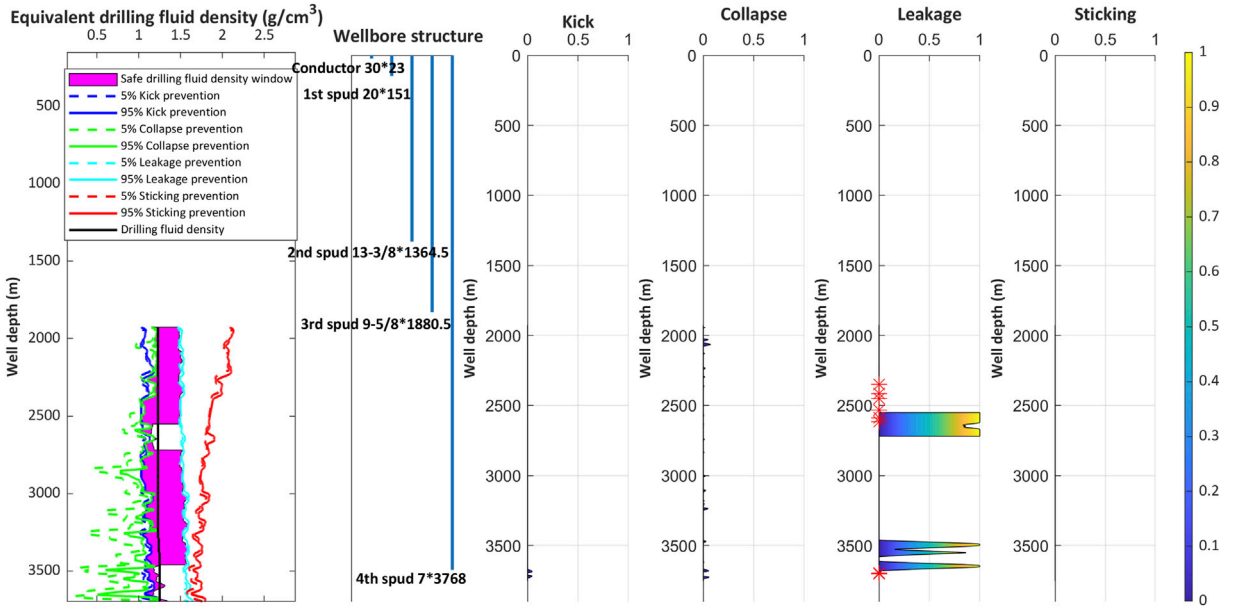

FIGURE 1
Safe drilling fluid density window with credibility and risk intensity profile.

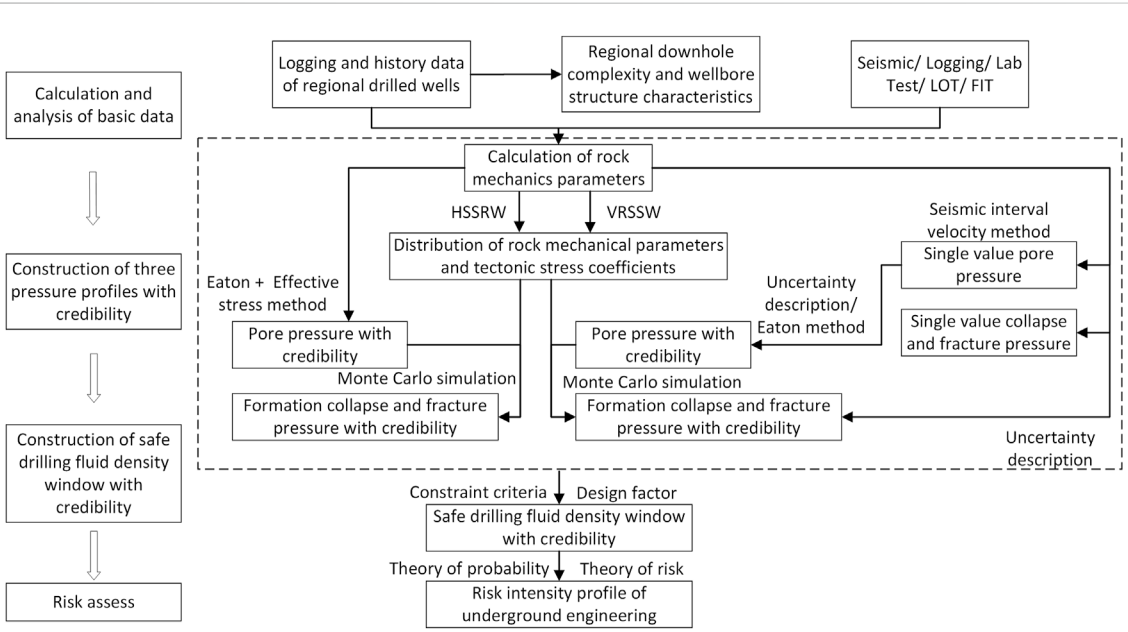

FIGURE 2
Schematic diagram of pre-drilling risk quantitative evaluation method.

response characteristics in the depth direction (longitudinal) of the well, to construct a four pressure profiles with credibility. Either technical route is based on the existing data and interpretation model, quantitatively describing the error (uncertainty) of formation pressure prediction results in the form of probability. The formation pressure profile is no longer a single determined value but is transformed into an interval, which considers the influence of parameter

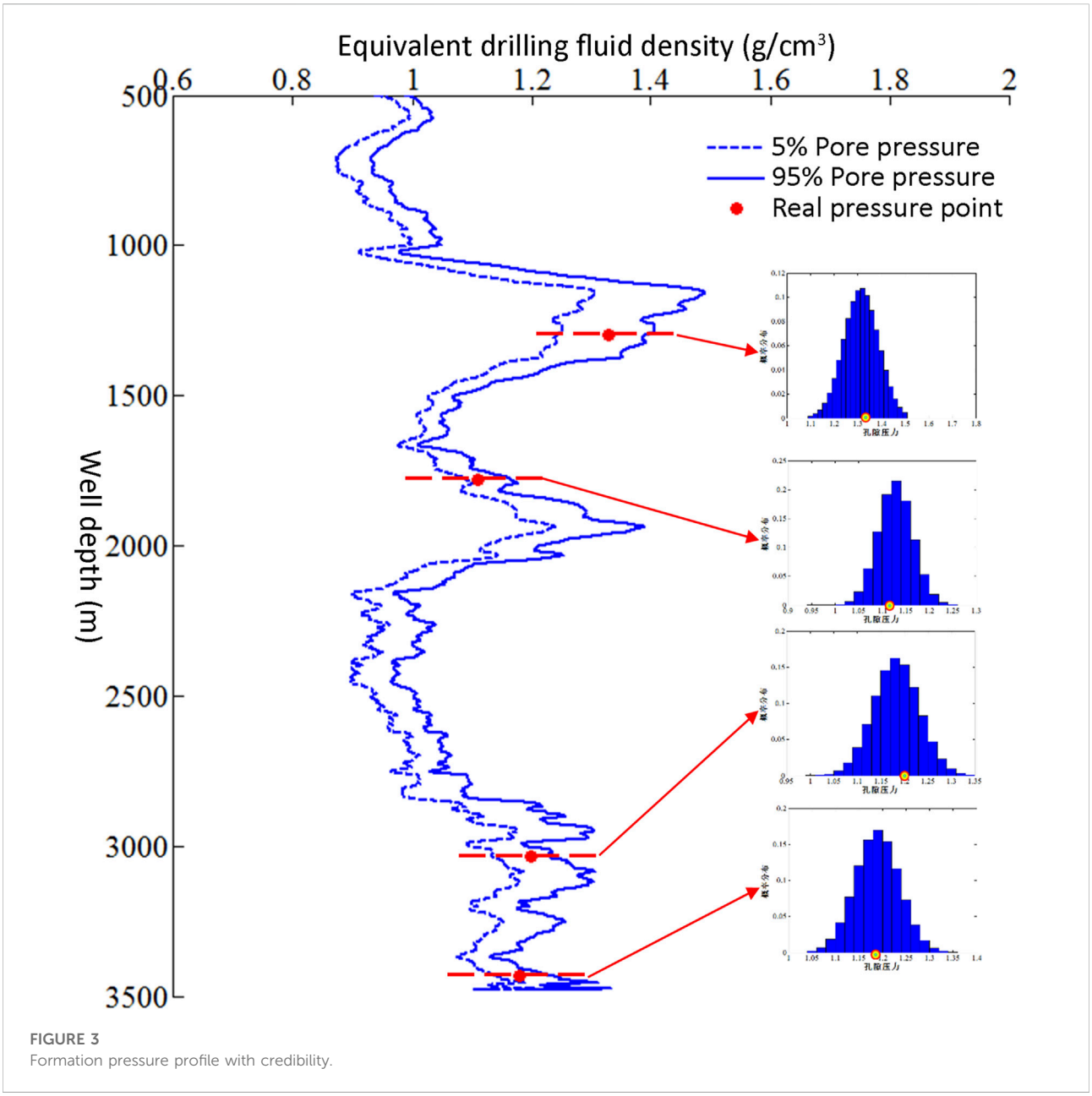

FIGURE 3
Formation pressure profile with credibility.

uncertainty in the prediction model, as shown in Figure 3. This method can evaluate the design scheme of the wellbore structure to be drilled, predict the potential drilling risks before drilling, and then optimize the scheme based on the prediction results, and finally realize risk avoidance.

MPD matching interval determination method

To accurately calculate the matching formation interval of MPD, the conventional drilling method is adopted in the upper normal pressure formation. And the risk assessment method in chapter 2.1 is used in the lower abnormal pressure formation. Based on the principles of risk avoidance, optimization of well structure, and reduction of pressure control cost, the potential risks and casing levels of conventional drilling and MPD in different wellbore sections are compared and analyzed. The specific process is shown in Figure 4 and described as follows:

1. According to the characteristics of the formation pressure profile, it can be divided into normal pressure region and abnormal pressure region. Generally, the upper part is the normal pressure area, assuming that the well depth at the cut-off point is H_1.

2. Using chapter 2.1, the safe drilling fluid density window with credibility is established. For the upper normal pressure formation, the conventional drilling technique is used to design from top to bottom in the safe drilling fluid density window with credibility. Assume that the maximum safe setting depth of the last spud casing is H_0 (H_0 can be greater than, equal to, or less than H_1).
3. Starting from H_0, the conventional drilling technique and MPD technique are used to design casing layers and setting depth respectively, and chapter 2.1 is used to evaluate potential risks.
4. It is assumed that the maximum safe setting depth of conventional drilling is H_2 (If H_2 equals to the target well depth, which means that there is no risk of conventional drilling in the whole well. Otherwise, it is risky to use conventional drilling technique for $H > H_2$ intervals). Taking H_0 as the starting point, H_2 as the ending point, and $\triangle H$ as the step length, calculate the number of casing layers C_i of the whole well when the MPD technique is used from $H_i = H_0 + \triangle H \times i$.
5. Then, the well depth H_j corresponding to $C_j = \min(C_i)$ is the peak of formation matching interval of MPD.

Intelligent determination method of casing level and setting depth under MPD

The basic principle of the casing level and setting depth design in the MPD mode mentioned in chapter 2.2 is to calculate the wellbore ECD profile by adjusting the controlled pressure parameters to match or balance the formation pressure. This is significantly different from the conventional drilling technique using the static equivalent density of drilling fluid. Aiming at the complex conditions of high temperature, high pressure and deep-water drilling, this paper adopts the accurate calculation method of wellbore ECD considering temperature pressure coupling, drill pipe eccentricity and drilling fluid fluidity [19–22]. Selecting appropriate MPD parameters for the open-hole section and obtaining the optimal wellbore ECD profile is one of the keys to the design of casing level and setting depth in MPD.

However, in current practice, it is necessary to rely on manual experience to determine "reasonable" pressure control parameters and "optimal" wellbore ECD profile, which is not only a heavy workload but also largely depends on human factors and the number of samples of different pressure control parameters calculated, lacking scientific and efficiency [11–13, 23]. In recent years, the rise of intelligent bionic algorithms such as particle swarm algorithm, genetic algorithm, annealing algorithm, ant colony algorithm, and artificial bee colony algorithm has brought opportunities for scientific and efficient solutions to optimization problems in engineering practice [24–30].

Therefore, according to the characteristics of MPD and the actual needs of well structure optimization design, it is necessary to put forward the method of optimizing pressure control parameters and wellbore ECD profile in the open-hole section based on the intelligent algorithm, and the method of determining casing layer and setting depth under pressure control conditions based on this, to improve the design efficiency and the accuracy of design results.

Feasibility analysis

By analyzing the principle of pressure control and the design principle of casing layer and casing depth, the artificial bee colony algorithm can be applied to the intelligent optimization of wellbore ECD and casing setting depth under pressure control.

The basic principle of the artificial bee colony algorithm is that the solution of the problem to be solved is regarded as the nectar source, and the more abundant the honey source and the better the quality, the better the solution quality. Through a group of artificial bees randomly searching the rich source, exchanging information, and switching roles, the optimal solution is finally obtained efficiently.

The application of the artificial bee colony algorithm should satisfy the following basic conditions [13, 17, 23]: 1) The problem to be solved is a multi-parameter optimization problem; 2) the objective function should be a continuous function or approximately a continuous function; 3) the variable has a certain value range.

In the well structure design of MPD, for the open-hole section determined by formation pressure window: 1) There is an optimal value of ECD profile under controlled pressure, and the corresponding pressure control parameters are the optimal pressure control parameters; 2) if the maximum casing depth in the open-hole section is taken as the objective function, the function is a continuous function of each control pressure parameter; 3) the variables of the objective function are different pressure control parameters, such as wellhead back pressure and drilling fluid density, which all have a certain value range. It can be seen that the optimization of pressure control parameters satisfies the basic conditions of applying the artificial bee colony algorithm.

On the other hand, there are generally more than 2 pressure control parameters for MPD. There are many combinations of various pressure control parameters within the adjustable range, and the wellbore ECD profiles under different pressure control parameter combinations are also quite different, which belongs to a typical multivariable optimization problem. If we rely on manual calculation, not only the workload is heavy, but also the calculation accuracy can not be guaranteed. If we use the artificial bee colony algorithm and rely on its efficient and stable intelligent optimization mechanism, it is expected to efficiently and accurately obtain the optimal wellbore ECD and its

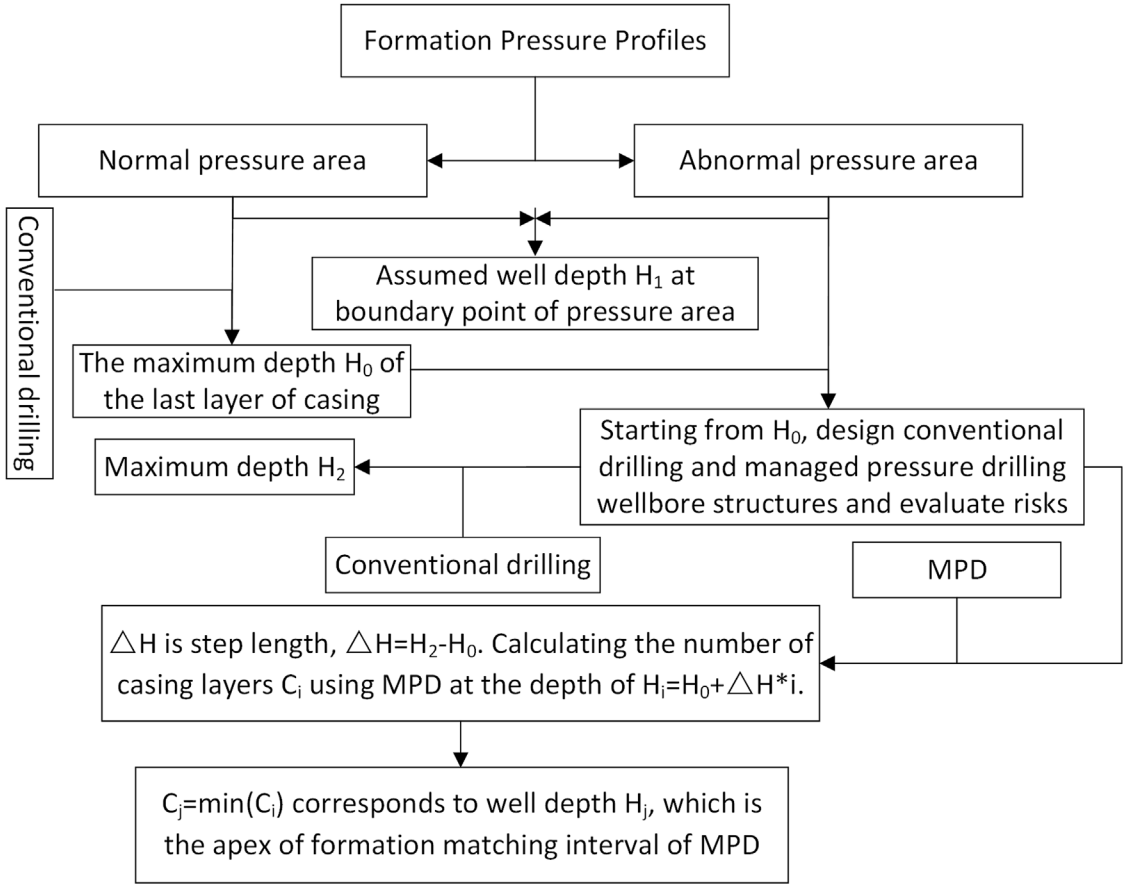

FIGURE 4
Flow chart of well structure optimization design of MPD based on artificial bee colony algorithm.

corresponding pressure control parameters in the open-hole section under the condition of multiple pressure control parameters.

The basic method of well structure design under MPD

The basic calculation steps of casing setting depth and optimal pressure control parameters in the open-hole section of MPD are as follows:

1) Geological must seal point determination:

According to the geological data, determine the necessary sealing stratum.

2) Safe pressure window determination:

The safety pressure window is determined according to the prediction results of formation pore pressure, formation fracture pressure, and formation collapse pressure before drilling and the design coefficient of the regional well bore structure. The lower limit of the safe pressure window at well depth H is $\rho_{\text{lower}}(H)$ and the upper limit is $\rho_{\text{upper}}(H)$.

3) Determination of adjustable range of pressure control parameters:

Controlled pressure parameters have a direct influence on the ECD profile of the wellbore. The pressure control parameters K_i (i = 1,2,. . .. . .) are determined according to the pressure control characteristics and actual working conditions of different pressure control drilling methods. The adjustable range of each pressure control parameter is:

$$K_L \le K_i \le K_H$$

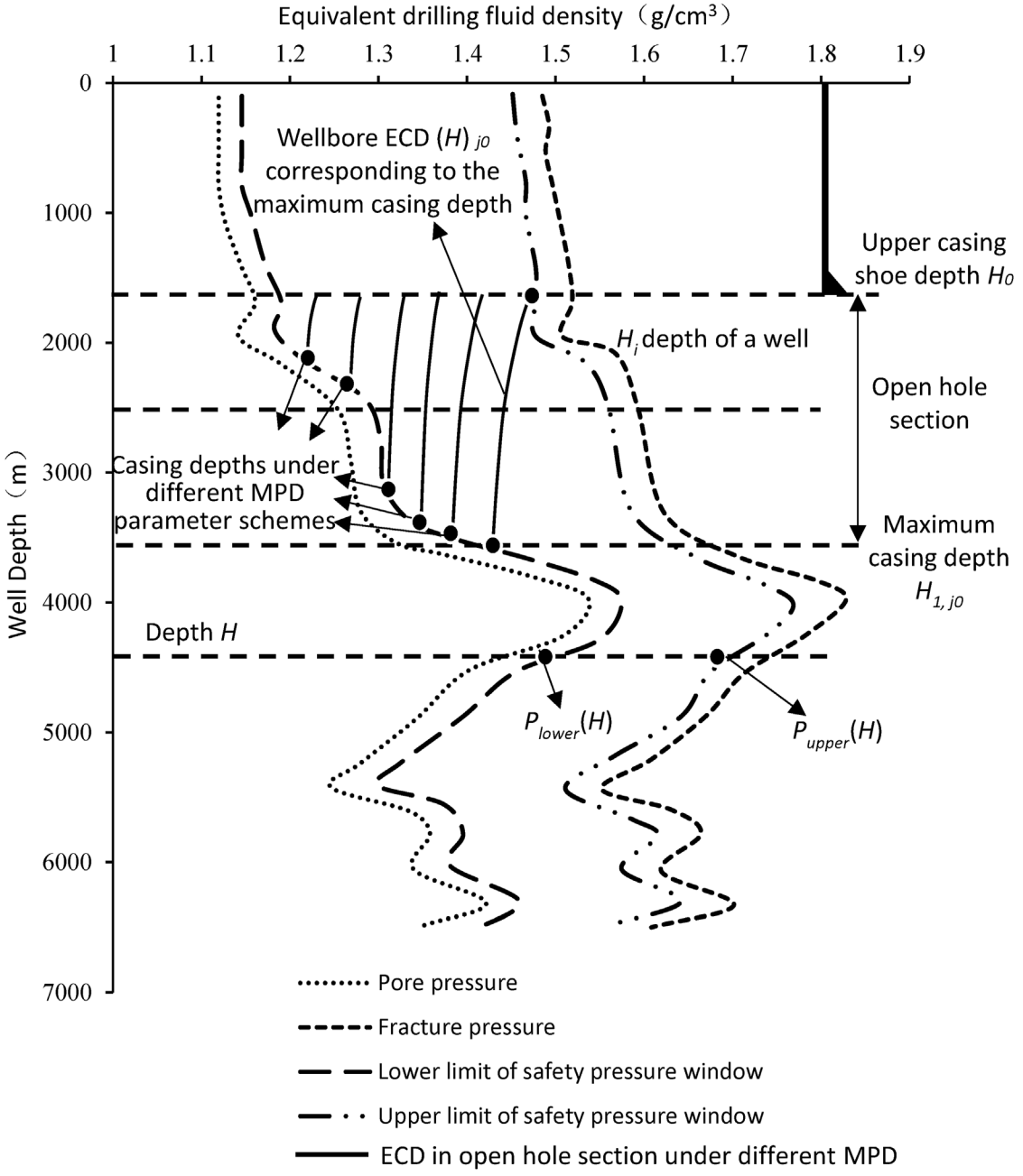

FIGURE 5
A well with reliable formation pressure profile and design results of casing layers and running depth under different drilling methods.

(4) Wellbore ECD calculation under different pressure control conditions:

Within the adjustable range of each controlled pressure parameter involved in Step (3), the wellbore ECD calculation model was used to calculate the wellbore ECD profile under different controlled pressure conditions.

Wellbore ECD under the condition of controlled pressure parameter combination scheme j is a function of well depth H:

$$\mathrm{ECD}(H)_j = f(K_i, H) \tag{1}$$

5) Determination of optimal pressure control parameters and casing setting depth in open-hole section:

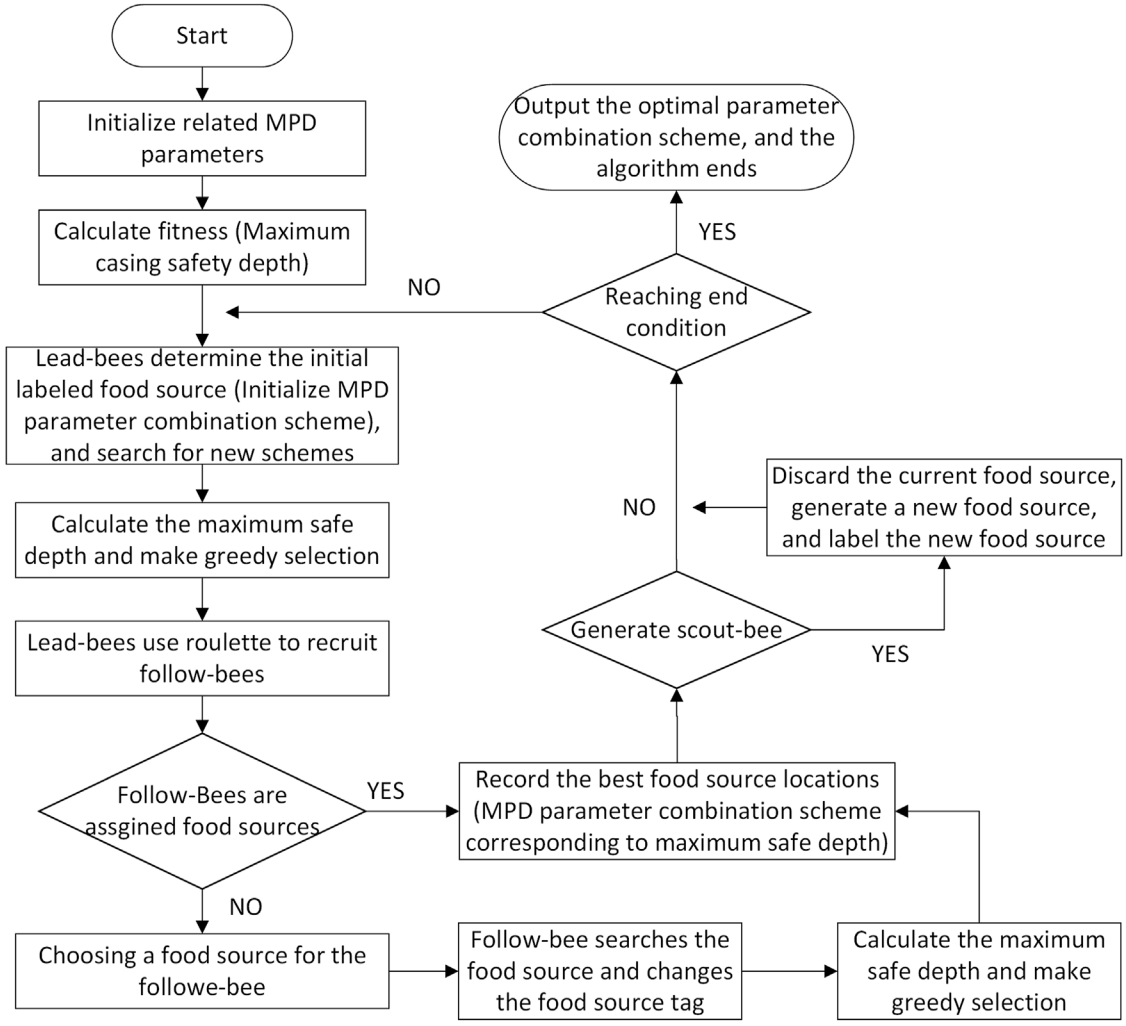

FIGURE 6
Schematic diagram of wellbore ECD distribution and determination of maximum casing depth under different pressure control parameters in open hole section.

Within the safe pressure window $[\rho_{\text{lower}}(H),\ \rho_{\text{upper}}(H)]$ determined in Step (2), the maximum safe well depth of wellbore ECD profile $H_{1,\ j}$ can be expressed as:

$$H_{1,j} = f^{-1}\left(\text{ECD}\left(H\right)_j\right) \tag{2}$$

For a certain pressure control parameter combination scheme j, the wellbore ECD profile at depth H_i in the open-hole section satisfies the following requirements:

$$\rho_{\text{lower}}\left(H_i\right) \le \text{ECD}\left(H_i\right)_j \le \rho_{\text{upper}}\left(H_i\right)$$

Then, the maximum casing setting depth H_1 of the open-hole section is:

$$\begin{aligned} H_1 &= \max\left(H_{1,j}\right) = \max\left(f^{-1}\left(\text{ECD}\left(H\right)_j\right)\right) \\ &= \max\left(f^{-1}\left(f\left(K_i, H\right)\right) = H_{1,j0}\right. \end{aligned} \tag{3}$$

Then, the maximum casing setting depth of the open-hole section is H_1, and the corresponding pressure control parameter scheme is $j0$.

The above is the basic calculation method of casing setting depth and optimal pressure control parameters in the open-hole section of MPD. The schematic diagram of the design result is shown in Figure 5. As the pressure control parameters of MPD are often more than two (for example, the pressure control parameters of CML controlled pressure drilling mainly include: displacement, mud pump position, mud slurry level depth; the pressure control parameters of bottom hole constant pressure MPD are as follows: Drilling fluid density, wellhead back pressure). There are

many combination schemes of various pressure control parameters within the adjustable range (the higher the accuracy requirements, the more calculation samples of various pressure control parameters, the number of combination schemes increases exponentially), and the wellbore ECD profile under different parameter combination schemes also varies greatly. Therefore, the conventional method requires a lot of calculation, which greatly reduces the design efficiency and cannot guarantee the optimization of design results.

An improved method based on the artificial bee colony algorithm

Since conventional calculation methods cannot satisfy the actual requirements of the optimization design of the well structure of MPD, the artificial bee colony algorithm is introduced to intelligently and efficiently optimize the casing setting depth H_1 and its corresponding optimal pressure control parameters in the open-hole section under the condition of pressure control. The basic process is shown in Figure 6, and the specific steps are as follows:

1) Initialize population: total number of bees *SN*; the number of leading bees and following bees is the number of pressure control parameter combination schemes, generally *SN*/2; maximum iteration times *MCN* (generally 1000) and control parameter *Limit* (generally 20); objective function $H = f^{-1}(f(K_i, H))$; the search range of each parameter { $K_L \le K_i \le K_H$; $\rho_{\text{lower}}(H_i) \le \text{ECD}(H_i)_j \le \rho_{\text{upper}}(H_i)$, $H_i \in [H_0, H_j]$ }, and within the range, the initial solutions are randomly generated $\{X_1, X_2, \ldots, X_{SN}\}$ (the initial solution is the scout-bee, which is a random combination scheme of MPD parameters, and is automatically generated by random).
2) Calculate and evaluate the fitness of each initial solution. Fitness function *fitness* is the objective function itself, that is, $H = f^{-1}(f(K_i, H))$.
3) The lead-bee uses the Eq. 4 to randomly search the neighborhood to get a new location (refer to each buzzer search to control pressure parameters combination scheme), under the principle of greedy choice, if the fitness of the new position (i.e., the maximum casing setting depth) is greater than that of the original position, the original position shall be updated with the new position; otherwise, the original position shall remain unchanged. When all lead-bees completed the neighborhood search, the probability P_i was calculated according to Eq. 5.

$$V_{ij} = X_{ij} + \Phi_{ij}\left(X_{ij} - X_{kj}\right) \tag{4}$$

$$P_i = \frac{fitness_i}{\sum_{i}^{SN} fitness_i} \tag{5}$$

Where, $j \in \{1, 2, \ldots, D\}$, $k \in \{1, 2, \ldots, SN\}$ and $k \neq i$.

4) Follow-bees use the calculated probability P_i to select the lead-bees based on the roulette principle. After the follow-bees complete the selection of the lead-bees, Eq. 4 is used to search the neighborhood and also select the position with high fitness according to the greedy selection principle.
5) Determine whether there is a solution to be abandoned. If the result of a lead-bee does not change after the *Limit* iteration, it will change from the lead-bee to the scout-bee and randomly generate a new position to replace the original position according to Eq. 6.

$$X_{ij} = X_{\min j} + rand(0, 1)\left(X_{\max j} - X_{\min j}\right) \tag{6}$$

6) Record the optimal solution of the bee colony so far.
7) If the current iteration number is greater than the maximum number *MCN*, the iteration ends and the algorithm ends. Otherwise, return step (2), the overall number of iterations *Cycle* = *Cycle*+1.

Example analysis

The basic information of well A is as follows:

The target depth of the well is 6600 m, and the geological sealing points in this area are mainly 200 m loose gravel layer and 1700 m easy-loss formation. The well structure design coefficients are as follows: the suction pressure coefficient is 0.036 g/cm^3; the surge pressure coefficient is 0.036 g/cm^3; the fracture pressure safety factor is 0.024 g/cm^3; the kick allowance is 0.06 g/cm^3; the differential pressure sticking factor is 22 MPa. The formation pore pressure and fracture pressure profile with credibility established by chapter 2.1 and the upper and lower limits of the safe drilling fluid density window are shown in Figure 7. This well is planned to use conventional drilling and bottom hole constant pressure MPD. The pressure control parameters are mainly drilling fluid density and wellhead back pressure. Among them, the maximum controlled pressure value of wellhead controlled pressure equipment in well A is 5 MPa.

According to the process shown in chapter 2.2 and Figure 4, by analyzing the pressure profile of the well, the depth at the cut-off point of the normal pressure area is 3350 m. Conventional drilling was designed from top to bottom within the safe drilling fluid density window, and the maximum safe setting depth of the last casing is H_0 = 3780 m. Starting from 3750 m, the conventional drilling and MPD techniques are used to design casing layers and setting depth respectively. And chapter 2.1 is used to evaluate potential risks. Among them, the conventional drilling technique can safely drill to the target well depth, and 2 casing layers are needed below H_0, that is, 5 casing layers are needed in the whole well.

Under the condition of MPD (with H_0 = 3780 m as the starting point, H_2 = 6600 m as the endpoint, 10 m as the step length) chapter 3.3 is used to design the casing layers and depth

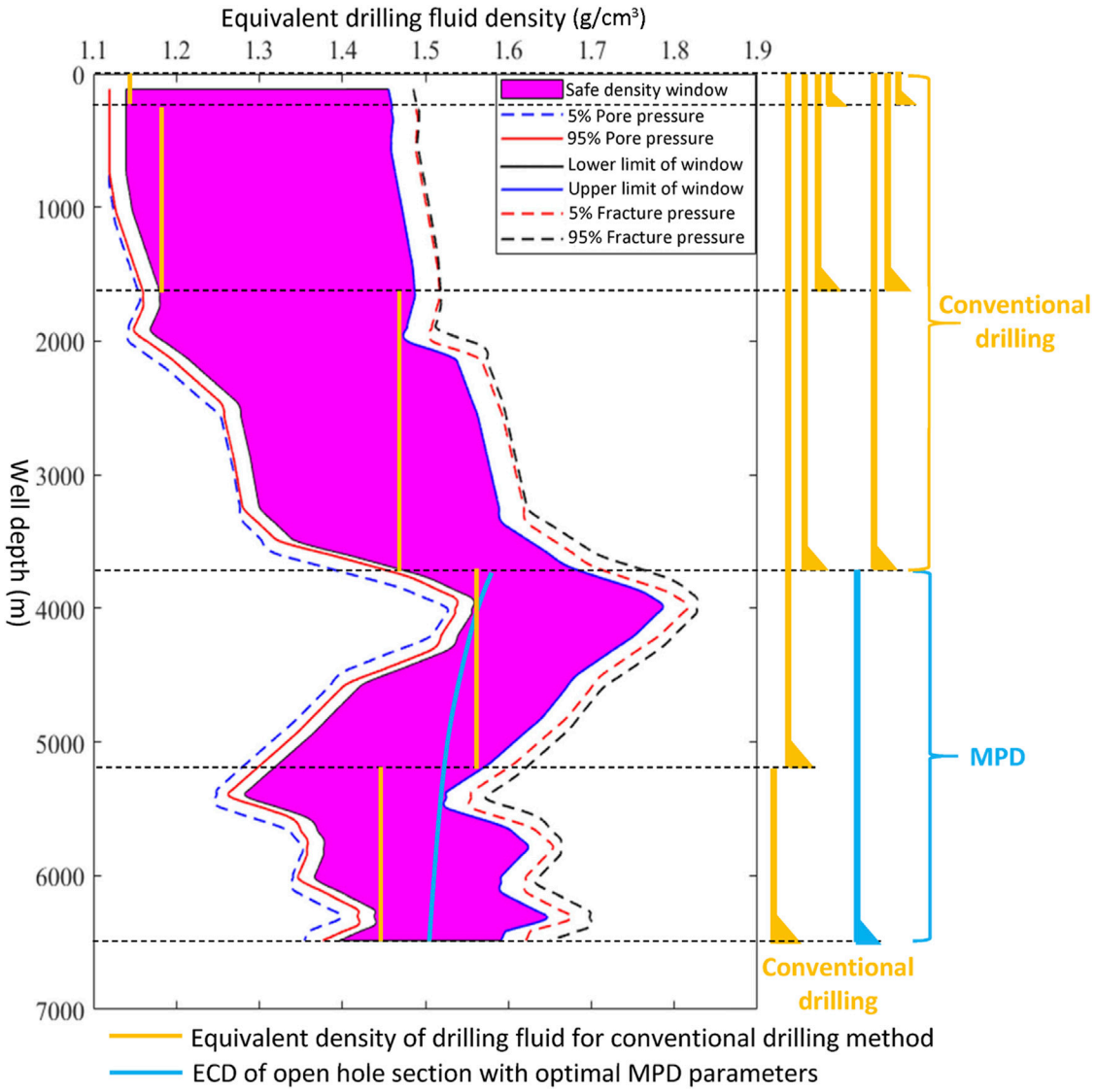

FIGURE 7
Calculation flow chart of controlled pressure matching formation interval.

TABLE 1 A Well design results of casing level and depth under different drilling methods and optimization results of pressure control parameters.

Casing level	Conventional drilling method		Conventional + managed pressure drilling			
	Casing setting depth(m)	Drilling fluid density (g/cm^3)	Casing setting depth(m)	Drilling fluid density (g/cm^3)	Wellhead back pressure (MPa)	Drilling way
One	200	1.13	200	1.13	—	Conventional
Two	1700	1.18	1700	1.18	—	
Three	3,780	1.46	3,780	1.46	—	
Four	5,176	1.56	6,600	1.48	4.2	Pressure control
Five	6,600	1.44	—	—	—	—

and optimize the controlled pressure parameters. The number of casing layers C_i in the whole well is calculated from H_i=(3,780 + 10 × i)m when the MPD technique is used. The results showed that: except for C_0 = 4 (that is, one layer of casing can be safely drilled to the target well depth by using MPD from H_0), C_i = 5 ($i \geq 1$) under other conditions, which is the same as the casing layer times under conventional drilling methods. Therefore, the well depth H_0 = 3780 m corresponding to C_0 = min (C_i) = 4 is the peak of the formation matching interval of MPD, and the controlled pressure interval is 3780–6600 m.

The design results of casing layers and setting depth under different drilling methods as well as the optimal pressure control parameters in controlled pressure formation intervals are shown in Table 1.

Conclusion

1) By introducing the quantitative evaluation method of drilling engineering risk, and based on the principle of "avoiding risks and reducing the cost of pressure control", a method for determining the matching formation interval for MPD under the "conventional + MPD" composite drilling method is proposed. On the premise of ensuring safety, it can reduce the well section of pressure control construction as much as possible, and optimize the casing layer, which provides a scientific basis for the accurate calculation of pressure control formation interval and the optimization design of well structure under the "conventional + MPD" composite drilling method.
2) By introducing the artificial bee colony algorithm, the intelligent determination method of casing layer and setting depth under MPD is established, which can quickly and accurately obtain the maximum casing setting depth and its corresponding optimal pressure control parameters of the open-hole section, and improve the scientificity, accuracy and efficiency of casing layer and depth under MPD.
3) The example calculation shows that if the conventional drilling method is adopted for well A, it can be safely drilled to the target layer, but the whole well needs five spuds. If the "upper conventional + lower MPD" drilling method is adopted, one layer of casing can be saved while ensuring safety. Through the analysis of the method established in this paper, the discrimination basis is provided for the selection of the MPD technique in complex formations, and theoretical support is provided for the determination of the applicable formation interval.

Data availability statement

The original contributions presented in the study are included in the article/Supplementary Material, further inquiries can be directed to the corresponding author.

Author contributions

All authors have contributed to the creation of this manuscript for important intellectual content and read and approved the final manuscript.

Conflict of interest

The authors declare that the research was conducted in the absence of any commercial or financial relationships that could be construed as a potential conflict of interest.

Publisher's note

All claims expressed in this article are solely those of the authors and do not necessarily represent those of their affiliated organizations, or those of the publisher, the editors and the reviewers. Any product that may be evaluated in this article, or claim that may be made by its manufacturer, is not guaranteed or endorsed by the publisher.

References

1. Jiang Z, Zhou Y, Wang Q. Managed pressure drilling system used in narrow density window drilling scenarios. *Nat Gas Industry* (2011) 31(08):76–9.

2. Krivolapov DS, Magda AV, Soroka TB, Dobrokhleb PY, Evdokimo SA, Gagloyev GG, et al. Managed pressure drilling as an advanced solution for deep hthp wells and long intervals with narrow safe pressure limits. In: SPE Annual Caspian Technical Conference; October 21–22, 2020 (2020).

3. Zein J, Irawan F, Hidayat AM, Amin RA, Norani B, Redzuan M, et al. Case study-constant bottom hole pressure of managed-pressure drilling utilization to maintain wellbore instability in east java drilling operation, Indonesia. In: SPE Asia Pacific Oil & Gas Conference and Exhibition; October 25–27, 2016; Perth, Australia (2016).

4. Siddiqi FA, Riskiawan A, Al-Yami A, Jain B, Louati I, Martanto R, et al. Successful managed pressure cementing with hydraulic simulations verification in a narrow pore-frac pressure window using managed pressure drilling in Saudi Arabia. In: SPE Annual Technical Conference and Exhibition; September 26–28, 2016; Dubai, UAE (2016).

5. Kazakbayeva Z, Kaidarov A, Magda A, Aliyev F, Patil H, Cook I, et al. Successful implementation of managed pressure drilling and managed pressure cementing techniques in fractured carbonate formation prone to total lost circulation in far north region. In: SPE Eastern Europe Subsurface Conference; November 23–24, 2021; Kyiv, Ukraine (2021).

6. Wang J, Li J, Liu G, Huang T, Yang H. Parameters optimization in deepwater dual-gradient drilling based on downhole separation. *Pet Exploration Develop* (2019) 46(4):819–25. doi:10.1016/s1876-3804(19)60240-5

7. Yan L, Wu H, Yan Y. Application of precise MPD in kick & loss well. *Nat Gas Industry* (2015) 35(2):59–63. doi:10.3787/j.issn.1000-0976.2015.02.009

8. Wang G. MPD wellbore pressure control method based on linear throttle Valve. *Oil Drilling Prod Tech* (2021) 43(2):197–202.

9. Huang Y, Yang J, Shi S. Application of MPD technology in offshore ultra-HTHP wells. *Oil Drilling Prod Tech* (2018) 40(6):699–705.

10. Mashaal MA, Fuller T, Brown CJ, Paterson R. Managed pressure drilling, casing and cementing enables success in conventionally undrillable wells in the harding field. In: SPE Annual Technical Conference and Exhibition; September 30–October 2, 2013; New Orleans, Louisiana, USA (2013).

11. Wang G, Liu J, Ding C, Fan H. Casing program optimization with the managed pressure drilling technique. *Acta Petrolei Sinica* (2013) 34(03):545–9. doi:10.7623/syxb201303019

12. Nguyen TC, de Oliveira R, Al-Safran E, Saasen A. Casing-design optimization with CAML technique and drilling-fluid performance. *SPE Drilling & Completion* (2017) 32(03):208–12. doi:10.2118/185951-pa

13. Xu Y. *Design method of controlled pressure drilling body structure*. East China: China University of Petroleum (2012).

14. Yan L, Wu H, Yan Y. Application of fine managed pressure drilling technique in complex wells with both blowout and lost circulation risks. *Nat Gas Industry B* (2015) 2(2-3):192–7. doi:10.1016/j.ngib.2015.07.010

15. Ke K, Guan Z, Zhou X. An approach to determining pre-drilling formation pore pressure with credibility for deep water exploration wells. *J China Univ Pet (Edition Nat Sciences)* (2009) 33(5):61–7.

16. Sheng YN, Guan ZC, Xu YQ. Quantitative description method for uncertainty of formation pore pressure. *Arab J Sci Eng* (2018) 43(5):2605–13. doi:10.1007/s13369-017-2863-x

17. Guan Z, Ke K, Lu B. An approach to casing program design with formation pressure uncertainties. *J China Univ Pet (Edition Nat Sciences)* (2009) 33(4):71–5.

18. Han C, Guan Z, Xu C, Lai F, Li P. Study on method of determining the safe operation window of drilling fluid density with credibility in deep igneous rock strata. *Math Probl Eng* (2021) 2021:11. doi:10.1155/2021/5514427

19. Ataga E, Ogbonna J. Accurate estimation of equivalent circulating density during high pressure high temperature (HPHT) drilling operations. In: Nigeria Annual International Conference and Exhibition; August 6–8, 2012; Lagos, Nigeria (2012).

20. Ashena R, Bahreini H, Ghalambor A, Sahraei E, Darab MAL. Investigation of parameters controlling equivalent circulating density ECD in managed pressure drilling MPD. In: SPE International Conference and Exhibition on Formation Damage Control; February 23–24, 2022; Lafayette, Louisiana, USA (2022).

21. Dokhani V, Ma Y, Yu M. Determination of equivalent circulating density of drilling fluids in deepwater drilling. *J Nat Gas Sci Eng* (2016) 34:1096–105. doi:10.1016/j.jngse.2016.08.009

22. Zhang B, Lu N, Guo Y, Wang Q, Cai M, Lou E. Modeling and analysis of sustained annular pressure and gas accumulation caused by tubing integrity failure in the production process of deep natural gas wells. *J Energ Resour Tech* (2022) 144(6). doi:10.1115/1.4051944

23. Yin Z, Chen G, Xu L, Jiang S. Optimization of casing program of deepwater well by dual-gradient drilling. *Nat Gas Industry* (2006) 26(12):112–4.

24. Liang H, Zou J, Zuo K, Khan MJ. An improved genetic algorithm optimization fuzzy controller applied to the wellhead back pressure control system. *Mech Syst Signal Process* (2020) 142:106708. doi:10.1016/j.ymssp.2020.106708

25. Jia D, Liu H, Zhang J, Gong B, Pei X, Wang Q, et al. Data-driven optimization for fine water injection in a mature oil field. *Pet Exploration Develop* (2020) 47(03):674–82. doi:10.1016/s1876-3804(20)60084-2

26. Karaboga D, Akay B. A comparative study of Artificial Bee Colony algorithm. *Appl Math Comput* (2009) 214(1):108–32. doi:10.1016/j.amc.2009.03.090

27. Karaboga D, Basturk B. A powerful and efficient algorithm for numerical function optimization: artificial bee colony (ABC) algorithm. *J Glob Optim* (2007) 39(3):459–71. doi:10.1007/s10898-007-9149-x

28. Karaboga D, Basturk B. On the performance of artificial bee colony (ABC) algorithm. *Appl soft Comput* (2008) 8(1):687–97. doi:10.1016/j.asoc.2007.05.007

29. Irani R, Nasimi R. Application of artificial bee colony-based neural network in bottom hole pressure prediction in underbalanced drilling. *J Pet Sci Eng* (2011) 78(1):6–12. doi:10.1016/j.petrol.2011.05.006

30. Liao Q, Zhang D. Probabilistic collocation method for strongly nonlinear problems: 3. Transform by time. *Water Resour Res* (2016) 52(3):2366–75. doi:10.1002/2015wr017724

Glossary

K_i is the control pressure parameteris each controlled pressure parameter under a combined scheme

K_L is the lower limit of pressure control parameters

K_H is the upper limit of controlled pressure parameters

ECD $(H)_j$ is the wellbore ECD under the condition of the jth combination scheme of control pressure parameters is the wellbore ECD under the condition of the jth combination of controlled pressure parameters, which is the function of well depth H

j is the order number of the combined scheme of control pressure parameters, $j = 1,2,\ldots$

K_i is the control pressure parameteris each controlled pressure parameter under a combined scheme

D is the dimension of the problem

X_{maxj} **and** X_{minj} represent the upper and lower top bounds of the jth dimension parameters respectively

ECD $(H)_j$ is the wellbore ECD under the condition of the jth combination scheme of control pressure parametersis the wellbore ECD under the condition of the jth combination of controlled pressure parameters, which is the function of well depth H

j0 is the order number of the pressure control parameter scheme corresponding to the maximum casing setting depth

X_{ij} refers to the jth dimension parameter of the ith individual bee, that is, the jth parameter value of the ith combination scheme of the pressure control parameter

X_{kj} refers to the jth dimension parameter of the kth individual bee, that is, the jth parameter value of the kth combination scheme of the pressure control parameters

V_{ij} is a new position generated near X_{ij}

φ_{ij} is the random number between [−1,1]

$fitness_i$ is the fitness value of the ith solution

P_i is the probability of follow-bees choosing lead-bees

ρ_d is static drilling fluid density, g/cm^3

$P_{wellhead}$ is the wellhead back pressure, MPa

frontiers | Frontiers in Physics

TYPE Brief Research Report
PUBLISHED 19 September 2022
DOI 10.3389/fphy.2022.1014842

OPEN ACCESS

EDITED BY
Weiqi Fu,
China University of Mining and Technology, China

REVIEWED BY
Keju Yan,
Texas Tech University, United States
Jun Yang,
Changzhou University, China

*CORRESPONDENCE
Bo Zhang,
zhangboupc@126.com
Nu Lu,
lunu@petrochina.com.cn

SPECIALTY SECTION
This article was submitted to Interdisciplinary Physics, a section of the journal Frontiers in Physics

RECEIVED 09 August 2022
ACCEPTED 24 August 2022
PUBLISHED 19 September 2022

CITATION
Zhang B, Zheng Y, Deng J, Lu N, Cao L, Wang Q and Luo L (2022), Modeling analysis of the temperature profile and trapped annular pressure induced by thermal-expanded liquid in a deep gas well.
Front. Phys. 10:1014842.
doi: 10.3389/fphy.2022.1014842

Modeling analysis of the temperature profile and trapped annular pressure induced by thermal-expanded liquid in a deep gas well

Bo Zhang[1]*, Yushan Zheng[1], Jinrui Deng[1], Nu Lu[2]*, Lihu Cao[3], Qing Wang[4] and Lihong Luo[5]

[1]CNPC, Research Institute of Safety and Environment Technology, Beijing, China, [2]Research Institute of Petroleum Exploration and Development, PetroChina, Beijing, China, [3]Research Institute of Oil & Gas Engineering, Tarim Oilfield Company, PetroChina, Korla, China, [4]CNPC Engineering Technology R&D Company Limited, Beijing, China, [5]Bazhou Branch Company of Xibu Drilling Engineering Company Limited, CNPC, Korla, China

The trapped annular pressure (TAP) caused by thermal expansion is one of the serious challenges for the safe production of a deep gas well. Therefore, this article proposes a model to calculate the temperature profile of the deep gas well based on the heat transfer process and the gas properties. With the help of the temperature model, the TAP in the tubing–casing annulus is analyzed according to the annular fluid distribution and the volume consistence law. The results indicate that the temperature inside the tubing string decreases faster under higher bottom hole pressure. When the tubing–casing annulus is totally filled with the annular protection liquid, the TAP continues increasing with the production rate. Considering the high production rate, the TAP is inevitable and high enough to damage the integrity of the deep gas well. The nitrogen gas mitigates the TAP by reducing the annular liquid volume and providing the extra space to accommodate the thermal-expanded annular liquid. A good mitigation performance can be achieved no matter how large the production rate is. The mitigation performance can be divided into the fast-decreasing stage, the efficient control stage, and the stable stage. These three stages occur as the nitrogen gas column length increases. The compression of the nitrogen gas volume plays a major role in the fast decrease stage while the reduction of the annular liquid plays a major role in the stable stage. For the best cost-effectiveness, the nitrogen gas column is recommended in the efficient control stage and should not exceed 15%.

KEYWORDS

deep gas well, temperature distribution, trapped annular pressure, fluid distribution, mitigation performance

1 Introduction

Deep natural gas plays an important role in the worldwide energy supply [1] for its high productivity and rich reserves. However, it is also characterized by extreme high temperature and pressure. Taking the Well Luntan-1 in the Tarim Basin as instance, the bottom hole pressure reaches 132 MPa and the bottom hole temperature reaches 178°C while its depth is 8,882 m. Due to the extreme high pressure, the tubing–casing annulus is usually filled with the protection liquid in order to balance the pressure difference [2], so as to avoid the tubing string burst. As a result, the TAP increase after the deep gas well is put into production even if the well integrity is perfect [3], because the annular protection liquid would be heated by the production gas from the high-temperature reservoir [4].

Although the TAP can be eliminated by releasing the thermal-expanded liquid, the cement or the tubing may also be damaged during the pressure rise and releasing process [5, 6], which would lead to the wellbore leakage [7]. Even worse, the tubing or the casing string may deform under the high TAP, just like the casing string in the Well Pompano A-31 [8] and the tubing string in the steam injection well in Canada [9]. Therefore, it is important to avoid the high TAP by taking some suitable control measures. Since the TAP is caucused by the wellbore temperature change, it is the foundation for the TAP control optimization to calculate the wellbore temperature. The available research studies have proved that engineering backgrounds have significant impacts on the calculation of the wellbore temperature [10]. For example, A.R.Hasan and Kabir [11] proposed a dimensionless formation temperature to describe the heat transfer between the wellbore and the formation. Wang et al. [12] calculated the wellbore temperature under the lost circulation. Wang et al. [13] built a model to calculate the deep-water well temperature during the cement operation based on the hydration reaction.

With regard to the deep gas well, the pressure and the temperature are so high that the gas properties would certainly be influenced, which would in turn have an impact on the wellbore temperature. Therefore, the temperature calculation of the deep gas well must consider the coupling relationship between the gas properties, temperature, and pressure. Otherwise, the TAP control may fail the expected goal.

Aiming to get the most optimizing control of the TAP, the various measures have been studied, including the thermal insulation [14], the release of the thermal-expanded liquid, and the increase of annular fluid compressibility [15]. Considering the cost and the operational difficulties, nitrogen gas is regarded as one of the most suitable measures to mitigate the TAP, because it is easy to obtain and not so expensive. More importantly, its control performance has been verified by both theory and experiment. Some classical and recent studies are as follows. Vargo et al. [16] analyzed the control law of the TAP by experiments. A water-based fluid and an oil-based fluid are selected to compare the mitigation performances by injecting the nitrogen gas. The results showed the different changing laws while both had good performances. Sun et al. [17] built a model to calculate the TAP when both gas and liquid exist in the casing annulus of the deep-water well. He showed that the injection volume of the nitrogen gas is one of the key parameters for the successful control. Up until now, nitrogen gas has been applied to control the TAP in the deepwater wells [17] and gas storage wells [18]. However, few researchers study the nitrogen gas applied in the deep gas well to mitigate the TAP in the tubing–casing annulus.

Therefore, this article aims to calculate the temperature profile of the deep gas well. Then, a method is provided to analyze the mitigation performance of the TAP by injection nitrogen gas. To improve the accuracy, the calculation considers the coupling relationship among the temperature, the pressure, and the gas properties. Not only that, the gas compression and the heat transfer are also taken into account to analyze the mitigation performance of the TAP, thus helping to achieve a reliable control performance and prevent well integrity failure, which can provide some support for the long-term safe production of the deep gas well.

2 Methods

2.1 The temperature profile in the tubing string of a deep gas well

2.1.1 Heat transfer of tubing string

The tubing string is the pathway for the high-temperature natural gas flowing from the deep reservoir to the ground. Therefore, the heat transfers from the tubing string to the formation during the production process due to the temperature difference between the natural gas and the nearby formation. To describe the aforementioned process by a mathematical model, the tubing string is divided into many micro units with the length of dz. The aforementioned process conforms to the energy conservation law and the momentum conservation law in a single micro unit, as expressed by Eq. 1:

$$\begin{cases} \dfrac{\mathrm{d}p}{\mathrm{d}z} + \rho_{\mathrm{f}} g \sin\theta + f\dfrac{\rho_{\mathrm{f}} v_{\mathrm{f}}^2}{2d_{\mathrm{tn}}} + \rho v_{\mathrm{f}} \dfrac{\mathrm{d}v_{\mathrm{f}}}{\mathrm{d}z} = 0 \\ C_{\mathrm{f}} \dfrac{\mathrm{d}T_{\mathrm{f}}}{\mathrm{d}z} + v_{\mathrm{f}} \dfrac{\mathrm{d}v_{\mathrm{f}}}{\mathrm{d}z} + \dfrac{1}{\rho_{\mathrm{f}}} \dfrac{\mathrm{d}p}{\mathrm{d}z} + g \sin\theta + \dfrac{1}{\omega_{\mathrm{f}}} \dfrac{\mathrm{d}Q}{\mathrm{d}z} = 0 \end{cases} \tag{1}$$

where p is the pressure, Pa; z is the length of the production string, m; ρ_{f} is the density of the natural gas inside the micro unit, kg/m^3; g is the gravity acceleration speed, m/s^2; θ is the well inclination, °; f is the friction factor between the natural gas and the tubing wall, dimensionless; v_{f} is the flow velocity of the natural gas inside the micro unit, m/s; d_{tn} is the tubing inner diameter, m; C_{f} is the specific gas capacity of the natural gas

inside the micro unit, J/(kgK); T_f is the temperature of the natural gas inside the micro unit, K; w_f is the gas mass flow rate, kg/s; Q is the heat flow rate along the wellbore radial direction, J/s.

The friction factor is determined by the flow conditions [19] and fluid rheological properties [20]. It is a key to calculate the pressure drop [21] and can be expressed by Eq. 2 [11]:

$$\begin{cases} f^{-0.5} = -2\log\left[\dfrac{Ra}{3.715d_{tn}} + \left(\dfrac{6.943}{\mathrm{Re}}\right)^{0.9}\right] \\ \mathrm{Re} = \dfrac{\rho_f v_f d_{tn}}{\mu} \end{cases} \tag{2}$$

where R_a is the roughness of the tubing wall, m; Re is the Reynolds number, dimensionless; and μ is the gas viscosity, Pa s.

The heat flow rate along the wellbore radial direction is expressed by Eq. 3:

$$\mathrm{d}Q = \frac{T_f - T_h}{R_{to}}\mathrm{d}z \tag{3}$$

where T_h is the temperature of the wellbore outer boundary, K; R_{to} is the heat resistance from the tubing to the wellbore outer boundary, mK/W.

The heat continues transferring to the formation after the heat transfers from the tubing to the wellbore outer boundary, which is an unsteady heat transfer in a cylindrical coordinate system, as expressed by Eq. 4:

$$\frac{1}{r}\frac{\partial}{\partial r}\left(r\frac{\partial T_e}{\partial r}\right) = \frac{1}{a_e}\frac{\partial T_e}{\partial t} \tag{4}$$

where r is the distance from the wellbore center to the formation, m; T_e is the formation temperature, K; α_e is the formation thermal diffusion coefficient, m^2/s; and t is the time, s.

As a differential equation, Eq. 4 can be turned into an equation about the formation temperature by the Laplace transformation with the specific boundary conditions, but the temperature is still difficult to calculate either by the analytic method or the numerical integration. Therefore, the dimensionless formation temperature is introduced to simplify the engineering calculation, which is fitting by the data of the analytic result and has been widely applied in petroleum engineering [22], as expressed by Eq. 5:

$$\mathrm{d}Q_{rf} = \frac{2\pi\lambda e(T_h - T_e)}{T_D}\mathrm{d}z \tag{5}$$

where λ_e is the formation of thermal conductivity, W/(m·°C); T_D is the dimensionless formation temperature, dimensionless.

The dimensionless temperature can be calculated by Eq. 6:

$$T_D = \begin{cases} 1.1281\sqrt{t_D}\left(1 - 0.3\sqrt{t_D}\right) t_D \le 1.5 \\ (0.4063 + 0.5\ln t_D)(1 + 0.6/t_D) t_D > 1.5 \end{cases} \tag{6}$$

$$tD = \frac{t\alpha e}{rw^2}$$

where t_D is the dimensionless time, dimensionless; r_w is the well radius, m。

2.1.2 Impact of temperature and pressure on gas properties

The gas PVT law indicates that both temperature and pressure have an impact on the gas density, as expressed by Eq. 7:

$$\rho_f = \frac{p_f M_g}{Z_g R T_f} \tag{7}$$

The gas compression factor is also related to temperature and pressure, which can be expressed by Eq. 8 [23]:

$$\begin{cases} Z_g = 1 + \left(0.31506 - \dfrac{1.0467}{T_{pr}} - \dfrac{1.0467}{T_{pr}^3}\right)\rho_{pr} + \left(0.5353 - \dfrac{0.6123}{T_{pr}} + \dfrac{0.6815}{T_{pr}^2}\right)\rho_{pr}^2 \\ \rho_{pr} = 0.27 p_{pr}/\left(Z_g T_{pr}\right) \\ T_{pr} = T/\left(92.2 + 176.7\gamma_g\right) \\ p_{pr} = p/\left(4.778 - 0.248\gamma_g\right) \end{cases} \tag{8}$$

where p_{pr} is the pseudo-reduced pressure, dimensionless; T_{pr} is the pseudo-reduced temperature, dimensionless; γ_g is the relative density of the production gas, dimensionless.

Following this, the gas-flow velocity can be obtained according to the mass conservation law, as expressed by Eq. 9:

$$\frac{\mathrm{d}v_f}{\mathrm{d}z} = -\frac{v_f}{\rho_f}\frac{\mathrm{d}\rho_f}{\mathrm{d}z} \tag{9}$$

The gas viscosity can be calculated by using the Satlan formula [24], as expressed by Eq. 10

$$\frac{\mu}{\mu_0} = \left(\frac{T_f}{T_0}\right)^{1.5}\frac{T_0 + B}{T_f + B} \tag{10}$$

where μ_0 is the gas viscosity, Pa s; T_0 is the temperature, K; and B is a constant, dimensionless.

2.1.3 Solution method and flow chart

Because of the coupling relationship stated in the aforementioned section, it is hard to get the temperature inside the tubing string directly. To solve this problem, the temperature and the pressure inside the single micro unit can be seen as stable when the length of the micro unit is short enough compared with the depth of the deep gas well. And then, the pressure can be expressed by Eq. 11:

$$p_f^i(t) = p_f^{i-1}(t) - \left(\rho_f^i g\sin\theta + f^i\frac{\rho_f\left(v_f^i\right)^2}{2d_{tn}}\right)\Delta z - \rho_f^i v_f^i \Delta v_f^i \tag{11}$$

$$\Delta v_f^i = \frac{v_f^i}{\rho_f^i}\frac{\rho_f^i - \rho_f^{i-1}}{\Delta z}$$

where i is the number of the micro unit, dimensionless; $\triangle z$ is the length of the micro unit, dimensionless; and T_{es} is the initial formation temperature, K.

Likewise, the temperature of the gas inside the tubing string can be obtained in the same way, as expressed by Eq. 12:

$$T_f^i(t) = \frac{1}{A+\Delta z}\left(AT_f^{i-1}(t) + \Delta z T_e^i + A\Delta z f^i \frac{(v_f^i)^2}{C_f d_{tn}}\right) \quad (12)$$

$$A = \frac{w_f C_f [T_D + 2\pi\lambda_e R_{to}^i]}{2\pi\lambda_e}$$

Where, A is a calculation parameter.

Both Eq. 11 and Eq. 12 should be calculated from the well-bottom to the well-head. The initial conditions are expressed by Eq. 13:

$$\begin{cases} T_f^0 = T_{fb} \\ p_f^0 = p_{fb} \end{cases} \quad (13)$$

where T_{fb} is the wellbottom temperature, K; p_{fb} is the bottom hole pressure, Pa.

The solving process has five steps. The first step is to start the calculation. The second step is to calculate the temperature and the pressure of the ith micro unit by using the gas properties in the i-1st micro unit. The third step is to recalculate the gas properties by using the temperature and the pressure in the ith micro unit. The forth step is to recalculate the temperature and the pressure in the ith micro unit by using the gas properties obtained in the second step. Following the aforementioned steps, the temperature and the pressure errors are compared. If the errors are acceptable, the calculation is continued to the i+1st micro unit. Otherwise, the calculation is back to the second step until the error is acceptable. The errors are determined by the values obtained from the second step and the forth step, as expressed by Eq. 14:

$$\begin{cases} E1 = |T_{f2} - T_{f4}|/T_{f2} \\ E2 = |p_{f2} - p_{f4}|/p_{f2} \\ EA = 0.01 \end{cases} \quad (14)$$

where $E1$ is the error of the temperature, dimensionless; $E2$ is the error of the pressure, dimensionless; T_{f2} is the temperature obtained from the second step, K; T_{f4} is the temperature obtained from the fourth step, K; p_{f2} is the temperature obtained from the second step, Pa; p_{f4} is the temperature obtained from the fourth step, Pa; and EA is the acceptable error, dimensionless.

2.2 The TAP caused by the thermal expansion

2.2.1 Calculation of the TAP

The wellbore temperature would redistribute due to the heat transfer during the production process. As a result, the temperature of the annular liquid increases and the TAP increases due to the thermal expansion of the annular fluid. The volume consistence law can explain the basic mechanism of the TAP [25, 26]. The trapped annulus has very limited volume to accommodate all of the thermal-expanded annular liquid, so the pressure increases to compress the annular liquid in order to keep the volumes of the trapped annulus and the annular liquid equal. As analyzed previously, the TAP is a function about the annular temperature, the annulus volume, and the annular liquid [27], as expressed by Eq. 15:

$$\Delta p_a = \left(\frac{\partial p_a}{\partial T_a}\right)\Delta T_a + \left(\frac{\partial p_a}{\partial V_a}\right)\Delta V_a + \left(\frac{\partial p_a}{\partial m}\right)\Delta m \quad (15)$$

According to the definitions of the annular liquid isobaric expansion coefficient and the isothermal compressibility, Eq. 15 can be turned into Eq. 16:

$$\Delta p_a = \frac{\alpha}{k_T}\Delta T_a - \frac{\Delta V_a}{k_T \cdot V_f} + \frac{\Delta V_f}{k_T \cdot V_f} \quad (16)$$

where Δp_a is the TAP, MPa; α is the annular liquid isobaric expansion coefficient, K^{-1}; k_T is the isothermal compressibility, MPa^{-1};ΔT_a is the increase of annular temperature, K; ΔV_a is the volume change of the trapped annulus, m^3; V_f is the volume of the annular liquid, m^3; V_a is the volume of the trapped annulus, m^3; and ΔV_f is the volume of the liquid flowing in or out the annulus, m^3.

It can be known that the temperature change of the annular liquid is indispensable to get the TAP. The temperature of the annular liquid can be calculated based on the wellbore radial heat conservation law and the radial heat-resistance distribution, as expressed by Eq. 17:

$$T_a^i = \frac{T_f^i(1+T_D) + 2\pi\lambda_e T_e^i (R_{to}^i - R_{zro}^i)}{T_D + 2\pi\lambda_e R_{to}^i} \quad (17)$$

where $T_a{}^i$ is the temperature of the ith annulus, K; R_{zro} is the thermal resistance of the ith annulus to the wellbore outer boundary, mK/W.

The annular liquid has exchanged the heat adequately with the formation before production, so its initial temperature can be regarded as the formation temperature. As a result, the temperature change of the annular liquid can be calculated by Eq. 18:

$$\Delta T_a^i = T_a^i - T_e^i \quad (18)$$

The average temperature change of the annular liquid can be obtained by Eq. 19:

$$\Delta T_a = \sum \Delta T_a^i / NI \quad (19)$$

where NI is the number of the annulus segment, dimensionless.

TABLE 1 Calculation parameters of the case well.

	Pipe string	Pipe and wellbore diameter/mm	Wall thickness/mm	Setting depth/m
Casing Program	Casing	508.00/660.40	12.70	508.0
	Casing	365.13/444.50	13.88	1800.0
	Casing	282.58/333.40	18.64	5758.0
	Casing	201.70/241.30	15.12	6684.0
	Liner	139.70/171.50	12.09	6242.9–6887.0
	Tubing	114.30/	12.70	1174.2
		114.30/	9.65	6186.0
		88.90/	6.45	Reservoir
Thermal Parameters	**Parameter**	**Value**	**Parameter**	**Value**
	Formation thermal diffusion coefficient	11.7×10^{-7} m^2/s	Formation density	2.35 g/cm^3
	Heat capacity of production gas	2310 J/ (kg·K)	Thermal conductivity of formation	5.1 W/(m·K)
	Thermal conductivity of annular liquid	0.61 W/(m·K)	Tubing inner wall toughness	1.6×10^{-5} m
	Thermal conductivity of production gas	0.025W/(m·K)	Relative density of production gas	0.75
	Gas adiabatic index	1.29	Viscosity of production gas	1.55×10^{-6} Pa s
	Annular liquid isobaric expansion coefficient	0.00013 K^{-1}	Annular liquid isothermal compressibility	0.00040 MPa^{-1}
	Thermal conductivity of cement	0.52 W/(m·K)	Thermal conductivity of casing and tubing	50.5 W/(m·K)
	Formation heat capacity	895 J/ (kg·K)	Length of well segment	1 m

2.2.2 Mitigation of the TAP

Different from the sustained annular pressure (TAP) caused by wellbore leakage, the TAP would not rebuild after taking some effective measures, so the server risk caused by the high TAP can be avoided. As stated in the introduction, the nitrogen gas has the great potential to mitigate the TAP. Moreover, nitrogen gas is more feasible to be injected into the deep gas well compared with the deepwater well with the subsea wellhead [28]. After injection, the nitrogen gas gathers as a column above the annular liquid column. To get a clear understanding of the injection volume, the relative length is defined to describe the injection volume of the nitrogen gas. The injection volume can be calculated by multiplying the length to the area of the trapped annulus, as expressed by Eq. 20:

$$L_{ND} = \frac{L_N}{L_A}\% \tag{20}$$

Where, L_{ND} is the relative length, %; L_N is the length of the nitrogen gas column, m; and L_A is the length of the tubing-casing annulus, m.

The nitrogen gas works in two aspects to mitigate the TAP. First is to decrease the volume of the annular liquid. The volume of the annular liquid is equal to the trapped annulus volume when the annulus is fully filled with the annular liquid, as expressed by Eq. 21. The injection of the nitrogen gas changes this situation by sharing the part volume of the trapped annulus, as expressed by Eq. 22. Accordingly, the expansion of the annular liquid is not large as before.

$$V_f = V_a \tag{21}$$

$$V_f = V_a - L_{ND} \times L_A \times A_a \tag{22}$$

Secondly, the nitrogen gas is easy to compress by the high pressure, so some extra space is available to accommodate the thermal-expanded annular liquid, which is called the volume compensation effect [26], as expressed by Eqs. 23, 24. As a result, the pressure need not necessary be so high to compress the annular liquid.

$$\Delta V_N = L_{ND} \times L_A \times A_a \left[1 - \frac{p_s T_c}{(\Delta p_a + p_s) T_s}\right] \tag{23}$$

$$\Delta V_f = -\Delta V_N \tag{24}$$

where, A_a is the area of the annulus cross section, m^2; p_s is the initial pressure imposed on the nitrogen gas, MPa; T_s is the initial temperature of the nitrogen gas, K; and T_c is the temperature of the nitrogen gas, K.

3 Results

A deep gas well with a depth of 6,850 m is selected as the case well. Its casing program is shown in Table 1 and the cement is back to the wellhead. The packer is in the depth of 6,680 m. The

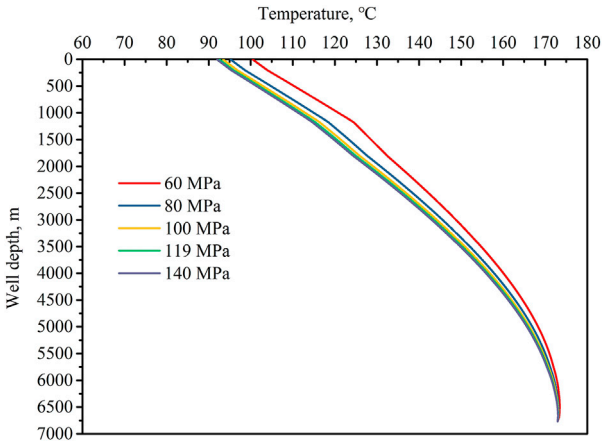

FIGURE 1
The temperature profiles of the production string under different pressures.

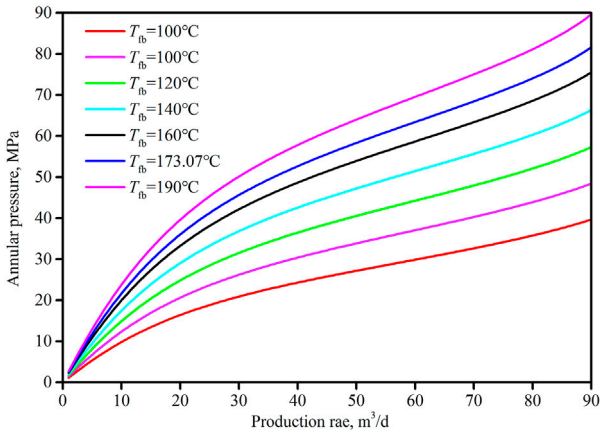

FIGURE 2
The changing law of the TAP as the production rate under different wellbottom temperatures.

wellbottom temperature is 173.07°C and the production rate is set as 40 × 10^4 m^3/d. The other parameters are shown in Table 1.

3.1 Results of the temperature profile

Figure 1 is the temperature inside the tubing string under different values of the bottom hole pressure. It can be seen that the temperature decreases from the wellbottom to the wellhead because of the heat transfer in the well's radial direction. Through the comparison of the temperature curves, it can be found that the temperature decreases faster under higher bottom hole pressure. For

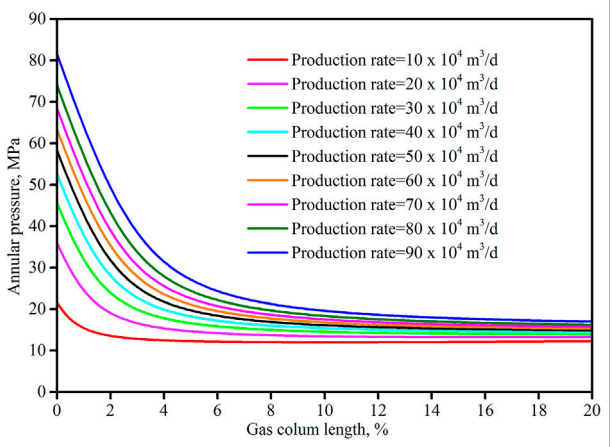

FIGURE 3
The changing law of annular pressure with the nitrogen gas column length under different production rates.

example, the wellhead temperature is 92.58°C when the bottom hole pressure is 119 MPa, while the wellhead temperature becomes 100.50°C when the bottom hole pressureis 60 MPa. This indicates that the coupling relationship dose exist between the temperature and the pressure. According to the volume consistence law, the temperature change and the trapped annular liquid are two essential conditions for the TAP. The temperature profiles shown in Figure 2 are all higher than the original formation temperature profile. With the existence of the annular protection liquid, the deep gas well obviously satisfies the basic conditions to generate the TAP.

3.2 Analysis of the TAP

Figure 2 is the TAP-changing law with the production rate when the tubing–casing annulus is totally filled with the annular protection liquid. The TAP increases as the production rate increases, because larger production rate can bring more heat to the annular liquid. The curves also show that the annular pressure increases faster under higher wellbottom temperature. Considering the high temperature and high production rate of the deep gas well, the high TAP is inevitable when the tubing–casing annulus is totally filled with the annular protection liquid. In Figure 3, the TAP can be as high as 81.61 MPa when the wellbottom temperature is 173.09°C and will increase to 89.66 MPa when the wellbottom temperature is 190°C. Such high annular pressures would certainly damage the well's safety barriers, like the casing, the tubing, the cement, the packers, and the wellhead [29, 30]. As a result, wellbore leakage may happen and finally bring about the SAP [31]. This would make the management of the deep gas well more complex and more difficult, even the abandonment of the expensive gas well.

3.3 Mitigation performance

The mitigation performance of nitrogen gas can be obtained by substituting Eq. 20 and Eq. 22 into Eq. 15. The results are shown in Figure 3. It can be seen that the TAP decreases as the nitrogen gas column length increases, but the decreasing speed becomes more and more slow. Taking the curve under 90×10^4 m^3/d as an example, the TAP is reduced from 81.61 MPa to 27.10 MPa when the nitrogen gas column length increases from zero to 5 %, while the decrease of the TAP is only 0.77 MPa (from 17.75 MPa to 16.98 MPa) when the nitrogen gas column length increases from 15 % to 20 %. This trend is consistent with the experimental results of Zhou et al. [32] and Wang et al. [33]. Their experiments indicated that the TAP decreases sharply when the nitrogen gas column length is within 5 % and seems stable when the nitrogen gas column length is close to 20 %. This shows that the nitrogen gas can achieve a good mitigation performance under different production rates of the deep gas well, but the nitrogen gas column length should be further analyzed.

According to the shape of the curves in Figure 3, the mitigation performance can be divided into the fast-decreasing stage, the efficient control stage, and the stable stage. In the fast-decreasing stage, the compression of the nitrogen gas volume plays a major role, but the TAP is still high and exceeds the mitigation goal. In the efficient stage, the compression of the nitrogen gas still plays the major role while the reduction of the annular liquid also starts working. The TAP is in a reasonable range in this stage although the decreasing speed is slower. In the stable stage, the TAP even seems unchanged when the nitrogen gas column length is long enough. In this stage, the reduction of the annular liquid plays a major role.

One thing to be noted that there is no universal division criteria for the three stages because the criteria may be different under different conditions. Commonly speaking and according to Figure 3, the nitrogen gas length is less than 3 % in the fast-decreasing stage and the nitrogen gas length is over 10 % in the stable stage. To get the most efficient mitigation performance, it is better to keep the mitigation performance in the efficient stage. The nitrogen gas column should not be over 15 %, or the mitigation performance can be improved very little.

4 Conclusion

1) A mode is established to calculate the temperature profile of the deep gas well by considering the coupling relationship among the temperature, pressure, and gas properties. The case well shows that the temperature decreases faster under higher bottom hole pressure, so the impact of the pressure on the temperature should not be ignored in the deep gas well. Comparing the temperature profiles and the original formation temperature profile, the deep gas well satisfies the basic conditions to generate the TAP.
2) The temperature change and the trapped annular liquid are two essential conditions for the TAP. When the tubing–casing annulus is totally filled with the annular protection liquid, the TAP increases as the production rate increases and increases faster under a higher wellbottom temperature. Considering the high production rate of the deep gas well, the TAP is inevitable and high enough to damage the integrity of the well's safety barriers without the suitable control measures, which can lead to the SAP in the deep gas well and make the situation more complex.
3) The nitrogen gas mitigates the TAP by reducing the annular liquid volume and providing the extra space to accommodate the thermal-expanded annular liquid. Based on the mitigation mechanism, a model is built to analyze the mitigation performance. The results show that the nitrogen gas can achieve a good mitigation performance under different production rates.
4) The mitigation performance can be divided into the fast-decreasing stage, the efficient control stage, and the stable stage. The compression of the nitrogen gas volume plays a major role in the fast-decreasing stage while the reduction of the annular liquid plays a major role in the stable stage. There are no universal division criteria for the three stages because of the different conditions. To get the most efficient mitigation performance, it is better to keep the mitigation performance in the efficient stage, and the nitrogen gas column should not be over 15 %.

Data availability statement

The original contributions presented in the study are included in the article/supplementary material; further inquiries can be directed to the corresponding authors.

Author contributions

BZ: Formal analysis, Writing-original draft preparation, Writing-review and editing, Funding acquisition; YZ: Formal analysis, Writing-original draft preparation; JZ: Methodology, Conceptualization; NL: Methodology, Conceptualization, Project administration, Supervision; LC: Data analysis; QW: Drawing figures, Funding acquisition; LL: Formal analysis.

Funding

This research is supported by CNPC Forward-looking Basic Strategic Technology Research Projects (2021DJ6504, 2021DJ6502, 2021DJ6501 and 2021DJ4902). The funder was

not involved in the study design, collection, analysis, interpretation of data, the writing of this article, or the decision to submit it for publication.

Conflict of interest

Authors BZ, YZ, and JD were employed by Research Institute of Safety and Environment Technology, CNPC. Author NL was employed by Research Institute of Petroleum Exploration and Development, PetroChina. Author LC was employed by Research Institute of Oil & Gas Engineering, Tarim Oilfield Company Petrochina. Author LL was employed by Bazhou Branch Company of Xibu Drilling Engineering Company Limited, CNPC. Author QW was employed by CNPC Engineering Technology R&D Company Limited, Beijing, China.

Publisher's note

All claims expressed in this article are solely those of the authors and do not necessarily represent those of their affiliated organizations, or those of the publisher, the editors, and the reviewers. Any product that may be evaluated in this article, or claim that may be made by its manufacturer, is not guaranteed or endorsed by the publisher.

References

1. Ge L, Cui H, Li Y, Sui X. Optimization and performance evaluation of foam discharge agent for deep aquatic condensate gas well. *Front Phys* (2022) 350. doi:10.3389/fphy.2022.887036

2. Maiti S, Gupta H, Vyas A, Kulkarni SD. Evaluating precision of annular pressure buildup (APB) estimation using machine-learning tools. *SPE Drill Compl* (2022) 37(01):93–103. doi:10.2118/196179-pa

3. Ai S, Cheng L, Huang S, Liu H, Zhang J, Fu L. A critical production model for deep HT/HP gas wells. *J Nat Gas Sci Eng* (2015) 22:132–40. doi:10.1016/j.jngse.2014.11.025

4. Zhang B, Xu Z, Lu N, Liu H, Liu J, Hu Z, et al. Characteristics of sustained annular pressure and fluid distribution in high pressure and high temperature gas wells considering multiple leakage of tubing string. *J Pet Sci Eng* (2021) 196:108083. doi:10.1016/j.petrol.2020.108083

5. Teodoriu C, Kosinowski C, Amani M, Schubert J, Shadravan A. Wellbore integrity and cement failure at HPHT conditions. *Int J Eng* (2013) 2(2):2305–8269.

6. Shadravan A, Schubert J, Amani M, Teodoriu C. Using fatigue-failure envelope for cement-sheath-integrity evaluation. *SPE Drill Compl* (2014) 30(01):68–75. doi:10.2118/168321-pa

7. Zhang B, Guan Z, Lu N, Hasan AR, Xu S, Zhang Z, et al. Control and analysis of sustained casing pressure caused by cement sealed integrity failure. OTC 28500. In: Offshore Technology Conference Asia held in Kuala Lumpur. Malaysia: Offshore Technology Conference (2018).

8. Pattillo PD, Cocales BW, Morey SC. Analysis of an annular pressure buildup failure during drill ahead. *SPE Drill Compl* (2006) 21(04):242–7. doi:10.2118/89775-pa

9. Brown J, Kenny N, Slagmulder Y. Unique cement design to mitigate trapped annular pressure TAP between two casing strings in steam injection wells. In: SPE Heavy Oil Conference and Exhibition. Kuwait: Society of Petroleum Engineers (2016). doi:10.2118/184102-MS

10. Fu W, Chen B, Zhang K, Liu J, Sun X, Huang B, et al. Rheological behavior of hydrate slurry with xanthan gum and carboxmethylcellulose under high shear rate conditions. *Energy Fuels* (2022) 36(6):3169–83. doi:10.1021/acs.energyfuels.1c04359

11. Hasan AR, Kabir CS. Wellbore heat-transfer modeling and applications. *J Pet Sci Eng* (2012) 86:127–36. doi:10.1016/j.petrol.2012.03.021

12. Wang J, Li J, Liu G, Song X. Development of a wellbore heat transfer model considering circulation loss. *Arab J Geosci* (2020) 13(2):85–12. doi:10.1007/s12517-020-5055-z

13. Wang X, Sun B, Liu S, Li Z, Liu Z, Wang Z, et al. A coupled model of temperature and pressure based on hydration kinetics during well cementing in deep water. *Pet Exploration Dev* (2020) 47(4):867–76. doi:10.1016/s1876-3804(20)60102-1

14. Pattillo PD, Bellarby JE, Ross GR, Gosch SW, McLaren GD. Thermal and mechanical considerations for design of insulated tubing. *SPE Drill Compl* (2004) 19(03):181–8. doi:10.2118/79870-pa

15. Zhang B, Guan Z, Lu N, Hasan AR, Wang Q, Xu B. Trapped annular pressure caused by thermal expansion in oil and gas wells: A review of prediction approaches, risk assessment and mitigation strategies. *J Pet Sci Eng* (2019) 172:70–82. doi:10.1016/j.petrol.2018.09.041

16. Vargo RF, Payne M, Faul R, LeBlanc J, Griffith JE. Practical and successful prevention of annular pressure buildup on the Marlin project. *SPE Drill Compl* (2003) 18(03):228–34. doi:10.2118/85113-pa

17. Sun T, Xinquan Z, Shujie L, Yanfeng C, Renjun X. Annular pressure buildup calculation when annulus contains gas. *Chem Technol Fuels Oils* (2018) 54(4):484–92. doi:10.1007/s10553-018-0950-7

18. Jiang M, Tan C, Li J, Cheng X, Li J. Comparisons between protection fluid and nitrogen column in tube-casing annulus of gas storage wells. *Acta Petrolei Sinica* (2017) 38(10):1210–6. doi:10.7623/syxb201710012

19. Fu W, Wang Z, Chen L, Sun B. Experimental investigation of methane hydrate formation in the carboxmethylcellulose (CMC) aqueous solution. *SPE J* (2020) 25(03):1042–56. doi:10.2118/199367-pa

20. Fu W, Wang Z, Zhang J, Cao Y, Sun B. Investigation of rheological properties of methane hydrate slurry with carboxmethylcellulose. *J Pet Sci Eng* (2020) 184:106504. doi:10.1016/j.petrol.2019.106504

21. Fu W, Yu J, Xu Y, Wang C, Huang B, Sun B. A pressure drop prediction model for hydrate slurry based on energy dissipation under laminar flow condition. *SPE J* (2022) 27:2257–67. doi:10.2118/209586-PA

22. Ferreira MV, Hafemann TE, Barbosa JR, da Silva AK, Hasan R. A numerical study on the thermal behavior of wellbores. *SPE Prod Operations* (2017) 32(04):564–74. doi:10.2118/180297-pa

23. Wang Y. *Research of gas liquid mixture flow characteristics through choke and its application*. Master Thesis. Xi'an: Xi'an Petroleum Unversity (2013).

24. Zhang B, Lu N, Guo Y, Wang Q, Cai M, Lou E. Modeling and analysis of sustained annular pressure and gas accumulation caused by tubing integrity failure in the production process of deep natural gas wells. *J Energ Resour Tech* (2022) 144(6):063005. doi:10.1115/1.4051944

25. Liu J, Fan H, Peng Q, Deng S, Kang B, Ren W. Research on the prediction model of annular pressure buildup in subsea wells. *J Nat Gas Sci Eng* (2015) 27:1677–83. doi:10.1016/j.jngse.2015.10.028

26. Zhang B, Xu Z, Guan Z, Li C, Liu H, Xie J, et al. Evaluation and analysis of nitrogen gas injected into deepwater wells to mitigate annular pressure caused by thermal expansion. *J Pet Sci Eng* (2019) 180:231–9. doi:10.1016/j.petrol.2019.05.040

27. Oudeman P, Bacarreza LJ. Field trial results of annular pressure behavior in a high-pressure/high-temperature well. *SPE Drill Compl* (1995) 10(2):84–8. doi:10.2118/26738-pa

28. Da Veiga AP, Martins IO, Barcelos JG, Ferreira MVD, Alves EB, da Silva AK, et al. Predicting thermal expansion pressure buildup in a deepwater oil well with an annulus partially filled with nitrogen. *J Pet Sci Eng* (2022) 208:109275. doi:10.1016/j.petrol.2021.109275

29. De Souza CO, de Sousa JRM, Ellwanger GB. Wellhead axial movements in subsea wells with partially cemented surface casings. *J Pet Sci Eng* (2020) 194:107537. doi:10.1016/j.petrol.2020.107537

30. Kiran R, Teodoriu C, Dadmohammadi Y, Nygaard R, Wood D, Mokhtari M, et al. Identification and evaluation of well integrity and causes of failure of well integrity barriers (A review). *J Nat Gas Sci Eng* (2017) 45:511–26. doi:10.1016/j.jngse.2017.05.009

31. Zhang B, Guan Z, Zhang Q, Han D. Prediction of sustained annular pressure and the pressure control measures for high pressure gas wells. *Pet Exploration Dev* (2015) 42(4):567–72. doi:10.1016/s1876-3804(15)30051-3

32. Zhou B, Yang J, Liu Z, Luo J, Huang X, Zhou R, et al. Mechanism of pressure management by injecting nitrogen in casing annulus of deepwater wells. *Pet Exploration Dev* (2015) 42(3):422–6. doi:10.1016/s1876-3804(15)30034-3

33. Wang L, Gao B, Hu T, Ma C. Design and application of foamed spacer to mitigate annular pressure induced by fluid thermal expansion. *Appl Therm Eng* (2020) 165:114524. doi:10.1016/j.applthermaleng.2019.114524

frontiers | Frontiers in Physics

TYPE Brief Research Report
PUBLISHED 23 September 2022
DOI 10.3389/fphy.2022.1028414

OPEN ACCESS

EDITED BY
Zhiyuan Wang,
China University of Petroleum, Huadong, China

REVIEWED BY
Xiukun Wang,
China University of Petroleum, Beijing, China
Wanju Yuan,
Geological Survey of Canada, Canada

*CORRESPONDENCE
Jun Yang,
yang233j@uregina.ca

SPECIALTY SECTION
This article was submitted to Interdisciplinary Physics, a section of the journal Frontiers in Physics

RECEIVED 26 August 2022
ACCEPTED 06 September 2022
PUBLISHED 23 September 2022

CITATION
Zhao J, He Y and Yang J (2022), Experimental and population balance model interpretation of foam physics in porous media.
Front. Phys. 10:1028414.
doi: 10.3389/fphy.2022.1028414

Experimental and population balance model interpretation of foam physics in porous media

Jing Zhao, Yanfeng He and Jun Yang*

School of Petroleum and Natural Gas Engineering, Changzhou University, Changzhou, Jiangsu, China

Foam has been used as an effective displacing fluid for gas mobility control in enhanced oil recovery (EOR) and subsurface remediation. In this study, a series of core flooding experiments are performed on cores with a wide permeability ranging from 3.3 to 2749 mD to evaluate the impact of foam quality and permeability on foam performance. It is found that the steady-state foam mobility control factor is related to permeability in a non-linear, non-monotonic manner. A full physics, mechanistic foam model is proposed by incorporating a novel flowing foam fraction relation grounded-up from pore-level observations, and a new kinetic expression of foam coalescence rate by oil based on pinch-off foam rupture mechanism into the population-balance framework of Almajid et al. (Advances in Water Resources, 2021, 150: 103877). The proposed model is applied to match foam flow experimental results in the absence and in the presence of oil. Results show that our model captures the high-quality and low-quality foam regimes observed in previous oil-free foam flow experiments. Within the medium permeability range, in the absence of oil, lower gas mobility is observed in the lower permeability core due to faster foam film thinning at higher capillary pressure, while in the presence of residual oil, the difference in foam mobility fades away due to the insignificant impact of capillary pressure on the stability of pseudoemulsion films.

KEYWORDS

foam behavior, enhanced oil recovery, flow regime, population balance model, CO_2 channeling

Abbreviations: k_f^0, foam generation constant; μ_g, gas viscosity; B, bridging coefficient; C_s*, a reference surfactant concentration for strong foam generation; C_s: surfactant concentration; E, entering coefficient; f_g*, critical foam quality; f_g, foam quality; K, absolute permeability of the porous media; n*, limiting foam texture; n_t, trapped foam texture; P_c*, limiting capillary pressure; P_c, capillary pressure; P_{cpf}*, critical rupture capillary pressure of the pseudoemulsion film; P_{cpf}, imposed capillary pressure; r_c, foam coalescence rate; r_{co}, foam coalescence rate by oil; r_g, foam generation rate; S, spreading coefficient; S_{gf}, flowing gas fraction; S_{gt}, trapped gas fraction; w, function type of foam generation; X_f, flowing foam fraction; σ, interfacial tension; φ, porosity.

1 Introduction

The substantial increase in CO_2 emissions due to the increase in fossil fuel energy consumption leads to global climate warming [1, 2]. CO_2 enhanced oil recovery (EOR), a promising technology to promote geological sequestration of CO_2 in oil reservoirs, has gained the spotlight in reducing carbon emissions. However, CO_2-EOR processes often suffer from severe viscous fingering and gas channeling, thereby CO_2 mobility control techniques are required to improve sweep efficiency. Foam fluids have been used for decades to control gas mobility due to its peculiar rheology and low environmental pollution. Understanding foam propagation characterises in porous media is of primary importance for CO_2-EOR processes optimization. Steps have been taken in this direction by previous authors [3–6]. It is recognized that foam mobility is directly dependent on the correlation between foam texture (i.e., number density of foam bubbles per unit volume) and medium permeability. Tsau and Heller [7] performed foam flow experiments with core permeabilities ranging from 30 to 900 mD and found foam mobility presents a linear relationship with core permeability in a log-log coordination. Zhao et al. [8] analyzed the foam flow phenomenology in porous media, including foam preferential flow path, local flow intermittency, and addressed that the correlation between bubble size and local permeability of the medium should be taken into account in large-scale mechanistic model development. However, at this point, most previous studies focused on limited range of permeability (>100 mD), and therefore some notably features of foam flow remain unclear. In this study, we set out to investigate foam behavior within a comprehensive permeability range (i.e., 3.3~2749 mD).

A popular choice of modeling foam propagation in porous media is population balance models (PBM) [9, 13, 14]. Typical foam PBMs tracks foam texture over time and tend to separate gas mobility into the effects of gas trapping and rheology. These models concentrated primarily on predicting transient and steady-state foam flow characteristics in oil-free media. However, foam physics is even more complicated when oil is involved. Previous authors showed that the prevalent classical entering (E), spreading (S), and bridging (B) coefficients Eqs. 1–3 cannot consistently predict the behavior of oil droplets at gas-water interface, thereby cannot accurately predict foam stability in the presence of oil; foam stability is essentially dependent on the stability of pseudoemulsion film (i.e., the asymmetrical aqueous film between oil and gas) [10].

$$E = \sigma_{gw} + \sigma_{ow} - \sigma_{go} \tag{1}$$

$$S = \sigma_{gw} - \sigma_{ow} - \sigma_{go} \tag{2}$$

$$S = \sigma_{gw}^2 + \sigma_{ow}^2 - \sigma_{go}^2 \tag{3}$$

Where σ denotes the interfacial tension, and the subscripts g, w, and o are gas, water, and oil, respectively. In recognition of this, in the pioneering work by Myers and Radke [9], a kinetic expression of the rate of foam coalescence by oil is derived based on the concept of pseudoemulsion film and is incorporated in the general population balance framework to elucidate foam behavior the presence of residual oil. Their model shows that foam is destabilized by oil and foam mobility is lower in higher permeability core whether or not the residual oil is present. In fact, the macroscopic foam flow processes can only be adequately simulated given that the values or functional relations of model parameters, such as flowing foam fraction (i.e., the ratio of flowing gas saturation to total gas saturation), foam generation rate and foam coalescence rate, are known [11]. Although many attempts have been made by previous authors on the modification of flowing foam fraction [12, 13], it is still not fully consistent with the experimental and statistics pore network results. Therefore, another motivation of the present work is to develop a full physics, mechanistic PBM for foam flow in porous media by inserting more meaningful mechanistic expressions for gas mobility and foam coalescence rate caused by oil.

In a summary, a series of core flooding experiments is performed in cores with permeabilities ranging from 3.3 to 2749 mD in the absence and in the presence of residual oil. The impact of foam quality and core permeability on foam mobility are examined. A foam population balance model based on a new flowing foam fraction relation which is more physical to foam flow in porous media, and a new expression of the rate of foam coalescence by oil, is proposed. The proposed model is evaluated by core flooding results in terms of aqueous phase saturation and pressure drop profiles. The results find application to the design of CO_2 foam EOR and environmental remediation.

2 Materials and methods

2.1 Experiment

2.1.1 Materials

The formation water is prepared with distilled water with a total salinity of 26,500 mg/L using sodium, calcium, magnesium and chloride ions. CO_2 with a purity of 99.9% is used to generate foam in core flooding experiments. The surfactant solution is a mixture of 0.5 wt% internal olefin sulfonate (IOS) and 0.5 wt% lauryl betaine (LB) in a 1:1 ratio. The crude oil sample is collected from an oil field in XinJiang province, and is centrifuged at 2000 rpm for 9 h to remove any solids and contaminations. The viscosity and density of crude oil are 10 cP and 0.82 g/cm^3, respectively. Four types of artificial cores are compressed under high pressure using minerals (i.e., quartz, kaolinite, illite, and calacite) with different concentrations. The permeabilities of artificial

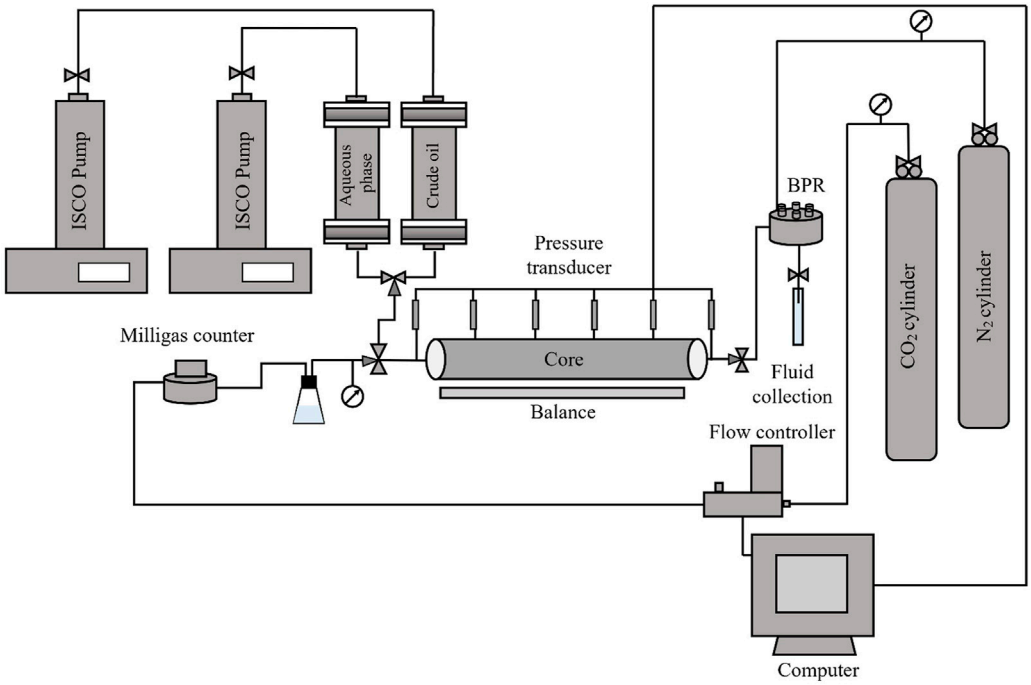

FIGURE 1
Schematic of foam flow experimental setup.

cores are 3.3, 55, 425, 1,580, and 2749 mD, respectively. All cores have a length and diameter of 50.16 and 3.5 cm. In order to avoid moisture, the cores are dried in the oven for 6 h at constant temperature of 110°C and then vacuumed before each test [14].

2.1.2 Experimental procedures

During oil-free foam flow experiments, the core is pre-saturated with brine. Two pore volume (PV) of brine and CO_2 are co-injected into the core using an ISCO 500D syringe pump and a gas mass flow controller (Brooks, United States) at varying flowrates. After that, CO_2 and surfactant solution are injected into the core simultaneously at varying foam qualities ($f_g = (q_g \times 100\%)/(q_g + q_l)$, where q_g and q_l are gas and liquid flowrates, respectively) until the pressure difference across the core reaches a steady-state.

For model validation, the procedures of oil-free foam flow experiments are similar to those stated above, except that CO_2 and surfactant solution are co-injected at a foam quality of 80% from the very beginning. In the presence of oil, the core is pre-saturated with the crude oil. 2 PV of brine is first injected, followed by co-injecting of surfactant solution and CO_2 at a foam quality of 80%. The total injection rate for all experiments is 0.1 cm^3/min, unless otherwise indicated. Six pressure taps are placed evenly (about 10 cm apart) to monitor the pressure evolution along the core sample. A back pressure regulator (BPR) is set at 3.0 MPa to control the pressure at core downstream (Figure 1). All experiments are performed at ambient temperature and pressure (T_{amb} = 22°C, P_{amb} = 1.0 atm).

2.2 Model development

In 1-D porous media, the mass balance of flowing bubble density can be described by [15],

$$\frac{\partial}{\partial t}\left[\varphi\left(S_{gf}n_f + S_{gt}n_t\right)\right] + \nabla.\left(u_g n_f\right) = \phi S_g\left(r_g - r_c\right) + Q_b \quad (4)$$

where S_g is the gas saturation, and subscripts f and t are the flowing and trapped gas, respectively. φ is porosity, u_f is the Darcy velocity, Q_b is a source/sink term of foam bubbles. r_g and r_c denote foam generation rate and foam coalescence rate. The competition of r_g and r_c governs the evolution of foam texture, and hence the mobility control ability of foam. The kinetic expressions of r_g and r_c are given as [1, 26]

$$r_g = k_1^0\left(1 - \left(\frac{n_f}{n^*}\right)^w\right)\bar{v}_w\bar{v}_g^{\frac{1}{3}} \quad (5)$$

where $k_1^0$is a reference foam coalescence rate coefficient, n^* is limiting foam texture and w determines the function type of foam generation. n^* is set at 4×10^{11} m^{-3} and w is kept at three in this study.

$$r_c = k_{-1}^0 \left(\frac{P_c}{P_c^*(C_s) - P_c} \right) \bar{v}_g n_f \tag{6}$$

where k_{-1}^0 is a constant, P_c is capillary pressure and P_c* is limiting capillary pressure. P_c* is governed by surfactant formulation, and can thus be written as [16],

$$P_c^*(C_s) = P_{c,max}^* tanh\left(\frac{C_s}{C_s^*} \right) \tag{7}$$

where C_s is the surfactant concentration, C_s* is a reference surfactant concentration for strong foam generation (C_s* is set at 0.1 wt% throughout this paper), and $P_{c,max}^*$ is the maximum P_c* value.

Phase mobilities are described by the standard Darcy's law,

$$u_i = -\frac{K k_{ri}}{\mu_i} \nabla \left(p_i + \rho_i g z \right) \tag{8}$$

where K is the absolute permeability of the porous media. k_{ri} is the relative permeability to phase $_i$, μ_i, p_i and ρ_i are the viscosity, pressure and density of phase i. g and z denote the gravitational constant and depth.

The gas apparent viscosity (μ_f) is given by,

$$\mu_f = \mu_g + \frac{\alpha n_f}{\bar{v}_g^c} \tag{9}$$

where μ_g is the gas viscosity, α is a constant dependent on the surfactant system. c is a power point exponent close to 1/3.

As indicated by Chen et al. [17], during the flow of a fluid with yield stress (i.e., Bingham fluid), the fraction of pores belonging to the open paths is strongly dependent on the applied pressure gradient. Considering the fact that in the flow of foam in porous media is essentially analogous to that of a Bingham fluid, we borrow from Chen et al. [17], and found a S shape change in flowing foam fraction ($X_f = S_{gf}/S_g$) with pressure gradient [18]. Therefore, instead of following the previous PBMs by reflecting the dependence of X_f on the trapped foam texture i.e., $X_f = 1\text{-}X_t = 1\text{-}X_{t,max}(\beta n_t/(1+\beta n_t))$, where $X_{t,max}$ is the maximum trapped foam, β is a trapping parameter, and n_t is the trapped foam texture, we here applied the equation proposed by Zhao et al. [18] and Tang and Kovseck [19] by showing the dependence of X_f on the applied pressure gradient,

$$X_f = \Psi \left[\frac{\nabla p_g}{n_f K^{\frac{1}{2}}} \right]^b \tag{10}$$

where Ψ is a constant of proportionality, and b is a percolation exponent which equals to 0.4 in this study.

As indicated previously, additional complications arise when oil is involved. In the presence of residual oil, foam stability strongly depends on the stability of pseudoemulsion film. Under this circumstance, oil exists in two forms, i.e., emulsified oil and solubilized oil. It is known that surfactant micelles containing solubilized oil is detrimental to foam film stability [20]. However, considering that the amount of solubilized oil is negligible compared with that of emulsified oil, we here only focus on the impact of emulsified oil. Therefore, foam coalescence rate by oil (r_{co}) is given by [9],

$$r_{co} = k_{-2} S_0 \left(\frac{\epsilon P_{cpf} / P_{cpf}^*}{1 + \epsilon P_{cpf} / P_{cpf}^*} \right) \bar{v}_g n_f \tag{11}$$

where S_o is oil saturation, ϵ is a constant, P_{cpf} denotes imposed capillary pressure, and P_{cpf}* is the critical rupture capillary pressure of the pseudoemulsion film [20].

$$P_{cpf} = P_{cgw}\left(\frac{\sigma_{ow}}{\sigma_{gw} + \sigma_{ow}} \right) + P_{cow}\left(\frac{\sigma_{gw}}{\sigma_{gw} + \sigma_{ow}} \right) \tag{12}$$

where σ_{ow} and σ_{gw} are set as 6 and 31 mN/m u_w and u_g are set 1.0, and 0.018 mPa·s throughout this study.

3 Results and discussions

3.1 Oil-free core flooding experiments

A series of core flooding tests in the absence of oil are performed on the core with the permeability of 55 mD. As seen, a critical foam quality (f_g* = 66.7%) exists in Figure 2A: in the upper left portion where $f_g > f_g$*, the steady-state pressure gradient (∇P_{ss}) is only dependent on the liquid velocity (i.e., high-quality regime), while in the lower right portion where $f_g < f_g$*, ∇P_{ss} is only sensitive to gas velocity (i.e., low-quality regime). This phenomenon agrees well with previous experimental observation of Almajid et al. [1] and Osterloh and Jante [21]. The dots in Figure 2A are acquired from the core flooding experiment. The experiment consists of surfactant solution and CO_2 co-injection at different injection velocities from 0.5 to 2.8 m/day, one of which is kept constant while the other changes for evaluation. Clearly, the agreement obtained between experimental and simulation results is quite good within the range of injection velocities investigated. Figure 2B presents the microscopic images of morphology of the produced foam bubbles produced and the corresponding bubble size distribution histograms at different injection conditions. It is seen that when u_g and u_l of 0.5 and 2.5 m/day (within Region I) are imposed, foam with small average bubble size (≈0.26 mm^2) is generated, while when u_g and u_l of 1.0 and 0.8 m/day (within Region II) are imposed, foam with much larger average bubble size (≈1.08 mm^2) is generated, which further proves that Regions I and II correspond to high-quality foam (or, equivalently, strong foam) and low-quality foam (weak foam), respectively. This result implies that foam mobility control performance is better at a lower liquid but larger gas velocity.

Figure 3A illustrates evolution of pressure difference over the course of core flooding experiments in cores with

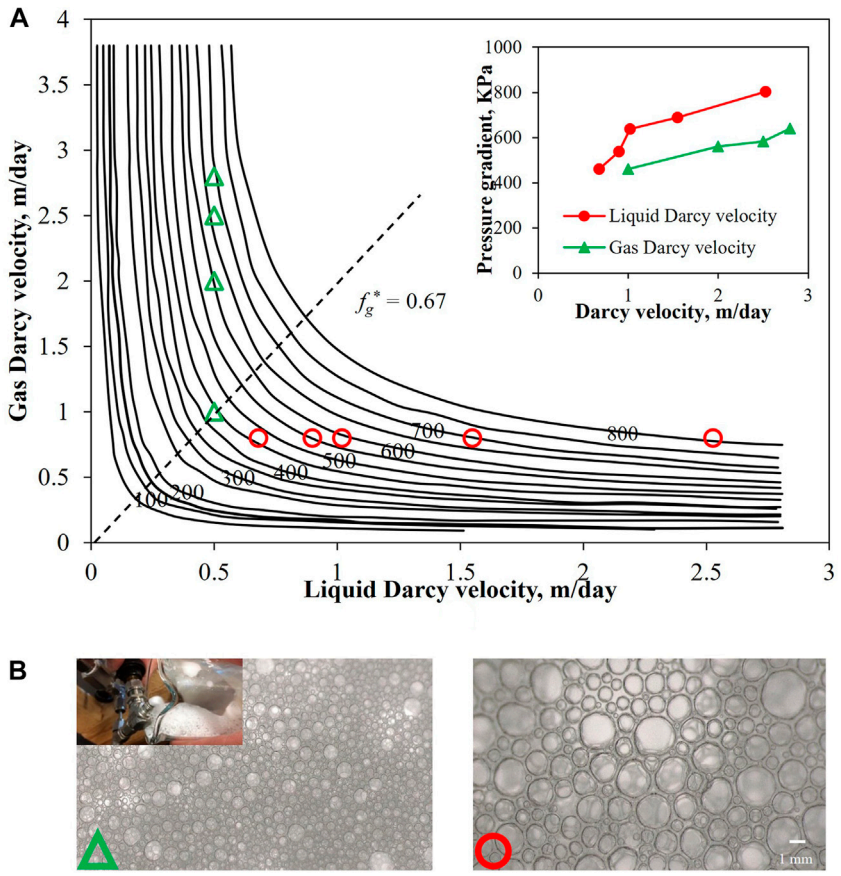

FIGURE 2
(A) Predicted (solid line) and measured (dots) steady-state pressure gradient as a function of gas and liquid Darcy velocities in the core with the permeability of 55 mD. Red dots are measured by varying the liquid velocity from 0.68 to 2.52 m/day at constant gas velocity of 0.8 m/day, and green dots are measured by varying the gas velocity from 1.0 to 1.75 m/day at constant liquid velocity of 0.5 m/day. **(B)** Optical micrographs of foam collected at the outlet of core at gas and liquid velocity of 0.5 and 2.5 m/day (left), 1.0 and 0.8 m/day (right), respectively.

permeabilities of 3.3 and 425 mD. The fluctuating pressure drop is attributed to the oscillatory or chaotic nature of foam flow and the core heterogeneity. It can be seen that in the first stage when CO_2 and brine are co-injected, the incremental in pressure gradient is small, indicating weak blocking effect, while in the second stage when foam is participated, the pressure gradient increases significantly. This phenomenon is attributed to Jamin effect; when foam propagates along the core, foam bubbles deform and produce additional resistance, thereby greater pressure drop is required to initiate and keep foam flowing. Similar trend is observed in the profiles of gas saturation during flooding in cores (Figures 3Bi). During CO_2 and brine co-injection, the gas saturation rises slowly and reaches a plateau value of around 10% for all tests. When foam injection starts, however, the gas saturation increases noticeably due to the formation of strong foam (more effective gas trapping). Meanwhile, it is noted that in the same core, the pressure gradient at the end of foam injection is the highest at f_g = 66.7% (rather than at f_g = 80% which possesses the highest gas fraction). If we look deeper, the complex interplay between flowrate and foam texture determines the blocking effect of foam [2]. Foam texture (the number of foam lamellae per unit volume of gas in porous media) is in fact very low at extremely high f_g (*e.g.*, f_g = 80%). Therefore, an optimal f_g that well balances the relationship between flowrate and foam texture must exist, which is 66.7% in this study. Also, only the pressure difference at f_g = 20% reaches a steady-state, while the rest are unstable by the end of foam injection. A possible explanation is that at f_g = 20% (i.e., weak foam), most of gas is flowing as a continuous phase, and therefore, after initial pressure incremental induced by foam generation, foam lamellae creation and destruction balance with each other within a shorter period of time.

Foam blocking ability is characterized by mobility reduction factor ($MRF = \Delta P_f/\Delta P_{CO2+brine}$, where ΔP_f and

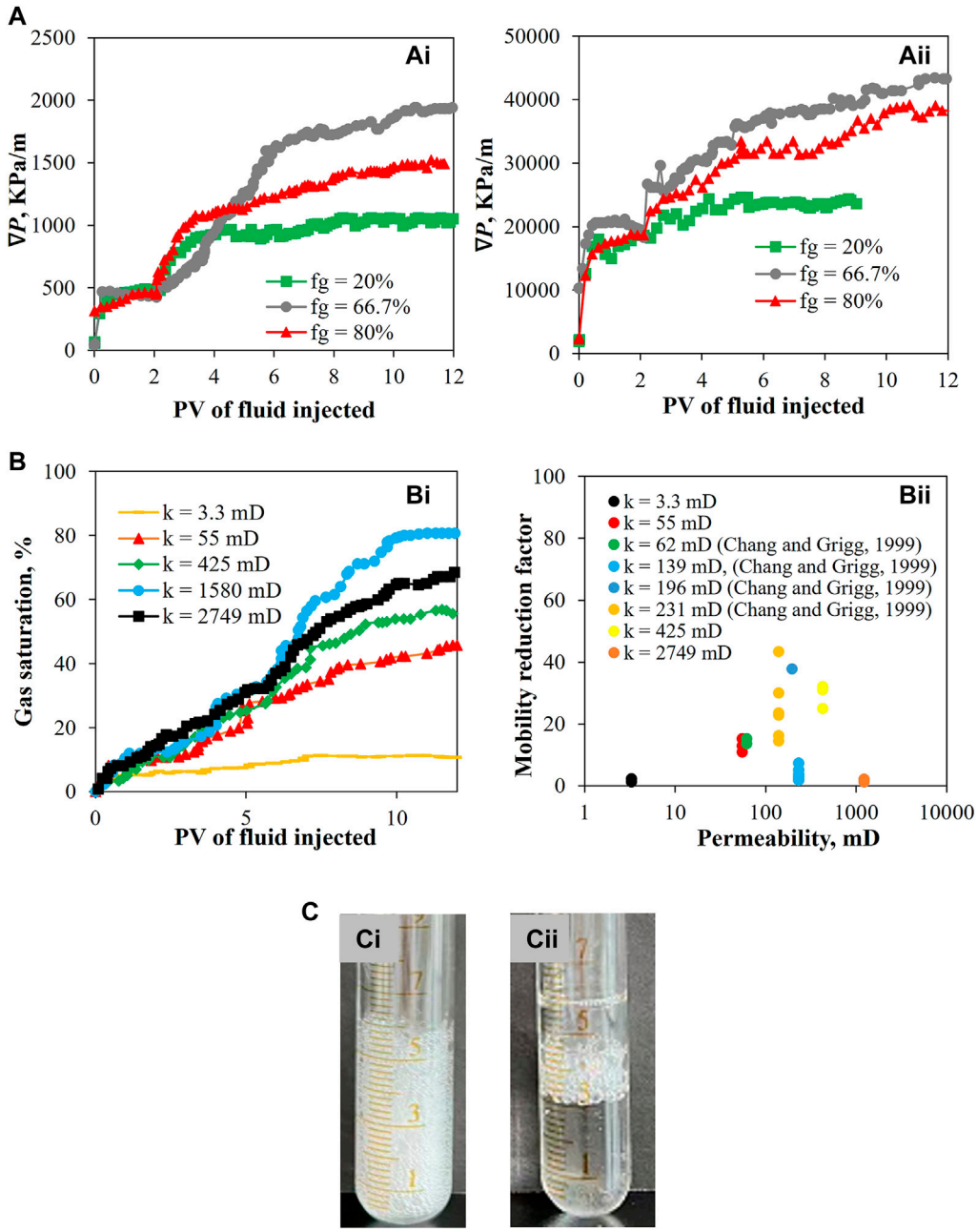

FIGURE 3
(A) Pressure difference evolution over the course of core flooding experiments in cores with permeabilities of **(Ai)** 3.3 mD, and **(Aii)** 425 mD, respectively. **(Bi)** Gas saturation evolution for foam flow experiments with different core permeabilities. **(Bii)** Steady-state mobility reduction factor for foam flow experiments with different core permeabilities obtained in the current work and previous work of Chang and Grigg [24]. **(C)** Foam produced at the outlet of cores with permeability of **(Ci)** 425 mD, and **(Cii)** 2749 mD, respectively.

$\Delta P_{CO2+brine}$ denote the pressure differences along the core during foam flooding and CO_2-brine co-injection) [22]. Figure 3Bii shows the steady-state *MRF* in core permeabilities ranging from 3.3 to 1,580 mD. It is seen that *MRF* demonstrates a nonlinear, non-monotonic function of core permeability, i.e., *MRF* first rises distinctly with permeability in the low-medium permeability range, and then decreases in the high permeability range, which is in consistent with the gas saturation results shown in Figure 3Bi. Foam mobility control ability is essentially related to Jamin effect, and thus to the underlying pore space characteristics. When foam flows along the core whose channels are much

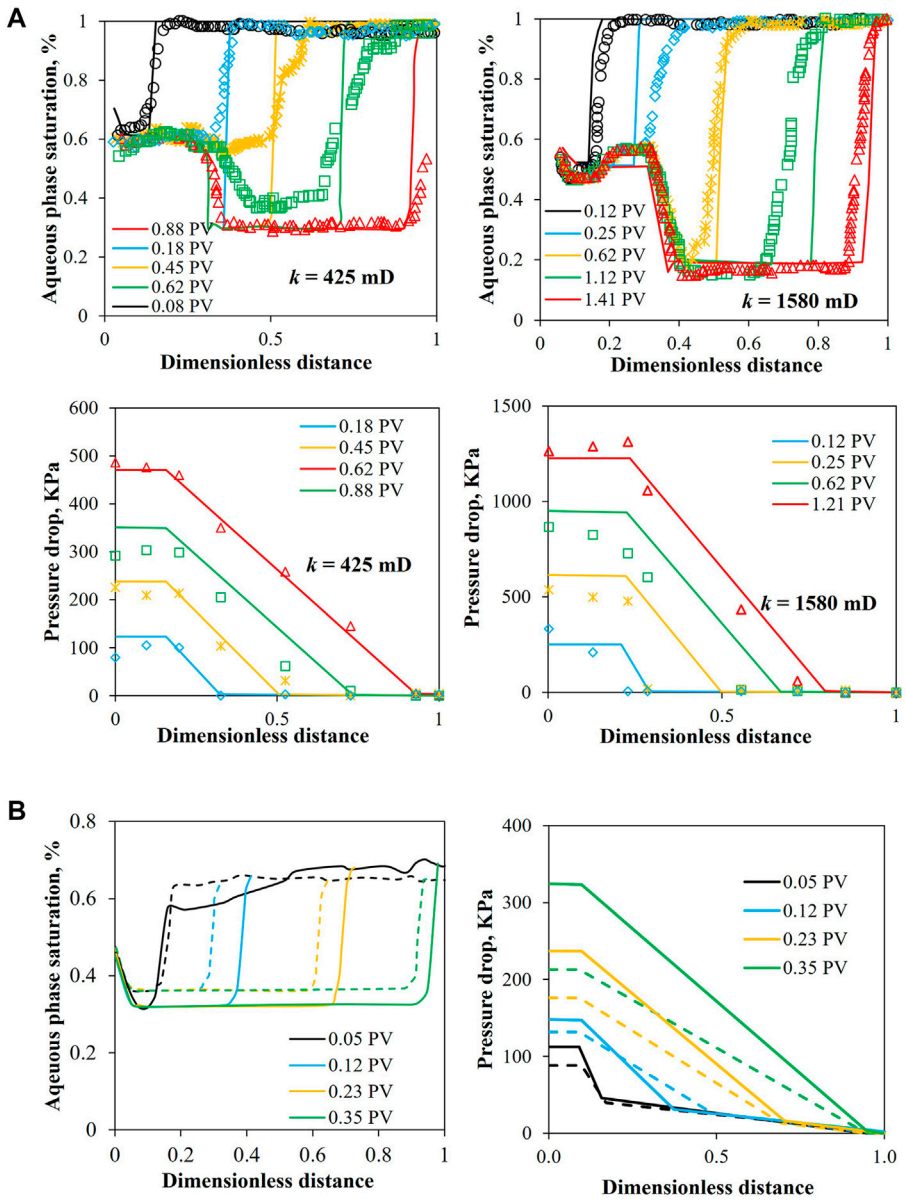

FIGURE 4
(A) Up: measured and predicted aqueous phase saturation profiles for oil-free foam flow in cores with permeabilities of 425 and 1,580 mD. Down: measured and predicted pressure drop profiles for oil-free foam flow in cores with permeabilities of 425 and 1,580 mD. **(B)** Predicted aqueous phase saturation profile and pressure drop profile in cores with permeabilities of 425 (dashed lines) and 1,580 mD (dotted lines) in the presence of residual oil.

smaller than the bubble size (i.e., low permeability cores), foam lamellae are sporadically generated, thereby only a small fraction of gas is trapped [23]. Moreover, the high local capillary pressure in low permeability media accelerates the thinning process of the existing foam lamellae; the gas trapping becomes even less effective, which consequently results in low *MRF* and gas saturation in low core permeability. When foam flows along the core whose channels are larger than the bubble size (i.e., high permeability cores), the flow of foam involves weaker bubble deformation (or, lower pressure difference), and thus foam tends to completely flow through the main channels instead of occupying them, which also results in low *MRF* and gas saturation. High permeability cores possess low pressure condition, and hence the pore space is occupied by enlarged bubbles due to gas compressibility, resulting in

lower gas saturation (Figure 3Bi), This is further proved by the much coarser bubbles collected at the core outlet at k = 2749 mD (Figure 3Cii).

3.2 Foam flow characteristics in the absence and in the presence of residual oil

We simulate the foam flow process in cores with the permeabilities of 425 and 1,580 mD in the absence and in the presence of residual oil, respectively. The parameters used in oil-free cases for lower permeability core (k = 425 mD) are k^o_{rw} = 1.0, k^o_{rg} = 1.0, a = 0.032, k^o_{-1} = 2.0 m^{-1}, k^o_1 = 2.5 × 10$^{-13/3}$ s$^{1/3}$, $P_{c,max}$* = 25.0 kPa, S_{wc} = 0.23; for higher permeability core (k = 1,580 mD) are k^o_{rw} = 1.0, k^o_{rg} = 0.67, a = 0.032, k^o_{-1} = 1.5 m^{-1}, k^o_1 = 2.0 × 10$^{-13/3}$ s$^{1/3}$, $P_{c,max}$* = 25.0 kPa, S_{wc} = 0.30. In the presence of residual oil, the parameters used for lower permeability core are k^o_{rw} = 0.54, k^o_{rg} = 1.0, a = 0.032, k^o_{-1} = 0.15 m^{-1}, k^o_{-2} = 35.0 m^{-1}, ϵ = 5.0, P_{cpf}* = 1.1 kPa, S_{wc} = 0.28; for higher permeability core are k^o_{rw} = 0.82, k^o_{rg} = 0.05, a = 0.032, k^o_{-1} = 0.5 m^{-1}, k^o_{-2} = 105.0 m^{-1}, ϵ = 5.0, P_{cpf}* = 1.1 kPa, S_{wc} = 0.31. The gas and liquid injection rates are 0.08 and 0.02 cm^3/min (f_g = 80%) for all tests.

Figure 4A shows the measured and simulated aqueous phase saturation (S_w) and pressure drop (ΔP) profiles. It is seen that in both cores, the gas phase initially advances through the core quickly, leading to the drainage of a considerable amount of liquid. A dramatic decrease in S_w is observed when the front arrives at a dimensionless distance of approximately 0.3, indicating the generation of strong foam; the generation of strong foam accompanies with more trapped gas in pore space, significantly reduced gas mobility, and more liquid displaced from additional pores. The model indeed predicts slightly slower front advancement. This may be attributed to the viscous instabilities or gas override, which are not accounted for in the present model. It is worthwhile noticing that in Myers and Radke's [9] model, the simulated aqueous phase saturation in the entrance region is normally underestimated due to the overprediction of foam bubble density. However, as pointed by Chen et al. [25], the entry length for net foam generation is approximately 12 cm, indicating that strong foam has not been generated in the entrance region; very small amount of gas is trapped in the core at the initial stage of displacement. Our model successfully captures this feature and predict the location where strong foam starts to form.

Figure 4B shows the simulated aqueous phase saturation and pressure drop profiles during foam flooding after 2 PV of brine injection. The residual oil saturations after brine injection are similar (~40% OOIP) for both cores. It is seen that the aqueous phase saturation profiles in the presence of oil are in general less sharper than those in the absence of oil, demonstrating less efficient water displacement. The pressure drop in the lower permeability core (k = 425 mD) is obviously lower than that in the higher core (k = 1,580 mD), while in the absence of oil, on the contrary, the pressure drop in two cores is similar. In the absence of oil, the pressure drop depends on the stability of individual foam films; larger capillary pressure in lower permeability core results in faster foam film thinning, coarser foam texture, and consequently in lower pressure drop. In the presence of oil, the pressure drop depends on the stability of individual pseudoemulsion films. An additional parameter, foam coalescence rate due to oil Eq. 11 is included in the PBM of Almajid et al. [1] to signify pseudoemulsion film stability [25–27]. The properties of surfactant solution and oil used here result in positive E and S coefficients, and hence in a P_{cpf}/P_{cpf}* value larger than one; the vast majority of pseudoemulsion films already rupture under this condition. Therefore, capillary pressure has insignificant impact on pseudoemulsion film stability, leading to similar pressure drop.

4 Conclusion

1) In the absence of oil, two distinct foam flow regimes: High-quality and low-quality regimes, are observed. At the core permeability of 55 mD, the critical foam quality (f_g*) at which the transition of foam regime occurs is around 66.7%. Foam mobility in porous media is non-monotonically related to core permeability: At low-medium permeability range, foam mobility increases with permeability, while at high permeability range, foam mobility decreases significantly with permeability.

2) A mechanistic, full-physics foam population balance model is proposed based on a new flowing foam fraction and a kinetic expression of foam coalescence due to oil. In the absence of oil, agreement between experiment and simulation in cores with permeabilities of 425 and 1,580 mD is satisfactory in terms of aqueous phase saturation and pressure drop profiles. The small discrepancies are probability attributed to the ignorance of viscous instabilities in the current model. The location where strong foam starts to generate is at the dimensionless distance of approximately 0.3 for both cores.

3) In the absence of residual oil, the pressure drop is lower in lower permeability core due to the faster foam film thinning under higher capillary pressure. In the presence of residual oil, the pressure drop in both cores is similar. A possible explanation is that majority of pseudoemulsion films already rupture within the permeability range investigated, thereby the impact of capillary pressure on foam film rupture is insignificant.

Data availability statement

The original contributions presented in the study are included in the article/supplementary material, further inquiries can be directed to the corresponding author.

Author contributions

JZ: Formal analysis, Writing-original draft preparation, Writing-review and editing, Funding, JY: Methodology, Conceptualization, Drawing figures, YH: Methodology, Conceptualization, Project administration, Supervision, Funding acquisition.

Funding

The authors declare that this research is supported by National Natural Science Foundation of China (No. 52004038).

Conflict of interest

The authors declare that the research was conducted in the absence of any commercial or financial relationships that could be construed as a potential conflict of interest.

Publisher's note

All claims expressed in this article are solely those of the authors and do not necessarily represent those of their affiliated organizations, or those of the publisher, the editors and the reviewers. Any product that may be evaluated in this article, or claim that may be made by its manufacturer, is not guaranteed or endorsed by the publisher.

References

1. Almajid MM, Wong ZY, Kovscek AR. Mechanistic foam flow model with variable flowing foam fraction and its implementation using automatic differentiation. *Adv Water Resour* (2021) 150:103877. doi:10.1016/j.advwatres.2021.103877

2. Géraud B, Jones SA, Cantat I, Dollet B, Méheust Y. The flow of a foam in a two-dimensional porous medium. *Water Resour Res* (2016) 52:773–90. doi:10.1002/2015wr017936

3. Zhang K, Li S, Liu L. Optimized foam-assisted CO2 enhanced oil recovery technology in tight oil reservoirs. *Fuel* (2020) 267:117099. doi:10.1016/j.fuel.2020.117099

4. Fu WQ, Yu J, Xu YH, Wang CL, Huang BX, Sun BJ. A pressure drop prediction model for hydrate slurry based on energy dissipation under laminar flow condition. *SPE J* (2022) 27(04):2257–67. doi:10.2118/209586-pa

5. Fu WQ, Chen BG, Zhang KB, Liu J, Sun XH, Huang BX, et al. Rheological behavior of hydrate slurry with xanthan gum and carboxmethylcellulose under high shear rate conditions. *Energy Fuels* (2022) 36(6):3169–83. doi:10.1021/acs.energyfuels.1c04359

6. Zhao J, Torabi F, Yang J. The role of emulsification and IFT reduction in recovering heavy oil during alkaline-surfactant-assisted CO2 foam flooding: An experimental study. *Fuel* (2022) 313:122942. doi:10.1016/j.fuel.2021.122942

7. Zhang B, Lu N, Guo Y, Wang Q, Cai M, Lou E. Modeling and analysis of sustained annular pressure and gas accumulation caused by tubing integrity failure in the production process of deep natural gas wells. *J Energ Resour Tech* (2022) 144(06):063005. doi:10.1115/1.4051944

8. Zhao J, Torabi F, Yang J. The synergistic role of silica nanoparticle and anionic surfactant on the static and dynamic CO2 foam stability for enhanced heavy oil recovery: An experimental study. *Fuel* (2021) 287:119443. doi:10.1016/j.fuel.2020.119443

9. Myers TJ, Radke CJ. Transient foam displacement in the presence of residual oil: Experiment and simulation using a population-balance model. *Ind Eng Chem Res* (2000) 39(8):2725–41. doi:10.1021/ie990909u

10. Mensire R, Lorenceau E. Stable oil-laden foams: Formation and evolution. *Adv Colloid Interf Sci* (2017) 247:465–76. doi:10.1016/j.cis.2017.07.027

11. Kharabaf H, Yortsos YC. Pore network model for foam formation and propagation in porous media. *SPE J* (1998) 3(01):42–53. doi:10.2118/36663-pa

12. Kovscek AR, Patzek TW, Radke CJ. A mechanistic population balance model for transient and steady-state foam flow in Boise sandstone. *Chem Eng Sci* (1995) 50(23):3783–99. doi:10.1016/0009-2509(95)00199-f

13. Kovscek AR, Chen Q, Gerritsen M. Modeling foam displacement with the local-equilibrium approxima- tion: Theory and experimental verification. *SPE J* (2010) 15(01):171–83.

14. Fu WQ, Yu J, Xiao Y, Wang CL, Huang BX, Sun B. A pressure drop prediction model for hydrate slurry based on energy dissipation under turbulent flow condition. *Fuel* (2022) 311(2022):12218. doi:10.1016/j.fuel.2021.122188

15. Aziz K, Settari A. *Petroleum reservoir simulation*. London: Applied Science Publishers (1979).

16. Aronson AS, Bergeron V, Fagan ME, Radke CJ. The influence of disjoining pressure on foam stability and flow in porous media. *Colloids Surf A: Physicochemical Eng Aspects* (1994) 83(2):109–20. doi:10.1016/0927-7757(94)80094-4

17. Chen M, Rossen W, Yortsos YC. The flow and displacement in porous media of fluids with yield stress. *Chem Eng Sci* (2005) 60(15):4183–202. doi:10.1016/j.ces.2005.02.054

18. Zhao J, Torabi F, Yang J. Role of viscous forces in foam flow in porous media at the pore level. *Ind Eng Chem Res* (2021) 60(7):3156–73. doi:10.1021/acs.iecr.0c05735

19. Tang G-Q, Kovscek AR. Trapped gas fraction during steady-state foam flow. *Transp Porous Med* (2006) 65(2):287–307. doi:10.1007/s11242-005-6093-4

20. Myers TJ. *The role of residual oil in the mechanistic simulation of foam flow in porous media: Experiment and simulation with the population-balance method*. Berkeley, CA: Ph.D. Dissertation, University of California (1999).

21. Oolman T, Godard ST, Pope GA, Jin M, Kirchner K. DNAPL flow behavior in a contaminated aquifer: Evaluation of field data. *Groundwater Monit Remediation* (1995) 15(4):125–37. doi:10.1111/j.1745-6592.1995.tb00560.x

22. Zhao J, Torabi F. Experimental investigation and modelling of CO_2 -foam flow in heavy oil systems. *Can J Chem Eng* (2019) 98(1):147–57. doi:10.1002/cjce.23573

23. Conn CA, Ma K, Hirasaki GJ, Biswal SL. Visualizing oil displacement with foam in a microfluidic device with permeability contrast. *Lab Chip* (2014) 14(20):3968–77. doi:10.1039/c4lc00620h

24. Chang S-H, Grigg RB. Effects of foam quality and flow rate on CO2-foam behavior at reservoir temperature and pressure. *SPE Reservoir Eval Eng* (1999) 2(3):248–54. doi:10.2118/56856-pa

25. Chen Q, Gerritsen M, Kovscek AR. Modeling foam displacement with the local-equilibrium approximation: Theory and experimental verification. *SPE J* (2010) 15(01):171–83. doi:10.2118/116735-pa

26. Denkov ND. Mechanisms of foam destruction by oil-based antifoams. *Langmuir* (2004) 20(22):9463–505. doi:10.1021/la049676o

27. Fu WQ, Wang ZY*, Zhang JB, Cao YY, Sun BJ. Investigation of rheological properties of methane hydrate slurry with carboxmethylcellulose. *J Pet Sci Eng* (2020) 184:106504. doi:10.1016/j.petrol.2019.106504

frontiers | Frontiers in Physics

TYPE Original Research
PUBLISHED 07 October 2022
DOI 10.3389/fphy.2022.1028671

OPEN ACCESS

EDITED BY
Weiqi Fu,
China University of Mining and Technology, China

REVIEWED BY
Yuanhang Chen,
Louisiana State University, United States
Bingbing Chen,
Dalian University of Technology, China

*CORRESPONDENCE
Baojiang Sun,
sunbj1128@vip.126.com

SPECIALTY SECTION
This article was submitted to Interdisciplinary Physics, a section of the journal Frontiers in Physics

RECEIVED 26 August 2022
ACCEPTED 20 September 2022
PUBLISHED 07 October 2022

CITATION
He H, Sun B, Sun X, Li X and Shan Z (2022), Study on flow characteristics of natural gas containing CO_2 invading wellbore during drilling.
Front. Phys. 10:1028671.
doi: 10.3389/fphy.2022.1028671

Study on flow characteristics of natural gas containing CO_2 invading wellbore during drilling

Haikang He[1], Baojiang Sun[1]*, Xiaohui Sun[1], Xuefeng Li[1] and Zhengfeng Shan[2]

[1]School of Petroleum Engineering, China University of Petroleum (East China), Qingdao, China, [2]Drilling Division of China Petroleum Offshore Engineering Co., Ltd., Beijing, China

The dissolution of invaded gas in the drilling fluid during drilling results in an increase in the gas invasion concealment. This is of great significance for the development of acid gas reservoirs to determine the solubility change and multiphase flow law in an annulus after invasion by natural gas with high CO_2 content. In this study, control equations of gas–liquid flow during drilling gas invasion are established considering the influence of gas solubility. For the prediction of gas solubility, the interaction parameters of CH_4 and water in the Peng–Robinson equation of state are optimised to establish a gas solubility prediction model. The solubility of natural gas with high CO_2 content in water and brine solution is measured through phase-equilibrium experiments. The results indicate that the newly optimised solubility model can accurately predict the solubility of CH_4 and CO_2 in water, and the prediction error is within 5%. Moreover, the prediction error for the solubility of CH_4 and CO_2 mixed gas is within 15%. The analysis of gas invasion in example engineering drilling applications reveals that an increase in the CO_2 content in the invaded gas leads to a slow change in the mud-pit increment, and the concealment strengthens as the distance between the gas-migration front and the wellhead increases. Gas solubility has a significant impact on the monitoring of gas invasion in low permeability reservoirs.

KEYWORDS

solubility, CO_2, gas invasion, multiphase flow, gas volume fraction

1 Introduction

The Liwan 3-1 gas field in China, with CH_4 content exceeding 80% and CO_2 content exceeding 3%, is a type of acidic gas field [1–7]. Romania, Mexico, and Indonesia have gas reservoirs with high CO_2 content, that is, the CO_2 concentration in the reservoir fluid is as high as 86% [8–10], and the CO_2 content in the natural gas produced at the Tugu Barat oilfield in Indonesia is as high as 76 mol% [11]. During the drilling and development of natural gas fields containing CO_2, formation fluid invasion can easily occur. A high amount of invaded gas dissolution in the drilling fluid makes it difficult to monitor the ground and increases the blowout risk. Several studies have focused on the law of gas dissolution in multiphase flow. For example, Yin et al. (2017) established an annular

multiphase transient flow model based on gas–liquid two-phase flow and flash theory, considering the dissolution of gas in an oil-based drilling fluid. The dissolution of gas led to a slow change of mud pit, and the mud pit increment associated with the oil-based drilling fluid was smaller than that of the water-based drilling fluid [12]. Sun et al. (2018) considered the phase change and dissolution of the acidic natural mixture in a drilling fluid and proposed a flow-transition criterion for multiphase flow. When the invading gas rises in a vertical wellbore, the gas phase change causes large volume expansion and increases the blowout risk. However, they focused on the gas phase state analysis and did not consider the gas dissolution effect [13]. Xu et al. (2018) used the standing bubble point formula to calculate the solubility of gas in oil. Neglecting the gas dissolution effect, the bottom-hole temperature was overestimated by 3.74°C, and the bottom-hole pressure increased by 2.92 MPa [14].

The O'Bryan formula [15] is widely used to predict the solubility of gas in an oil-based drilling fluid. A water-based drilling fluid system is mainly composed of water and salt; therefore, the solubility of water-based drilling fluids is typically studied using water and salt water. Wiebe and Gaddy (1939), Briones et al. (1987), and Sabirzyanov et al. (2003) conducted a large number of experimental studies on the solubility of CO_2 gas in water [16–18]. It was found that the temperature could be as high as 373.15 K and the pressure could reach 70 MPa. However, studies on the solubility of a mixture of CH_4 and CO_2 in water and salt water remain limited. Dhima (1999) measured the solubility of CO_2 + CH_4 mixture in water at 344.5 K and 10–100 MPa [19]. Subsequently, Qin et al. (2008), Ghafri (2014), and Loring et al. (2017) obtained the vapour–liquid equilibrium data for the CO_2 + CH_4 + H_2O ternary system at 323.15–423.15 K and 1–20 MPa [20–22]. Zirrahi et al. [23] recalculated the mutual parameters between gases in the Peng–Robinson equation of state (PR-EOS) [24] using existing experimental data for mixed gas solubility. The prediction deviation of the solubility of the acidic mixed gas in water was less than 5%; however, the applicability must be evaluated based on the adjustment of the fitting parameters of the experimental data. Ziabakhsh-Ganji and Kooi [25] improved the state equation to establish a gas solubility prediction model. Although the model could accurately predict the solubility of single gas in water and brine, the prediction accuracy of the solubility of mixed gases remains unknown. Li [26] predicted the phase equilibrium of CO_2–CH_4–H_2S–brine using fugacity-fugacity and fugacity-activity models and found that the fugacity-activity model was more accurate in predicting the solubility of CO_2 + CH_4 mixed gas.

Research on the effect of gas dissolution on multiphase flow has focused on oil-based drilling fluids, and water-based drilling fluids have typically been neglected because of the low solubility of gases in water. Furthermore, the accuracy and applicability of existing prediction models are insufficient for determining the water solubility of a mixed gas containing CO_2. Therefore, according to the characteristics of deep-water drilling, a gas–liquid two-phase flow control model incorporating the gas dissolution effect was established in this study. To realise accurate prediction and analysis of gas solubility, the interaction parameters of CH_4 and water in the PR-EOS were optimised to establish a gas solubility prediction model. The finite difference method was used to solve the proposed multiphase flow model. The influence of gas solubility on gas phase flow law during gas invasion was analysed using an example to provide guidance for the control safety of field wells.

2 Gas–liquid control model

2.1 Gas–liquid two-phase flow equation

According to the law of mass conservation, a physical model of continuity, momentum, and energy was established by considering the dissolution of gas in a drilling fluid based on the following assumptions.

1) The flow in the wellbore is one-dimensional.
2) The dissolution of gas in the drilling fluid is completed instantaneously.
3) The compressibility change of drilling fluid is negligible.
4) The influence of rock debris can be neglected.

The continuity equation for the free gas phase can be expressed as follows:

$$\frac{\partial}{\partial t}\left(\rho_g E_g A\right) + \frac{\partial}{\partial z}\left(\rho_g u_g E_g A\right) = q_g - m_{g\text{-}L} \tag{1}$$

where $m_{g\text{-}L}$ is the mass transfer rate from gas phase to liquid phase [kg/(m s)], which can be expressed as

$$\frac{\partial}{\partial t}\left(\rho_{sg} R_{sm} E_m A\right) + \frac{\partial}{\partial z}\left(\rho_{sg} R_{sm} u_m E_m A\right) = m_{g\text{-}L} \tag{2}$$

The mass conservation of the liquid phase can be expressed as

$$\frac{\partial}{\partial t}\left(A\rho_m E_m\right) + \frac{\partial}{\partial z}\left(A\rho_m u_m E_m\right) = m_{g\text{-}L} \tag{3}$$

Considering the slippage of the gas–liquid phase, the momentum equation of the gas–liquid phase can be expressed as

$$\begin{aligned}&\frac{\partial}{\partial t}\left(A\rho_g u_g E_g + A\rho_m u_m E_m\right) + \frac{\partial}{\partial z}\left(A\rho_g u_g^2 E_g + A\rho_m u_m^2 E_m\right)\\ &= -Ag\cos\alpha\left(\rho_g E_g + \rho_m E_m\right) - \frac{d\left(AP\right)}{dz} - A\left|\frac{dF_r}{dz}\right|\end{aligned} \tag{4}$$

Latent heat of phase change exists during the process of gas–liquid phase equilibrium. Considering the existence of heat associated with phase change, the energy equation of the annulus in a wellbore is expressed as follows.

Gas phase:

$$\frac{\partial}{\partial t}\left(A\rho_g E_g C_{pg} T_a\right) + \frac{\partial}{\partial z}\left(w_g C_{pg} T_a\right) = \frac{Q_{A,g} - Q_{D,g}}{dz} \tag{5}$$

Liquid phase:

$$\frac{\partial}{\partial t}\left(A\rho_m E_m C_{pm} T_a\right) + \frac{\partial}{\partial z}\left(w_m C_{pm} T_a\right) = \frac{Q_{A,m} - Q_{D,m}}{dz} \tag{6}$$

Phase-change heat:

$$\frac{\partial}{\partial t}\left(\rho_m E_m R_{sm}\right) \tag{7}$$

Therefore, the energy equation in the wellbore annulus can be expressed as

$$\frac{\partial}{\partial t}\left(A\rho_g E_g C_{pg} T_a + A\rho_m E_m C_{pm} T_a\right) + \frac{\partial}{\partial z}\left(w_g C_{pg} T_a + w_m C_{pm} T_a\right) = \frac{Q_{A,g} - Q_{D,g}}{dz} + \frac{Q_{A,m} - Q_{D,m}}{dz} + \frac{\partial}{\partial t}\left(\rho_m E_m R_{sm}\right) \tag{8}$$

2.2 Calculation of frictional pressure drop

2.2.1 Single phase flow

Sun et al. applied the power-law for fluid flow to liquid phase flow [27] to obtain the following equation:

$$F_r = \frac{2 f u_{am}^2 \rho_{am}}{D_e} \tag{9}$$

When Re < 2,000,

$$f = \frac{8k}{\rho_{am} u_{am}^2}\left[\frac{8u_{am}}{D_e}\frac{3n+1}{4n}\right]^n \tag{10}$$

When Re > 2,000,

$$\frac{1}{\sqrt{f}} = \frac{2k}{n^{0.75}}\log\left[\mathrm{Re}\left(\frac{f}{4}\right)^{1-\frac{n}{2}}\right] - \frac{0.2}{n^{1.2}} \tag{11}$$

2.2.2 Gas–liquid two-phase flow

Bubbly flow:

$$F_r = \frac{2 f u_{am}^2 \rho_{am}}{D_e} \tag{12}$$

Slug and churn flows:

$$F_r = \frac{2 f\left(1 - E_g\right) u_{am}^2 \rho_{am}}{D_e} \tag{13}$$

$$\frac{1}{\sqrt{f}} = -4\log\left(\frac{\varepsilon_e}{3.71 D_e} - 5.05\log\frac{A}{\mathrm{Re}}\right) \tag{14}$$

$$A = \left(\frac{\varepsilon_e}{2.549 D_e}\right)^{1.11} + \left(\frac{7.149}{\mathrm{Re}}\right)^{0.898} \tag{15}$$

Annular fog flow:

$$F_r = \frac{2 f u_{am}^2 \rho_{am}}{D_e E_g^2} \tag{16}$$

$$f = 0.079\left[1 + \frac{75\left(1 - E_g\right)}{\mathrm{Reg}^{0.25}}\right] \tag{17}$$

2.3 Development of gas inflow model

The occurrence of gas kicks in deep-water drilling wellbores induces multiphase flow in the wellbore as well as gas inflow from the reservoir, which are influenced by each other. For example, when the wellbore pressure is lower than the pore pressure of the open-hole section, a gas surge occurs. Subsequently, once the gas enters the wellbore, the flow rate, gas porosity, and fluid pressure change. The gas inflow can be calculated using the following [28]

$$Q_g = 2\pi K \frac{p_e^2 - p^2}{\mu \ln \frac{2.25\frac{K}{\mu_g C_t} t}{R_w^2}} \frac{Tz}{P z_e T_e} \rho_g \tag{18}$$

PR-EOS was used for calculating the physical properties of the fluid components in the wellbore. The auxiliary equations such as velocity and two-phase flow-state discrimination equations were obtained from Gao et al. [29].

3 Gas solubility

3.1 Gas solubility calculation model

The gas–liquid two-phase equilibrium in a closed system can be expressed as follows:

$$f_i^v = f_i^l \tag{19}$$

$$f_i^v = p\phi_i^v y_i \tag{20}$$

$$f_i^l = p\phi_i^l x_i \tag{21}$$

PR-EOS was used for calculating the fugacity coefficients of component *i* in the gas and liquid phases, and its basic form can be expressed as follows:

$$P = \frac{RT}{V - b} + \frac{a}{V(V + b) + b(V + b)} \tag{22}$$

For a single gas, the parameters *a* and *b* are

$$b = 0.0778\frac{RT_c}{P_c} \tag{23}$$

$$a = a(T_c)\alpha(T) \tag{24}$$

$$a(T_c) = 0.45724\frac{(RT_c)^2}{P_c} \tag{25}$$

$$\alpha(T) = \left[1 + \beta\left(1 - \sqrt{\frac{T}{T_c}}\right)\right]^2 \quad (26)$$

$$\beta = 0.37464 + 1.54226\omega - 0.26992\omega^2 \quad (27)$$

A non-random mixing rule was used for calculating the mixed gas parameters a and b, as follows:

$$a_{mix} = \sum_i \sum_j y_i y_j \left(a_i a_j\right)^{0.5} \left(1 - k_{ij}\right) \quad (28)$$

$$b_{mix} = \sum_i y_i b_i \quad (29)$$

where k_{ij} is the interaction parameter between i and j components, with $k_{ij} = k_{ji}$. For calculating the fugacity coefficients, combined with van der Waals mixing rule [30], the following expression was used:

$$\ln \phi_i = \frac{b_i}{b}(Z-1) - \ln(Z-B) - \frac{A}{2\sqrt{2}B}\left(\frac{2\sum_{i=1}^{N} y_j a_{ij}}{a} - \frac{b_j}{b}\right)\ln\left(\frac{Z + (1+\sqrt{2})B}{Z + (1-\sqrt{2})B}\right) \quad (30)$$

The compression factor is calculated as

$$Z^3 - (1-B)Z^2 + \left(A - 2B - 3B^2\right)Z - \left(AB - B^2 - B^3\right) = 0 \quad (31)$$

where the parameters A and B are functions of temperature and pressure and are expressed as follows:

$$A = \frac{aP}{(RT)^2} \quad (32)$$

$$B = \frac{bP}{RT} \quad (33)$$

3.2 Optimization of interaction parameters between methane-water

The binary interaction parameter in PR-EOS reflects the nature of the interaction between two molecules in a mixed system of gas and water and is the key parameter for obtaining an accurate prediction of phase equilibrium using PR-EOS. Interaction parameters are typically determined based on the optimised regression of the experimental data for gas–liquid phase equilibrium. There are several reports on the solubility of CH_4 in water, and the data incorporated in this study are presented in the Appendix. The interaction parameters were calculated at different temperatures and pressures (see Figure 1). Evidently, the interaction parameters increase with an increase in temperature, whereas they exhibit a decreasing trend with an increase in pressure; however, the fluctuation range is not significantly affected by temperature. The interaction parameters were fitted as a function of temperature and pressure, as follows:

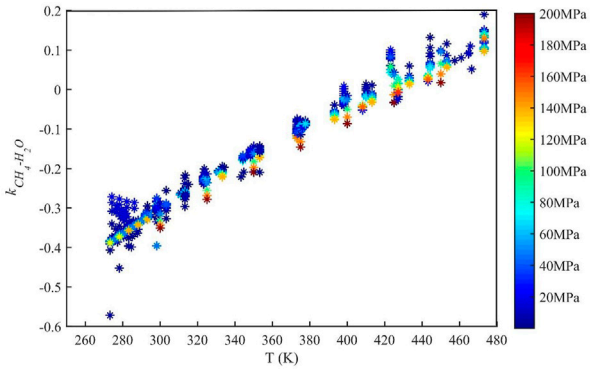

FIGURE 1
Variation in the interaction parameters of CH_4 and water with temperature and pressure.

$$k_{CH_4-H_2O} = -1.45 + 2.96 \times 10^{-4}P + 0.00469T - 1.22 \times 10^{-6}P^2 - 2.85 \times 10^{-6}T^2 - 8.62 \times 10^{-7}PT \quad (34)$$

3.2.1 Experimental evaluation of gas solubility

To verify the applicability of the gas solubility prediction model established by optimising the parameters of PR-EOS, the solubility of CO_2, CH_4, and CO_2 + CH_4 mixed gas in water was measured using a phase-equilibrium experimental device. The accuracy of the model prediction was expressed by the average relative deviation percentage $ARD\%$, and average absolute relative deviation $AARD\%$.

$$ARD\% = \left(\frac{\left|y_i{}^{exp} - y_i^{predict}\right|}{y_i{}^{exp}}\right) \times 100 \quad (35)$$

$$AARD\% = \frac{1}{N}\sum (ARD\%) \quad (36)$$

3.2.1.1 Materials

The purity of CO_2 and CH_4 was greater than 99.9%, and the purity of CH_4 in the CO_2 + CH_4 mixed gas was greater than 49.9%. Figure 2 shows the experimental flow diagram. The high-temperature and high-pressure reactor used had a volume of 300 ml, with a maximum pressure and temperature resistance of 60 MPa and 473 K, respectively. A constant-speed and constant-pressure pump (D-250L) was used for pressurisation, with a maximum pressure of 70 MPa.

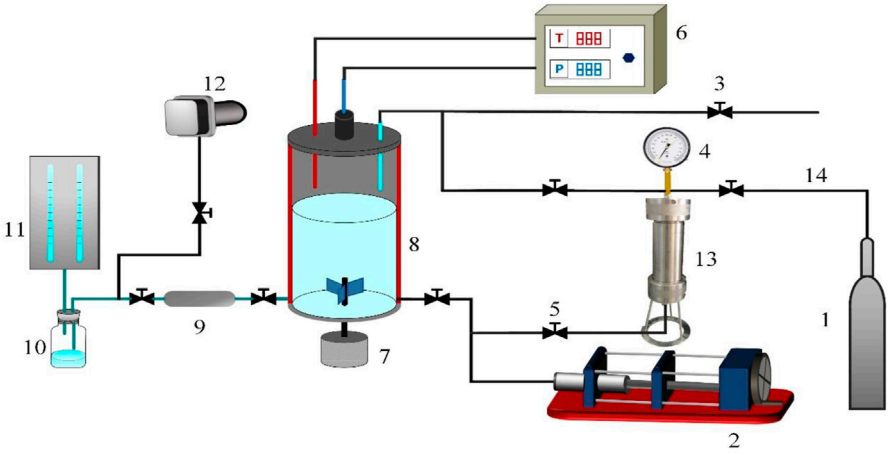

1 – high-pressure gas cylinder; 2 – constant-speed and constant-pressure pump; 3 – pipeline vent; 4 – pressure gauge; 5 – screw valve; 6 – temperature and pressure control box; 7 – electromagnetic stirrer; 8 – high-temperature autoclave; 9 – high-pressure sampler; 10 – flask; 11 – gas meter; 12 – vacuum pump; 13 – high-pressure intermediate vessel; 14 – pipeline

FIGURE 2
Schematic of the experimental flow.

3.2.1.2 Experimental procedure

The operational process for gas solubility measurement is as follows.

1) The experimental device is cleaned and checked for air tightness. Deionized water is used to clean the high-temperature and high-pressure reaction kettle 2–3 times; the intermediate vessel and reaction kettle are connected; the pressure of the reaction kettle is increased to 5 MPa. If the pressure of the reaction kettle and intermediate vessel is stable without fluctuation within 2 h, the sealing of the experimental device is considered adequate. Otherwise, the connection is rechecked.
2) The phase-equilibrium experiment is conducted by pressurising and heating. A vacuum is generated in the reaction kettle using a vacuum pump. Approximately 200 ml of liquid is injected with a constant-speed and constant-pressure pump, and the heating device is turned on to increase the temperature to the pre-set value. The reaction kettle is filled with gas to a certain pre-set pressure through the intermediate vessel to form a gas–liquid mixed state in the kettle. During the pressurisation process, certain temperature fluctuations occur because of the adiabatic condition in the reaction kettle; therefore, the temperature must be stabilised to the pre-set temperature. After stirring for 1–2 h with an electromagnetic stirrer, the pressure change in the kettle is no longer monitored. If the pressure is stable within 2–3 h, the gas–liquid equilibrium is considered stable.
3) The measurement data is recorded, sampled, and analysed. A vacuum pump is used to generate a vacuum in the sampler and extract the liquid in the kettle. A constant-speed and constant-pressure pump is used to inject the liquid into the reaction kettle and maintain a stable pressure in the kettle. A gas meter is used to measure the volume of the precipitated gas. After the gas is collected, the gas and liquid volumes are recorded in real-time. The average value of the three measurements is calculated and chromatographic analysis of the precipitated gas is performed.
4) Steps 2)–3) are repeated to perform the solubility measurements at different pressures and temperatures. After the experiment is completed, the exhaust pipeline is vented.

3.2.1.3 Accuracy verification of experimental methods

To verify that the aforementioned experimental devices and methods can be used for solubility measurements, the measurement results of CO_2 gas at 325.15 K were compared with previously reported experimental data [18, 20, 31], as presented in Table 1. Evidently, the maximum ARD% of our experimental data compared with reported data is 3.54, and the minimum ARD% is 1.55, indicating good accuracy. Therefore, the proposed experimental apparatus and method can be used for gas solubility measurements.

TABLE 1 Comparison between experimental and previously reported values of CO_2 solubility in water measured at 323.15 K.

P (MPa)	Experimental value	Reported value	ARD%	Reference
10	0.02000	0.01868	2.63	[18]
20	0.02094	0.02151	2.71	[18]
20	0.02095	0.02020	3.55	[31]
30	0.02408	0.02494	3.54	[18]
40	0.02446	0.02484	1.55	[16]

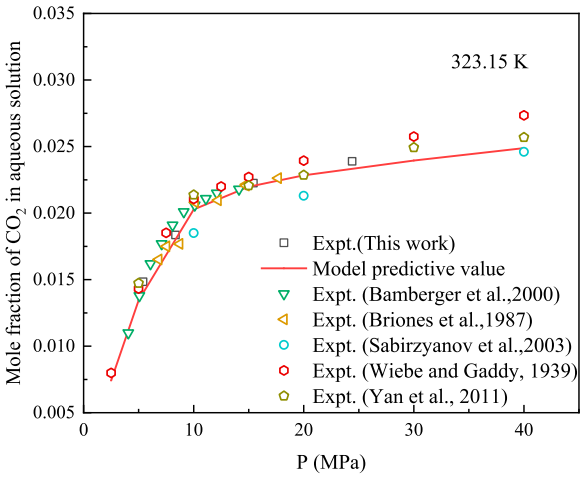

FIGURE 3
Comparison between predicted data of CO_2 solubility model and experimental data at 323.15 K.

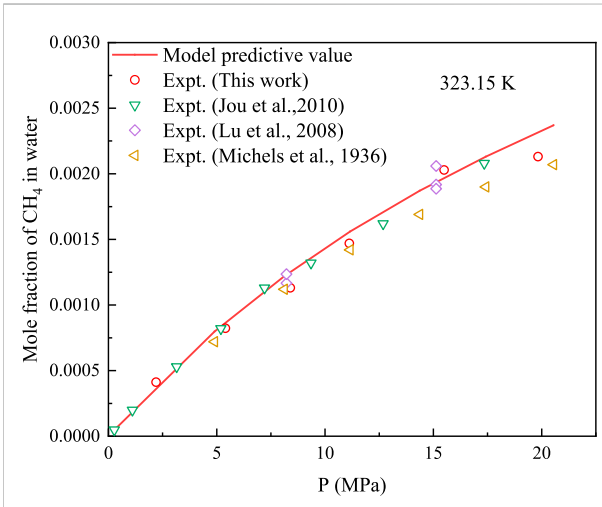

FIGURE 4
Comparison between predicted data of CH_4 solubility model and experimental data at 323.15 K.

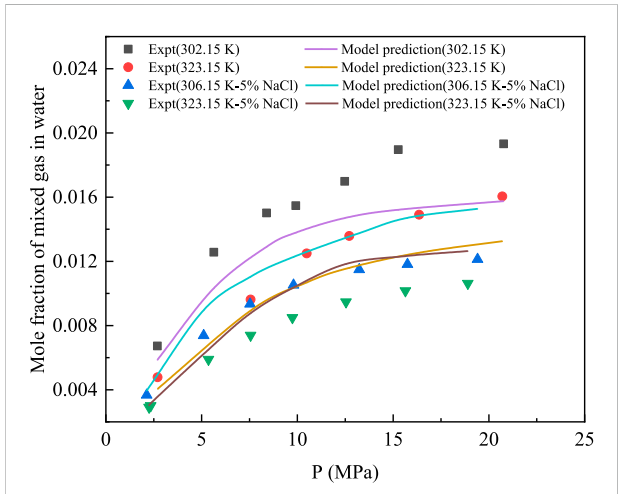

FIGURE 5
Comparison between the predicted data of CH_4 solubility model and the experimental data at 323.15 K.

3.2.2 Verification of prediction accuracy of gas solubility model

3.2.2.1 Prediction of single-gas solubility model

Solubility of CH_4 and CO_2 in water at 323.15 K was measured using the proposed experimental device. The developed solubility-prediction model was used to predict and analyse the solubility of CO_2 and CH_4 in water, as shown in Figures 3, 4. The experimental data obtained in this study were compared with previously reported data [16–18, 32–35] for model analysis.

At 323.15 K, the AARD% of the model predicted and experimental values for CH_4 was 5.66, and the AARD% for the solubility of CO_2 in water was 3.71. Therefore, the proposed solubility-prediction model can be used to accurately predict the solubility of CH_4 and CO_2.

3.2.2.2 Prediction of mixed gas solubility model

The solubility of the $CH_4 + CO_2$ mixture in water and 5% NaCl aqueous solution was measured at 302.15 K and 323.15 K. The established solubility model was used to predict the experimental results, as shown in Figure 5. Evidently, the model predicted values are not consistent with the experimental values and a certain

deviation exists. For the solubility of the mixture in water, the AARD % of the model predicted and experimental values was 14.80. The AARD% of the mixed gas in 5% NaCl was 14.32, showing a certain deviation. This is because this study only investigated the interaction parameters of CH_4 gas and water. The interaction parameters of CO_2–H_2O are 0.19014, as reported by Ziabakhsh-Ganji and Kooi [25], and the interaction parameters of CO_2–CH_4 are 0.1 [36]. Therefore, the selection of interaction parameters resulted in a lower model predicted value for CO_2.

4 Solution of multiphase flow model

The finite difference method was used to calculate the differences in the proposed multiphase flow model [37]. The basic difference calculation can be expressed as follows:

$$Y_{j+1}^{n+1} - Y_j^{n+1} = \frac{\Delta z}{2\Delta t}\left(X_j^n + X_{j+1}^n - X_j^{n+1} - X_{j+1}^{n+1}\right) \tag{37}$$

The discretisation of the differential equation describing the gas phase non-production interval can be expressed as follows:

$$\begin{aligned}&\left(\rho_g u_g E_g A\right)_{j+1}^{n+1} - \left(\rho_g u_g E_g A\right)_j^{n+1}\\ &= \frac{\Delta z}{2\Delta t}\left[\left(\rho_g E_g A\right)_j^{n+1} - \left(\rho_g E_g A\right)_j^n + \left(\rho_g E_g A\right)_{j+1}^{n+1} - \left(\rho_g E_g A\right)_{j+1}^n\right]\\ &\quad -\frac{\Delta z}{2}\left[\left(m_{g-l}\right)_j^{n+1} + \left(m_{g-l}\right)_{j+1}^{n+1}\right]\end{aligned} \tag{38}$$

The discretisation of the differential equation of the dissolved phase can be expressed as follows:

$$\begin{aligned}&\left(\rho_{sg} R_{sm} E_m A u_m\right)_{j+1}^{n+1} - \left(\rho_{sg} R_{sm} E_m A u_m\right)_j^{n+1} = \frac{\Delta z}{2\Delta t}\left[\left(\rho_{sg} R_{sm} E_m A\right)_j^n\right.\\ &\left.+\left(\rho_{sg} R_{sm} E_m A\right)_{j+1}^n - \left(\rho_{sg} R_{sm} E_m A\right)_j^{n+1} - \left(\rho_{sg} R_{sm} E_m A\right)_{j+1}^{n+1}\right]\\ &\quad - \frac{\Delta z}{2}\left[\left(m_{g-l}\right)_j^{n+1} + \left(m_{g-l}\right)_{j+1}^{n+1}\right]\end{aligned} \tag{39}$$

The phase discretisation of the drilling fluid differential equation can be expressed as follows:

$$\begin{aligned}&\left(\rho_m u_m E_m A\right)_{j+1}^{n+1} - \left(\rho_m u_m E_m A\right)_j^{n+1}\\ &= \frac{\Delta z}{2\Delta t}\left[\left(\rho_m E_m A\right)_j^{n+1} - \left(\rho_m E_m A\right)_j^n + \left(\rho_m E_m A\right)_{j+1}^{n+1} - \left(\rho_m E_m A\right)_{j+1}^n\right]\\ &\quad +\frac{\Delta z}{2}\left[\left(m_{g-l}\right)_j^{n+1} + \left(m_{g-l}\right)_{j+1}^{n+1}\right]\end{aligned} \tag{40}$$

The momentum equation discretisation can be expressed as follows:

$$\begin{aligned}&\left(AP + AF_r\right)_{j+1}^{n+1} - \left(AP + AF_r\right)_j^{n+1} + \left(AE_g\rho_g u_g^2 + AE_m\rho_m u_m^2\right)_{j+1}^{n+1}\\ &\quad - \left(AE_g\rho_g u_g^2 + AE_m\rho_m u_m^2\right)_j^{n+1} = \frac{\Delta z}{2\Delta t}\left[\left(AE_g\rho_g u_g + AE_m\rho_m u_m\right)_{j+1}^{n+1}\right.\\ &\quad - \left(AE_g\rho_g u_g + AE_m\rho_m u_m\right)_{j+1}^n\\ &\quad + \left(AE_g\rho_g u_g + AE_m\rho_m u_m\right)_{j+1}^{n+1}\\ &\quad \left. - \left(AE_g\rho_g u_g + AE_m\rho_m u_m\right)_{j+1}^n\right]\\ &\quad - \frac{\Delta z}{2}\left[\left(Ag\cos\alpha\left(E_g\rho_g + E_m\rho_m\right)\right)_j^{n+1}\right.\\ &\quad \left.-\left(Ag\cos\alpha\left(E_g\rho_g + E_m\rho_m\right)\right)_{j+1}^{n+1}\right]\end{aligned} \tag{41}$$

The flow diagram of the solution process in the proposed model is illustrated in Figure 6. The specific steps of the multiphase flow model are as follows:

1) The bottom-hole pressure $p_j^{n(0)}$ at time n is estimated, and the temperature T_j^n at time n is calculated.
2) The dissolved gas at node j and time n is calculated. The relationship between the calculated gas dissolution and the formation-gas inflow or production is examined, as follows.
   ① If the calculated gas dissolution is less than the gas inflow, the gas dissolution at the current time is the calculated gas solubility.
   ② If the calculated gas dissolution is greater than the gas inflow, the gas dissolution at the current time is the inflow of formation gas.
3) According to the calculated temperature and pressure at node j at time n, output of each phase, and dissolved amount of gas, the physical property parameters of each component phase at node j and time n are calculated using the equation of state.
4) The continuity equation is used to calculate the velocity and volume fraction $E_{i,j}^{n(0)}$ of each component phase at node j and time n using the known parameters of spatial node $j + 1$ at time n;
5) The pressure p_{j+1}^n at node $j + 1$ and time n is estimated, Steps 2)–4) are repeated, and $p_{j+1}^{n(0)}$ at node $j + 1$ and time n is calculated using the momentum equation. If $|p_{j+1}^n - p_{j+1}^{n(0)}| \le \varepsilon$, the calculation is considered correct. The parameters calculated at node $j + 1$ and time n are used as the known conditions at time $n + 1$. Otherwise, the calculation is repeated.
6) Steps 2)–5) are repeated to calculate the wellhead parameters, and the calculated wellhead back pressure is p_h. Compared with the measured wellhead back pressure P_h^0, if $|p_h - p_h^o| \le \varepsilon$ is true, the assumption of bottom-hole pressure p_j^n at time n is considered correct. Otherwise, Step 2) is repeated and a new value is assigned to bottom-hole pressure $p_j^{n(0)}$ at time n.

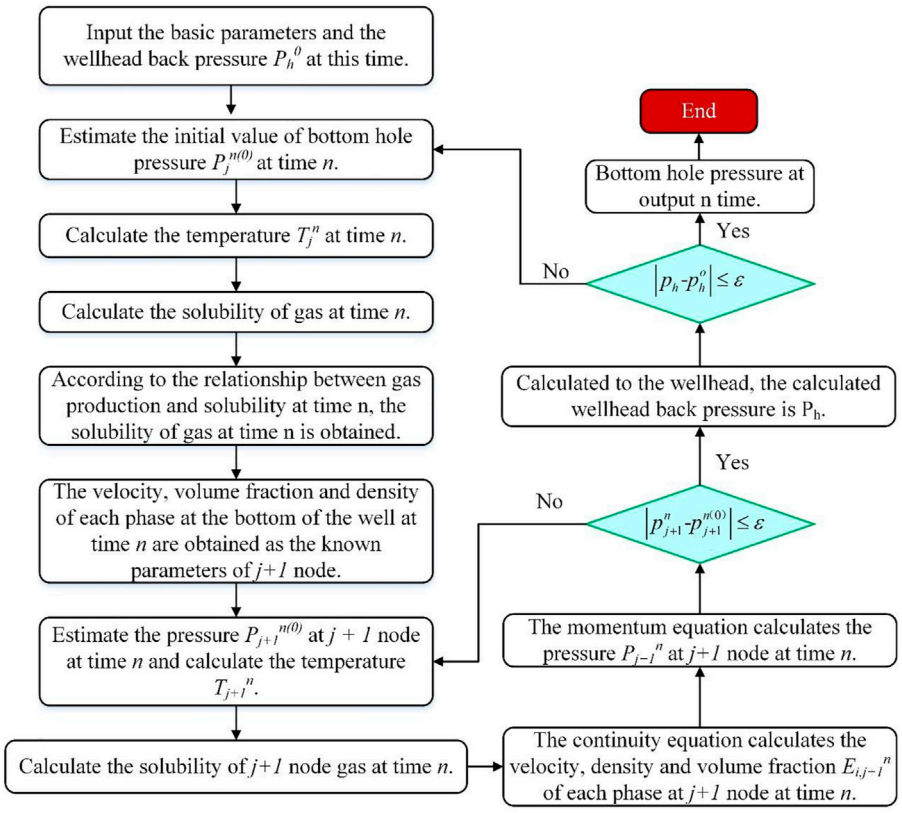

FIGURE 6
Flowchart of multiphase flow model solution.

TABLE 2 Specifications of the example well.

Reservoir temperature (°C)	145	Reservoir pressure (MPa)	68
Length of intrusion section (m)	2	Porosity (%)	12
Permeability (md)	10	Drilling rate (m h^{-1})	10
Seawater temperature (°C)	15	Gas invasion time (s)	1,680
Water depth (m)	839	Well depth (m)	3,735
Gas-influx point (m)	3,735	Displacement (L s^{-1})	36
Mud density (kg m^{-3})	1,280	Mud viscosity (cp)	35
Gas type		90% CH_4 + 10% CO_2	

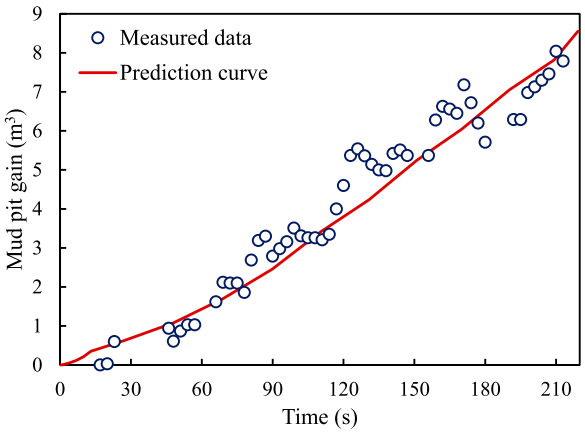

FIGURE 7
Variation in the relationship between mud-pit increment and bottom-hole pressure with invasion time.

5 Results and discussion

5.1 Analysis of gas–liquid flow law

A deep-water vertical well in the South China Sea was used as an example to perform a project case analysis. The basic data are listed in Table 2.

Figure 7 shows the deviation between the calculated mud-pit increment and the measured values. It can be observed that the mud-pit increment rapidly changes in the range of 0–210 s.

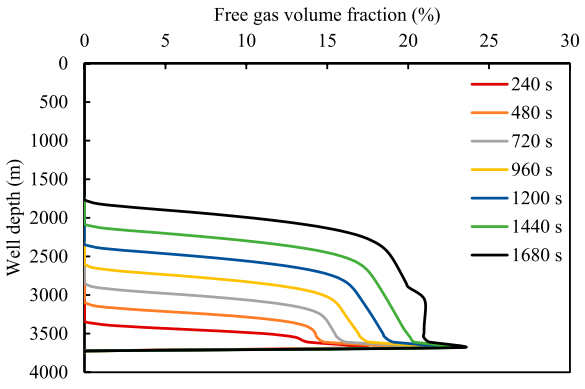

FIGURE 8
Relationship between free gas integral number and well depth for different time durations.

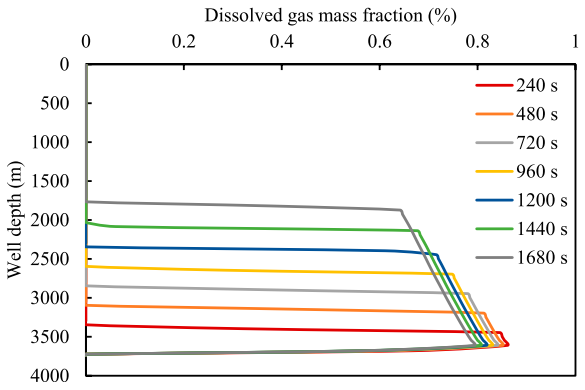

FIGURE 9
Relationship between dissolved gas mass fraction and well depth.

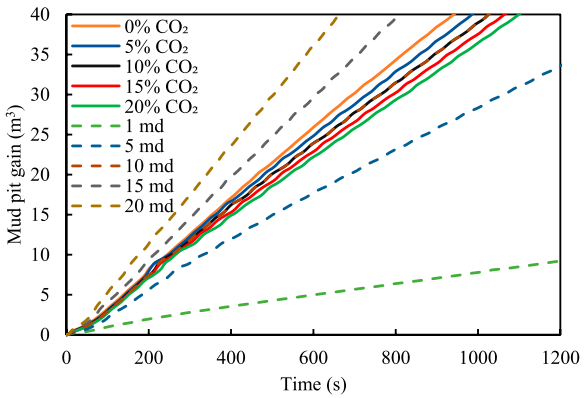

FIGURE 10
Variation in the mud pit increment with time for different gas types and permeabilities.

Furthermore, the difference between the calculated curve and the measured points is small, and the error between the predicted and the measured values remains within 15%. In actual engineering projects involving drilling, the measured data fluctuates owing to the influence of tide, instrument error, and typhoon.

Figures 8, 9 show the variation in the relationship between the volume fraction of the free gas and the mass fraction of the dissolved gas with invasion time. As the well depth decreases, both the mass fraction of the dissolved gas and the corresponding free gas integral number gradually decrease. This is because the amount of gas invaded by the formation is limited, and the gas gradually extends to the front. The gas dissolution causes the volume fraction of the gas at the front to decrease. However, when the well depth is fixed, volume fraction of the free gas increases with an increase in invasion time, primarily because the amount of dissolved gas in the drilling fluid reaches the saturated state, and the amount of gas released increases. As is evident from Figure 9, the dissolved gas content in the wellbore has a certain limit and does not increase beyond the liquid saturation value.

5.2 Influence of CO_2 content and reservoir permeability on multiphase flow

The gas–liquid two-phase flow law was simulated and analysed for a reservoir permeability of 10 md, gas invasion time of 1,200 s, and displacement of 36 L/s. Figure 10 shows the variations in the mud-pit increment with gas invasion time under different acid gas contents and permeabilities. If the invaded gas does not contain CO_2, the mud pit changes rapidly and the gas invasion monitoring time is shorter. By contrast, if the invaded gas contains a high concentration of CO_2, the incremental change time of the mud pit increases. If the monitoring value of the mud-pit increment is considered as 10 m^3, it can be monitored in 252 s when the gas without CO_2 is dissolved. When 10% CO_2 is present in the invading gas, the monitoring time of gas invasion increases by 10 s. Similarly, the monitoring time of the gas containing 20% CO_2 is increased by 22 s. Therefore, the dissolution of an acid gas causes a certain lag and increased risk in gas invasion monitoring. For the 90% CH_4 + 10% CO_2 intrusive gas, the monitoring time changes in mud pits with different permeabilities. With an increase in invasion time, the mud-pit increment changes rapidly under high permeability. If 5 m^3 is used as the monitoring standard, the time required to attain the monitoring value under high permeability is shorter. This is because an increase in gas invasion under high permeability results in an increase in gas content in the wellbore.

Figures 11, 12 show the relationship between the volume fraction of the free gas and the mass fraction of the dissolved gas for different acid gas contents and well depths. Evidently, the

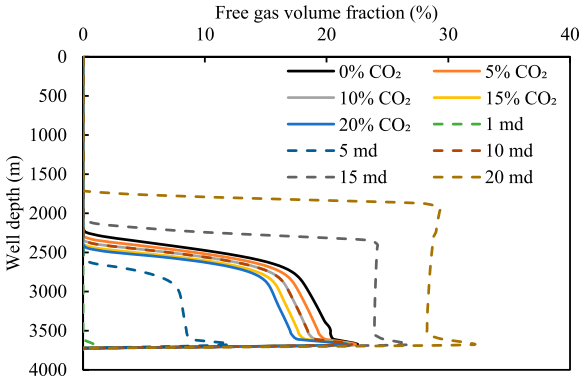

FIGURE 11
Variation in the free gas integral number with well depth for different intrusive gases and permeabilities.

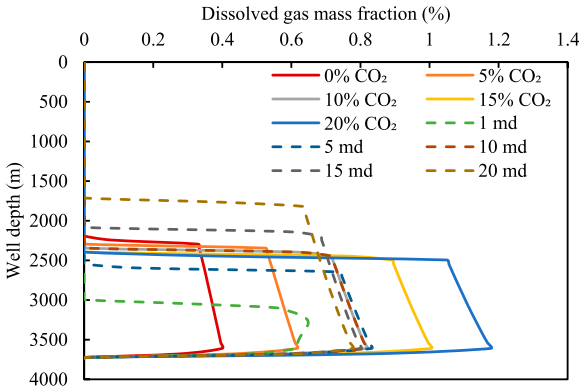

FIGURE 12
Relationship between mass fraction of dissolved gas and well depth for different intrusive gases and permeabilities.

number of free gas integrals decreases and the corresponding dissolved gas content increases with an increase in the CO_2 content. This is because an increase in the acid gas content leads to a rapid increase in the amount of dissolved gas in the drilling fluid; consequently, more gas enters the drilling fluid, resulting in a decrease in the number of free gas integrals.

For the 90% CH_4 + 10% CO_2 intrusive gas, the changes in the free gas and dissolved gas under different reservoir permeabilities are examined. Under a low permeability of 1 md, the amount of invading gas is small. Therefore, the gas is completely dissolved in the drilling fluid, causing the integral number of free gas to be 0 (see Figure 11). With an increase in permeability, the amount of invading gas in the wellbore increases, because the solubility of the gas in the drilling fluid is limited. The integral number of free gas increases gradually with an increase in permeability, and the position of the gas movement front is closer to the wellhead. Therefore, the dissolution of gases makes timely detection of gas invasion under low permeability difficult; therefore, the concealment is enhanced.

6 Conclusion

In this study, a multiphase flow model considering gas dissolution was established, and the auxiliary equations of gas solubility were examined based on the dynamic analysis of the migration process of an acid gas invading a wellbore. The main conclusion are as follows.

1) By optimising the interaction parameters of CH_4 and water, a new solubility model was established. The prediction accuracy of CH_4 gas solubility was maintained at 96.4%. However, the prediction error for the mixed gas composed of CO_2 and CH_4 was large, and the accuracy was less than 85%.
2) The higher the CO_2 content in the invading gas, the greater the amount of dissolved gas in the drilling fluid, the lower the volume fraction of the free gas phase in the wellbore, and the farther the gas front was from the wellhead. Furthermore, the dissolution of gas with high CO_2 content caused an increase in the time required for the mud pit increment to reach the warning or critical value.
3) The greater the permeability of the reservoir, the smaller the influence of gas dissolution. For a low permeability reservoir, the influence of gas dissolution plays a key role, resulting in a slow change in the free gas integral number in the wellbore. Moreover, the ground monitoring time was significantly increased, making gas invasion monitoring challenging.

Data availability statement

The original contributions presented in the study are included in the article/supplementary material, further inquiries can be directed to the corresponding author.

Author contributions

HH: Methodology, Writing—Original draft preparation. BS: Conceptualization, Supervision, Funding acquisition. XS: Validation, Data curation, Funding acquisition. XL: Data curation. ZS: Data curation.

Funding

The author sincerely thanks the Postdoctoral innovative talents support program in China (BX2021374), and the National Natural Science Foundation—Youth Foundation (5210040269) to provide fund support.

Conflict of interest

Author ZS was employed by the company Drilling Division of China Petroleum Offshore Engineering Co., Ltd.

The remaining authors declare that the research was conducted in the absence of any commercial or financial relationships that could be construed as a potential conflict of interest.

Publisher's note

References

1. Gao G, Gang W, Zhang G, He W, Cui X, Shen H, et al. Physical simulation of gas reservoir formation in the Liwan 3-1 deep-water gas field in the Baiyun sag, Pearl River Mouth Basin. *Nat Gas Industry B* (2015) 2(1):77–87. doi:10.1016/j.ngib.2015.02.006

2. Zhang G, Wang D, Lan L, Liu S, Su L, Wang L, et al. The geological characteristics of the large- and medium-sized gas fields in the South China Sea. *Acta Oceanol Sin* (2021) 40(2):1–12. doi:10.1007/s13131-021-1754-x

3. Zhu W, Huang B, Mi L, Wilkins RWT, Fu N, Xiao X. Geochemistry, origin, and deep-water exploration potential of natural gases in the Pearl River Mouth and Qiongdongnan basins, South China Sea. *Am Assoc Pet Geol Bull* (2009) 93(6):741–61. doi:10.1306/02170908099

4. Sun BJ, Fu WQ, Wang N, Wang ZY, Gao YH. Multiphase flow modeling of gas intrusion in oil-based drilling mud. *J Pet Sci Eng* (2019) 174:1142–51. doi:10.1016/j.petrol.2018.12.018

5. Chen B, Sun H, Zhou H, Yang M, Wang D. Effects of pressure and sea water flow on natural gas hydrate production characteristics in marine sediment. *Appl Energ* (2019) 238:274–83. doi:10.1016/j.apenergy.2019.01.095

6. Chen B, Sun H, Zheng J, Yang M New insights on water-gas flow and hydrate decomposition behaviors in natural gas hydrates deposits with various saturations [J]. *Appl. Energy* (2020) 259:114185.

7. Sun H, Chen B, Pang W, Song Y, Yang M. Investigation on plugging prediction of multiphase flow in natural gas hydrate sediment with different field scales. *Fuel* (2022) 325:124936. doi:10.1016/j.fuel.2022.124936

8. Fu WQ, Wang ZY, Sun BJ, Xu JC, Chen LT, Wang XR. Rheological properties of methane hydrate slurry in the presence of xanthan gum. *SPE J* (2020) 25(5):2341–52. doi:10.2118/199903-pa

9. Fu WQ, Wang ZY, Chen LT, Sun BJ. Experimental investigation of methane hydrate formation in the carboxmethylcellulose (CMC) aqueous solution. *SPE J* (2020) 25(3):1042–56. doi:10.2118/199367-pa

10. Popp VV, Marinescu M, Manoiu D, Popp A, Chitu PM "Possibilities of energy recovery from CO_2 reservoirs[C]," in SPE Annual Technical Conference and Exhibition (OnePetro) (1998).

11. Prakasa Y, Hartanto E, Sulistyo D. *United nations conference of plenipotentiaries on a supplementary convention on the abolition of slavery, the slave trade, and institutions and practices similar to slavery* (1998).Carbon dioxide generation in Tugu Barat-C field and role in hydrocarbon migration

12. Yin B, Liu G, Li X. Multiphase transient flow model in wellbore annuli during gas kick in deepwater drilling based on oil-based mud. *Appl Math Model* (2017) 51(11):159–98. doi:10.1016/j.apm.2017.06.029

13. Sun B, Guo Y, Sun W, Gao Y, Li H, Wang Z, et al. Multiphase flow behavior for acid-gas mixture and drilling fluid flow in vertical wellbore[J]. *J Pet Sci Eng* (2018) 165:388–396. doi:10.1016/j.petrol.2018.02.016

14. Xu Z, Song X, Li G, Zhu Z, Zhu B Gas kick simulation in oil-based drilling fluids with the gas solubility effect during high-temperature and high-pressure well drilling[J]. *Appl Therm Eng* (2019) 149:1080–1097.

15. O'bryan PL. *Well control problems associated with gas solubility in oil-based drilling fluids [D]*. Louisiana: Louisiana State University (1988).

16. Wiebe R, Gaddy VL. The solubility in water of carbon dioxide at 50, 75 and 100°, at pressures to 700 atmospheres. *J Am Chem Soc* (1939) 61(2):315–8. doi:10.1021/ja01871a025

17. Briones JA, Mullins JC, Thies MC, Kim BU. Ternary phase equilibria for acetic acid-water mixtures with supercritical carbon dioxide. *Fluid Phase Equilibria* (1987) 36(2):235–46. doi:10.1016/0378-3812(87)85026-4

18. Sabirzyanov AN, Shagiakhmetov RA, Gabitov FR, Tarzimanov AA, Gumerov FM. Water solubility of carbon dioxide under supercritical and subcritical conditions[J]. *Theor Foundations Chem Eng* (2003) 37(1):51–3. doi:10.1023/a:1022256927236

19. Dhima A, De Hemptinne JC, Jose J. Solubility of hydrocarbons and CO_2 mixtures in water under high pressure[J]. *Ind Eng Chem Res* (1999) 38(8):3144–61. doi:10.1021/ie980768g

20. Qin J, Rosenbauer RJ, Duan Z. Experimental measurements of vapor–liquid equilibria of the $H_2O + CO_2 + CH_4$ ternary system. *J Chem Eng Data* (2009) 53(6):1246–9. doi:10.1021/je700473e

21. Loring JS, Bacon DH, Springer RD, Anderko A, Gopinath S, Yonkofski CM, et al. Water solubility at saturation for CO_2–CH_4 mixtures at 323.2 K and 9.000 MPa. *J Chem Eng Data* (2017) 62(5):1608–14. doi:10.1021/acs.jced.6b00999

22. Al Ghafri SZ, Forte E, Maitland GC, Rodriguez-Henríquez JJ, Trusler JM Experimental and modeling study of the phase behavior of (methane + CO2 + water) mixtures[J]. *The J Phys Chem B* (2014) 118(49):14461–78.doi:10.1021/jp509678g

23. Zirrahi M, Azin R, Hassanzadeh H, Moshfeghian M. Mutual solubility of CH4, CO2, H2S, and their mixtures in brine under subsurface disposal conditions. *Fluid Phase Equilibria* (2012) 32:80–93. doi:10.1016/j.fluid.2012.03.017

24. Peng DY, Robinson DB. A new two-constant equation of state. *Ind Eng Chem Fund* (1976) 15(1):59–64. doi:10.1021/i160057a011

25. Ziabakhsh-Ganji Z, Kooi H. An Equation of State for thermodynamic equilibrium of gas mixtures and brines to allow simulation of the effects of impurities in subsurface CO2 storage. *Int J Greenhouse Gas Control* (2012) 11(1):S21–S34. doi:10.1016/j.ijggc.2012.07.025

26. Li J, Wei L, Li X. Modeling of CO2-CH4-H2S-brine based on cubic EOS and fugacity-activity approach and their comparisons. *Energ Proced* (2014) 63:3598–607. doi:10.1016/j.egypro.2014.11.390

27. Sun B, Gong P, Wang Z. Simulation of gas kick with high H2S content in deep well. *J Hydrodyn* (2013) 25(2):264–73. doi:10.1016/s1001-6058(13)60362-5

28. Zhang J, Du D, Hou J. *Petrol-gas permeation fluid mechanics*. 2nd ed.. Dong Ying, China: China University of Petroleum Press (2010). (in Chinese).

29. Gao Y. *Study on multi-phase flow in wellbore and well control in deep water drilling*. China: China University of Petroleum (2007). p. 47–64.Doctoral dissertation

30. Van der Waals JD. *Over de Continuiteit van den Gas-en Vloeistoftoestand[M]*. Leiden: Sijthoff (1873).

31. Tödheide K, Franck EU. Das Zweiphasengebiet und die kritische Kurve im System Kohlendioxid–Wasser bis zu Drucken von 3500 bar. *Z für Physikalische Chem* (1963) 37(5-6):387–401. doi:10.1524/zpch.1963.37.5_6.387

32. Yan W, Huang S, Stenby EH. Measurement and modeling of CO2 solubility in NaCl brine and CO2–saturated NaCl brine density. *Int J Greenhouse Gas Control* (2011) 5(6):1460–77. doi:10.1016/j.ijggc.2011.08.004

33. Lu W, Chou I M, Burruss R. Determination of methane concentrations in water in equilibrium with sI methane hydrate in the absence of a vapor phase by *in situ* Raman spectroscopy. *Geochimica Et Cosmochimica Acta* (2008) 72(2):412–22. doi:10.1016/j.gca.2007.11.006

34. Michels A, Gerver J, Bijl A. The influence of pressure on the solubility of gases. *Physica* (1936) 3(8):797–808. doi:10.1016/s0031-8914(36)80353-x

35. Jou FY, Mather AE. The solubility of methane in aqueous solutions of monoethanolamine, diethanolamine and triethanolamine[J]. *Can J Chem Eng* (2010) 76(3):945–51. doi:10.1002/cjce.5450760512

36. Li H, Yan J. Evaluating cubic equations of state for calculation of vapor–liquid equilibrium of CO2 and CO2-mixtures for CO2 capture and storage processes. *Appl Energ* (2009) 86(6):826–36. doi:10.1016/j.apenergy.2008.05.018

37. Smith GD. *Numerical solution of partial equations: Finite difference methods [M]*. Oxford University Press (1978).

38. Addicks J, Owren GA, Fredheim AO, Tangvik K. Solubility of carbon dioxide and methane in aqueous methyldiethanolamine solutions. *J Chem Eng Data* (2002) 47(4):855–60. doi:10.1021/je010292z

39. Böttger A, Kamps ÁPS, Maurer G An experimental investigation of the phase equilibrium of the binary system (methane+ water) at low temperatures: Solubility of methane in water and three-phase (vapour+ liquid+ hydrate) equilibrium[J]. *Fluid Ph Equilibria* (2016) 407:209–16.

40. Bttger A, Kamps LP, Maurer G. An experimental investigation of the phase equilibrium of the binary system (methane+water) at low temperatures: Solubility of methane in water and three-phase (vapour+liquid+hydrate) equilibrium[J]. *Fluid Phase Equilibr* (2016) 407:209–16. doi:10.1016/j.fluid.2015.03.041

41. Blount CW, Price LC, Solubility of methane in water under natural conditions: A laboratory study. *Final report*, 1, 30. 1982.

42. Bamberger AGS, Sieder G, Maurer G. High-pressure (vapor+liquid) equilibrium in binary mixtures of (carbon dioxide+water or acetic acid) at temperatures from 313 to 353 K[J]. *J Supercrit Fluids* (2000) 17(2):97–110.

43. Chapoy A, Mohammadi AH, Richon D, Tohidi B. Gas solubility measurement and modeling for methane-water and methane-ethane-n-butane-water systems at low temperature conditions[J]. *Fluid Phase Equilibr* (2004) 220(1):111–9. doi:10.1016/j.fluid.2004.02.010

44. Dendy Sloan E, Koh C, *[Chemical industries] clathrate hydrates of natural gases*, 3rd ed. Volume 20074156 || Estimation techniques for phase equilibria of natural gas hydrates. 2007.

45. Cramer SD. Solubility of methane in brines from 0 to 300.degree.C. *Ind Eng Chem Res* (1984) 23(3).

46. Culberson OL, Mcketta JJ. Phase equilibria in hydrocarbon-water systems III - the solubility of methane in water at pressures to 10, 000 PSIA. *J Pet Tech* (1951) 3(08):223–6. doi:10.2118/951223-g

47. Duffy JR, Smith NO, Nagy B. Solubility of natural gases in aqueous salt solutions—I. *Geochim Cosmochim Acta* (1961) 24(1-2):23–31. doi:10.1016/0016-7037(61)90004-7

48. Eslamimanesh A, Mohammadi AH, Richon D. Thermodynamic consistency test for experimental solubility data in carbon dioxide/methane + water system inside and outside gas hydrate formation region. *J Chem Eng Data* (2011) 56(4): 1573–86. doi:10.1021/je1012185

49. Gao J, Zheng DQ, Guo TM. Solubilities of methane, nitrogen, carbon dioxide, and a natural gas mixture in aqueous sodium bicarbonate solutions under high pressure and elevated temperature. *J Chem Eng Data* (1997) 42(1):69–73. doi:10.1021/je960275n

50. Kiepe J, Horstmann S, Kai F, Gmehling J. Experimental determination and prediction of gas solubility data for methane + water solutions containing different monovalent electrolytes. *Ind Eng Chem Res* (2003) 42(21):3216. doi:10.1021/ie0401298

51. Kim YS, Ryu SK, Yang SO, Lee CS. Liquid WaterHydrate equilibrium measurements and unified predictions of hydrate-containing phase equilibria for methane, ethane, propane, and their mixtures. *Ind Eng Chem Res* (2003) 42(11): 2409–14. doi:10.1021/ie0209374

52. Mcgee KA, Susak NJ, Sutton AJ, Haas JL. The solubility of methane in sodium chloride brines. *Open-File Rep* (1981) 81:1294. doi:10.3133/ofr811294

53. Frost M, Karakatsani E, Solms NV, Richon D, Kontogeorgis GM. Vapor–liquid equilibrium of methane with water and methanol. Measurements and modeling. *J Chem Eng Data* (2013) 59(4):961–7. doi:10.1021/je400684k

54. O'Sullivan TD, Smith NO. Solubility and partial molar volume of nitrogen and methane in water and in aqueous sodium chloride from 50 to 125.deg. and 100 to 600 atm. *J Phys Chem* (1970) 74(7):1460–6. doi:10.1021/j100702a012

55. Ou W, Geng L, Lu W, Guo H, Qu K, Mao P. Quantitative Raman spectroscopic investigation of geo-fluids high-pressure phase equilibria: Part II. Accurate determination of CH4 solubility in water from 273 to 603 K and from 5 to 140 MPa and refining the parameters of the thermodynamic model. *Fluid Phase Equilib* (2015) 391:18–30. doi:10.1016/j.fluid.2015.01.025

56. Price LC. Aqueous solubility of methane at elevated pressures and temperatures. *Aapg Bull* (1979) 63:1527. doi:10.1306/2F9185E0-16CE-11D7-8645000102C1865D

57. Yang SO, Cho SH, Lee H, Lee CS. Measurement and prediction of phase equilibria for water + methane in hydrate forming conditions. *Fluid Phase Equilib* (2001) 185(1-2):53–63. doi:10.1016/s0378-3812(01)00456-3

58. Yokoyama C, Wakana S, Kaminishi G, Takahashi S. Vapor-liquid equilibria in the methane-diethylene glycol-water system at 298.15 and 323.15 K. *J Chem Eng Data* (1988) 33(3):274–6. doi:10.1021/je00053a015

Nomenclature

Abbreviations

A cross-sectional area of annulus, m^2

a, b relevant parameters of equation of state, dimensionless

A, B relevant parameters of equation of state, dimensionless

AARD% average absolute relative deviation percent

ARD% average relative deviation percent

C_{pg} heat capacities of the gas, J/(kg K)

C_{pm} heat capacities of the liquid phases, J/(kg K)

C_t compression coefficient, 1/Pa

D_e equivalent diameter, m

E_g volume fraction of gas, dimensionless

Em volume fraction of drilling fluid, dimensionless

f_i^l fugacities of component *i* in liquid phase, Pa

f_i^v fugacities of component *i* in gas phase, Pa

f friction coefficient, dimensionless

F_r frictional pressure of the wellbore, Pa

g acceleration due to gravity, m/s^2

k correction factor, dimensionless

K permeability, m^2

k_{ij} interaction parameters of component *i* and component *j*, dimensionless

$m_{g\text{-}L}$ mass transfer rate from gas phase to liquid phase, kg/(m s)

n flow index of the mixed fluids, dimensionless

N Number of digital points, dimensionless

P pressure, Pa

P_c critical pressure, MPa

P_e reservoir pressure, Pa

$Q_{A,g}$ heat exchange between the gas phase and annulus per unit time, J

$Q_{A,m}$ heat exchange between the gas phase and drill pipe per unit time, J

$Q_{D,g}$ heat exchange between the gas phase and drill pipe per unit time, J

$Q_{D,m}$ heat exchange between the gas phase and drill pipe per unit time, J

Q_g gas flow rate, m^3/h

q_g mass of gas produced per unit time and thickness, kg/(s m)

R gas constant, 8.314 J/(mol K)

Re Reynolds number of the mixed fluid, dimensionless

R_{sm} solubility of gas in drilling fluid (m^3/m^3).

R_w reservoir radius, m

T temperatures, K

T_a annulus fluid temperature, K

T_c critical temperature, K

T_e reservoir temperatures, K

u_{am} average velocity of the mixed fluid, m/s

u_g velocity of gas, m/s

u_m upward velocity of drilling fluid, m/s

V molar volume of gas, m^3/mol

w_g mass flow rates of the gas, kg/s

w_m mass flow rates of liquid, kg/s

x_i molar content of component *i* liquid gas phase

y_i^{exp} experimental data measured under experimental conditions

y_i molar content of component *i* in the gas phase

$y_i^{predict}$ predicted value

z coordinate along the flow direction, *m*

Z gas compressibility, dimensionless

Z_e gas compressibility coefficients under reservoir

Greek symbols

α well deviation angle, °

ε_e equivalent absolute roughness, dimensionless

μ reservoir fluid viscosity, cp

ρ_{am} average density of the mixed fluid, kg/m^3

ρ_g density of gas at local temperature and pressure, kg/cm^3

ρ_m density of drilling fluid under local temperature and pressure, kg/cm^3

ρ_{sg} density of standard gas under local temperature and pressure, kg/cm^3

φ_i^l fugacity coefficients of component *i* in liquid phase, dimensionless

φ_i^v fugacity coefficients of component i in the gas phase, dimensionless

ω eccentricity factor

Appendix

An experimental database for the CH_4 solubility in water was prepared by collecting the CH_4 solubility values reported in the existing literature, as listed in Table A3.

TABLE A3 CH_4 solubility in water database.

Source	T/K	P/MPa	*N*
[38]	298.15	7.36–17.82	4
[39]	310.93–344.26	4.14–34.47	8
[40]	283.14–298.15	1.151–10.36	14
[41]	373.15–513.15	24.1318–155.133	40
[42]	298.15–398.15	0.27–17.07	43
[43]	275.11–313.11	0.97–18.0	16
[44]	273.15–278.15	0.1–50	24
[45]	277.2–573.2	1.1–13.2	16
[46]	298.2–444.3	2.23–68.91	71
[19]	344	20–100	4
[47]	298.15–303.15	0.317–5.171	17
[48]	298.15–473.15	2.351–150	65
[49]	324.15–375.65	5.6–61.78	26
[50]	313–473	0.34–9.3	26
[51]	298.15	2.3–16.6	22
[23]	274.15–294.05	8.22–40	85
[52]	464.75–545.75	10.3–12.36	7
[53]	283.09–323.56	5.01–19.49	22
[34]	298.15–423.15	4.06–46.91	39
[54]	324.3–398.15	10.13–61.61	18
[55]	273.15–553.15	5–140	238
[56]	427.15–627.15	0.1–197	71
[20]	375	10.9–49.9	8
[57]	298.15	2.33–12.68	19
[58]	298.15–323.15	3–8	6

frontiers | Frontiers in Physics

TYPE Original Research
PUBLISHED 31 October 2022
DOI 10.3389/fphy.2022.1049547

OPEN ACCESS

EDITED BY
Weiqi Fu,
China University of Mining and Technology, China

REVIEWED BY
Jiahui Chen,
University of Alberta, Canada
Youqiang Liao,
Institute of Rock and Soil Mechanics (CAS), China

*CORRESPONDENCE
Xiaohui Sun,
sxh049306@163.com

SPECIALTY SECTION
This article was submitted to Interdisciplinary Physics, a section of the journal Frontiers in Physics

RECEIVED 20 September 2022
ACCEPTED 05 October 2022
PUBLISHED 31 October 2022

CITATION
Wang X, Huang L, Li X, Bi S, Li H, Zhang J and Sun X (2022), Wellbore multiphase flow behaviors of gas kick in deep water horizontal drilling.
Front. Phys. 10:1049547.
doi: 10.3389/fphy.2022.1049547

Wellbore multiphase flow behaviors of gas kick in deep water horizontal drilling

Xiansi Wang[1], Lianlu Huang[1], Xiangpeng Li[1], Shaokun Bi[2], Hua Li[1], Jianbo Zhang[2] and Xiaohui Sun[2]*

[1]Drilling Division, CNPC Offshore Engineering Co., Ltd., Tianjin, China, [2]School of Petroleum Engineering, China University of Petroleum (East China), Huangdao, China

During the deepwater drilling, the complicated gas-liquid-solid multiphase flow will occur if the formation gas enters and migrates in the wellbore. Through understanding of the wellbore flow behaviors is of great importance for the blowout prevention and well control. Considering the dynamic mass and heat transfer process in wellbore caused by alternating ambient temperature field, a multiphase flow model of multicomponent fluid in wellbore is deduced and developed, including the continuity equation, momentum conservation equation and energy conservation equation. Furthermore, the corresponding initial and boundary conditions are proposed for different working conditions in deepwater drilling, and an efficient numerical solution method is established, including dynamic mesh generation method and discrete solution method of partial differential equations. Applied in a deep-water kicking well, the proposed model is used to analyze the multiphase flow rules in the wellbore. The results show that in the process of annular fluid returning from the bottomhole, the pressure generally decreases linearly, while the temperature change is nonlinear. The temperature first rises and then falls at the formation section, and first falls and then rises at the seawater section. Furthermore, the pit gain increases approximately in a quadratic polynomial relationship, caused by the rise and expansion of gas in the wellbore, and the pressure drop and gas influx rate increase at the bottomhole. In the process of kick evolution, the standpipe pressure and bottomhole pressure gradually decrease, which can be an important sign for kick detection.

KEYWORDS

gas kick detection, multiphase flow (G/L/S), deepwater well, numerical solution, transient heat transfer

1 Introduction

During deepwater drilling, the formation gas intrudes into the wellbore and blowout occurs, which is a great threat to safe and efficient drilling. In 2010, the Deepwater Horizon drilling platform in the Gulf of Mexico blew out, causing direct economic losses of more than 68 billion US dollars. In addition, it also caused huge casualties and well completion disasters [1–3]. Therefore, studying the rules of wellbore multiphase flow

during gas kick has important engineering value for accurately understanding the gas invasion process and make well control plan for the blowout prevention.

Since the 1960s, great efforts have been made to study the multiphase flow model in gas kick. Leblanc and Leuis (1968) established a kick model based on the homogeneous flow theory [4], but the model ignores the friction and pressure loss in the annulus and gas-liquid slippage velocity, which is only suitable for simplified calculation. The kick flow model established by Records (1972) considers the influence of friction and pressure loss in the annulus, but the calculation result of the model has a significant error compared with the field measurements [5]. Horberock and Stanbery (1981) established the momentum conservation equation of fluid in vertical pipeline. Based on the theory of homogeneous flow, the gas-liquid flow characteristic are analyzed [6]. Considering gas-liquid slippage and pressure loss of two-phase flow, Santos (1982) introduced the concept of void fraction and established a deep-well kick flow model [7]. Nickens (1987) analyzed the wellbore multiphase flow parameters considering the gas-liquid phase transition, slippage and mass transfer [8]. They studied the effects of wellbore shape, BHA and hydraulic parameters on wellbore pressure distribution. On this basis, Ohara (1995) proposed a deep-water well control model [9], in which the flow process of mud at different stages in the well is divided into several sub models for simulation. In particular, Nunes (2002) proposed an analytical model of wellbore multiphase flow and the corresponding numerical solution method [10]. The model can calculate the pressure distribution and gas distribution in the wellbore and choke line at different times. Wang and Sun (2009) established a multiphase flow model in a gas kick [11], which can be applied to the wellbore multiphase flow simulation in the process of gas kick and well killing in deepwater drilling. Pourafshary et al (2009) considered the coupling between wellbore fluid and reservoir fluid and the slippage of multicomponent gas and liquid phase, and established the unsteady wellbore two-phase flow model assuming that the gas phase and liquid phase are in phase equilibrium on any wellbore section [12]. Lu and Connell (2014) considered the phase transition process in wellbore multiphase flow and established the unsteady model of wellbore liquid injection process based on phase stability analysis and phase separation calculation [13]. Udegbunam et al. (2014) analyzed the influence of uncertainty of parameters such as pipe string dimension, slippage velocity, friction coefficient and reservoir characteristics on flow characteristics during underbalanced drilling [14]. Fu et al. (2020) [15–17] experimentally studied and modelled the methane hydrate formation under bubbly flow condition in the deep-water drilling wellbore. The methane hydrate formation in drilling mud altered the rheology of drilling mud which made it exhibit non-Newtonian behavior [18] and increased the pressure losses of drilling mud in the wellbore [19, 20]. Their works are significant for increasing accuracy of predicting pressure loss in wellbore and provided a solid stone for modelling the multiphase flow behavior in deepwater wellbore. Recently, Sun et al (2018) developed several models to analyze the effect of phase transition on gas kick migration in wellbore [21–29].

During deepwater drilling, the multiphase flow rules of gas kick is more complex than that of onshore well kick, caused by the alternating change of low temperature at seawater section and high temperature at deep formation section. The flow in wellbore is a complex dynamic mass and heat transfer process. Therefore, it is necessary to establish an accurate multiphase and multicomponent flow model to obtain the dynamic distribution of flow parameters such as fluid velocity, pressure and temperature in the process of blowout evolution. In this paper, considering the dynamic mass and heat transfer process in wellbore, a multiphase flow model in wellbore of multicomponent fluid is deduced and established. Furthermore, the corresponding initial and boundary conditions are presented for different working conditions in deepwater drilling and an efficient numerical solution method is established, including dynamic mesh generation method and discrete solution method of partial differential equation. Last, a detailed analysis has been performed to evaluate the wellbore multiphase flow process of a deep-water kicking well.

2 Wellbore multiphase flow model of gas kick

2.1 Assumptions

There are complex changes in multiphase flow parameters in deepwater drilling. The model assumptions are as follows.

1) Fluid flow is regarded as one-dimensional flow along the wellbore, ignoring the rotation of drilling tools and the axial migration of drilling fluid.
2) There is stable radial heat transfer between wellbore and formation, and the rock is homogeneous.
3) Ignore the changes in physical property of formation rock, drilling tools, casing and cement sheath.
4) Ignore the heat generated by the friction of the drilling tool.
5) The dissolution of gas is instantaneous.

2.2 Continuity equation and momentum conservation equation

As a gas kick occurs in deepwater drilling, the gas phase, drilling fluid phase, cuttings phase and hydrate may exist in the wellbore at the same time. According to the principle of mass conservation, the continuity equations of each phase in the wellbore are developed as follows:

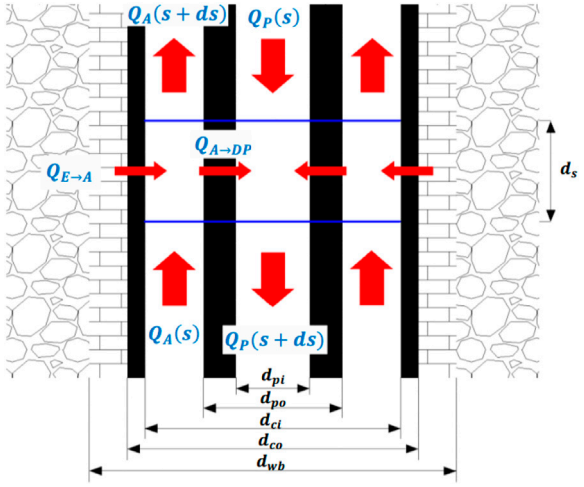

FIGURE 1
Schematic of energy conservation equation derivation in kick multiphase flow model.

$$\frac{\partial\left(E_g A\rho_g\right)}{\partial t}+\frac{\partial}{\partial s}\left(\rho_g v_g E_g A+R_g\rho_g V_w E_w A\right)=q_g+x_g r_H \quad (1)$$

$$\frac{\partial\left(E_w A\rho_w\right)}{\partial t}+\frac{\partial}{\partial s}\left(\rho_w v_w E_w A-R_g\rho_g V_w E_w A\right)=-\left(1+x_g\right)r_H \quad (2)$$

$$\frac{\partial\left(E_c A\rho_c\right)}{\partial t}+\frac{\partial}{\partial s}\left(\rho_c v_c E_c A\right)=q_c \quad (3)$$

$$\frac{\partial\left(E_H A\rho_H\right)}{\partial t}+\frac{\partial}{\partial s}\left(\rho_H v_H E_H A\right)=r_H \quad (4)$$

Where, ρ_g is density of produced gas, kg/m^3; v_g is flow velocity of produced gas, m/s; E_g is the local volume fraction of produced gas, dimensionless; A is local annulus sectional area, m^2; q_g is mass of gas produced per unit thickness per unit time, kg/(s·m); x_g is the mass fraction of natural gas in gas hydrate, dimensionless; r_H is the formation/decomposition rate of gas hydrate per unit length in the wellbore [23–25], kg/(s · m); E_w is local volume fraction of drilling fluid, dimensionless; v_w is local upward velocity of drilling fluid, m/s; R_g is the local solubility of gas, m^3/m^3; ρ_g is the density of gas, kg/m^3; ρ_w and ρ_c are the density of drilling fluid and rock cuttings, kg/m^3; v_w, v_c are the velocity of drilling fluid and cuttings, m/s; q_c is the migration rate of rock cuttings, kg/s.

Based on the momentum conservation principle of fluid in the wellbore, the equation of pressure field distribution is obtained as follows:

$$\begin{aligned}&\frac{\partial}{\partial t}\left(AE_g\rho_g V_g+AE_w\rho_w V_w+AE_c\rho_c V_c+AE_H\rho_H V_H\right)\\&+\frac{\partial\left(AE_g\rho_g V_g^2+AE_w\rho_w V_w^2+AE_c\rho_c V_c^2+AE_H\rho_H V_H^2\right)}{\partial s}\\&+Agcos\alpha\left(E_g\rho_g+E_w\rho_w+E_c\rho_c+E_H\rho_H\right)+\frac{\partial(AP)}{\partial s}+\frac{\partial(AF_r)}{\partial s}\\&=0\end{aligned} \quad (5)$$

2.3 Energy conservation equation

2.3.1 Transient wellbore temperature field

The schematic of energy conservation in the model is shown in Figure 1. Assuming that the flow is gas-liquid two-phase flow, the energy equation of wellbore unsteady flow and heat transfer is proposed. The annular element of the well section below the mudline is analyzed as follows.

① The heat flowing into the micro element from the lower end face $Q_A(s+ds)$

Each parameter is a function of time and position, $T_a=T_a(s,t)$, $m_i=m_i(s,t)$, $C_i=C_i(s,t)$. As shown in Figure 1, the temperature at the lower surface is $T_a+\frac{\partial T_a}{\partial s}ds$, and each parameter is $\sum[(m_iC_i)+\frac{\partial(m_iC_i)}{\partial s}ds]$

$$Q_A(s+ds)=\sum\left[(m_iC_i)+\frac{\partial(m_iC_i)}{\partial s}ds\right]\left(T_a+\frac{\partial T_a}{\partial s}ds\right) \quad (6)$$

Where, i is each component in the wellbore, respectively, g (gas), w (drilling fluid), C (rock cuttings) and H (hydrate); m_i is the mass flow rate of each component, kg/s; C_i is the specific heat capacity of each component, J/(kg· ˚C).

② The heat flowing into the micro element from the lower end face $Q_A(s)$

The temperature at the upper end is T_a,

$$Q_A(s)=\sum(m_iC_i)T_a \quad (7)$$

③ Heat flowing from the formation into the annulus $Q_{E\to A}$

$$Q_{E\to A}=\frac{1}{\alpha}(T_E-T_a)ds \quad (8)$$

$$\alpha=\frac{\sum w_i}{2\pi}\left(\frac{k_E+r_{co}U_A T_D}{r_{co}U_A k_E}\right) \quad (9)$$

In which, U_A is the total heat transfer coefficient between annulus fluid and formation, which is related to the thermal resistance of annulus fluid, casing and cement sheath. Generally, the thermal resistance of steel is small, and the temperature of inner and outer walls of casing can be approximately equal,

$$\frac{1}{U_A}=\frac{1}{h_a}+\frac{r_{ci}\ln(r_{co}/r_{ci})}{k_c}+\frac{r_{co}\ln(r_{wb}/r_{co})}{k_{ce}} \quad (10)$$

T_D is the transient heat transfer function, which is simulated as follows

$$T_D=1.128\sqrt{t_D}\left(1-0.3\sqrt{t_D}\right)\quad 10^{-10}\le t_D\le 1.5 \quad (11)$$

$$T_D=[0.4036+0.5\ln(t_D)]\left(1+\frac{0.6}{t_D}\right)\quad t_D\ge 1.5 \quad (12)$$

$$t_D = \frac{k_e t}{C_e \rho_e r_{wb}^2} \tag{13}$$

In case of the seawater section,

$$\frac{1}{U_A} = \frac{1}{h_a} + \frac{r_{ci}\, ln(r_{rso}/r_{rsi})}{k_{rs}} \tag{14}$$

Where, k_{rs} is the thermal conductivity of riser.

④ Heat flowing into the drilling tool from the annulus $Q_{A\to DP}$

$$Q_{A\to DP} = \frac{1}{\beta_A}(T_a - T_{DP})ds \tag{15}$$

$$\alpha = \frac{\sum w_i}{2\pi r_{pi} U_{DP}} \tag{16}$$

$$\frac{1}{U_{DP}} = \frac{1}{h_{DP}} + \frac{r_{pi}\, ln\left(r_{po}/r_{pi}\right)}{k_p} \tag{17}$$

⑤ Heat change inside the wellbore unit dQ

$$dQ = \frac{\partial}{\partial t}\sum(\rho_i E_i C_i A)T_a ds \tag{18}$$

According to the energy conservation, the heat change inside the unit body = the heat flowing into the unit body—the heat flowing out of the unit body, i.e.

$$dQ = Q_A(s+ds) - Q_A(s) + Q_{E\to A} - Q_{A\to DP} \tag{19}$$

$$\begin{aligned}\frac{\partial}{\partial t}\sum(\rho_i E_i C_i A)T_a ds = &\sum\left[(m_i C_i) + \frac{\partial(m_i C_i)}{\partial s}ds\right]\left(T_a + \frac{\partial T_a}{\partial s}ds\right)\\ &- \sum(m_i C_i)T_a + \frac{1}{\alpha}(T_E - T_a)ds\\ &- \frac{1}{\beta_A}(T_a - T_{DP})ds\end{aligned} \tag{20}$$

Since $\sum[\frac{\partial(m_i C_i)}{\partial s}ds](\frac{\partial T_a}{\partial s}ds) = 0$, we obtain

$$\begin{aligned}\frac{\partial}{\partial t}\sum(\rho_i E_i C_i A)T_a ds = &\sum[(m_i C_i)]\left(\frac{\partial T_a}{\partial s}ds\right)\\ &+ \sum\left[\frac{\partial(m_i C_i)}{\partial s}ds\right](T_a)\\ &+ \sum\left[\frac{\partial(m_i C_i)}{\partial s}ds\right]\left(\frac{\partial T_a}{\partial s}ds\right)\\ &+ \frac{1}{\alpha}(T_E - T_a)ds\\ &- \frac{1}{\beta_A}(T_a - T_{DP})ds \approx \sum\left[\frac{\partial(m_i C_i T_a)}{\partial s}ds\right]\\ &+ \frac{1}{\alpha}(T_E - T_a)ds - \frac{1}{\beta_A}(T_a - T_{DP})ds\end{aligned} \tag{21}$$

Therefore, the temperature field equation in the annulus is obtained as,

$$\begin{aligned}\frac{\partial}{\partial t}\sum(\rho_i E_i C_i A)T_a = &\sum\left[\frac{\partial\sum(m_i C_i T_a)}{\partial s}\right] + \frac{1}{\alpha}(T_E - T_a)\\ &- \frac{1}{\beta_A}(T_a - T_{DP})\end{aligned} \tag{22}$$

Similarly, the equation of temperature field in drill pipe is obtained as,

$$\frac{\partial\left(\rho_w C_w A T_p\right)}{\partial t} + \frac{\partial\left(C_w m_w T_p\right)}{\partial s} = \frac{2}{\beta_A}(T_a - T_{DP}) \tag{23}$$

2.3.2 Ambient temperature field

1) Seawater temperature field.

The complex ambient temperature field is one of the key factors affecting the multiphase flow rules in wellbore. The temperature at seawater section decreases gradually with water depth, and the variation trend is nonlinear. However, the temperature at formation rock section gradually increases with well depth, and the change trend is related to the formation temperature gradient.

The simulation methods of seawater temperature in spring, summer and autumn (Gao, 2007 [30]) are as follows.

① Water depth $h \le 200$ m,

$$\text{Spring: } T_{sea} = \frac{T_s(200-h) + 13.68h}{200} \quad 0 \le h \le 200\,\text{m} \tag{24}$$

$$\text{Summer: } T_{sea} = T_s \quad 0 \le h < 20\,\text{m} \tag{25}$$

$$T_{sea} = \frac{T_s(200-h) + 13.7(h-20)}{180} \quad 20 \le h < 200\,\text{m} \tag{26}$$

$$\text{Autumn: } T_{sea} = T_s \quad 0 \le \text{h} < 50\,\text{m} \tag{27}$$

$$T_{sea} = \frac{T_s(200-h) + 13.7(h-20)}{150} \quad 50 \le \text{h} < 200\,\text{m} \tag{28}$$

$$\text{Winter: } T_{sea} = T_s \quad 0 \le \text{h} < 100\,\text{m} \tag{29}$$

$$T_{sea} = \frac{T_s(200-h) + 13.7(h-20)}{100} \quad 100 \le \text{h} < 200\,\text{m} \tag{30}$$

Where, T_{sea} is seawater temperature, ˚C; T_s is the seawater surface temperature, ˚C.

② Water depth $h > 200$ m

$$T_{sea} = 39.4 + \frac{37.1}{(1 + e^{(h+130.1)/402.7})} \quad 0 \le h < 100\text{m} \tag{31}$$

2) Formation temperature field.

The variation of formation temperature field in deep-water drilling is similar to that in onshore drilling. The formation temperature gradient is mainly related to the lithology and sedimentary characteristics of the rocks.

$$T_E(h) = T_0 + \int_{h_0}^{h} \Delta T\, dL \tag{32}$$

Where, T_0 is seawater temperature at mudline, °C; h_0 is the sea water depth, m; h is the vertical depth, m.

3 Definite solution condition and numerical solution method

3.1 Initial and boundary conditions

3.1.1 Initial condition

1) Initial conditions of temperature field

① Start circulating

At initial condition, the fluid temperature in the wellbore is the same as the ambient temperature:

$$T_p = T_a = T_E \tag{33}$$

② Gas kick process

The initial condition of temperature field in gas kick is the temperature distribution of drill pipe and annulus calculated at the moment before gas kick.

2) Initial conditions of pressure field

During normal drilling, there is no gas influx

$$E_H(s,0) = E_g(s,0) = 0 \tag{34}$$

$$E_c(s,0) = \frac{E_g(s,0)}{C_c V_{sl}(s,0) + V_{cr}(s,0)} \tag{35}$$

$$E_w(s,0) = 1 - E_c(s,0) \tag{36}$$

$$V_{sw}(s,0) = \frac{Q_m}{A(s)} \tag{37}$$

$$V_w(s,0) = \frac{V_{sw}(s,0)}{E_w(s,0)} \tag{38}$$

$$V_{sc}(s,0) = \frac{q_c}{\rho_c A(s)} \tag{39}$$

$$V_c(s,0) = \frac{V_{sc}(s,0)}{E_c(s,0)} \tag{40}$$

$$P(s,0) = P(s) \tag{41}$$

Where, Q_m is the displacement of mud pump, m^3/s; q_c is the displacement of rock cuttings, m^3/s.

Regarding the calculation of flow parameters during pump shutdown and well killing, the initial conditions are the distribution of flow parameters in the wellbore at the moment before the change of working conditions.

3.1.2 Boundary condition

1) Boundary conditions of temperature field

Because the liquid temperature at the drill string inlet can be measured directly, the boundary condition of the temperature field is

$$T_p(0,t) = T_{in} \tag{42}$$

At the same time, the temperatures of the liquid in the drill string and the annulus liquid at the bottom of the well are equal, i.e.

$$T_p(H,t) = T_a(H,t) \tag{43}$$

Where, T_{in} is the inlet temperature of drill string, °C; T_{in} is the well depth, m.

2) Boundary conditions of pressure field and velocity field

During a gas kick, the boundary conditions of pressure and flow velocity parameters are as follows.

$$P(0,t) = P_s \tag{44}$$

$$q_g(H,t) = q_g \tag{45}$$

$$q_c(H,t) = q_c \tag{46}$$

$$r_H(i,t) = r_H \tag{47}$$

Where, P_s is wellhead back pressure, Pa.

3.2 Numerical solution method

3.2.1 Meshing

It is very difficult to obtain the analytical solution directly for the established multiphase flow model. In this study, the corresponding numerical algorithm is established for the above model. Firstly, the wellbore needs to be meshed, and the spatial grid length (usually long at the bottom and short at the top) is dynamically selected according to the fluid velocity and gas rising velocity in the wellbore. Then set the initial time step, and automatically adjust the time step according to the calculation speed requirements.

According to the gas rising speed v_g, average fluid velocity v_m, and the time step Δt_j, the time step is determined as

$$\Delta S_j = \frac{\Delta t_j |U|}{C_0} \tag{48}$$

Where, Δt_j is the time step of node j, s; ΔS_j is the spatial step of node j, m; $|U|$ is the absolute value of the correlation speed at node j, $U = \min(v_g, v_m)$; C_0 is the Courant number. In order to achieve the accuracy and stability of calculation, $C_0 < 1$。

The schematic diagram of spatial grid division is shown in Figure 2. The length of any spatial grid is $\Delta S_j = S_{j+1} - D_j$. Theoretically, because the velocity in the drill pipe is greater than that in the annulus, in order to speed up the calculation. The spatial grid step in the drill pipe should be greater than that in the annulus at the same position. However, for facilitating the coupling calculation between drill pipe and annulus and ensure the calculation accuracy, the spatial grid in drill pipe is the same as that in annulus.

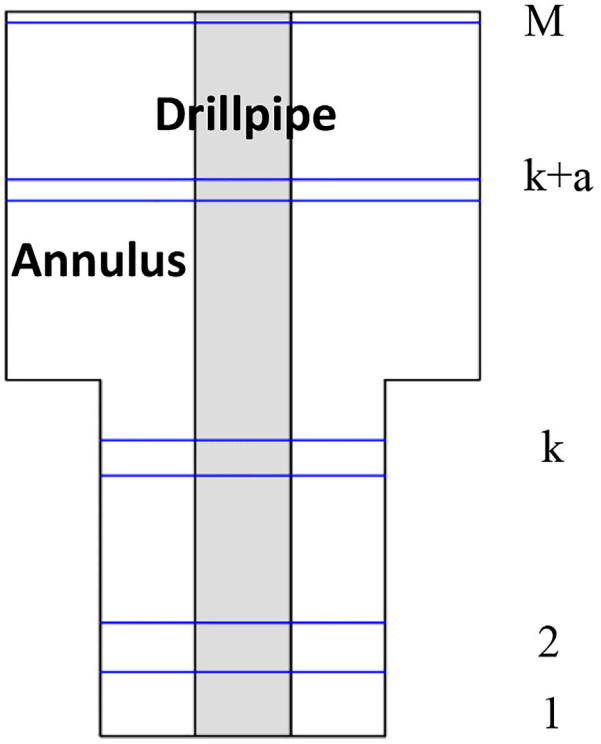

FIGURE 2
Discrete grids of space domain and time domain for kick multiphase flow model.

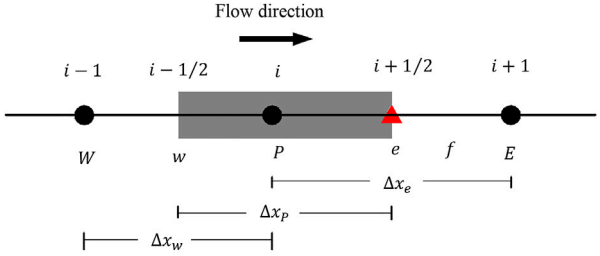

FIGURE 3
Schematic of space domain in *x* direction.

3.2.2 Model discretization

The dynamic grid difference model are used in this study. Taking the gas phase continuity equation as an example, the CV discrete method (control volume method) is adopted,

$$\frac{\partial\left(E_g A\rho_g\right)}{\partial t}+\frac{\partial}{\partial s}\left(\rho_g v_g E_g A+R_g\rho_g V_w E_w A\right)=q_g+x_g r_H \quad (49)$$

The schematic of spatial grid division is shown in Figure 3. Where, E represents $i+1$ node, W represents $i-1$ node, P represents i node, e represents $i+1/2$ node, and w represents $i-1/2$ node.

Eq. 49 can be differenced as follows:

$$\int\frac{\partial}{\partial t}\left(E_g A\rho_g\right)dV\approx\left[\left(E_g A\rho_g\right)_P-\left(E_g A\rho_g\right)_P^0\right]\frac{\Delta V}{\Delta T} \quad (50)$$

$$\begin{aligned}\int\frac{\partial}{\partial s}\left(\rho_g v_g E_g A+R_g\rho_g V_w E_w A\right)dV\approx&\left[\xi_e\left(\rho_g v_g E_g A+R_g\rho_g V_w E_w A\right)_E\right.\\&\left.+\bar{\xi}_e\left(\rho_g v_g E_g A+R_g\rho_g V_w E_w A\right)_P\right]A_e\\&-\left[\xi_w\left(\rho_g v_g E_g A+R_g\rho_g V_w E_w A\right)_P\right.\\&\left.+\bar{\xi}_e\left(\rho_g v_g E_g A+R_g\rho_g V_w E_w A\right)_W\right]A_w\end{aligned} \quad (51)$$

$$\int R_\phi dV\approx\bar{R}_\phi\Delta V-R_\phi^{'}\phi_P\Delta V\quad R_\phi=Rq_g+x_g r_H \quad (52)$$

Where, ξ and ξ' is the convection difference weight factor. The difference form of the continuity equation of gas phase is

$$\begin{aligned}&\left[\left(E_g A\rho_g\right)_P-\left(E_g A\rho_g\right)_P^0\right]\frac{\Delta V}{\Delta T}+\left\{\left[\xi_e\left(\rho_g v_g E_g A+R_g\rho_g V_w E_w A\right)_E\right.\right.\\&\left.+\bar{\xi}_e\left(\rho_g v_g E_g A+R_g\rho_g V_w E_w A\right)_P\right]A_e\\&-\left[\xi_w\left(\rho_g v_g E_g A+R_g\rho_g V_w E_w A\right)_P\right.\\&\left.\left.+\bar{\xi}_w\left(\rho_g v_g E_g A+R_g\rho_g V_w E_w A\right)_W\right]A_w\right\}\\&=\bar{R}_\phi\Delta V-R_\phi^{'}\phi_P\Delta V\end{aligned} \quad (53)$$

Similarly, the momentum equation and energy equation of wellbore multiphase flow model can be obtained and solved [29].

4 Simulation analysis

Using the proposed multiphase flow model, the flow parameter, and temperature and pressure distributions in the drill pipe and annulus are analyzed. The parameters of the field well are shown in Tables 1, 2.

4.1 Temperature and pressure fields

Figure 4 shows the temperature distribution in the wellbore under different displacements. On the one hand, the heat in the annulus is transferred to the drill pipe, and the mud temperature in the drill pipe increases gradually. On the other hand, the mud in the annulus exchanges heat with the surroundings. In the seawater section, the heat in the annulus is mainly transmitted to the seawater; and in the formation section, the heat in the annulus is mainly transmitted to the formation section. At a specific well depth, when the heat absorbed by the mud in the annulus from the outside is greater than the heat transmitted to

TABLE 1 Thermo-dynamic parameters in the case.

Parameter	Density (kg/m³)	Specific heat capacity [J/(kg·°C)]	Thermal conductivity [W/(m·K)]
Drill pipe/Casing	7800	400	53.0
Cement	2000	882	0.085
Formation	2650	1000	5.2

TABLE 2 Parameters of wellbore geometry structure.

Parameter	Inner radius (m)	Outer radius (m)	Roughness (mm)
Drill pipe	0.119	0.140	0.005
Casing	0.222	0.244	0.005
Cement	0.244	0.384	--

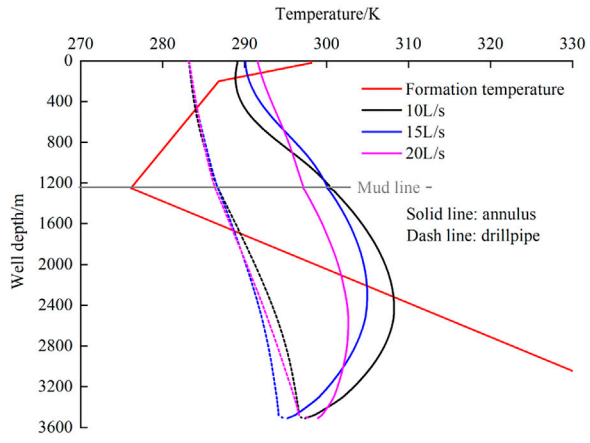

FIGURE 4
Temperature distribution in the drill pipe and annulus with different displacements.

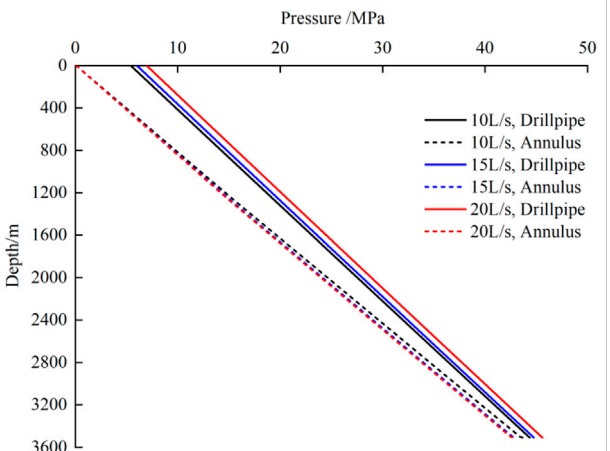

FIGURE 5
Pressure distribution in the drill pipe and annulus with different discharge capacities.

the drill pipe, its temperature gradually increases; on the contrary, its temperature gradually decreases. Therefore, when the mud returns from the annulus, the temperature gradually rises near the bottomhole. As the formation temperature decreases and enters the seawater section, the annulus temperature decreases gradually. Near the sea surface, the mud temperature rises slightly.

With the increase of displacement, the temperature variation rate in drill pipe and annulus decreases. Because the larger the mud displacement, the less sufficient the heat exchange with the surroundings.

Figure 5 shows the wellbore pressure distribution under different displacements. With the increase of well depth, the pressure in drill pipe and annulus varies linearly. However, affected by the influence of annulus friction and bit pressure drop, the pressure in the drill pipe is greater than that in the annulus.

4.2 Sensitivity analysis

As seen in Figure 6, the difference between inflow and outflow rates increases linearly with time. Because the change of outlet flow during gas kick is mainly caused by gas rise in the wellbore and the continuous entry of new gas into the wellbore. In the early stage, the gas mainly remain at the bottomhole, and its volume change is inversely proportional to pressure, while the

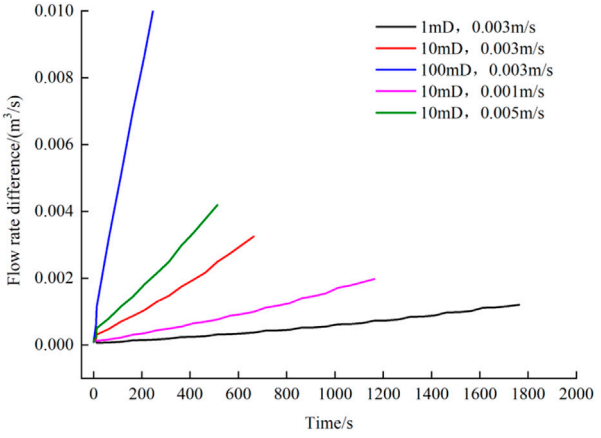

FIGURE 6
Change of mud flow rate in the inlet and outlet under different kick conditions.

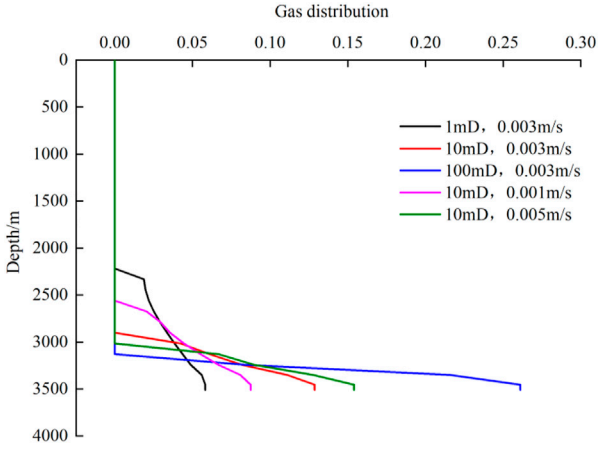

FIGURE 8
Gas distribution in the annulus when pit gain is 1 m^3 under different kick conditions.

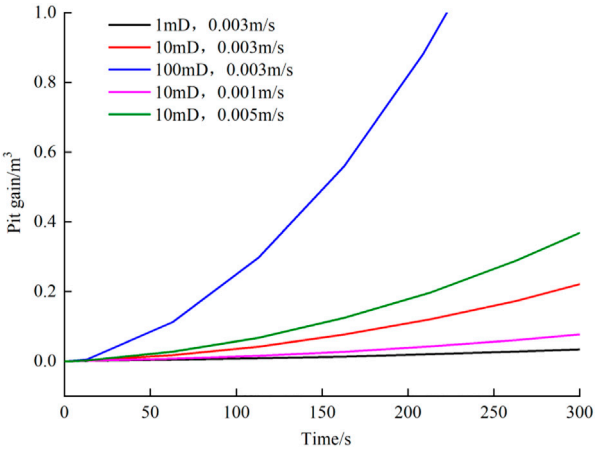

FIGURE 7
Change of pit gain with time under different kick conditions.

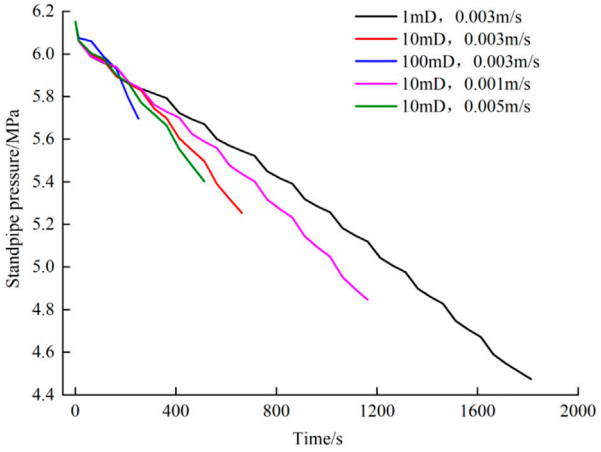

FIGURE 9
Curve of standpipe pressure variation under different kick conditions.

change of wellbore pressure is linearly related to the well depth. Therefore, the expansion of gas volume is approximately proportional to the well depth. On the other hand, at the initial stage, regardless of the change of bottom hole pressure, gas enters the wellbore at a constant overflow rate.

Figure 7 shows the change curve of mud pit increment during overflow. When the time is 5 min, the pit gain increases approximately in a quadratic polynomial relationship with the increase of time. Under the same conditions, with the increase of ROP(Rate of Penetration) or reservoir permeability, the pit gain increases, and the increasing range is accelerated. Because with the increase of permeability and reservoir exposure thickness, various effects such as bottom hole pressure reduction, overflow speed acceleration, bubble rise and expansion, result in the intensification of gas kick.

Therefore, when drilling in high pressure and high permeability formation, the ROP (rate of penetration) should be controlled and the early detection of overflow should be strengthened.

Figure 8 shows the gas distribution when the pit gain is 1 m^3. As seen, with the increase of reservoir permeability or ROP, the shorter the time required for pit gain reaching 1 m^3, the shorter the gas rising distance and the lower the gas volume fraction. Therefore, the gas section with high void fraction is prone to

rapid expansion at the wellhead, which has a greater impact on well control.

Figure 9 shows the variations of the standpipe pressure with time. The change of standpipe pressure is the same as that of bottom hole pressure. At the initial stage of gas kick, the previous gas in the wellbore slip and expand at a constant rising speed, and the new gas from the reservoir enter the wellbore at a constant rate. The change of bottomhole pressure is mainly caused by the loss of hydrostatic pressure in the wellbore.

5 Conclusion

Using the proposed model, the multiphase flow rules in the wellbore during the gas kick is analyzed. The results show that in the process of annular fluid returning from the bottom of the well, the pressure generally decreases linearly while the temperature change is nonlinear. It first rises and then falls at the formation section, and first falls and then rises at the seawater section. With the increase of displacement, the temperature change rate in drill pipe and annulus decreases. Because the larger the mud displacement, the less sufficient the heat exchange with the surroundings. In the process of gas kick, the difference between inflow and outflow rates increases linearly with time, and the pit gain increases approximately in a quadratic polynomial relationship. Furthermore, in the process of kick evolution, the standpipe pressure and bottomhole pressure gradually decrease.

Data availability statement

The original contributions presented in the study are included in the article/supplementary material, further inquiries can be directed to the corresponding author.

Author contributions

XW: Methodology; LH: Original draft preparation XL: Investigation; SB: Supervision: HL: Software, Validation: JZ: Material correlation calculation; XS: Writing- Reviewing and Editing.

Funding

This work was supported by the National Natural Science Foundation–Youth Foundation (5210040269), Postdoctoral innovative talents support program in Shandong Province (SDBX2020005), Postdoctoral innovative talents support program in China (BX2021374) and Postdoctoral Applied Research Project of Qingdao (qdyy20200086).

Conflict of interest

XW, LH, XL, HL, were empolyed by CNPC Offshore Engineering Co., Ltd.

The remaining authors declare that the research was conducted in the absence of any commercial or financial relationships that could be construed as a potential conflict of interest.

Publisher's note

References

1. Levy JK, Gopalakrishnan C. Promoting ecological sustainability and community resilience in the US Gulf Coast after the 2010 Deepwater Horizon oil spill. *J Nat Resour Pol Res* (2010) 2(3):297–315. doi:10.1080/19390459.2010.500462

2. Hagerty CL. *Deepwater Horizon oil spill: Selected issues for congress*. Diane Publishing (2010).

3. Norse EA, Amos J. Impacts, perception, and policy implications of the Deepwater Horizon oil and gas disaster. *Envtl L Rep News Anal* (2010) 40:11058.

4. Leblanc JL, Lewis RL. A mathematical model of a gas kick. *J Pet Technology* (1968) 20(8):888–98. doi:10.2118/1860-pa

5. Records LR. Mud system and well control. *Pet Eng* (1972) 44:97–108.

6. Hoberock LL, Stanbery SR. Pressure dynamics in wells during gas kicks: Part 1 - component models and results. *J Pet Technology* (1981) 33(8):1357–66. doi:10.2118/9256-pa

7. Santos OLA. *Mathematical model of a gas kick when drilling in deep waters*. Colorado School of Mines (1982).

8. Nickens HVA. A dynamic computer model of a kicking well. *SPE Drilling Eng* (1987) 2(2):159–73. doi:10.2118/14183-pa

9. Ohara S. *Improved method for selecting kick tolerance during deepwater drilling operations*. Baton Rouge: Louisiana State University and Agricultural & Mechanical College (1996).

10. Nunes JOL, Bannwart AC, Ribeiro PR. Mathematical modeling of gas kicks in deep water scenario[C]. In: IADC/SPE Asia Pacific Drilling Technology (2002).

11. Wang ZY, Sun BJ. Annular multiphase flow behavior during deep water drilling and the effect of hydrate phase transition. *Pet Sci* (2009) 6(1):57–63. doi:10.1007/s12182-009-0010-3

12. Pourafshary P, Varavei A, Sepehrnoori K, Podio A. A compositional wellbore/reservoir simulator to model multiphase flow and temperature distribution. *J Pet Sci Eng* (2009) 69:40–52. doi:10.1016/j.petrol.2009.02.012

13. Lu M, Connell LD. Transient, thermal wellbore flow of multispecies carbon dioxide mixtures with phase transition during geological storage. *Int J Multiphase Flow* (2014) 63:82–92. doi:10.1016/j.ijmultiphaseflow.2014.04.002

14. Udegbunam JE, Lohne HP, Fjelde KK, Arild Ø, Ford E Improved underbalanced operations with uncertainty analysis[C]. In: IADC/SPE Drilling Conference and Exhibition (2014).

15. Fu WQ, Wang ZY, Zhang JB, Sun BJ. Methane hydrate formation in a water-continuous vertical flow loop with xanthan gum. *Fuel* (2020) 265:116963. doi:10.1016/j.fuel.2019.116963

16. Sun BJ, Fu WQ, Wang N, Wang ZY, Gao YH. Multiphase flow modeling of gas intrusion in oil-based drilling mud. *J Pet Sci Eng* (2019) 174:1142–51. doi:10.1016/j.petrol.2018.12.018

17. Fu WQ, Wang ZY, Chen LT, Sun BJ. Experimental investigation of methane hydrate formation in the carboxmethylcellulose (CMC) aqueous solution. *SPE J* (2020) 25(3):1042–56. doi:10.2118/199367-pa

18. Fu WQ, Wei W, Wang H, Huang BX, Wang ZY. Study on the rheology of CO_2 hydrate slurry by using the capillary method. *J Mar Sci Eng* (2022) 10:1224. doi:10.3390/jmse10091224

19. Fu WQ, Yu J, Xiao Y, Wang CL, Huang BX, Sun B. A pressure drop prediction model for hydrate slurry based on energy dissipation under turbulent flow condition. *Fuel* (2022) 311(2022):122188. doi:10.1016/j.fuel.2021.122188

20. Fu WQ, Yu J, Xu YH, Wang CL, Huang BX, Sun BJ. A pressure drop prediction model for hydrate slurry based on energy dissipation under laminar flow condition. *SPE J* (2022) 27(04):2257–67. doi:10.2118/209586-pa

21. Liao Y, Wang Z, Sun X, Lou W, Liu H, Sun B. Modeling of hydrate dissociation surface area in porous media considering arrangements of sand grains and morphologies of hydrates. *Chem Eng J* (2022) 312:133830. doi:10.1016/j.cej.2021.133830

22. Liao Y, Wang Z, Sun X, Sun B, Linga P. Modeling and characterizing the thermal and kinetic behavior of methane hydrate dissociation in sandy porous media. *Appl Energ* (2022) 312:118804. doi:10.1016/j.apenergy.2022.118804

23. Sun X, Wang Z, Sun B, Chen L, Zhang J. Modeling of dynamic hydrate shell growth on bubble surface considering multiple factor interactions. *Chem Eng J* (2018) 331:221–33. doi:10.1016/j.cej.2017.08.105

24. Sun X, Sun B, Wang Z, Chen L, Gao Y. A new model for hydrodynamics and mass transfer of hydrated bubble rising in deep water. *Chem Eng Sci* (2017) 173:168–78. doi:10.1016/j.ces.2017.07.040

25. Sun X, Sun B, Wang Z, Chen L, Gao Y. A hydrate shell growth model in bubble flow of water-dominated system considering intrinsic kinetics, mass and heat transfer mechanisms. *Int J Heat Mass Transfer* (2018) 117:940–50. doi:10.1016/j.ijheatmasstransfer.2017.10.045

26. Sun X, Sun B, Zhang S, Wang Z, Gao Y, Li H. A new pattern recognition model for gas kick diagnosis in deepwater drilling. *J Pet Sci Eng* (2018) 167:418–25. doi:10.1016/j.petrol.2018.04.035

27. Sun X, Sun B, Gao Y, Wang Z. A model of multiphase flow dynamics considering the hydrated bubble behaviors and its application to deepwater kick simulation. *J Energ Resour Technology* (2018) 140(8). doi:10.1115/1.4040190

28. Sun X, Wang Z, Li H, He H, Sun B. A simple model for the prediction of mutual solubility in CO_2-brine system at geological conditions. *Desalination* (2021) 504:114972. doi:10.1016/j.desal.2021.114972

29. Sun B, Sun X, Wang Z, Chen Y. Effects of phase transition on gas kick migration in deepwater horizontal drilling. *J Nat Gas Sci Eng* (2017) 46:710–29. doi:10.1016/j.jngse.2017.09.001

30. Gao Y. *Study on multi-phase flow in wellbore and well control in deep water drilling*. DongyingEast China: China University of Petroleum (2007).

frontiers | Frontiers in Physics

TYPE Brief Research Report
PUBLISHED 10 November 2022
DOI 10.3389/fphy.2022.1050229

OPEN ACCESS

EDITED BY
Jianjun Zhu,
China University of Petroleum, Beijing, China

REVIEWED BY
Yingtao Yang,
University of Aberdeen, United Kingdom
Jinjie Wang,
China University of Geosciences Wuhan, China

*CORRESPONDENCE
Jinsheng Sun,
sunjsdri@cnpc.com.cn
Bo Zhang,
zhangboupc@126.com

SPECIALTY SECTION
This article was submitted to Interdisciplinary Physics, a section of the journal Frontiers in Physics

RECEIVED 21 September 2022
ACCEPTED 17 October 2022
PUBLISHED 10 November 2022

CITATION
Cao L, Sun J, Zhang B, Lu N and Xu Y (2022), Sensitivity analysis of the temperature profile changing law in the production string of a high-pressure high-temperature gas well considering the coupling relation among the gas flow friction, gas properties, temperature, and pressure. *Front. Phys.* 10:1050229. doi: 10.3389/fphy.2022.1050229

Sensitivity analysis of the temperature profile changing law in the production string of a high-pressure high-temperature gas well considering the coupling relation among the gas flow friction, gas properties, temperature, and pressure

Lihu Cao[1,2], Jinsheng Sun[1]*, Bo Zhang[3]*, Nu Lu[4] and Yuqiang Xu[1]

[1]School of Petroleum Engineering, China University of Petroleum (East China), Qingdao, China, [2]Oil and Gas Engineering Research Institute of Tarim Oilfield, PetroChina, Beijing, China, [3]CNPC Research Institute of Safety and Environment Technology, Beijing, China, [4]PetroChina Research Institute of Petroleum Exploration and Development, Beijing, China

The temperature profile plays an important role in well integrity, flow assurance, and well test. Meanwhile, the impact of engineering conditions should not be ignored while calculating the well temperature profile. Therefore, in this study, we established a model to analyze the changing law of the temperature profile inside the production string of a high-pressure/high-temperature gas well (HPHT gas well). The proposed model considers the flow friction caused by a high production rate. Meanwhile, the variations in gas properties are taken into account to increase the model accuracy, including gas density, flow velocity, and viscosity. The analysis indicates that the temperature in the production string decreases more and more quickly from the reservoir to the wellhead. The wellhead temperature changes more and more slowly with time. When the reservoir temperature is too low to maintain production, it is useful to regulate the production rate or inject the thermal insulating fluid into the annulus to avoid the block caused by wax deposition or hydrate deposition. Considering the sensitivity, feasibility, and cost, it is recommended to change the well temperature profile by adjusting the production rate. If not applicable, the thermal conductivity can also be optimized to change the temperature profile.

KEYWORDS

HPHT gas well, temperature profile, production string, coupling relation, changing law, sensitivity analysis

Introduction

Due to the worldwide rapid increase in the consumption and extensive application of natural gas for both industrial and civil purposes, natural gas development has stepped into more harsh strata and conditions, such as gas hydrate [1–3], shale/tight gas [4, 5], deep water formation [6, 7], deep/ultra-deep stratum [8, 9], and coalbed methane [10]. Among the aforesaid resources of natural gas, the deep/ultra-deep stratum has great potential for its rich reserves and high productivity. Deep/ultra-deep natural gas is usually buried 5,000 m or deeper under the ground, so the bottom hole temperature can be as high as 180 °C [11, 12]. As a result, the temperature profile in the production string is unavoidably changed by the natural gas from the reservoir. Meanwhile, the temperature profile is an important index for production safety. The applications are as follows. First is well integrity. The increase in temperature can lead to trapped annular pressure [13, 14]. This can cause casing collapse [15, 16], cement integrity failure [17, 18], packer sealing failure [19], and tubing deformation [20]. In addition to trapped annular pressure, thermal stress would also damage well integrity [21], such as the tubing buckling and cement strength reduction. Second is flow assurance. The wax and gas hydrate would block the production pathway when the temperature is not high enough [22, 23]. In some gas wells with high content of sulfur, sulfur deposition can also block the production pathway [24]. When the abovementioned incidents happen, effective measures such as heating, chemical plugging removal, and ultrasound removal [25, 26] must be taken to restart production. Third is the production test. The well temperature distribution can reflect the reservoir energy, so it is a classical method to estimate the productivity by analyzing the wellbore transient temperature during the production test [27, 28].

Henceforth, substantial efforts have been devoted to calculate the wellbore temperature. The available research works indicate that the calculation should consider different engineering conditions, such as cement hydration [29], drilling circulation [30], thermal insulation [31], and gas properties [32, 33]. For an HPHT gas well, there are two factors that cannot be ignored: first, the gas flow friction would generate heat and decrease pressure because of the high production rate [34]. Second, the gas properties would vary because the temperature and pressure decrease remarkably from the reservoir to the wellhead. For this reason, this study establishes a model to analyze the changing law of the temperature profile in HPHT gas wells. The model considers the gas flow friction and variation in properties in order to match the actual condition as closely as possible. A dimensionless index is introduced to evaluate the influencing factors, thus providing support for safe and effective production of HPHT gas wells.

Calculation method of the temperature profile inside the production string

Conservation law in the production string

The reservoir gas is the heat resource to redistribute the wellbore temperature. To calculate the temperature, some assumptions are essential. First, the wellbore cross-section is taken as a circle, and the pipes are concentric. Second, thermal conductivity is used to express the wellbore heat transfer capacity. Third, the production is stable without large fluctuations, and the heat transfer along the flow direction is so minor that it can be ignored. Based on the aforementioned assumptions, the energy conservation equation can be established in the micro-unit of the production string, including the internal energy, kinetic energy, pressure energy, gravitational potential energy, and heat transfer, as expressed by Eq. 1:

$$C_f \frac{dT_f}{dz} + v_f \frac{dv_f}{dz} + \frac{1}{\rho_f}\frac{dp}{dz} + g\sin\theta + \frac{1}{w_f}\frac{dQ}{dz} = 0 \tag{1}$$

where C_f is the gas heat capacity inside the production string, J/(kgK); dT_f is the gas temperature change inside the production string, K; dz is the length of the micro-unit of the production string, m; v_f is the flow velocity of gas, m/s; dv_f is the flow velocity change of gas, m/s; ρ_f is the gas density inside the production string, kg/m^3; p is the gas pressure inside the production string, Pa; g is the gravity speed, m/s^2; θ is the well inclination angle, °; w_f is the gas mass flow rate, kg/s; and dQ is the heat transfer along the well radial direction, J/s.

In addition to the energy conservation law, the momentum conservation law can also be applied in the micro-unit of the production string, as expressed by Eq. 2:

$$\frac{dp}{dz} + \rho_f g\sin\theta + f\frac{\rho_f v_f^2}{2d_{tn}} + \rho_f v_f \frac{dv_f}{dz} = 0 \tag{2}$$

where f is the friction efficient between the gas flow and production string, dimensionless; and d_{tn} is the inner diameter of the production string, m.

Likewise, the mass conservation law can also be applied in the micro-unit of the production string, as expressed by Eq. 3:

$$\rho_f \frac{dv_f}{dz} + v_f \frac{d\rho_f}{dz} = 0. \tag{3}$$

Heat transfer along the well radial direction

The heat transfers through the tubing, annular liquid, casing, and cement sheath and finally comes to the formation. This process can be divided into two parts. The

first part is the heat transfer from the production string to the cement sheath and the second is from the cement sheath to the formation. According to the semi-steady method [35, 36], the first part can be seen as a state, so the heat transfer can be expressed by Eq. 4:

$$dQ_{rw} = \frac{T_f - T_h}{R_{to}} dz \tag{4}$$

where dQ_{rw} is the heat transfer from the production string to the cement sheath, J/s; T_f is the gas temperature inside the production string, K; T_h is the temperature of the cement sheath, K; and R_{to} is the thermal resistance from the production string to the cement sheath, mk/W.

As shown in Figure 1, R_{to} is the thermal resistance from the production string to the cement sheath and can be obtained by the thermal resistance series principle, as expressed by Eq. 5:

$$R_{to} = R_{tct} + R_{cht} + \sum_{k=1}^{m} R_{tc}^{k} + \sum_{j=1}^{n} R_{te}^{j} \tag{5}$$

where R_{tct} is the thermal resistance of the tubing wall, mk/W; R_{cht} is the thermal resistance of the annular liquid, mk/W; R_{tc}^{k} is the thermal resistance of the kth casing wall, mk/W; and R_{te}^{j} is the thermal resistance of the jth cement sheath, mk/W.

Hasan and Kabir [37] verified that the heat transfer from the cement sheath to the formation conforms to Fourier heat conduction law, which can be expressed by Eq. 6:

$$dQ_{rf} = \frac{2\pi\lambda e (T_h - T_e)}{T_D} dz \tag{6}$$

where λ_e is the formation of thermal conductivity outside the cement sheath, W/(mk); T_e is the temperature of the formation outside the cement sheath, k; and T_D is the dimensionless temperature of the formation outside the cement sheath, dimensionless.

The formation temperature can be expressed by Eq. 7 when the formation temperature is seen as a linear distribution:

$$T_e = T_o + g_t (h - z) \tag{7}$$

where T_o is the surface ground temperature, k; g_t is the geothermal gradient, k/100 m; h is the well depth, m; and z is the distance from the formation outside the cement sheath to the well bottom, m.

The dimensionless temperature of formation can be expressed by Eqs 8 and 9, as proposed by Hasan and Kabir [37]:

$$T_D = \begin{cases} 1.1281\sqrt{t_D}\left(1 - 0.3\sqrt{t_D}\right), & t_D \le 1.5, \\ (0.4063 + 0.5\ln t_D)(1 + 0.6/t_D), & t_D > 1.5 \end{cases} \tag{8}$$

$$tD = \frac{t\alpha e}{rw^2} \tag{9}$$

where t_D is the dimensionless production time, dimensionless; t is the production time, s; α_e is the formation thermal diffusion coefficient, m^2/s; and r_w is the wellbore radius, m.

According to the semi-steady method and the conservation principle of radial heat flow, the heat transfer in the two aforementioned parts is equal. Then, the temperature of the cement sheath, T_h, can be expressed by Eq. 10:

$$T_h = \frac{T_D T_f + 2\pi\lambda_e R_{to} T_e}{T_D + 2\pi\lambda_e R_{to}}. \tag{10}$$

The heat transfer on the radial direction can be obtained by combining Eq. 10 and Eq. 6, as expressed by Eq. 11:

$$dQ = \frac{2\pi\lambda_e (T_f - T_e)}{T_D + 2\pi\lambda_e R_{to}} dz. \tag{11}$$

Impact of the gas flow friction

The gas flow friction can increase the gas internal energy while decreasing the pressure energy. The friction efficient is the key parameter to calculate gas flow friction [38], as expressed by Eq. 12:

$$f = \begin{cases} \dfrac{64}{\mathrm{Re}}, & \mathrm{Re} \le 2000 \\ \left[1.14 - 21g\left(\dfrac{Ra}{d_{tn}} + \dfrac{21.25}{\mathrm{Re}^{0.9}}\right)\right]^{-2}, & \mathrm{Re} > 2000 \end{cases} \tag{12}$$

where R_a is the roughness of the production string inner wall, m; and Re is the Reynolds number, dimensionless.

The Reynolds number can be expressed by Eq. 13:

$$\mathrm{Re} = \frac{\rho_f v_f d_{tn}}{\mu} \tag{13}$$

where μ is the gas viscosity, Pas.

After the friction efficient is obtained, the gas pressure inside the production string can be expressed by Eq. 14:

$$\frac{dp}{dz} = -\rho_f g \sin\theta - f\frac{\rho_f v_f^2}{2d_{tn}} - \rho_f v_f \frac{dv_f}{dz} \tag{14}$$

Likewise, the gas temperature in the production string can be obtained by substituting Eq. 15 and Eq. 11 into Eq. 1, as expressed by Eq. 14:

$$\frac{dT_f}{dz} = f\frac{\rho_f v_f^2}{2C_f d_{tn}} - \frac{2\pi\lambda_e (T_f - T_e)}{w_f C_f (T_D + 2\pi\lambda_e R_{to})} \tag{15}$$

Impact of the gas properties

According to the mass conservation law, the change of gas flow velocity can be calculated by Eq. 16:

$$\frac{dv_f}{dz} = -\frac{v_f d\rho_f}{\rho_f dz} \tag{16}$$

Natural gas is compressible, so its density can be expressed by Eq. 16:

$$\rho_f = \frac{p_f M_g}{Z_g R T_f} \tag{17}$$

where M_g is the molar mass of gas, kg/mol; Z_g is the gas compression factor, dimensionless; and R is the gas constant, J/(kgmol).

The gas compression factor is related to the pressure and temperature [39], as expressed by Eq. 18:

$$\begin{cases} Z_g = \dfrac{A_1 + A_2 \ln p_r + A_3 (\ln p_r)^2 + A_4 (\ln p_r)^3 + A_5/T_r + A_6/T_r^2}{1 + A_7 \ln p_r + A_8 (\ln p_r)^2 + A_9/T_r + A_{10}/T_r^2} \\ p_r = \dfrac{10^{-6} p_f}{4.666 + 0.103\gamma_g - 0.25\gamma_g^2}, \\ T_r = \dfrac{273.15 + T_f}{93.3 + 181\gamma_g - 7\gamma_g^2}, \end{cases} \tag{18}$$

where A_1, A_2, A_3, A_4, A_5, A_6, A_7, A_8, A_9, and A_{10} are constants, dimensionless; p_r is the pseudo-contrast pressure, dimensionless; T_r is the pseudo-contrast temperature, dimensionless; and γ_g is the gas relative density, dimensionless.

The value of the constants used in Eq. 17 are as follows: A1 = 1.1153, A2 = 0.079, A3 = 0.01588, A4 = 0.00886, A5 = −2.1619, A6 = 1.1575, A7 = −0.05368, A8 = 0.014655, A9 = −1.80997, and A10 = 0.9548. In addition to the velocity and density, the viscosity also changes with the temperature, as expressed by Eq. 19:

$$\frac{\mu}{\mu_0} = \left(\frac{T_f}{T_0}\right)^{1.5} \frac{T_0 + 110.4}{T_f + 110.4} \tag{19}$$

where μ_0 is the gas viscosity under normal temperature, Pas; and T_0 is the test temperature, k.

Solution method

Solution of the temperature profile inside the production string

It can be observed from the aforementioned calculation method that a coupling relationship exists among the temperature, pressure, and gas properties. In order to solve Eq. 14, the well should be divided into a short section in the axial direction with length $\triangle z$. The short section is numbered as 0, 1, 2, 3, ..., i-1, i+1, ..., $h/\triangle z$. As a result, the temperature of the ith section can be expressed by Eq. 20 by the difference of Eq. 15:

$$\begin{aligned} T_f^i(t) &= \frac{1}{A + \Delta z}\left(A T_f^{i-1}(t) + \Delta z T_e^i + A \Delta z f^{i-1} \frac{\left(v_f^{i-1}\right)^2}{2 C_f d_{tn}}\right) \\ A &= \frac{w_f C_f \left[T_D + 2\pi\lambda_e R_{to}^i\right]}{2\pi\lambda_e} \end{aligned} \tag{20}$$

where A is a calculation parameter.

As shown in Figure 2, the gas properties used in Eq. 20 are obtained under the pressure and temperature of the last well section, as expressed by Eq. 21:

$$G_i = f\left(T_f^{i-1}, p_f^{i-1}\right) \tag{21}$$

where G_i is the gas properties used to calculate the temperature of the ith well section, including velocity, density, and viscosity shown in 1.4.

Solution of the pressure profile inside the production string

Moreover, the gas properties also change in that the flow friction influences the wellbore pressure and temperature. The gas pressure can also be calculated, as expressed by Eq. 22:

$$p_f^i = p_f^{i-1} - \left(\rho_f^i g \sin\theta + f^i \frac{\rho_f^i \left(v_f^i\right)^2}{2 d_{tn}}\right)\Delta z - \rho_f^i v_f^i \Delta v_f^i \tag{22}$$

where $\triangle v_f$ is the change of gas velocity in the short well section, m/s.

Because the well bottom temperature and pressure are available through well logging, the calculation starts from the well bottom, as expressed by Eq. 23.

$$\begin{cases} T_f^0 = T_b, \\ p_f^0 = p_b, \\ \triangle v_f^0 = 0, \\ G_1 = f\left(T_f^0, p_f^0\right) \end{cases} \tag{23}$$

where T_b is the well bottom temperature, K; and p_b is the well bottom pressure, Pa.

Changing law of the temperature profile

Changing law under different factors

An HPHT gas well is selected from Ref. [40] as a case well to study the changing law. The basic parameters can be found in the reference. The temperature distributions in the production string under different influencing factors are shown in Figure 3. The detailed analysis is as follows:

1) Changing law under different production times. As shown in Figure 3A1, the temperature inside the production string decreases from the well bottom to the wellhead more and more quickly. According to Figure 3A2, the wellhead temperature increases as the production prolongs, but the increasing rate gradually decreases, and the increment value is not so large. For example, the wellhead temperatures are

358.33K, 361.77K, 364.56K, 365.73K, and 367.62K, respectively, under the production times of 10, 50, 200, 365, and 1000 days. This indicates that the largest temperature difference appears at the wellhead. Moreover, the changing rate of the temperature profile becomes slower and slower as the production continues. This means that the wellhead temperature would keep stable under normal production. However, the production histories of some gas wells showed that the wellhead temperature sometimes fluctuates remarkably. This situation may be caused by some incidents, such as reservoir energy depletion, production string block, or water invasion.

2) Changing law under different production rates. As shown in Figure 3B1, the whole temperature profile increases as the production increases. Alternatively, the temperature change becomes smaller and smaller as the well depth increases. Combining Figure 3B2, it can be observed that the maximum temperature change appears at the wellhead. For example, the wellhead temperatures are 349.85K, 365.73K, 390.77K, and 416.21K, respectively, under the production rates of 300 000 m^3/d, 400 000 m^3/d, 600 000 m^3/d, and 800 000 m^3/d, while the temperatures at the well bottom are equal. This can be explained by two reasons: first, a larger production rate brings more heat from the deep gas reservoir. Second, the heat generated by the flow friction increases. For some gas wells blocked by the wax deposition or the gas hydrate, the production rate can be increased in order to enhance the temperature profile of the gas wells.
3) Changing law under different values of the annular liquid thermal conductivity. The main function of the annular liquid is to prevent tubing collapse by balancing the pressure difference [41]. Meanwhile, the annular liquid also plays a role in thermal insulation by improving its thermal conductivity [42]. As shown in Figure 3C1, the annular liquid with higher thermal conductivity can enhance the temperature profile inside the production string. Similar to the impact of the annular liquid thermal conductivity, the maximum temperature change appears at the wellhead, but the trend is the opposite. Taking the wellhead temperature in Figure 3C2 as an example, the temperature increases from 358.58K to 374.42K when the annular liquid thermal conductivity decreases from 1.0 W/(mK) to 0.4 W/(mK). Hence, the annular liquid with low thermal conductivity can be applied to mitigate the trapped annular pressure. If necessary, the annular liquid thermal conductivity can be even lower, thus increasing the temperature profile. Likewise, this can also be used in the prevention of wax deposition or the gas hydrate block in low-temperature gas wells.
4) Changing law under different values of the gas-specific heat capacity. As shown in Figure 3D1, the temperature profile increases as the gas heat capacity increases. According to Figure 3D2, the wellhead temperature has an approximate positive linear relation with the gas-specific heat capacity, which is the same as the impact of the production rate. Since natural gas is compressible, the temperature has an impact on the heat capacity. Currently, there are several methods to express the impact of temperature on gas capacity, including the formula HYSYS software and API formula. However, these methods may not be applicable when the natural gas is mixed with different kinds of gas or the temperature is very high [43]. Therefore, the gas heat capacity should be tested in order to improve the calculation accuracy of temperature distribution in gas wells. On the other hand, the specific heat capacity of the production fluid would also change when the water enters the wellbore, thus leading to a change in the well temperature distribution.

FIGURE 1
Heat transfer along the well radial direction.

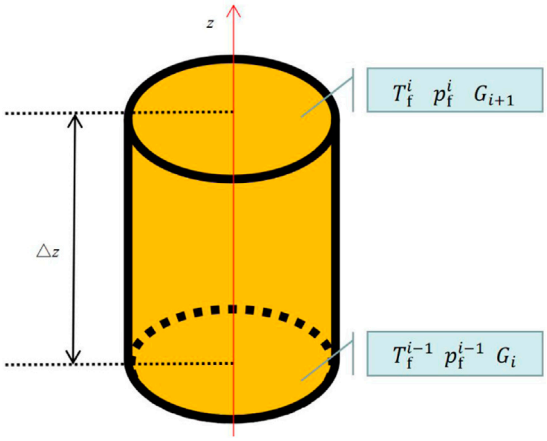

FIGURE 2
Sketch map of the short section of the production string.

Evaluation of the influencing factors

The wellhead is convenient to observe, so it can be taken as an index to reflect the wellbore temperature distribution and reservoir temperature. As stated previously, the changing law and the changing degree are different under the influences of different factors. Limited by the value ranges and the units of different factors, it is hard to directly compare the sensitivities of the influencing factors. For this reason, a

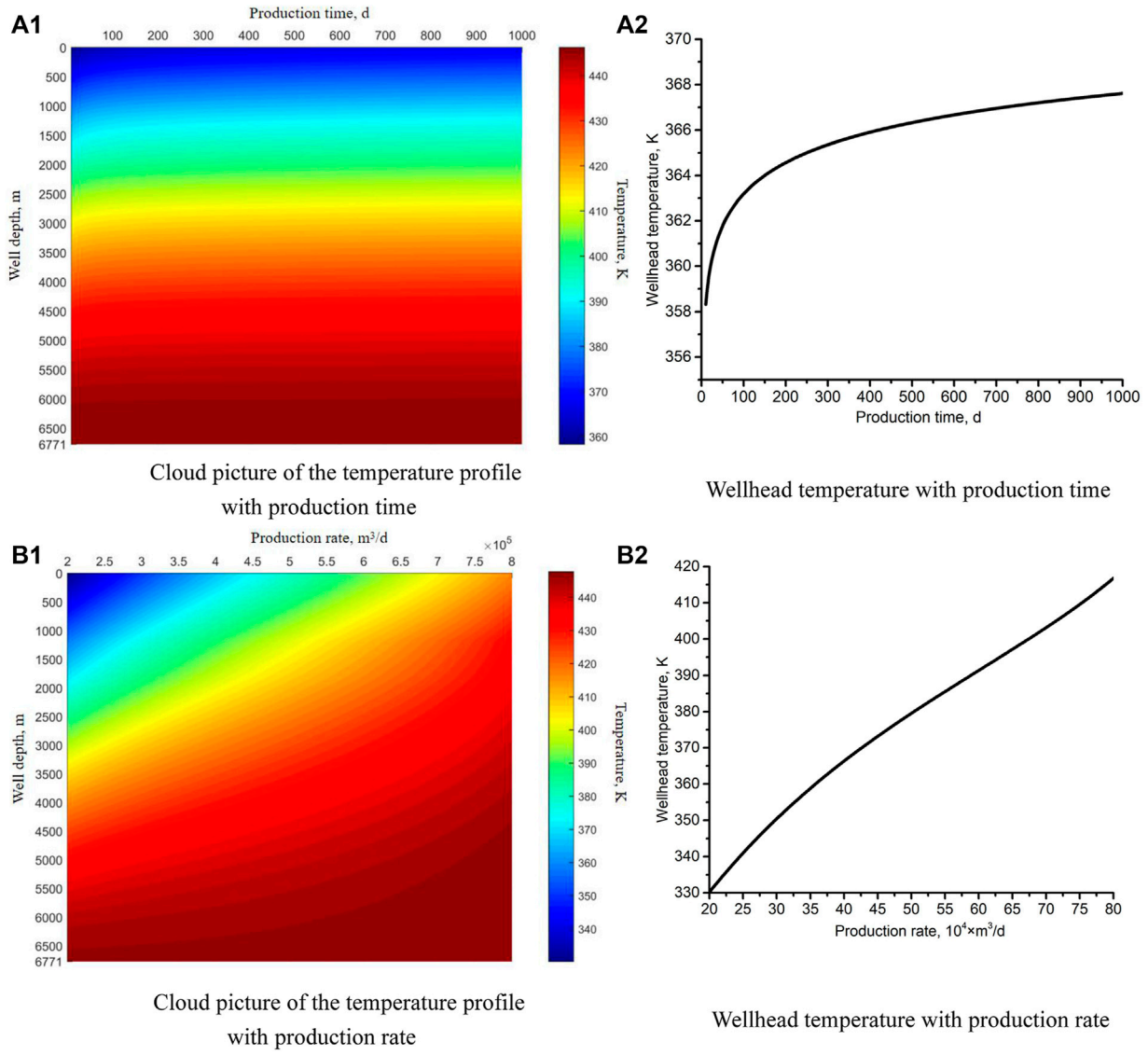

FIGURE 3
(Continued).

new dimensionless index is proposed by Zhang et al. [44], which is called the ratio of standard deviation coefficient. To eliminate the impact of the factors' units, this index is the ratio of the standard deviation coefficient of wellhead temperature and influencing factor. To eliminate the impact of the value range, it is necessary to get the starting point of the value range back to 0. Based on the two principles, the ratio of the standard deviation coefficient can be obtained in three steps. The first step is to get the starting point of the value range back to 0, as expressed by Eq. 24:

$$x_j^{'} = x_j - \min(x_1, x_2, x_3 \ldots\ldots x_n) \tag{24}$$

where $x_j^{'}$ is the jth value of the factor x after returning to 0; x_j is the jth value of the factor x; and n is the number of the factor values.

The second step is to calculate the standard deviation of the influencing factors and the wellhead temperature, as expressed by Eq. 25:

$$\sigma = \sqrt{\frac{\sum_{j=1}^{j=n}\left(x_j^{'} - x_{ifa}\right)^2}{n}} \tag{25}$$

where σ is the standard deviation and x_{ifa} is the average value of the factor value change.

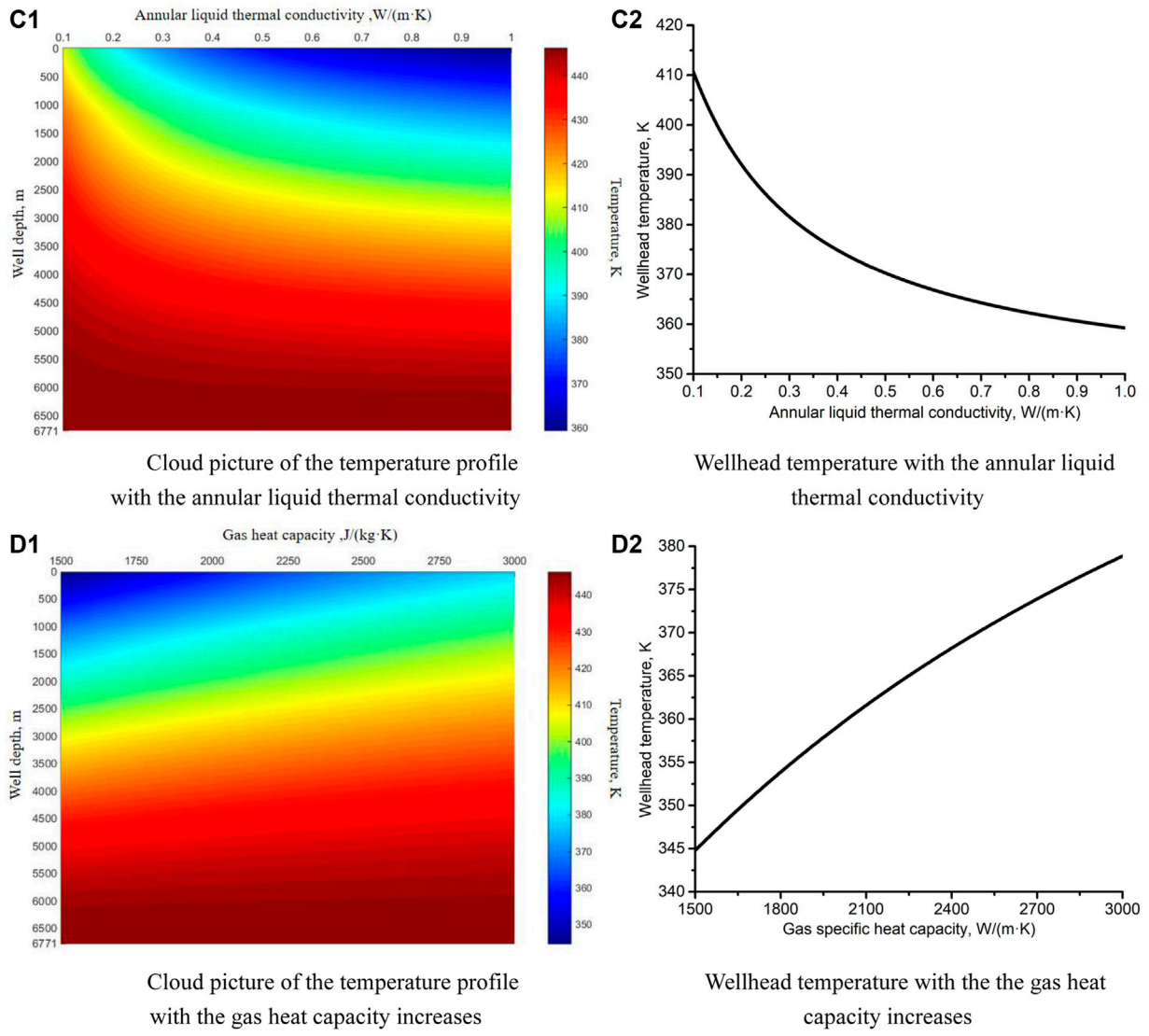

FIGURE 3
(Continued). Changing law of the temperature profile under different factors. **(A1)** and **(A2)** are the impacts of production time. **(B1)** and **(B2)** are the impacts of production rate. **(C1)** and **(C2)** are the impacts of annular liquid thermal conductivity. **(D1)** and **(D2)** are the impacts of gas heat capacity.

Finally, the ratio of the standard deviation coefficient can be expressed by Eq. 26:

$$C_r = \frac{\sigma_p x_{ifa}}{\sigma_x T_{head}} \times 100\% \quad (26)$$

where C_r is the ratio of the standard deviation coefficient, dimensionless; σ_p is the wellhead temperature standard deviation, K; σ_x is the standard deviation of the influencing factor; and T_{head} is the average value of the wellhead temperature, K.

Figure 4 shows the evaluation results. The sensitivity is presented by the new index, the ratio of the standard deviation coefficient. Here, the sensitivity in Figure 4 means the ability of the influencing factors to change the wellhead temperature. The higher the sensitivity is, the stronger the ability is. The horizontal axis represents the feasibility to adjust the wellhead temperature through the related factor. It can be seen that the gas-specific heat capacity has the highest sensitivity, while the production time has the lowest. Nevertheless, there are few methods to change the gas heat capacity in that this is a property determined by the production fluid. The production time can only be adjusted by stopping or continuing production. In other words, adjustment of the production time would disturb the production. The production rate can be adjusted through the oil nozzle. The only disadvantage is

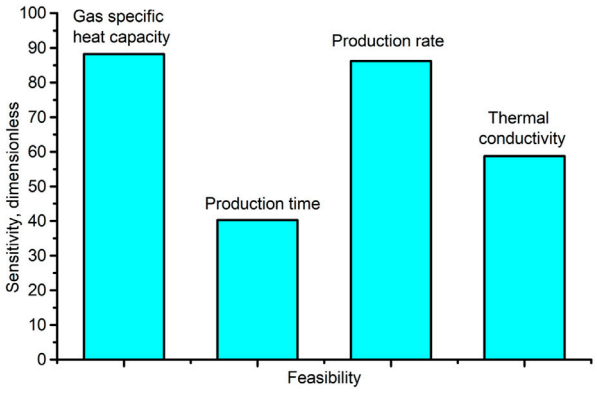

FIGURE 4
Feasibility and sensitivity of the influencing factors.

that the reservoir energy may be not able to last long at high production rate. The thermal conductivity of the annular liquid is easy to adjust by selecting different kinds of thermal-insulated liquids [45]. Given the cost, it is recommended to change the well temperature profile by adjusting the production rate. If not applicable, the thermal conductivity can be optimized to change the temperature profile.

Conclusion

1) The wellhead temperature increases as the production time increases, but the changing rate of the temperature profile becomes slower and slower as the production continues. Therefore, the obvious change in wellhead temperature can reflect potential production incidents of gas wells, such as reservoir energy depletion, production string block, or water invasion.
2) The production rate and annular liquid thermal conductivity can improve the temperature profile inside the production string, which can be used to prevent wax or hydrate deposition in gas wells with low temperature. The gas-specific heat capacity and temperature have a coupling relationship, so the changing law of gas-specific heat should be considered to improve the calculation accuracy.
3) Considering the sensitivity, feasibility, and cost, it is recommended to change the well temperature profile by adjusting the production rate. If not applicable, the thermal conductivity can be optimized to change the temperature profile.

Data availability statement

The original contributions presented in the study are included in the article/Supplementary Material; further inquiries can be directed to the corresponding author.

Author contributions

LC: data analysis, writing—original draft preparation, and methodology; JS: methodology, conceptualization, and supervision; BZ: writing—original draft preparation, funding acquisition, and supervision; NL: conceptualization, project administration, and drawing figures; YX: formal analysis.

Funding

This study received funding from CNPC Forward-looking Basic Strategic Technology Research Projects (Nos. 2021DJ6504, 2021DJ6502, 2021DJ6501, 2021DJ0806, and 2021DJ4902). The funder was not involved in the study design, collection, analysis, interpretation of data, writing of the manuscript, or the decision to submit it for publication.

Conflict of interest

Author LC was employed by Research Institute of Oil and Gas Engineering of Tarim Oilfield, PetroChina. Authors BZ were employed by Research Institute of Safety and Environment Technology, CNPC. Author NL was employed by Research Institute of Petroleum Exploration and Development, PetroChina.

The remaining authors declare that the research was conducted in the absence of any commercial or financial relationships that could be construed as a potential conflict of interest.

Publisher's note

All claims expressed in this article are solely those of the authors and do not necessarily represent those of their affiliated organizations, or those of the publisher, the editors, and the reviewers. Any product that may be evaluated in this article, or claim that may be made by its manufacturer, is not guaranteed or endorsed by the publisher.

References

1. Fu W., Wang Z., Sun B., Xu J., Chen L., Wang X. Rheological properties of methane hydrate slurry in the presence of xanthan gum. *SPE J* (2020) 25(5): 2341–52. doi:10.2118/199903-pa

2. Fu W., Wang Z., Zhang J., Sun B. Methane hydrate formation in a water-continuous vertical flow loop with xanthan gum. *Fuel* (2020) 265:116963. doi:10.1016/j.fuel.2019.116963

3. Zhang B., Jiang R., Sun B., Lu N., Hou J., Bai Y., et al. Establishment of the productivity prediction method of Class III gas hydrate developed by depressurization and horizontal well based on production performance and inflow relationship. *Fuel* (2022) 308:122006. doi:10.1016/j.fuel.2021.122006

4. Gong W., You L., Xu J., Kang Y., Zhou Y. Experimental study on the permeability jail range of tight gas reservoirs through the gas–water relative permeability curve. *Front Phys* (2022) 695. doi:10.3389/fphy.2022.923762

5. Lu N., Zhang B., Wang T., Fu Q. Modeling research on the extreme hydraulic extension length of horizontal well: Impact of formation properties, drilling bit and cutting parameters. *J Pet Explor Prod Technol* (2021) 11(3):1211–22. doi:10.1007/s13202-021-01106-4

6. Vargo R. F., Payne M., Faul R., LeBlanc J., Griffith J. E. Practical and successful prevention of annular pressure buildup on the Marlin project. *SPE drilling & completion* (2003) 18(3):228–34. doi:10.2118/85113-pa

7. Wang J., Sun J., Xie W., Chen H., Wang C., Yu Y., et al. Simulation and analysis of multiphase flow in a novel deepwater closed-cycle riserless drilling method with a subsea pump+ gas combined lift. *Front Phys* (2022) 565. doi:10.3389/fphy.2022.946516

8. Cao L., Sun J., Zhang B. (2022). Safety control Technology of ultra-high pressure gas wells with annular pressure: Case study of Tarim Oilfield. Paper presented at the Offshore Technology Conference Asia. OTC-31458-MS Kuala Lumpur, Malaysia March 22-25. Dallas, United States. doi:10.4043/31458-MS

9. Xu Y., Han C., Sun J., He B., Guan Z., Zhao Y. Formation interval determination method of MPD based on risk aversion and casing level optimization. *Front Phys* (2022) 734. doi:10.3389/fphy.2022.976379

10. Moore T. A. Coalbed methane: A review. *Int J Coal Geology* (2012) 101:36–81. doi:10.1016/j.coal.2012.05.011

11. Chen J., Wang X., Sun Y., Ni Y., Xiang B., Liao J. Factors controlling natural gas accumulation in the southern margin of junggar basin and potential exploration targets. *Front Earth Sci (Lausanne)* (2021) 9:112. doi:10.3389/feart.2021.635230

12. Zhang B., Lu N., Guo Y., Wang Q., Cai M., Lou E. Modeling and analysis of sustained annular pressure and gas accumulation caused by tubing integrity failure in the production process of deep natural gas wells. *J Energ Resour Tech* (2022) 144(6):063005. doi:10.1115/1.4051944

13. Ding L., Rao J., Xia C. Transient prediction of annular pressure between packers in high-pressure low-permeability wells during high-rate, staged acid jobs. *Oil Gas Sci Technol – Rev IFP Energies Nouvelles* (2020) 75:49. doi:10.2516/ogst/2020046

14. Zhang B., Xu Z., Guan Z., Li C., Liu H., Xie J., et al. Evaluation and analysis of nitrogen gas injected into deepwater wells to mitigate annular pressure caused by thermal expansion. *J Pet Sci Eng* (2019) 180:231–9. doi:10.1016/j.petrol.2019.05.040

15. Bradford D. W., Fritchie D. G., Gibson D. H., Gosch S. W., Pattillo P. D., Sharp J. W., et al. Marlin failure analysis and redesign: Part 1—description of failure. *SPE Drilling & Completion* (2004) 19(2):104–11. doi:10.2118/88814-pa

16. Zhang B., Sun B., Deng J., Lu N., Zhang Z., Fan H., et al. Method to optimize the volume of nitrogen gas injected into the trapped annulus to mitigate thermal-expanded pressure in oil and gas wells. *J Nat Gas Sci Eng* (2021) 96:104334. doi:10.1016/j.jngse.2021.104334

17. Li C., Guan Z., Zhao X., Yan Y., Zhang B., Wang Q., et al. A new method to protect the cementing sealing integrity of carbon dioxide geological storage well: An experiment and mechanism study. *Eng Fracture Mech* (2020) 236:107213. doi:10.1016/j.engfracmech.2020.107213

18. Zhang B., Guan Z., Lu N., Hasan A. R., Xu S., Zhang Z., et al. (2018).Control and analysis of sustained casing pressure caused by cement sealed integrity failure. Paper presented at Offshore Technology Conference Asia held in. OTC-28500-MS Kuala Lumpur, Malaysia: doi:10.4043/28500-MS

19. Li C., Guan Z., Zhang B., Wang Q., Xie H., Yan Y., et al. Failure and mitigation study of packer in the deepwater HTHP gas well considering the temperature-pressure effect during well completion test. *Case Stud Therm Eng* (2021) 26:101021. doi:10.1016/j.csite.2021.101021

20. Mainguy M., Innes R. Explaining sustained A-annulus pressure in major North Sea high-pressure/high-temperature fields. *SPE Drilling & Completion* (2019) 34(1):71–80. doi:10.2118/194001-pa

21. Ichim A., Teodoriu H. C. Investigations on the surface well cement integrity induced by thermal cycles considering an improved overall transfer coefficient. *J Pet Sci Eng* (2017) 154:479–87. doi:10.1016/j.petrol.2017.02.013

22. Cao L., Sun J., Liu J., Liu J. Experiment and application of wax deposition in dabei deep condensate gas wells with high pressure. *Energies* (2022) 15(17):6200. doi:10.3390/en15176200

23. Zhang J., Wang Z., Duan W., Fu W., Sun B., Sun J., et al. Real-time estimation and management of hydrate plugging risk during deepwater gas well testing. *SPE J* (2020) 25(6):3250–64. doi:10.2118/197151-pa

24. Roberts B. E. The effect of sulfur deposition on gaswell inflow performance. *SPE Reservoir Eng* (1997) 12(02):118–23. doi:10.2118/36707-pa

25. Mo L., Sun W., Jiang S., Zhao X., Ma H., Liu B., et al. Removal of colloidal precipitation plugging with high-power ultrasound. *Ultrason Sonochem* (2020) 69:105259. doi:10.1016/j.ultsonch.2020.105259

26. Wang Z., Tong S., Wang C., Zhang J., Fu W., Sun B. Hydrate deposition prediction model for deep-water gas wells under shut-in conditions. *Fuel* (2020) 275:117944. doi:10.1016/j.fuel.2020.117944

27. Izgec B., Kabir C. S., Zhu D., Hasan A. R. Transient fluid and heat flow modeling in coupled wellbore/reservoir systems. *SPE Reservoir Eval Eng* (2007) 10(3):294–301. doi:10.2118/102070-pa

28. Galvao M. S., Carvalho M. S., Barreto A. B. A coupled transient wellbore/reservoir-temperature analytical model. *SPE J* (2019) 24(5):2335–61. doi:10.2118/195592-pa

29. Wang X., Sun B., Liu S., Zhong L., Liu Z., Wang Z., et al. A coupled model of temperature and pressure based on hydration kinetics during well cementing in deep water. *Pet Exploration Dev* (2020) 47(4):867–76. doi:10.1016/s1876-3804(20)60102-1

30. Mao L., Liu Q., Nie K., Wang G. Temperature prediction model of gas wells for deep-water production in South China Sea. *J Nat Gas Sci Eng* (2016) 36:708–18. doi:10.1016/j.jngse.2016.11.015

31. Guan Z. C., Zhang B., Wang Q., Liu Y. W., Xu Y. Q., Zhang Q. Design of thermal-insulated pipes applied in deepwater well to mitigate annular pressure build-up. *Appl Therm Eng* (2016) 98:129–36. doi:10.1016/j.applthermaleng.2015.12.030

32. Hasan A. R., Kabir C. S., Lin. D. Analytic wellbore temperature model for transient gas-well testing. *SPE Reservoir Eval Eng* (2005) 8(3):240–7. doi:10.2118/84288-pa

33. Zheng J., Dou Y. H., Cao Y., Yan X. Prediction and analysis of wellbore temperature and pressure of HTHP gas wells considering multifactor coupling. *J Fail Anal Preven* (2020) 20(1):137–44. doi:10.1007/s11668-020-00811-2

34. Ai S., Cheng L., Huang S., Liu H., Zhang J., Fu L. A critical production model for deep HT/HP gas wells. *J Nat Gas Sci Eng* (2015) 22:132–40. doi:10.1016/j.jngse.2014.11.025

35. Ramey H. J., Jr. Wellbore heat transmission. *J Pet Tech* (1962) 14(4):427–35. doi:10.2118/96-pa

36. Holst P. H., Flock D. L. Wellbore behaviour during saturated steam injection. *J Can Pet Tech* (1966) 5(04):184–93. doi:10.2118/66-04-05

37. Hasan A. R., Kabir C. S., Wang X. A robust steady-state model for flowing-fluid temperature in complex wells. *SPE Prod Operations* (2009) 24(2):269–76. doi:10.2118/109765-pa

38. Thome J. R., Ribatski G. State-of-the-art of two-phase flow and flow boiling heat transfer and pressure drop of CO2 in macro-and micro-channels. *Int J Refrigeration* (2005) 28(8):1149–68. doi:10.1016/j.ijrefrig.2005.07.005

39. Heidaryan E., Salarabadi A., Moghadasi J. A novel correlation approach for prediction of natural gas compressibility factor. *J Nat Gas Chem* (2010) 2(18):189–92. doi:10.1016/s1003-9953(09)60050-5

40. Zhang B., Xu Z., Lu N., Liu H., Liu J., Hu Z., et al. Characteristics of sustained annular pressure and fluid distribution in high pressure and high temperature gas wells considering multiple leakage of tubing string. *J Pet Sci Eng* (2021) 196:108083. doi:10.1016/j.petrol.2020.108083

41. Liu H., Cao L., Xie J., Yang X., Zeng N., Zhang X., Chen F. (2019). Research and practice of full life cycle well integrity in HTHP well, Tarim Oilfield. Paper presented at International Petroleum Technology Conference. Beijing, China. Dallas, United States IPTC-19403-MS doi:10.2523/IPTC-19403-MS

42. Ezzat A. M., Miller J. J., Ezell R., Perez G. P. (2007). High-performance water-based insulating packer fluids. Paper presented at SPE Annual Technical Conference and Exhibition. SPE-109130-MS Anaheim, CA, USA. Dallas, United States.

43. Yuan W., Yang W., Liao T., Ma Y. Comparative study on equations of ideal gas specific heat capacity. *Pet Eng Construction* (2021) 47(2):25–9. doi:10.3969/j.issn.1001-2206.2021.02.006

44. Zhang B., Guan Z., Sheng Y., Wang Q., Xu C. Impact of wellbore fluid properties on trapped annular pressure in deepwater wells. *Pet Exploration Dev* (2016) 43(5):869–75. doi:10.1016/s1876-3804(16)30104-5

45. Zhang B., Guan Z., Wang Q., Xuan L., Liu Y., Sheng Y. (2016). Appropriate completion to prevent potential damage of annular pressure buildup in deepwater wells. Paper presented at IADC/SPE Asia Pacific Drilling Technology Conference. Singapore. Dallas, United States SPE-180542-MS doi:10.2118/180542-MS

frontiers | Frontiers in Physics

TYPE Original Research
PUBLISHED 28 November 2022
DOI 10.3389/fphy.2022.1056593

OPEN ACCESS

EDITED BY
Jianjun Zhu,
China University of Petroleum, Beijing, China

REVIEWED BY
Wenqiang Lou,
Yangtze University, China
Dan Ma,
China University of Mining and Technology, China
Hai Wang,
University of Calgary, Canada

*CORRESPONDENCE
Xiaohui Sun,
sxh049306@163.com

SPECIALTY SECTION
This article was submitted to Interdisciplinary Physics, a section of the journal Frontiers in Physics

RECEIVED 29 September 2022
ACCEPTED 24 October 2022
PUBLISHED 28 November 2022

CITATION
Miao D, Hu J, Zhang J, Wang J and Sun X (2022), The behaviors of bubble migration and pressure build-up during a dynamic shut-in procedure in deep-water drilling.
Front. Phys. 10:1056593.
doi: 10.3389/fphy.2022.1056593

The behaviors of bubble migration and pressure build-up during a dynamic shut-in procedure in deep-water drilling

Dianyuan Miao[1], Junjie Hu[2], Jianbo Zhang[2], JinTang Wang[2] and Xiaohui Sun[2]*

[1]CNOOC EnerTech-Drilling & Production Co., Tianjin, China, [2]School of Petroleum Engineering, China University of Petroleum (East China), Qingdao, China

A dynamic shut-in procedure is commonly adopted after a kick incident in order to build up the wellbore pressure, obtain reservoir information, and thereby handle the gas kick. In deep-water scenarios, the hydrate growth behaviors have a significant effect on gas migration and interphase mass transfer, which has not been quantitatively analyzed during the well shut-in process. In this study, a comprehensive mechanistic model of wellbore dynamics is developed considering gas migration and phase transitions. The simulation results show that the wellbore pressure field can be built up in different trends during different well shut-in periods, governed by gas seepage from the reservoir and gas migration along the wellbore, respectively. Masking the migration of free gas, the phase transition phenomena have a significant influence on the wellbore dynamics and bottomhole pressure. This work adds further insights into quantitatively characterizing the hydrate growth behaviors and interphase mass transfer rules of gas bubbles during a dynamic well shut-in procedure.

KEYWORDS

gas influx, well shut-in, pressure build-up, gas migration, phase transition

1 Introduction

As a gas kick occurs in deep-water drilling, uncontrolled gas migration can greatly threaten the flow assurance in the wellbore [1]. The well shut-in procedure is commonly conducted as rapidly as possible to stop the formation from flowing, reduce the risk of fracturing the casing shoe, and secure the well. Moreover, the pressure build-up process during a dynamic shut-in procedure is somewhat similar to the pressure transient analysis, which implies the early response of reservoir behaviors and the flow regime [2]. During a well shut-in procedure, estimates can be made of the formation pressure and the influx information, of which accuracy is vital to the success of the following well control operations [3].

Generally, the variation of the wellbore pressure during a well shut-in process is driven by two mechanisms of gas migration: 1) the continuing influx enters the closed system of wellbore fluids due to the pressure underbalance at the open-hole section, and 2)

the gas bubbles in the wellbore ascend continuously due to the buoyancy. At present, the theoretical and experimental research studies indicated that the surface pressures are carried upward by a complicated flow process, which is closely related to the influx type and size, reservoir characteristics, fluid rheology and compressibility, well expansion, and fluid loss [4–7]. Particularly, the preliminary analysis revealed that gas dissolution has an important influence on pressure build-up behaviors [6, 8]. This is because the free gas goes into the solution in the drilling fluid and there is no further gas migration, as a kind of phase transition phenomenon. Interestingly, it can be expected that the free gas will convert into solid hydrates affected by the low temperature and high pressure in deep-water drilling [9–11]. Recently, several studies have been performed to analyze the effect of phase transition on the wellbore flow [12–14]. Fu et al. [15–17] showed a new insight into multiphase flow modeling and proposed a novel pressure loss prediction model for the multiphase flow in the wellbore and pipeline based on the energy dissipation theory. The accuracy of the developed model is significantly enhanced by coupling it with the methane hydrate formation model and the hydrate slurry rheology model and reveals the effects of phase transition on the pressure loss of the multiphase flow [14, 17, 18].

The dynamic interphase mass transfer during gas dissolution and hydrate growth may mask the early response of the pressure build-up and gas influx. Considering the reservoir coupling and gas slippage in the wellbore, Billingham et al. [2] and Ren et al. [7] have developed pioneering models to describe the variations of the bottomhole pressure during a well shut-in procedure. However, in these models, the distribution of free gas is simplified, namely, the gas influx is assumed to fill the annulus and exist as a single bubble/continuous slug during its upward migration, which was revealed to be invalid [5]. Therefore, the characteristics of a pressure build-up can be overestimated since the migration of free gas was simplified, and the phase transitions were neglected. Therefore, a novel wellbore dynamic model considering the flow regime and phase transition effects is necessary to help drilling engineers obtain a thorough understanding of the kick evolution mechanism and the wellbore pressure build-up characteristics.

2 Model development

Although the kicking well is shut in, the gas can continuously flow into the semi-closed wellbore driven by the pressure underbalance and the difference in the densities of the gas and liquid. Gas migration, accompanied by the increase in the wellbore pressure, can compress the wellbore and fluid and promote the rates of gas dissolution and hydrate phase transition. In turn, the pressure field updates gradually through the synergistic action of multiple factors. Therefore, the build-up of surface pressure can be closely related to reservoir coupling, bubble rise, phase transition of the fluid, wellbore compressibility, etc. In this regard, it usually takes a long period for the surface pressure to stabilize. The potential reasons affecting the variation of wellbore pressure can be as follows:

1) Reservoir coupling. There exists the mass exchange between the wellbore and reservoir at the open-hole section. Gas enters the wellbore due to pressure underbalance, whereas the drilling fluid can filter into the formation as the bottomhole pressure exceeds the reservoir pressure.
2) Wellbore compressibility. The drilling fluid usually has enough compressibility that the elasticity of the wellbore should be considered.
3) Gas expansion. The gas bubbles expand gradually as they ascend in the wellbore.
4) Gas dissolution. The gas influx can be dissolved in the drilling fluid, which masks the early response of the gas kick.
5) Hydrate phase transition. The free gas can convert into solid hydrates, accompanied by variations of phase volumes.

2.1 Pressure variation in a semi-closed wellbore

In the semi-closed wellbore, the flow dynamic is significantly unsteady and is affected by gas migration. Considering volume conservation, the following equation can be obtained [9]:

$$\left(Q_g - Q_{loss}\right)\Delta t + V_w C_w \left[P_w|_{t+\Delta t} - P_w|_t\right] = \sum_{i=1}^{N}\left\{\left(m_{gi} - \frac{M_g}{M_g + N_h M_w}\Delta m_{hi} - \Delta m_{soli}\right)\Big/\rho_g\Big|_{h_i + v_g \Delta t} - \frac{m_{gi}}{\rho_g|_{h_i}}\right\} + \sum_{i=1}^{N}\left\{\frac{\Delta m_{hi}}{\rho_h} + \frac{\Delta m_{soli}}{\rho_{soli}}\right\} + \sum_{i=1}^{N}\left\{E_{Li} C_L \left(P_{fi}|_{t+\Delta t} - P_{fi}|_t\right)\right\}, \tag{1}$$

where Q_g is the gas influx rate at the open-hole section, which can be estimated using a transient reservoir model [19], m^3/s; Q_{loss} is the static filtration rate of the drilling fluid, m^3/s; Δt is the time interval, s; V_w is the volume of the wellbore, m^3; C_w is the compressibility coefficient of the wellbore, 1/Pa; P_w is the bottomhole pressure, Pa; t is the well shut-in time, s; i is the segment number, $0 \le i \le N$; m_{gi} is the mass of the free gas in segment i of the wellbore, kg; M_g is the molecular mass of the gas, kg/mol; M_w is the molecular mass of water, kg/mol; N_h is the hydration number, and $N_h = 5.75$ for methane hydrate; Δm_{hi} is the hydrate growth rate in segment i of the wellbore, kg; Δm_{soli} is the gas dissolution rate in segment i of the wellbore, kg; ρ_g is the gas density, kg/m^3; h_i is the depth of segment i, m; v_g is the gas rise velocity, m/s; ρ_h is the hydrate density, kg/m^3; ρ_{soli} is the density of the dissolved gas in segment i, kg/m^3; E_{Li} is the volume of the drilling fluid in segment i of the wellbore, m^3; C_L is the compressibility of the drilling fluid, 1/Pa; and P_{fi} is the fluid pressure in segment i of the wellbore, Pa.

In Eq. 1, the terms on the left-hand side represent the gas influx, fluid loss, and wellbore expansion, respectively, while the

terms on the right-hand side represent the gas expansion, hydrate growth, gas dissolution, and compressibility of the drilling fluid.

In order to obtain an accurate pressure profile along the wellbore, it is necessary to estimate the interphase mass transfer rates during gas migration.

2.2 Phase transition rates

The previous studies in the literature indicated that the gas hydrate can form and cover the gas bubble as it rises in the wellbore [20–23]. Formed on the bubble surface, the hydrate shell can reduce the gas dissolution rate and bubble rise velocity. Furthermore, the hydrate growth rate is governed by the mass transport processes of gas and water molecules through the shell, as shown in Figure 1.

2.2.1 Gas dissolution

According to the diffusion theory, the gas dissolution rate is dominated by the mass transfer coefficient and unsaturation of the dissolved gas. Considering the aggregating state of the gas hydrate at the gas/liquid interface, Sun et al. [20] developed a gas dissolution model for a hydrated bubble.

$$\Delta m_{soli} = N_b J_k \rho_g \tag{2}$$

$$J_k = 2.496\pi(R+\delta)^2 (C_{ins} - C_\infty) v_g^{1/3} \left[\frac{D_g}{2(R+\delta)}\right]^{\frac{2}{3}} \left(1 + 0.5\sqrt{\mathrm{Re}}\right)^{0.48} \tag{3}$$

where N_b is the number of gas bubbles in a segment of the wellbore; R is the bubble radius, m; δ is the thickness of the hydrate shell, m; C_{ins} is the gas solubility at the hydrate/liquid interface, m^3/m^3; C_∞ is the gas concentration in the liquid bulk, m^3/m^3; D_g is the gas diffusion coefficient in the liquid, m^2/s; J_k is the gas dissolution rate on the outside of the hydrate shell, m^3/s; and v_g is the bubble rise velocity, m/s.

The gas dissolution can be significantly reduced by hydrate formation. On one hand, the occurrence of the hydrate phase can disturb the previous gas/liquid equilibrium state, and the gas solubility is decreased in the presence of a gas hydrate. On the other hand, as the hydrate shell thickens at the gas/liquid interface, the bubble rise velocity is reduced and the internal circulation is prevented, which leads to the decrease in the mass transfer coefficient [24].

In Eq. 3, the gas dissolution coefficient is closely related to the gas migration velocity. Considering the steady motion state of the hydrated bubble, the expression of the bubble rise velocity can be obtained [25]:

$$v_g = \left\{\frac{8g}{3C_D}\frac{\left[(R+\delta)^3(\rho_w - \rho_h) + R^3(\rho_h - \rho_g)\right]}{(R+\delta)^2\rho_w}\right\}^{1/2} \tag{4}$$

where C_D is the drag coefficient, which is affected by the flow behaviors of gas bubbles and the properties of fluids. As for the migration of gas bubbles in the non-Newtonian drilling fluid, we proposed an empirical model based on the laboratory experiment of bubble rise [26].

$$C_D = \begin{cases} 1.12 \times \frac{24}{\mathrm{Re}}\left(1 + 0.173\mathrm{Re}^{0.675}\right) & \mathrm{Re} < 10, \\ 0.813 \times \frac{24}{\mathrm{Re}}\left(1 + 24\mathrm{Re}^{-1.125}\right) & 10 \le \mathrm{Re} \le 100 \\ 1.07 \times \frac{24}{\mathrm{Re}^{0.825}}\left(-1 + 0.037\mathrm{Re}^{0.825}\right) & \mathrm{Re} > 100 \end{cases} \tag{5}$$

where Re is the terminal Reynolds number of a gas bubble.

2.2.2 Hydrate growth

The previous experimental research indicated that the hydrate shell covering the bubble surface can prevent the direct contact between the gas and liquid. It means that the mass transfer across the shell becomes the dominant mechanism for continuous hydrate growth [27]. Considering the structure of hydrate crystals and the pore-throat properties of the hydrate shell, a unified model for dynamic hydrate shell growth on the bubble surface was developed by Sun et al. [20]:

$$\Delta m_{hi} = N_b\left[\frac{M_g + nM_w}{nM_w}\rho_w J_{perm} + \frac{M_g + nM_w}{M_g}\rho_g(-J_{diff} + J_k)\right], \tag{6}$$

where J_{perm} and J_{diff} are the rates of water imbibition and gas diffusion through the hydrate film, m^3/s.

$$J_{perm} = \frac{\pi\sigma R^2}{4\mu_w\delta} a\Delta T\,\mathrm{erfc}\left(\frac{\delta}{\Delta T} + b\Delta T + c\right), \tag{7}$$

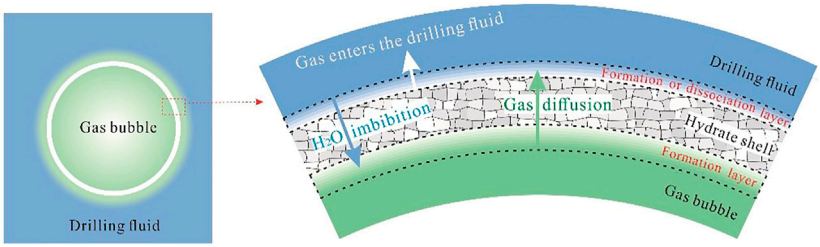

FIGURE 1
Schematic representation of hydrate shell growth on the bubble surface (adapted from Sun et al. [22]).

TABLE 1 Basic simulation parameters.

Item	Value	Item	Value
Well type	Horizontal well	Measured depth	2,800 m
Water depth	1,500 m	Inner diameter of the drillpipe	107.95 mm
Outer diameter of the drillpipe	146.05 mm	Open-hole section	0.5 m
Mud weight	1,200 kg/m^3	Inner diameter of the casing	220.4 mm
Outer diameter of the casing	244.5 mm	Mud viscosity	15 cp
Initial volume of the gas influx	1 m^3	Reservoir pressure	35 MPa
Rock permeability	10 mD	Porosity	0.13
Supply radius of the reservoir	50 m	Total compressibility	2.0 E-04 (1/MPa)

$$J_{diff} = 4\pi D_h \frac{R(R+\delta)}{\delta}(C_i - C_o), \tag{8}$$

where σ is the water/gas interfacial tension, N/m; μ_w is the viscosity of water, Pa·s; D_h is the gas diffusion coefficient in the hydrate shell, m^2/s; C_i is the gas concentration on the inner surface of the hydrate shell, m^3/m^3; and C_o is the gas concentration on the outer surface of the hydrate shell, m^3/m^3.

3 Results and analysis

Using the proposed model, the variation rules of the pressure build-up and phase volumes are simulated and analyzed. The basic simulation parameters are shown in Table 1.

3.1 Analysis of the well shut-in procedure

Figure 2 shows the bottomhole pressure at different times. As seen, variations of the bottomhole pressure can be divided into two periods.

At the early time of the well shut-in process, the reservoir gas percolates into the wellbore and the fluid pressure increases. In this period, the bottomhole pressure rapidly approaches the reservoir pressure driven by the continuous gas influx. At about 200 s, the reservoir pressure can be estimated by the pressure build-up curve.

At the later period of the well shut-in process (t > 200 s), the slippage of gas bubbles can be the dominant factor for wellbore dynamics, and the bottomhole pressure increases gradually. However, the pressure field changes more gently than that in the first period. It can be expected that the bottomhole pressure will increase continuously, and there is the risk of fracturing the casing shoe if the well cannot be shut in as rapidly as possible and the initial volume of gas influx is large.

3.2 Effect of phase transition

Figure 3 shows the variations of mass and volume of different phases. Commonly, the mass of free gas is governed by reservoir coupling and phase transitions. It increases rapidly in early time because the gas influx enters the wellbore continuously when the bottomhole pressure is less than the formation pressure. Subsequently, due to gas dissolution and hydrate growth, the mass of free gas decreases gradually as gas bubbles ascend. Furthermore, the volume of the free gas decreases gradually

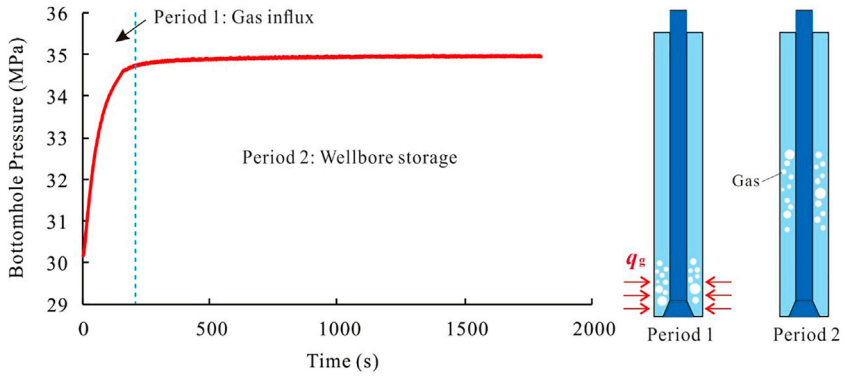

FIGURE 2
Variations of the bottomhole pressure throughout the well shut-in process.

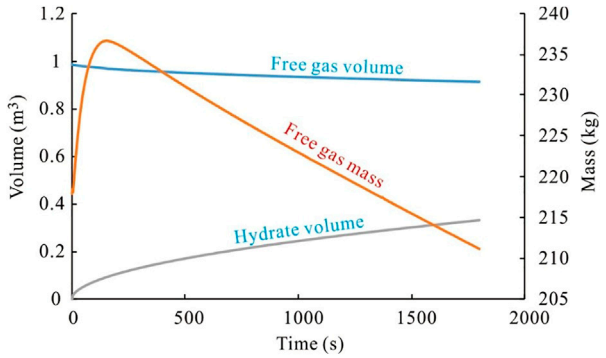

FIGURE 3
Volume and mass of the gas and hydrate phases in the wellbore.

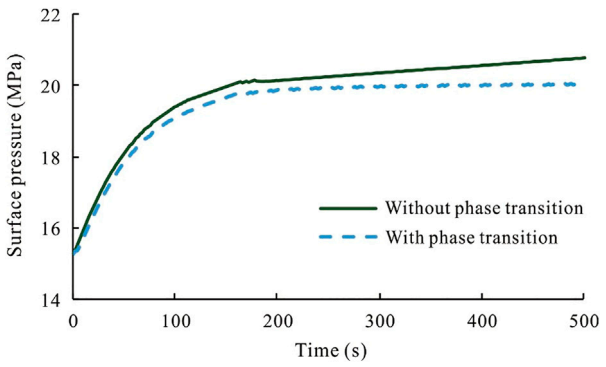

FIGURE 4
Comparison of surface pressures considering phase transitions or not.

with time because the gas bubbles are compressed, affected by the increase in the wellbore pressure, and accompanied by conversion into other phases.

In the hydrate phase stability field, the hydrates will grow on the bubble surface. In this regard, the volume of the gas hydrate increases gradually with time. It should be noted that gas dissolution and hydrate formation can significantly mask the migration of the gas influx and the build-up of the surface pressure.

Figure 4 shows the influence of phase transitions on variations in the surface pressure. As seen, the pressure can be overestimated if the phase transition effects are neglected. This is because a part of the free gas which compresses the wellbore and liquid will dissolve into the drilling fluid and convert to solid hydrates.

4 Conclusion

In this study, we proposed a novel wellbore dynamic model for predicting the behaviors of bubble migration and the pressure build-up during a dynamic shut-in procedure in deep-water drilling. In the model, the mechanism of the interphase mass transfer during gas dissolution and hydrate growth is considered. The proposed model is applied to a field well, and the following general conclusions are drawn from the simulation analysis:

1) During a dynamic well shut-in procedure, the build-up process of the wellbore pressure can be divided into two periods. It first increases rapidly, affected by reservoir coupling, and then increases slightly, affected by gas slippage in the wellbore. Special attention should be paid to the risk of fracturing the casing shoe when the initial volume of the gas influx is large.
2) The pressure build-up process can be significantly overestimated if the phase transitions are neglected. However, the development of the gas kick may be masked due to the interphase mass transfer. There also exists the probability that the free gas will evolve and increase the wellbore pressure.

Data availability statement

The original contributions presented in the study are included in the article/Supplementary Material; further inquiries can be directed to the corresponding author.

Author contributions

DM: conceptualization, investigation, formal analysis, and writing—original draft; JH: data curation and writing—original draft; JZ: visualization and investigation; JW: resources, supervision; XS: conceptualization, funding acquisition, resources, supervision, and writing—review and editing.

Funding

This work was supported by the National Natural Science Foundations of China (52104056, U21B200505), the National Key Research and Development Program of China (2021YFC2800803), and the Natural Science Foundation—Youth Foundation in Shandong province (ZR2021QE155).

Conflict of interest

DM was employed by CNOOC EnerTech-Drilling & Production Co.

The remaining authors declare that the research was conducted in the absence of any commercial or financial relationships that could be construed as a potential conflict of interest.

Publisher's note

References

1. Sun X, Sun B, Zhang S. A new pattern recognition model for gas kick diagnosis in deepwater drilling[J]. *J Pet Sci Eng* (2018) 167:418–25. doi:10.1016/j.petrol.2018.04.035

2. Billingham J, Thompson M, White DB. Advanced influx analysis gives more information following a kick [C]. In: SPE/IADC Drilling Conference; 22-25 February(1993); Amsterdam, Netherlands (1993). SPE-25710-MS.

3. Sun X, Liao Y, Wang Z, Zhao X, Sun B. Modelling of formation pore pressure inversion during tight reservoir drilling. *Geofluids* (2021) 2021:6626381–11. doi:10.1155/2021/6626381

4. Lage ACVM, Nakagawa EY, Cordovil AGDP. Experimental tests for gas kick migration analysis [C]. In: SPE-26953-MS, SPE Latin America/Caribbean Petroleum Engineering Conference; 27-29 April, 1994; Buenos Aires, Argentina (1994).

5. Matthews JL, Bourgoyne AT. Techniques for handling upward migration of gas kicks in a shut-in well [C]. In: SPE-11376-MS, IADC/SPE Drilling Conference; February 20-23, 1983; New Orleans: Louisiana (1983).

6. Guner S, Elshehabi T, Bilgesu I. The effects of gas kick migration on wellbore pressure [C]. In: Aade National Technical Conference and Exhibition Held at the Hilton Houston North Hotel; Houston, Texas, April 11–12, 2017 (2017).

7. Ren M, Li X, Liu S, Wang Y. Characteristics of wellbore pressure change during shut-in after blowout [J]. *J China Univ Pet* (2015) 39(3):113–9. (in Chinese). doi:10.3969/j.issn.1673-5005.2015.03.015

8. Schilhab LC, Rezmer IM. Factors affecting shut-in pressure rise: Kicks in Offshore HPHT wells [C]. In: OTC-8559-MS, Offshore Technology Conference; 5-8 May1997; Houston, Texas (1997).

9. Sun B, Sun X, Wang Z, Chen Y. Effects of phase transition on gas kick migration in deep water horizontal drilling. *J Nat Gas Sci Eng* (2017) 46:710–29. doi:10.1016/j.jngse.2017.09.001

10. Sun B, Sun X, Wang Z, Chen Y. Effects of phase transition on gas kick migration in deepwater horizontal drilling. *J Nat Gas Sci Eng* (2017) 46:710–29. doi:10.1016/j.jngse.2017.09.001

11. Fu W, Wang Z, Zhang J, Sun B. Methane hydrate formation in a water-continuous vertical flow loop with xanthan gum. *Fuel* (2020) 265:116963. doi:10.1016/j.fuel.2019.116963

12. Fu W, Yu J, Xiao Y, Wang C, Huang B, Sun B. A pressure drop prediction model for hydrate slurry based on energy dissipation under turbulent flow condition. *Fuel* (2022) 311:122188. doi:10.1016/j.fuel.2021.122188

13. Yuwei LI, Min L, Jizhou T, Chen M, Fu X. A hydraulic fracture height mathematical model considering the influence of plastic region at fracture tip. *Pet Exploration Dev* (2020) 47(1):184–95. doi:10.1016/s1876-3804(20)60017-9

14. Lou W, Wang Z, Pan S, Sun B, Zhang J, Chen W. Prediction model and energy dissipation analysis of Taylor bubble rise velocity in yield stress fluid. *Chem Eng J* (2020) 396:125261. doi:10.1016/j.cej.2020.125261

15. Sun B, Fu W, Wang N, Wang Z, Gao Y. Multiphase flow modeling of gas intrusion in oil-based drilling mud. *J Pet Sci Eng* (2019) 174:1142–51. doi:10.1016/j.petrol.2018.12.018

16. Fu W, Wang Z, Chen L, Sun B. Experimental investigation of methane hydrate formation in the carboxmethylcellulose (CMC) aqueous solution. *SPE J* (2020) 25(3):1042–56. doi:10.2118/199367-pa

17. Fu W, Yu J, Xu Y, Wang C, Huang B, Sun B. A pressure drop prediction model for hydrate slurry based on energy dissipation under laminar flow condition. *SPE J* (2022) 27(04):2257–67. doi:10.2118/209586-pa

18. Fu W, Wei W, Wang H, Huang B, Wang Z. Study on the rheology of CO2 hydrate slurry by using the capillary method. *J Mar Sci Eng* (2022) 10:1224. doi:10.3390/jmse10091224

19. Vefring EH, Nygaard GH, Lorentzen RJ, Naevdal G, Fjelde KK. Reservoir characterization during underbalanced drilling (UBD): Methodology and active tests. *SPE J* (2006) 11(2):181–92. doi:10.2118/81634-pa

20. Sun X, Wang Z, Sun B, Chen L, Zhang J. Modeling of dynamic hydrate shell growth on bubble surface considering multiple factor interactions. *Chem Eng J* (2018) 331:221–33. doi:10.1016/j.cej.2017.08.105

21. Sun X, Sun B, Wang Z, Chen L, Gao Y. A hydrate shell growth model in bubble flow of water-dominated system considering intrinsic kinetics, mass and heat transfer mechanisms. *Int J Heat Mass Transfer* (2018) 117:940–50. doi:10.1016/j.ijheatmasstransfer.2017.10.045

22. Sun X, Sun B, Gao Y, Wang Z. A model of multiphase flow dynamics considering the hydrated bubble behaviors and its application to deepwater kick simulation. *J Energ Resour Tech* (2018) 140(8):082004. doi:10.1115/1.4040190

23. Sun X, Xia A, Sun B, Liao Y, Wang Z, Gao Y. Research on the heat and mass transfer mechanisms for growth of hydrate shell from gas bubbles. *Can J Chem Eng* (2019) 97(6):1953–60. doi:10.1002/cjce.23462

24. Clift R, Grace JR, Weber ME. *Bubbles, drops, and particles [M]*. United States: Courier Corporation (2005).

25. Sun X, Sun B, Wang Z, Chen L, Gao Y. A new model for hydrodynamics and mass transfer of hydrated bubble rising in deep water. *Chem Eng Sci* (2017) 173:168–78. doi:10.1016/j.ces.2017.07.040

26. Sun B, Guo Y, Wang Z, Yang X, Gong P, Wang J, et al. Experimental study on the drag coefficient of single bubbles rising in static non-Newtonian fluids in wellbore. *J Nat Gas Sci Eng* (2015) 26(26):867–72. doi:10.1016/j.jngse.2015.07.020

27. Sun CY, Peng BZ, Dandekar A, Ma QL, Chen GJ. Studies on hydrate film growth. *Annu Rep Prog Chem Sect C: Phys Chem* (2010) 106:77–100. doi:10.1039/b811053k

Nomenclature

Variables

C_D drag coefficient

C_i gas concentration on the inner surface of the hydrate shell, m^3/m^3

C_{ins} gas solubility at the hydrate/liquid interface, m^3/m^3

C_L compressibility of the drilling fluid, 1/Pa

C_o gas concentration on the outer surface of the hydrate shell, m^3/m^3

C_w compressibility coefficient of the wellbore, 1/Pa

C_∞ gas concentration in the liquid bulk, m^3/m^3

D_g gas diffusion coefficient in the liquid, m^2/s

D_h gas diffusion coefficient in the hydrate shell, m^2/s

E_{Li} volume of the drilling fluid in segment i of the wellbore, m^3

h_i depth of segment i, m

i segment number

J_{diff} gas diffusion rate through the hydrate film, m^3/s

J_k gas dissolution rate on the outside of the hydrate shell, m^3/s

J_{perm} water imbibition rate through the hydrate film, m^3/s

M_g molecular mass of gas, kg/mol

M_w molecular mass of water, kg/mol

m_{gi} mass of free gas in segment i of the wellbore, kg

Δm_{hi} hydrate growth rate in segment i of the wellbore, kg

Δm_{soli} gas dissolution rate in segment i of the wellbore, kg

N_b number of gas bubbles in a segment of the wellbore

N_h hydration number

P_f fluid pressure in segment i of the wellbore, Pa

P_w bottomhole pressure, Pa

Q_g gas influx rate at the open-hole section, m^3/s

Q_{loss} static filtration rate of the drilling fluid, m^3/s

R bubble radius, m

Re terminal Reynolds number of gas bubbles

Δt time interval, s

t well shut-in time, s

v_g gas rise velocity, m/s

V_w volume of the wellbore, m^3

Greek symbols

ρ_g gas density, kg/m^3

ρ_h hydrate density, kg/m^3

ρ_{soli} density of the dissolved gas in segment i, kg/m^3

σ water/gas interfacial tension, N/m

μ_w viscosity of water, Pa·s

δ thickness of the hydrate shell, m

Frontiers in Physics

Investigates complex questions in physics to understand the nature of the physical world

Addresses the biggest questions in physics, from macro to micro, and from theoretical to experimental and applied physics.

Discover the latest Research Topics

See more →

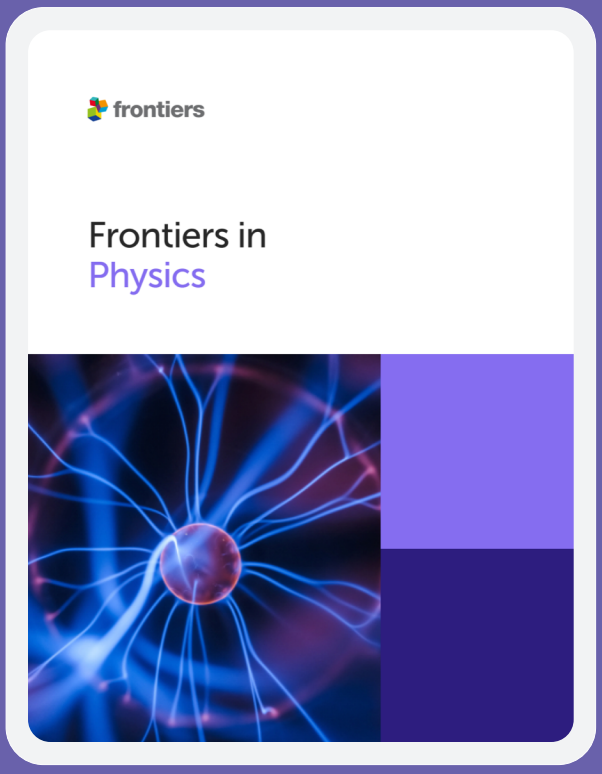

Frontiers

Avenue du Tribunal-Fédéral 34
1005 Lausanne, Switzerland
frontiersin.org

Contact us

+41 (0)21 510 17 00
frontiersin.org/about/contact